Modelling the physiological basis of cerebral blood flow



Selena Milanovic

St Cross College

University of Oxford

A thesis submitted for the degree of

Doctor of Philosophy

Hilary Term 2021

To my grandmothers:

Vera Đokić and Nedeljka Milanović,
who are the pillars of my strength
and the roots of my humour.

Acknowledgements

Personal

As a DPhil student, you often fantasise about the day you will be writing the acknowledgements of your manuscript, thinking a sense of accomplishment is all you will feel at the end of such a vast project. But when the day comes, a wave of melancholy for the days gone by washes over you. Looking back at the past few years, I find it truly difficult to express my gratitude in a handful of succinct paragraphs, but I will try, knowing that these words of thanks will do no justice to the encompassing support I received.

Indubitably, I wish to start by saying that none of this would have been possible without the unceasing guidance of my supervisor, Prof. Stephen Payne. To him, I will always be grateful for trusting in me and letting me explore the world of physiological modelling with more freedom and patience than one could ever ask for. If I were to mention the key lesson that he taught me, it would be the importance of standing on my own two feet. For that, and so much more, I cherish him as one of my life's mentors.

Being part of the Cerebral Haemodynamics Group (CHG), and seeing it grow from me as the only member to what is now a 14-people team, has been a wonderful journey. To Minh and Albert, who have been with me since the early days, I want to say thank you for being the most fun lab pals. I will always fondly remember the way we used to stick together, when at conferences we decided to be brave enough to approach the "brain modelling legends" in person, for the very first time.

To Dr. Moss Zhao, who became one of my dearest friends, I owe more thanks than this section allows. His infectious enthusiasm, regardless of whether our late night discussions were about brain perfusion or mountain hikes, was the fuel that my code and I so often needed.

Luna and Tara, my forever little sisters, I thank for joyfully trotting around the globe to come visit me countless times throughout my academic career. Finally, my gratitude goes to my father, Krstivoje, for introducing me to the beauty of numbers and to my mother, Dušica, for reminding me that numbers aren't everything.

Institutional

Throughout my DPhil, I have been incredibly lucky to be supported by institutions and communities that helped me develop far beyond my scientific curiosity. To my college, St Cross, I will forever be grateful for the warm and welcoming environment it engulfed me in. The enriching conversations about history and architecture that marked every formal dinner will forever be one of my fondest memories. To the rowing club, that took me to the river more often than the graduate department of studies should ever know, I am thankful for reminding me of my resilience and the importance of letting go.

I also want to thank the Women in Engineering society for presenting me with the opportunity to be involved in outreach programmes, aiming to inspire the next generation of young scientists. These engagements were always deeply gratifying and showed me the tangible impact one can have.

Above all, I owe my thanks to the University of Oxford, for letting me into a world where my hunger for knowledge expanded far beyond the science book shelves. At last, with a heavy heart and the spirit of a hitchhiker, all there is left to say is:

So long, and thanks for all the formals.

Research dissemination

Journal publication

Selena Milanovic, Kira Shaw, Catherine Hall, Stephen Payne. *Investigating the role of pericytes in cerebral autoregulation: a modelling study*, Physiological Measurement - Focus on Cerebral Blood Flow 42.5 (2021).

Awards

- **Best student presentation, International Cerebral Autoregulation Research Network (CARNet) conference**
  April 22nd-24th 2021, Online.
- **Winner of the Lightning Round Competition, Medtronic**
  Awarded for excelling at pitching my PhD research in 3 minutes and 3 slides; August 24th 2020, Online.
- **Best student presentation, Virtual Physiological Human (VPH) Conference**
  August 25th - 28th 2019, Online.
- **STEM for Britain speaker, House of Commons, Parliament of the United Kingdom**
  My PhD work was selected as one of the most promising research projects in the UK and I was therefore extended the honour of presenting it to MPs; March 9th 2020
- **Best student presentation, Intracranial Pressure (ICP) and Cerebral Autoregulation Research Network (CARNet) conference**
  September 9th-13th 2019, Leuven, Belgium.

Public talks

- **Invited speaker, Medtronic**
  Understanding brain degenerative diseases through modelling, October 29th 2020, Online.
- **Seminar, Institute of Biomedical Engineering, University of Oxford**
  Cerebral blood flow regulators: oxygen, glucose and pericytes, October 4th 2019.

Conferences

- **Cerebral Autoregulation Research Network (CARNet): Oral presentation**
  International conference at which I offered an oral presentation; April 22nd - 24th 2021, Online.

- **Virtual Physiological Human: Poster presentation**
  International conference at which I offered a poster presentation; August 25th - 28th 2019, Online.

- **Intracranial Pressure (ICP) and Cerebral Autoregulation Research Network (CARNet): Oral presentation**
  Annual international conference of my field of research at which I offered an oral presentation; September 9th-13th 2019, Leuven, Belgium.

- **Brain: Poster presentation**
  International symposium on cerebral blood flow and metabolism; my poster was kindly presented by my supervisor; July 4th -7th 2019, Yokohoma, Japan.

- **Integrated control of cerebral blood flow, Royal Society Meeting**
  Series of talks on cerebral autoregulation by leading experts in the field; December 3rd - 4th 2019, Buckinghamshire, UK.

- **Cerebral Autoregulation Research Network (CARNet): Poster presentation**
  Annual international conference at which I offered a poster presentation; June 18th - 19th 2018, Oxford, UK.

- **Neuron and Brain Mechanics symposium**
  Series of talks on brain tissue mechanics by leading experts in the field; March 22nd-23rd 2018, Oxford, UK.

Abstract

Problem: In a time when brain degenerative diseases are the leading cause of disabilities and death, affecting over 300 M people worldwide, investigating the nature of the onset of brain degeneration is an imperative. Dysfunctions in CBF regulation are an early sign of disease onset, yet the inadequacy of imaging techniques to provide information on microvascular vessels (diameter $<$ 1mm) and the poor translatability of animal experimental data both promote the use of computational research tools. Therefore, quantifying the role that each regulatory variable has in changing CBF has the potential of providing a clearer picture of how the brain behaves in health and disease. **Aim:** A novel mathematical model that defines the relationship between the metabolic demands of the tissue and the active vasculature response is presented here. **Methods:** As nutrient exchange occurs at a small length scale in the brain, particular effort was dedicated to designing a microvasculature network model that would be adequate for an investigation of the relationship between nutrient supply and demand. Hence, large vessels that can be imaged (diameter $>$ 1mm) were modelled using an electrical circuit equivalent, while the microvasculature bed's role in regulating CBF was modelled through a bifurcating network of vessels representative of the physiological geometry. Small arteries and capillaries are the only actively regulating vessels, whose changes in diameter are achieved by an oxygen-sensitive compliance and by experimentally determined pericyte cell activity respectively. **Results:** It was experimentally determined that upon neural activation, pericyte cells dilate capillaries by 2.5%, increasing CBF locally to match the metabolic demand of the active brain region. Moreover, the role of three CBF drivers: oxygen, pericytes and neurons, was quantified computationally. Under steady state conditions the cerebral autoregulation curve was successfully simulated across a wide range of ABP. For rapid changes in ABP, oxygen alone plays a key role in modulating the peak CBF increase (30%) but is weak in modulating the speed of the response (11 s). On the other hand, neural activation and the resulting pericyte activity accelerate the speed of the dynamic vasculature response (4 s), ultimately providing results that are in very close agreement with experimental data of human CBF regulation. **Conclusion:** The dynamic analysis underlined the essential role of a fast response in the microvascular bed driven by pericytes. These findings support the widely accepted experimental findings that suggest that an inadequate response of the microvascular bed is one of the first dysfunctions in the cascade of events that lead to brain degenerative diseases.

Contents

List of Figures **xii**

List of Tables **xx**

List of Abbreviations **xxii**

1 Introduction **1**
- 1.1 Motivation . . . 2
  - 1.1.1 The imaging gap . . . 3
- 1.2 Computational research . . . 4
- 1.3 Aim . . . 5
- 1.4 Outline . . . 6

2 Background **8**
- 2.1 Physiology . . . 9
  - 2.1.1 Arterial supply . . . 9
  - 2.1.2 Venous return . . . 10
  - 2.1.3 Capillary bed . . . 11
  - 2.1.4 Structure and geometry . . . 12
  - 2.1.5 Vessel tone . . . 13
- 2.2 Blood flow regulation . . . 14
  - 2.2.1 Cerebral autoregulation . . . 16
  - 2.2.2 Capillary reactivity . . . 17
  - 2.2.3 Blood flow reduction . . . 18
  - 2.2.4 Cellular metabolism . . . 20
- 2.3 Cerebral diseases . . . 21
  - 2.3.1 Alzheimer's disease . . . 22
  - 2.3.2 Ischaemic stroke . . . 22
  - 2.3.3 Diabetic retinopathy . . . 22
- 2.4 Modelling techniques . . . 23
  - 2.4.1 Whole brain models . . . 24
  - 2.4.2 Network models . . . 27
  - 2.4.3 Biochemical feedback models . . . 28

2.4.4 Capillary bed models 30
2.5 Summary 31

3 Neurovascular coupling **33**
3.1 Blood 34
3.2 Poiseuille's Law 35
3.3 Viscosity 36
3.4 Metabolic sensitivity in the neurovascular unit 37
3.4.1 Oxygen sensitivity 38
3.4.2 Glucose consumption 38
3.4.3 Pericyte activity 39
3.4.4 Neurons 41
3.4.5 Metabolite interactions 41
3.5 Modelling glucose consumption 43
3.5.1 Relating metabolism and blood flow 47
3.6 Summary 51

4 Experimental data analysis **53**
4.1 Experimental setup 54
4.2 Capillary diameter variation 55
4.2.1 Processing 56
4.2.2 Selection 57
4.2.3 Vessel trace 58
4.2.4 Imaging depth 60
4.3 Frequency analysis 63
4.3.1 Imaging depth dependence 65
4.4 Data fitting 66
4.4.1 Time constants 69
4.5 Statistical significance 70
4.6 Calcium concentration 73
4.7 Local metabolic and haemodynamic changes 74
4.7.1 Blood flow and volume 75
4.7.2 Oxygen metabolism 80
4.8 Summary 84

5 Cerebrovascular model **88**
5.1 Electrical circuit . . . 89
5.1.1 Lumped parameter model . . . 90
5.2 Network model . . . 93
5.2.1 Flow . . . 95
5.2.2 Oxygen supply . . . 96
5.3 Model feedback . . . 99
5.3.1 Flow . . . 99
5.3.2 Oxygen . . . 100
5.3.3 Oxygen and pericytes . . . 101
5.3.4 Neural activation . . . 101
5.4 BOLD signal . . . 102
5.5 Summary . . . 103

6 Simulation results **104**
6.1 Steady state . . . 105
6.1.1 Small vessel compliance . . . 105
6.1.2 Blood flow . . . 107
6.1.3 Blood volume . . . 110
6.2 Dynamic response . . . 112
6.2.1 Oxygen partial tissue pressure . . . 112
6.2.2 Vessel compliance . . . 113
6.2.3 Blood flow . . . 114
6.2.4 Cerebrovascular resistance . . . 116
6.2.5 Blood volume . . . 119
6.2.6 $CMRO_2$ and BOLD . . . 120
6.3 Summary . . . 121

7 Discussion **124**
7.1 Cerebral perfusion . . . 125
7.2 Nutrient consumption . . . 126
7.2.1 Glucose . . . 127
7.2.2 Oxygen . . . 128
7.3 Methods . . . 131
7.3.1 Experimental procedure . . . 131
7.3.2 Modelling approach . . . 132
7.4 Computational results . . . 133
7.4.1 Feedback mechanisms . . . 133
7.4.2 Vessel compliance . . . 134
7.4.3 Blood flow . . . 136

7.4.4 Blood volume 140
7.4.5 $CMRO_2$ and BOLD 141
7.5 Pericyte activity 143
7.5.1 Large and small capillaries 144
7.5.2 Blood flow and volume 146
7.5.3 Calcium signalling 148
7.6 Study limitations 149
7.6.1 Experimental 149
7.6.2 Computational 150
7.7 Summary 153

8 Conclusion **155**
8.1 Synopsis 156
8.2 Result implications 162
8.2.1 Clinical relevance 163
8.3 Future work 165

Appendices

References **174**

List of Figures

1.1 Data of the 2018 report of the Office of National Statistics [3] show that the yearly economical burden of dementia patients exceeds that of cancer and cardiac patients combined, yet it only accounts for 11% of the total research funds. 3

2.1 The internal carotid and vertebral arteries (left); jugular vein and superficial temporal veins (right). Reproduction of a lithograph plate from *Gray's Anatomy of the Human Body, 20th edition*. 10
2.2 The arteries on the base of the brain forming the circle of Willis (left); large venous vessels and sinuses of the brain (right). Reproduction of a lithograph plate from *Gray's Anatomy of the Human Body, 20th edition*. 10
2.3 Microvasculature of the collateral sulcus in the temporal lobe, (a) general view; (b) and (c) are fractions of the collateral sulcus; (d) depth range of vessels obtained from confocal microscopy imaging. Figure reproduced from Cassot et al. (2006) [15]. 11
2.4 Schematic representation of factors contributing to the regulation of blood flow. Reproduced without modification from Duffin et al. (2009) [26]. 14
2.5 Interaction between parameters governing nutrient supply in the brain. Reproduced without modification from Duffin et al. (2009) [26]. 15
2.6 The cerebral autoregulation mechanism ensures a steady CBF over a wide range of ABP. When pressure drops below the LLA the vessels collapse, while an ABP above the ULA causes endothelial layer damage. 16
2.7 Region-specific brain vascular dysfunction including deficiencies in CBF maintenance and BBB breakdown are commonly found in the early stages of multiple neurodegenerative disorders. Sweeney et al. (2018) [44] highlighted the brain regions where these dysfunctions occur and the brain degenerative diseases associated to these disruptions in perfusion. The quoted diseases are Alzheimer's disease (AD), Parkinson's disease (PD), Huntington's disease (HD), amyotrophic lateral sclerosis (ALS) and multiple sclerosis (MS). Figure modified and reproduced from [44]. 19

2.8 Oxygen and glucose are delivered (dotted red arrow) through the blood by capillary vessels. Subsequently, glucose transforms into pyruvate through glycolisis and enters the mitochondria. Here, together with oxygen molecules, it starts the oxidative phosphorylation process generating energy in form of ATP. 21
2.9 Capillary constriction linked diseases: (a) Alzheimer's Disease; (b) cerebral ischaemia; (c) diabetic retinopathy. The outermost layer is the basal lamina (red); the pericyte (green) is wrapped around the endothelial cell (beige); β-amyloid plaques (blue) and polymorphonuclear leukocyte (yellow). Modified picture taken from Hamilton et al. (2010) [46] 23
2.10 Schematic representation of the model proposed by Boas (2008) where the dashed lines represent the microvascular vessel group. [55] . . . 27

3.1 (a) Empirically derived dependence of blood viscosity on haematocrit in an in vitro model; (b) Empirically derived dependence of blood viscosity on haematocrit in an in vivo model. Figures reproduced without changes from [2]. 37
3.2 (a) Graphical representation of pericytes wrapping around the endothelial layer longitudinally (1) and transverse section (2); (b) fluorescent markers can be used to identify pericytes where the pericyte is in red (1) and endothelial layer is in green (2). The scale bar in the section b(3) measures $20\mu m$. Modified picture taken from [36]. 39
3.3 Schematic of the physiological cascade of events relating neural activity to CBF regulation. Brain activation induces an increase in Ca^{2+} in the tissue, activating pericytes, which by relaxing dilate capillaries ultimately reduce the resistance of the capillary bed (R_N). Simultaneously, neural activity increases nutrient consumption, with oxygen sensitivity of the tissue driving the compliance of small arteries (C_{sa}). The combined effect of these two cascades of events regulates CBF, aiming to supply the nutrient consumption increase given by brain activation. 42
3.4 A simplified representation of pericyte activity and nutrient exchange between capillary and tissue. A key difference between oxygen and glucose supply is that while oxygen diffuses freely, glucose relies on transport proteins. This is taken into account by including a time delay variable in the glucose model. 43
3.5 ADP (a) and ATP (b) percentage variation upon a 40% increase in CBF at $t = 0$. 47

3.6 Capillary (a) and tissue (b) oxygen and glucose levels percentage variation upon a 40% increase in CBF at $t = 0$. 47
3.7 LAC , GLC_t (a) and $CMRO_2$ and CMR_{glc} percentage variation in the tissue upon a 40% increase in CBF at $t = 0$. 50

4.1 Illustration of the imaging setup, used with permission of Shaw and Hall. (a) Awake mouse walking on a rotating cylinder with a fixed probe on the head; (b) locomotion recording of moving and still mouse; (c) virtual reality maze and (d) drifting gratings used as visual stimulation. 57
4.2 Baseline diameters of capillary vessels. The 26 vessels considered were taken from 6 different mice, each represented by one colour. . . 58
4.3 Example of data processing for Vessel 1 (a) visual stimulus intervals; (b) Ca^{2+} trace over time; (c) normalized vessel trace over time; (d) ensemble average of diameter change. 59
4.4 Averaged capillary diameter change to a $5s$ visual stimulus for all 26 (a) and 8 responsive (b) vessels. 60
4.5 Averaged capillary diameter change to a $5s$ visual stimulus for all 12 (a) and 4 responsive (b) vessels. 60
4.6 Capillary vessel imaged at $0-50\mu m$ depth, where (a)shows the vessel at rest and (b)shows the vessel dilation. 61
4.7 Capillary vessel imaged at $50-150\mu m$ depth, where (a)shows the vessel at rest and (b)shows the vessel dilation. 61
4.8 Capillary vessel imaged at $150-250\mu m$ depth, where (a)shows the vessel at rest and (b)shows the vessel dilation. 61
4.9 Capillary vessel imaged at $250-350\mu m$ depth, where (a)shows the vessel at rest and (b)shows the vessel dilation. 62
4.10 Averaged capillary diameter variation upon visual stimulation across 4 imaging depth ranges. 62
4.11 Large vessels ($6-10\mu m$); Unnormalised power spectra trace (a) Normalized power spectra trace for 1/f noise (b). The locomotion frequency is illustrated by a vertical dotted line at 0.1 Hz. 64
4.12 Small vessels ($2-6\mu m$); Unnormalised power spectra trace (a) Normalized power spectra trace for 1/f noise (b). The locomotion frequency is illustrated by a vertical dotted line at 0.1 Hz. 64
4.13 All vessels ($2-10\mu m$); Unnormalised power spectra trace (a) Normalized power spectra trace for 1/f noise (b). The locomotion frequency is illustrated by a vertical dotted line at 0.1 Hz. 65

4.14 Imaging depth ($0 - 50\mu m$); Unnormalised power spectra trace (a) Normalized power spectra trace for 1/f noise (b). The locomotion frequency is illustrated by a vertical dotted line at 0.1 Hz. 66
4.15 Imaging depth ($50 - 150\mu m$); Unnormalised power spectra trace (a) Normalized power spectra trace for 1/f noise (b). The locomotion frequency is illustrated by a vertical dotted line at 0.1 Hz. 66
4.16 Imaging depth ($150 - 250\mu m$); Unnormalised power spectra trace (a) Normalized power spectra trace for 1/f noise (b). The locomotion frequency is illustrated by a vertical dotted line at 0.1 Hz. 67
4.17 Imaging depth ($250 - 350\mu m$); Unnormalised power spectra trace (a) Normalized power spectra trace for 1/f noise (b). The locomotion frequency is illustrated by a vertical dotted line at 0.1 Hz. 67
4.18 Rectangular function representing the single stimulus over time. . . 67
4.19 Model fit with respect to capillary diameter ($6 - 10\mu m$) (a) and ($2 - 6\mu m$) (b) percentage change data points. 69
4.20 Model fit across 4 imaging depths for all responsive vessels. 70
4.21 Time constants variation with imaging depth (per depth category) and respective error bars. 70
4.22 Ca^{2+} concentration change during the neural activation. 73
4.23 In response to the visual stimulus, the peak Ca^{2+} increase is (a) 15.84% for vessels with $2 - 6\mu m$ diameter; and (b) 28.77% for vessels with $6 - 10\mu m$ 74
4.24 In response to a visual stimulus at $t = 0s$, CBF increases by an average of 5.53% across 23 measurements. 76
4.25 In response to a visual stimulus at $t = 0s$, CBV increases by an average of 3.25% across 23 measurements. 76
4.26 Mouse 1; in response to a visual stimulus at $t = 0s$, the average peak CBF (i.e. the equivalent of the Hbt measurement) increase over 4 measurements is 5.53%. 77
4.27 Mouse 2; in response to a visual stimulus at $t = 0s$, the average peak CBF (i.e. the equivalent of the Hbt measurement) increase over 9 measurements is 5.15%. 78
4.28 Mouse 3; in response to a visual stimulus at $t = 0s$, the average peak CBF (i.e. the equivalent of the Hbt measurement) increase over 1 measurement is 1.41%. 78
4.29 Mouse 4; in response to a visual stimulus at $t = 0s$, the average peak CBF (i.e. the equivalent of the Hbt measurement) increase over 3 measurements is 9.04%. 79

4.30 Mouse 5; in response to a visual stimulus at $t = 0s$, the average peak CBF (i.e. the equivalent of the Hbt measurement) increase over 4 measurements is 5.39%. 79
4.31 Mouse 1; in response to a visual stimulus at $t = 0s$, the average peak CBV (i.e. the equivalent of the Hbt measurement) increase over 4 measurements is 4.02%. 79
4.32 Mouse 2; in response to a visual stimulus at $t = 0s$, the average peak CBV (i.e. the equivalent of the Hbt measurement) increase over 9 measurements is 3.05%. 80
4.33 Mouse 3; in response to a visual stimulus at $t = 0s$, the average peak CBV (i.e. the equivalent of the Hbt measurement) increase over 1 measurement is 0.54%. 80
4.34 Mouse 4; in response to a visual stimulus at $t = 0s$, the average peak CBV (i.e. the equivalent of the Hbt measurement) increase over 3 measurements is 6.71%. 80
4.35 Mouse 5; in response to a visual stimulus at $t = 0s$, the average peak CBV (i.e. the equivalent of the Hbt measurement) increase over 4 measurements is 3.35%. 81
4.36 The relationship between CBF and CBV is best represented with a Grubb exponent of 0.73. 81
4.37 In response to a visual stimulus at $t = 0s$, $CMRO_2$ increases by an average of 6.09% across 23 measurements. 82
4.38 Mouse 1; in response to a visual stimulus at $t = 0s$, the average peak $CMRO_2$ increase over 4 measurements is 4.39%. 83
4.39 Mouse 2; in response to a visual stimulus at $t = 0s$, the average peak $CMRO_2$ increase over 9 measurements is 6.57%. 84
4.40 Mouse 3; in response to a visual stimulus at $t = 0s$, the average peak $CMRO_2$ increase over 1 measurement is 5.58%. 84
4.41 Mouse 4; in response to a visual stimulus at $t = 0s$, the average peak $CMRO_2$ increase over 3 measurements is 7.50%. 84
4.42 Mouse 5; in response to a visual stimulus at $t = 0s$, the average peak $CMRO_2$ increase over 4 measurements is 5.39%. 85
4.43 The local increase in calcium results in a CBV increase by 3.25% (yellow); CMRO2 increase by 6.09% (blue) and a CBF increase by 5.53% (red). 85
4.44 In response to a stimulus at $t = 0s$, OEF increases by 0.70% and subsequently drops by a maximum of -2.02% while MTT increases by a maximum of 1.07% and drops by -2.50%. 86

5.1 Schematic representation of the haemodynamic model. A network model representing the behaviour of 6 arteriole generations (red), 1 capillary bed (green) and 6 venule generations (blue) is incorporated in a lumped parameter model whose elements reflect the active or passive role of arteries and veins. 90
5.2 Baseline conditions for the microvasculature network. Across the 13 generations of arterioles (red), capillaries (green) and venules (blue), the (a) pressure drop; (b) oxygen saturation drop are shown (c) tissue volume supplied and (d) oxygen partial tissue pressure. 100
5.3 (a) Nodal blood pressure (p_b) and oxygen saturation (S_{O_2}) for each generation are denoted with a circle, showing the fitted Severinghaus function; (b) volume averaged oxygen partial tissue pressure $\langle\overline{p_t}\rangle$ sensitivity to changes in inlet pressure P_{in} in the first generation of the microvasculature with the baseline value marked. 101

6.1 Vessel compliance across four feedbacks: (a) the flow (F_0) based; the oxygen (F_1) based; (c) the oxygen and pericytes ($F_1 + F_2$); (d) the oxygen, pericytes and neural feedback ($F_1 + F_2 + F_3$). 106
6.2 Vessel volume change across four feedbacks: (a) the flow (F_0) based; the oxygen (F_1) based; (c) the oxygen and pericytes ($F_1 + F_2$); (d) the oxygen, pericytes and neural feedback ($F_1 + F_2 + F_3$). 107
6.3 Cerebral autoregulation across a wide range of ABP for all four feedbacks: (a) the flow (F_0) based; the oxygen (F_1) based; (c) the oxygen and pericytes ($F_1 + F_2$); (d) the oxygen, pericytes and neural feedback ($F_1 + F_2 + F_3$). The models have been validated with data points from cats and mice cited in the literature [110]. 109
6.4 Blood flow and volume relationship for venous volume (V_v), arterial volume (V_a) and total cerebral blood volume (CBV) for the neural feedback model. Experimental data on rats were extracted from Lee et al. [114]. 111
6.5 Partial tissue pressure increases by 18.93% upon a 10% increase in ABP at $t = 0$ and settles to a 2.62% higher baseline in about 6 s. . 112
6.6 Vasculature compliance during dynamic CBF regulation in the for all four feedbacks: (a) the flow (F_0) based; (b) the oxygen (F_1) based; (c) the oxygen and pericytes ($F_1 + F_2$); (d) the oxygen, pericytes and neural feedback ($F_1 + F_2 + F_3$). 113
6.7 Cerebral blood flow variation upon a 10% increase in ABP at $t = 0$ for all four feedbacks: (green) the flow (F_0) based; (blue) the oxygen (F_1) based; (red) the oxygen and pericytes ($F_1 + F_2$); (orange) the oxygen, pericytes and neural feedback ($F_1 + F_2 + F_3$). 114

6.8 Cerebral blood flow variation upon a 10% increase in ABP at $t = 0$ for six baseline conditions of $\overline{ABP}$: 60mmHg (light green), 80 mmHg (dark green), 100mmHg (orange), 120mmHg (red) and 140mmHg (blue). 116
6.9 Graphic representation of the dynamic CBF change upon a 10% increase in ABP for six baseline conditions of $\overline{ABP}$ over the steady state CA curve. 117
6.10 Cerebrovascular resistance variation upon a 10% increase in ABP at $t = 0$ for all four feedbacks: (green) the flow (F_0) based; (blue) the oxygen (F_1) based; (red) the oxygen and pericytes ($F_1 + F_2$); (orange) the oxygen, pericytes and neural feedback ($F_1 + F_2 + F_3$). . 117
6.11 Cerebrovascular resistance change ($drCVR/dt$) during dynamic CBF regulation in the for all four feedbacks: (a) the flow (F_0) based; the oxygen (F_1) based; (c) the oxygen and pericytes ($F_1 + F_2$); (d) the oxygen, pericytes and neural feedback ($F_1 + F_2 + F_3$). 118
6.12 In the feedback ($F_1 + F_2 + F_3$) model: (a) CBV increases by 14.88% and flow by 26.32 upon a 10% increase in ABP at $t = 0$; and (b) arterial volume (V_a) increases by 11.98% and venous volume increases by 2.76%. 120
6.13 $CMRO_2$ increases by 9.10% (a) and BOLD increases by 0.74% (b) upon a 10% increase in ABP at $t = 0$. 121
6.14 Simulation results of the variation in BOLD response across a range of M_{BOLD} values (1-10) experimentally determined by Bulte et al. (2007) [116] for different brain areas. The scale bar indicates the range of peak BOLD signal change. 122

7.1 Haemodynamic response to a decrease in CPP. 125
7.2 Metabolic parameters variability resulting from CBF increase. . . . 128

1 Schematic summary of the process of pericyte activity model definition from raw data. 169
2 Vessel 1; Unnormalised power spectra trace (a) Normalized power spectra trace for 1/f noise (b). 170
3 Vessel 4; Unnormalised power spectra trace (a) Normalized power spectra trace for 1/f noise (b). 170
4 Vessel 11; Unnormalised power spectra trace (a) Normalized power spectra trace for 1/f noise (b). 170
5 Vessel 15; Unnormalised power spectra trace (a) Normalized power spectra trace for 1/f noise (b). 171

6 Vessel 16; Unnormalised power spectra trace (a) Normalized power spectra trace for 1/f noise (b). 171
7 Vessel 18; Unnormalised power spectra trace (a) Normalized power spectra trace for 1/f noise (b). 171
8 Vessel 22; Unnormalised power spectra trace (a) Normalized power spectra trace for 1/f noise (b). 172
9 Vessel 23; Unnormalised power spectra trace (a) Normalized power spectra trace for 1/f noise (b). 172
10 Vessel 2; Unnormalised power spectra trace (a) Normalized power spectra trace for 1/f noise (b). 172
11 Vessel 7; Unnormalised power spectra trace (a) Normalized power spectra trace for 1/f noise (b). 173
12 Vessel 13; Unnormalised power spectra trace (a) Normalized power spectra trace for 1/f noise (b). 173
13 Vessel 24; Unnormalised power spectra trace (a) Normalized power spectra trace for 1/f noise (b). 173

List of Tables

2.1 List of selected capillary models characterised by type (cast or statistical), vessel number, supplied tissue volume and species. . . . 31

3.1 Baseline values of the glucose modelling, extracted from Aubert et al. (2002) [82] 46
3.2 Median values from experimental data from healthy humans presented by Sokoloff (1991) [85]. 49
3.3 Comprehensive overview of the metabolic response to a step-wise increase in CBF. The changes in concentrations of the O_2 and glucose in the capillaries and tissue are presented along with the metabolic increase of each nutrient. 51

4.1 Imaging depth dependent vessel dilation across 4 imaging depth categories. The average peak dilation is reported for large and small capillaries. 63
4.2 Model fit peak dilations for each imaging depth category. 69
4.3 Comprehensive table of all capillary vessel diameters and dilation, depth and time constants for relevant vessels, where D is the diameter, D_{ch} is the diameter change, d is the depth and CV is the coefficient of variance. 71
4.4 Mean values μ, standard deviations σ and error-bars err for each time constant per imaging depth category. 72
4.5 Individual time constant data analysis reporting the p-value, R-squared, R-squared adjusted and root mean square error (RMSE). 73
4.6 Time constant values for the Ca^{2+} fitting function. 74

5.1 Baseline values and constant parameters used in the model. 93
5.2 Vessel parameters for the bifurcating network of 13 generations (6 arterial, 1 capillary and 6 venous): number of vessels n per generation, vessel diameter D, vessel length L, wall thickness h, velocity v and dynamic viscosity μ. 95

5.3 Vessel parameters for the bifurcating network of 13 generations (6 arterial, 1 capillary and 6 venous): pressure drop Δp_b, oxygen saturation S_{O_2}, supplied tissue volume V_t and oxygen partial tissue pressure p_t. 99

6.1 Overview of the characteristic responses of all 4 feedback models. The table shows the differences in lower limit of autoregulation (LLA), upper limit of autoregulation (ULA); peak CBF change; minimum CBF change; the peak small vessel compliance change $C_{sa,N,max}$ and the maximum $V_{sa,N,max}$ small vessel volume change. 110

6.2 Evaluation of the goodness-of-fit of the SS model to the data. For each feedback mechanism, the p-value, R-squared, R-squared adjusted and root mean square error (RMSE) are reported. 111

6.3 Overview of the dynamic responses for six different $\overline{ABP}$ conditions. The peak CBF percentage change (CBF_{max}) is quantified, along with the percentage difference in baseline value ($\Delta\overline{CBF}$) and total response time. 116

6.4 Overview of the dynamic responses of all 4 feedback models. The table shows the maximum changes in arterial compliance $C_{sa,max}$, flow CBF_{max}, total blood volume CBV_{max}, arterial blood volume $V_{A,max}$, venous blood volume $V_{V,max}$, cerebrovascular resistance CVR_{max}, response time and rate of regulation ROR. 119

List of Abbreviations

ABP . . . . . arterial blood pressure

AD . . . . . Alzheimer's disease

ADP . . . . . adenosine diphosphate

ATP . . . . . adenosine triphosphate

BBB . . . . . blood brain barrier

BOLD . . . . . blood oxygenation level dependent

CA . . . . . cerebral autoregulation

CBF . . . . . cerebral blood flow

CBV . . . . . cerebral blood volume

CMR . . . . . cerebral metabolic rate

CNS . . . . . central nervous system

CPP . . . . . cerebral perfusion pressure

CSF . . . . . cerebrospinal fluid

CVR . . . . . cerebrovascular resistance

ICP . . . . . intracranial pressure

LLA . . . . . lower limit of autoregulation

MCI . . . . . mild cognitive impairment

RBC . . . . . red blood cell

ROR . . . . . rate of regulation

SMC . . . . . smooth muscle cell

ULA . . . . . upper limit of autoregulation

WBC . . . . . white blood cell

Svi junaci nikom ponikoše
i u crnu zemlju pogledaše.

And all the heroes retreated
looking at the black earth.

— Serbian epic poem (1720)

1 Introduction

Contents

1.1 Motivation **2**
1.1.1 The imaging gap 3
1.2 Computational research **4**
1.3 Aim **5**
1.4 Outline **6**

The central processing unit that enables us to navigate this world is a meticulously organised $1.5kg$ light system of vessels, tissue, blood and water. To function, the brain relies on $700km$ of vasculature, [1] which is the approximate distance between this manuscript and the International Space Station *and back*. To enable a constant supply of nutrients to the tissue, a tight coupling between metabolic demand and blood flow is essential, with flow being continuously adjusted locally and globally. An impairment in this mechanism leads to cell death in a matter of minutes, as permanent damage is induced. [2] This renders the study of cerebral blood flow (CBF) regulation highly relevant for clinical applications but also very complex as the variables governing it are numerous and are interconnected.

1.1 Motivation

The most common diseases related to brain perfusion deficiencies are stroke and dementia. Within the UK only, approximately 100,000 people have a stroke each year. This can be induced by ischaemia or a haemorrhagic bleed, with the former being the most prevalent one at a ratio of 85:15. The past few years have shown a decrease in stroke rate in both occurrence and death. This can be associated to a lowering in blood pressure across the population as more efforts have been made to reduce the incidence of diabetes, high cholesterol levels and smoking. In addition, today people who are considered to be at risk now monitor blood pressure more regularly and hypertension is treated more actively. [3]

Dementia, on the other hand, has recently overtaken cardiac disease as the leading cause of death in England and Wales. The 2018 report of the Office of National Statistics states that within the UK 0.9 M people are affected by dementia, a number that is expected to reach 1.3 M by 2030. [4] Every year, dementia costs the UK health and social sector about $£12B$, which is more than all cancer and cardiac patients combined (see Figure 1.1). [3]

Strikingly, the resources spent on brain degenerative diseases research do not reflect the threat that they represent. Indeed, almost 89% of all research funds is invested in fighting cancer and cardiac diseases, leaving stroke and dementia scientists with a mere 11%. [3] In summary, the burden of brain degenerative diseases is large and increasing, posing a challenge to the sustainability of the UK's healthcare system. From a global perspective, brain degenerative diseases affect about 300M people worldwide and contribute to about 16.5% of deaths. Moreover, the burden of the disease is such that about 23% of healthy life years are lost. [5] With the global trend of an ageing population, the threat of disabling neurological conditions means that governments will face an increased demand for treatment and support services in the near future. Despite these daunting numbers, scientific research on the topic remains critically underfunded compared to other diseases and therefore the development of effective prevention and treatment strategies are hindered.

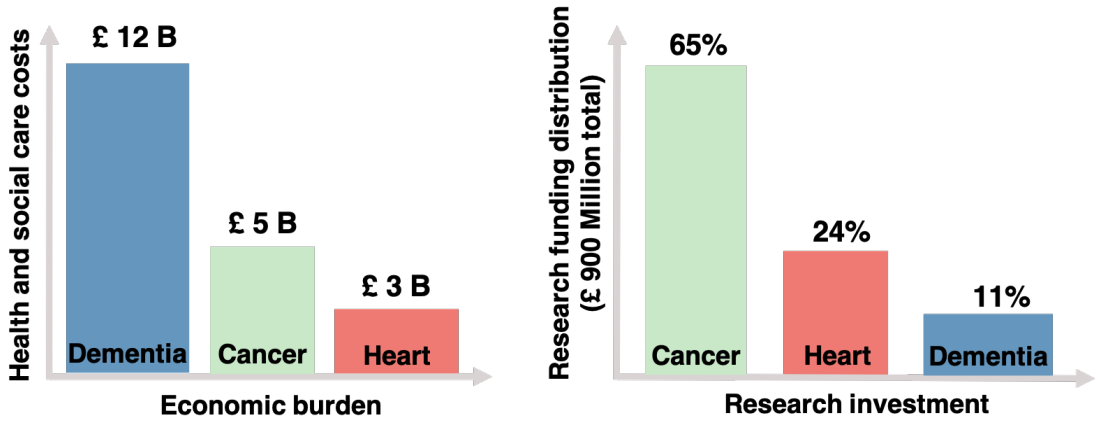

Figure 1.1: Data of the 2018 report of the Office of National Statistics [3] show that the yearly economical burden of dementia patients exceeds that of cancer and cardiac patients combined, yet it only accounts for 11% of the total research funds.

1.1.1 The imaging gap

Both dementia and stroke are caused by a lack of nutrient supply to the brain tissue. The microvasculature plays a crucial role in tissue perfusion and therefore it is necessary to gain insight into its functioning. On a length scale below 1 mm however, imaging techniques do not currently suffice to provide us with the necessary information on the physiological interactions that ensure a healthy cerebral blood flow (CBF). Indeed, below the 1 mm vessel length scale there are relatively few data on human cerebrovasculature, most of which stem from post-mortem anatomical studies such as the classic study by Duvernoy et al. (1981) [6].

At the capillary length scale, where an intricate network of blood vessels supplies brain tissue with nutrients, data are very difficult to acquire and as a result, the studies describing the interaction of the variables that govern the speedy local regulation of CBF are few. While the insights on the vascular network geometry stemming from post-mortem studies are highly valuable, it is also important to note that the translatability of these data to living healthy human subjects is compromised by the fact that the characteristics of the brain tissue and vasculature (e.g. stiffness) change in a matter of minutes after death.

Individual vessels can be imaged in animal models but given the poor translatability

of animal data to human models, this approach has significant limitations. Furthermore, animal studies are also often limited by ethical approvals and availability of animals. A comprehensive understanding of CBF through mathematical models can therefore help us clarify the link between metabolic demand and blood flow regulation. This is necessary in particular for the phenomenon of autoregulation, during which the brain maintains a constant blood flow over a wide range of arterial pressure. Indeed, the exact method with which the brain combines local and global stimuli to respond in an adequate manner is yet to be defined.

1.2 Computational research

Mathematical models represent a suitable approach for complementing imaging techniques in the investigation of the relationship between flow and metabolism which occurs at the microvasculature length scale. An advantage of mathematical modelling is the possibility of coupling them, with the aim of investigating the role of the vasculature at different length scales. Such models can then be applied to study the relation between metabolic demand of the tissue and blood flow. This is a topic of high interest, since diseases such as stroke and dementia are tightly related to deficiencies of oxygen supply to the tissue. [7] Modelling can therefore provide an insight into what imaging techniques fail to describe due to the small scale at which oxygen diffusion occurs.

Also, in the recent years the field of modelling has gained importance and is now regarded as an integral part of research evidence both in Europe and the United states. Indeed, the FDA and the EMA recently recognised modelling and simulation as valid scientific evidence for which guidelines for the correct reporting of computational modelling have been published. [2] Indeed, in the EU modelling is now regarded as an integral part of physiological research technologies [8].

An example is the Virtual Physiological Human (VPH) research project which revolves around a technological framework that aims to allow a collaborative investigation of the human body within a single complex system. The purpose of the project is to gain physiological insights using novel integrated computational

models of the mechanical, physical and biochemical functions of a living human body. [9] The VPH project's purpose is also in strong synergy with the growing need of personalised healthcare, which is bound to shape the future of the medical field.

Given the high complexity of the human brain and the great variability of the characteristics of its physiological mechanisms, it is clear that developing clinically insightful computational tools is an ambitious task that can only be achieved though international cooperation. It is thus that inter-disciplinary research groups, such as the Cerebral Autoregulation Research Network (CARNet: www.carnet.org), originated with the mission to advance the fundamental understanding of CBF regulation and to develop new clinical applications across a wide range of cerebrovascular disease.

1.3 Aim

This research project describes a new model of human CBF regulation, one that aims to provide an extended insight into the physiological phenomena that couple metabolic demand and CBF. The use for the model developed here is that of serving as a foundation for the understanding of the intricate neurovascular coupling relationships, by attempting to quantify the individual contribution of a selected group of variables (oxygen, pericytes and neural activity) in driving CBF regulation. To achieve this, the individual and cumulative effects of three key variables were studied in the regulation of CBF. Firstly, metabolism was considered to be a strong vasodilator, with oxygen partial tissue pressure acting as a modulator of arterial compliance. Secondly, the activity of pericyte cells was introduced as a capillary dilator, further contributing to an active regulation of CBF. Ultimately, neural activity was introduced to emulate a fast vaso-reactivity, resulting in a brain vasculature model whose time response corresponds with that measured experimentally in humans.

Given that the neurovascular coupling mechanism occurs at a small length scale, a microvasculature network of arterioles, capillaries and venules was coupled with a

lumped parameter model of large arteries and veins. This resulted in a model of the complete brain vasculature whose local and global responses were analysed. The activity of pericyte cells was derived from experimental data on pericyte induced capillary diameter variation in mice. Finally, the time response of the model to changes in pressure was analysed, quantifying the role of the proposed CBF regulators and comparing the model's results with human data.

1.4 Outline

The research presented in this manuscript spans from experimental to computational techniques while consistently aiming to be aligned with the need for an extensive understanding of the physiological mechanisms that enable a healthy brain function. A brief outline of the contents is presented here with the aim of serving as a broad overview of the research questions that were answered and of how they relate to the aim.

Chapter 1 introduces the clinical need to more clearly delineate the tight coupling of blood flow and metabolism in the brain.

Chapter 2 is a concise overview of the anatomy and physiology of the brain. Particular attention was given to describing the vasculature geometry in detail, highlighting the specific role and characteristic function of the arterial, venous and capillary beds. Lastly, commonly used modelling techniques that the mathematical model presented here relies on are introduced.

Chapter 3 outlines the haemodynamic laws that the proposed mathematical model relies on, along with the metabolic processes that occur on a cellular level. Subsequently, the role of glucose metabolism as a CBF regulator was computationally defined.

Chapter 4 presents the experimental part of the study, from which the mathematical formulations of active capillary dilation were derived. Moreover, the local changes in oxygen metabolism as a result of neural activation were quantified.

Chapter 5 introduces the cerebrovascular model's structure and governing equations. Large vessels were studied through an electrical equivalent model, while the microvasculature's role in regulating CBF was investigated through a bifurcating network model.

Chapter 6 displays the outcomes of a steady state and a dynamic model analysis. Changes in blood flow, volume and metabolism were quantified and compared to available human data on CBF regulation.

Chapter 7 analyses the implications of the results and limitations of the experimental analysis and the computational model. For the experimental section, the measured local changes in CBF and $CMRO_2$ resulting from the pericyte-induced capillary dilation are discussed. On the other hand, the computationally determined effect of each CBF regulating variable is analysed.

Chapter 8 concludes the manuscript by defining the impact and clinical implications of the presented results. Ultimately, a path towards the future research to be conducted is outlined.

There is nothing new,
except what has been forgotten.

— Marie Antoinette (1755 - 1793)

2 Background

Contents

2.1 Physiology 9
2.1.1 Arterial supply 9
2.1.2 Venous return 10
2.1.3 Capillary bed 11
2.1.4 Structure and geometry 12
2.1.5 Vessel tone 13
2.2 Blood flow regulation 14
2.2.1 Cerebral autoregulation 16
2.2.2 Capillary reactivity 17
2.2.3 Blood flow reduction 18
2.2.4 Cellular metabolism 20
2.3 Cerebral diseases 21
2.3.1 Alzheimer's disease 22
2.3.2 Ischaemic stroke 22
2.3.3 Diabetic retinopathy 22
2.4 Modelling techniques 23
2.4.1 Whole brain models 24
2.4.2 Network models 27
2.4.3 Biochemical feedback models 28
2.4.4 Capillary bed models 30
2.5 Summary 31

2.1 Physiology

Given its strong dependence on nutrient supply, the brain is equipped with a complex vasculature network that perfuses the tissue continuously and removes its waste products. Arteries supply the tissue with oxygenated blood and subsequently veins return the de-oxygenated blood to the heart.

2.1.1 Arterial supply

The aorta carries oxygenated blood away from the heart, it next branches into the common carotid arteries which subsequently branch into the internal carotid arteries, as shown in Figure 2.1. The tissue of the surface of the cranium is supplied by the external carotid arteries whilst the internal carotid arteries penetrate the cranium through the carotid canal in the temporal bone, supplying about 70% of total CBF. [10] Together with the vertebral arteries, which enter the cranium through the neck and supply the remaining 30% of CBF, they form the four main vessels that supply blood to the brain. The vertebral arteries join to form the basilar artery, which connects to the internal carotid arteries through the circle of Willis. [11]

This confluence of arteries comprises of the left and right anterior cerebral arteries, the anterior communicating artery and the posterior communicating arteries and its function is to maintain perfusion of the brain despite changes in flow. [12] A schematic of the large arterial vessels in the brain is provided in Figure 2.2. It is worth noting that the standard structure of the circle of Willis presents substantial variations across the population and in many cases a complete circle of Willis is not present. [13], [14]

An early study by Alpers et al. (1959) [13] reported that 48% of the subjects had some type of variation of the circle of Willis structure, a number that was later on confirmed by Papantchev et al. (2013) [14] who reported a value of 58.6%. Despite these abnormalities, the subjects presented no adverse vascular behaviour. In the case of a vessel blockage however, a difference in vascularisation geometry was found likely to influence the response to changes in blood supply. [14]

2.1.2 Venous return

After the nutrient supply, the de-oxygenated blood flows back to the circulation through a series of veins and sinuses that drain at a confluence at the back of the head (see Figure 2.2). The superior sagittal sinus absorbs the cerebrospinal fluid (CSF) from the meninges and along with the occipital and straight sinus it drains into the transverse sinuses. These connect to the sigmoid sinuses which subsequently join the jugular veins and blood then flows back to the heart for re-oxygenation. [11]

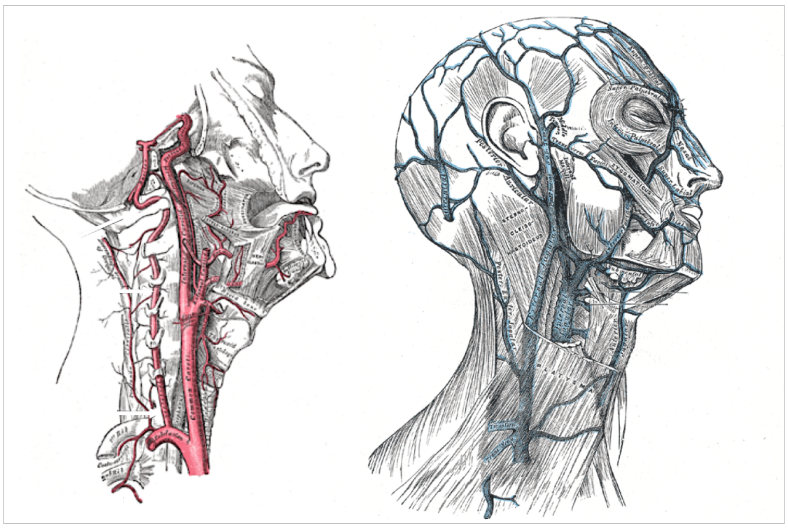

Figure 2.1: The internal carotid and vertebral arteries (left); jugular vein and superficial temporal veins (right). Reproduction of a lithograph plate from *Gray's Anatomy of the Human Body, 20th edition.*

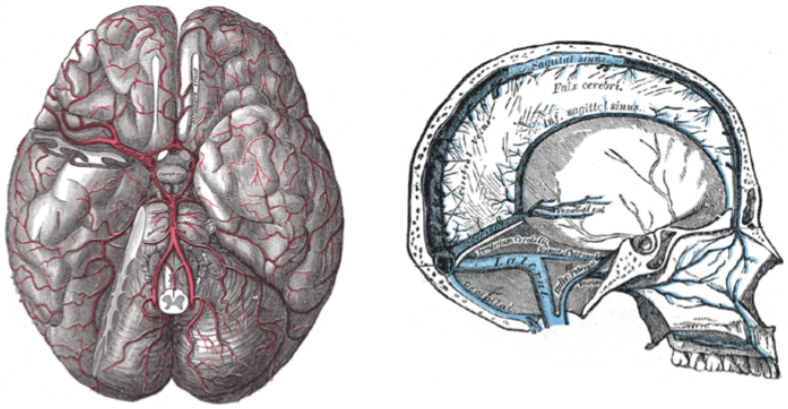

Figure 2.2: The arteries on the base of the brain forming the circle of Willis (left); large venous vessels and sinuses of the brain (right). Reproduction of a lithograph plate from *Gray's Anatomy of the Human Body, 20th edition.*

2.1.3 Capillary bed

The primary role of the capillary network is the supply of nutrients to the tissue, hence its structural properties are tightly linked to the local functional requirements. At this length scale, flow can be adjusted rapidly to changes in metabolic demand. Imaging data on capillary vessels are very hard to acquire, given that a tissue voxel of 1 mm^3 contains up to 10,000 capillaries. [2]

In 1981 Duvernoy et al. published a study [6] whose aim was to visualise the complex network structure perfusing the brain. Following death, 25 brains were injected with a low intensity resin and high resolution images were obtained using a scanning electron microscope. Despite the scarce quantitative information these images provided, they provided a detailed outline of cortical pial vessels and highlight differences in geometry between subjects. [6]

The first quantitative study of the cerebral microcirculation was performed by Cassot et al. (2006) [15]. Similarly to Duvernoy et al. (1981), an injection of India ink served as a marker. Confocal laser microscopy was then used to provide the images. An example is shown in Figure 2.3, where the vasculature of the collateral sulcus in the temporal lobe is shown. Furthermore, the authors investigated the connectivity of the network, concluding that 94.4% of the vessels present bifurcations, with the remaining 4.3% and 1.3% being trifurcations and simple and multiple nodes respectively. [15]

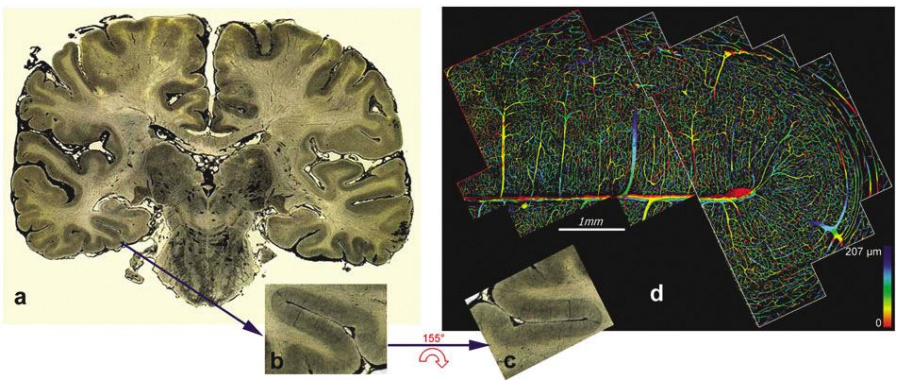

Figure 2.3: Microvasculature of the collateral sulcus in the temporal lobe, (a) general view; (b) and (c) are fractions of the collateral sulcus; (d) depth range of vessels obtained from confocal microscopy imaging. Figure reproduced from Cassot et al. (2006) [15].

2.1.4 Structure and geometry

The two defining characteristics of vessels are their structure and their geometry. Additionally, due to its strong dependence on nutrient supply, the adaptability of the vasculature, in terms of geometry and vessel response, plays an important role. Experimental studies [16], [17], [18] have shown that the response to changes in flow is governed by the adaptability of the vessels' physiology as well as their orientation. There is a clear distinction in structure between arterial, venous and capillary vessels, since their physiological characteristics are defined by their function.

Both arterial and venous vessels consist of a three layered structure whilst capillaries are made up of a single layer of endothelial cells. This fundamental difference is governed by the difference in pressure at which they operate. Indeed, the thin capillary membrane is fundamental for nutrient diffusion from the blood to the tissue. On the other hand, arteries are characterised by a thick layer of smooth muscle cells that enable a rapid and significant change in diameter. The structure of venous vessels is very similar to the arterial one, the most marked difference being a thinner smooth muscle layer given that they operate at a lower blood pressure compared to arteries. [19]

Both arterial and venous vessels show a tree-like structure, enabling them to penetrate the deeper layers of the tissue. Indeed, smaller scale vessels are found in the white matter, a volume of the tissue which is characterised by an elevated number of axons and fewer neuronal cells. Each tissue voxel is supplied by a vessel unit, with a ratio of around 3:1 arterioles to venules. [6]

The physiological differences between vessel layers lead to a distinction in mechanical properties. This renders the assumption of any homogenous mechanical properties a simplification. A common assumption is that the vessel wall is a purely elastic material, whereas it actually exhibits a viscoelastic behaviour with energy being dissipated within the wall after every pulsation. [19]

The cerebral cortex, which is the outermost layer of the brain, is about 2-4 mm thick and is composed of grey matter, a volume predominant with neuronal cells and few axons. [20] The folded arrangement of the cerebral cortex serves the purpose of

increasing surface area, which is thought to be essential for a greater development of diversity of functional areas. [21], [22] In humans, these functional modules comprise memory, perception and language and similarities in the structural architecture of the cortex have been found to link individuals with similarly developed functional abilities across the population. [23]

2.1.5 Vessel tone

The modulation of flow is achieved through changes in vessel resistance which consequently are mainly attributed to changes in diameter, as vessel length essentially remains constant. Indeed, the resistance of a vessel (R) is inversely proportional to its radius (r) raised to the fourth power ($R = 1/r^4$), therefore providing a very high degree of control. A decrease in blood pressure causes a decrease in vessel radius, thus increasing resistance which obstructs flow. At this point, the myogenic response is activated, leading to vasodilation (i.e. increasing vessel radius) to ensure the maintenance of flow. [24]

The presence of maximal dilation and constriction of vessels represents the lower limit of autoregulation (LLA) and the upper limit of autoregulation (ULA) of the cerebral autoregulation (CA) curve. The delayed response of the compliance suggests that before the start of the active response is manifested, the passive response needs to be overcome. This suggests that the myogenic response is a strong process whose changes in magnitude will show significant effects within the autoregulatory mechanism. The active response occurs at an arteriolar level, given their structural predisposition for it (i.e. the thick smooth muscle layer) and arteriolar tone can therefore be assumed to be governed by local, neural and hormonal stimuli in decreasing order of magnitude. [24]

The venous network is governed by the same parameters regulating arteriolar tone, only with a lower sensitivity due to their lower baseline tone. The primary role of the venous bed remains the control of blood volume, as it constitutes approximately 75% of the total cerebral blood volume (CBV). The co-dependence of the arteriolar, capillary and venous vascular bed makes it difficult to quantify

their individual contributions to CBF regulation without a mathematical model. Therefore, flow regulation models need to aim to distinguish between scale, geometry and vasculature dependent stimuli. Indeed, the experimental study by Hamel (2006) [25] has concluded that different parts of the nervous system govern the behaviour of different vessels. Examples are the peripheral nerve ganglia that control surface brain vessels and intrinsic brain neurons that govern vasculature tone changes in the deep brain.

2.2 Blood flow regulation

Cerebral blood flow is regulated by a set of interdependent stimuli, which can be roughly grouped into five categories: metabolic, autoregulatory, neurogenic, chemical and sympathetic. There is a high variation in sensitivity to these factors, it being the highest for metabolic, chemical and systemic responses and very low for the remaining ones (see Figure 2.4). [26] The autoregulatory and chemical stimuli are governed by changes in arterial blood pressure and partial CO_2 pressure respectively. They can be regarded as being global in nature, given that they are set by the sympathetic circulation. On the contrary, the remaining stimuli can be considered as being local in nature. [2]

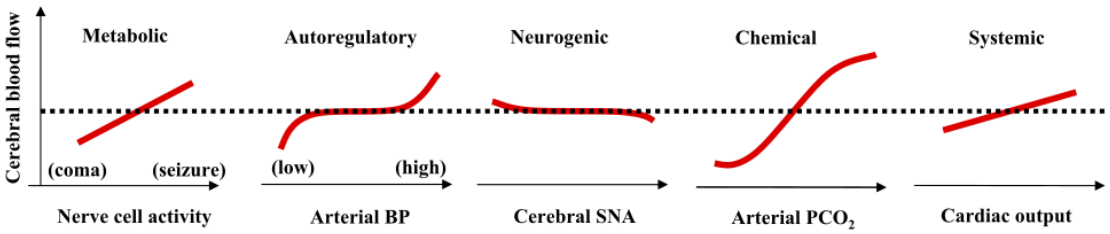

Figure 2.4: Schematic representation of factors contributing to the regulation of blood flow. Reproduced without modification from Duffin et al. (2009) [26].

A scheme representing the interaction between the numerous parameters influencing blood flow regulation is presented in Figure 2.5. Cerebral perfusion pressure (CPP), which is the net pressure gradient driving oxygen delivery to the tissue, is given by the difference between arterial blood pressure (ABP) and intracranial pressure (ICP). The necessity for clinicians to operate with CPP rather than ABP

or ICP, stems from the fact that both ABP and ICP baseline values vary greatly between individuals and as CBF ultimately depends on the combined effect of ABP and ICP, CPP is clinically considered as the true driving pressure. While often used interchangeably across the literature, it is worth noting that cerebral perfusion differs from CBF, as the former expresses the flow passing through a network in a defined tissue voxel (typically in units of ml/100g/min) whilst the latter represents the flow in an individual vessel over time (ml/s).

The amount of flow that reaches the tissue is strongly influenced by vessel resistance which responds to three main inputs: the myogenic, the sympathetic and the metabolic responses. The myogenic response is influenced by changes in CPP and CO_2 levels in the blood. The metabolic response on the other hand, influences CBF by relating oxygen concentration to the demand. Finally, the sympathetic response is governed by the input of the central nervous system. These responses are not independent from each other, therefore changes in one will be reflected in the others.

Similarly to the responses, also the principal parameters are interconnected. Changes in CBF will influence CBV, and together with CSF volume changes affect the ICP. The interdependence of these parameters can be inferred from the fact that the skull represents a fixed volume and that both water and blood are incompressible fluids. [2]

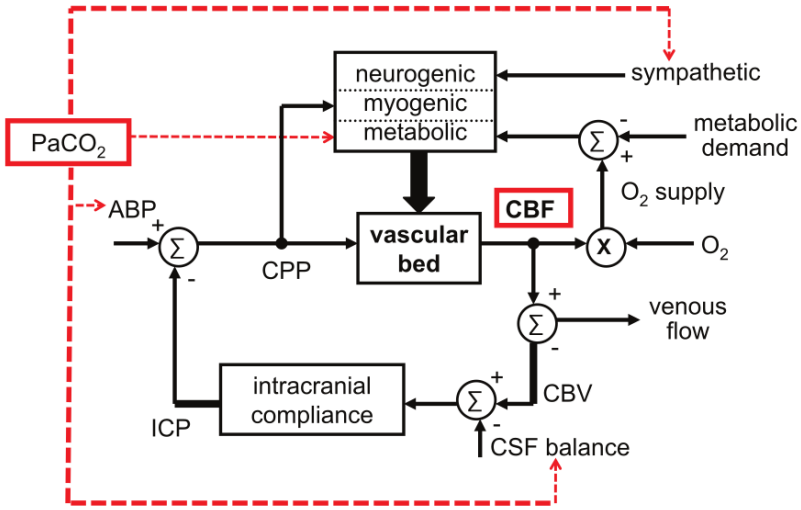

Figure 2.5: Interaction between parameters governing nutrient supply in the brain. Reproduced without modification from Duffin et al. (2009) [26].

2.2.1 Cerebral autoregulation

The process through which the brain's vasculature sustains an adequate and stable CBF is defined as cerebral autoregulation (CA) and is shown in Figure 2.6. It is through this mechanisms that a stable CBF is sustained over a range of approximately ±50% change in ABP from its baseline value (100 mmHg). [24] The first to define this mechanism and to coin its name was Lassen in 1959 [27]. Based on CBF and ABP measurements from 11 human studies, he defined the averaged relation between them and also defined the LLA. [27] The ULA was defined later by Strandgaard et al. (1975) [28].

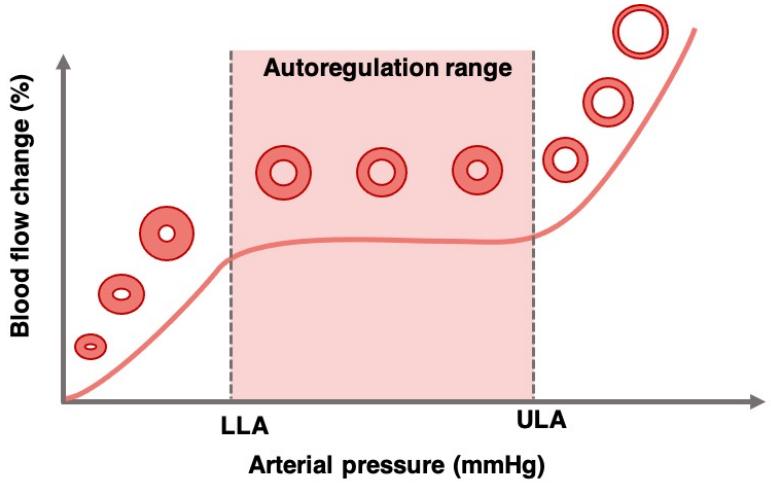

Figure 2.6: The cerebral autoregulation mechanism ensures a steady CBF over a wide range of ABP. When pressure drops below the LLA the vessels collapse, while an ABP above the ULA causes endothelial layer damage.

Autoregulation can be defined as being dependent of vessel tone, neurogenic control and gas levels. [2] While the presence of a plateau in the cerebral autoregulation (CA) curve is a now widely accepted notion, its width and slope have received particular attention in the recent years [29], [30], [31]. Indeed, in a human experimental study presented by Rickards (2015) [30] a narrower and steeper CA plateau is proposed, where the ULA occurs at a CBF percentage change higher than its baseline.

This is a sound approach for two reasons: firstly, the high variability in the vasculature geometry between individuals (despite having the same age, gender

and lifestyle) suggests that CA is not a mechanism whose characteristic values are homogenous across the population [32]; secondly, even within a single individual, fluctuations in temperature [33] and hormones [34] render the concept of homeostasis one that is not focused on precise baseline values but rather baseline ranges.
Ultimately, the mechanisms driving CA remain poorly understood, given the subject-dependent baseline of ABP, the differences in vascular geometry and the lack of defined guidelines for the experimental procedures aiming to define CA across the population. [35] Indeed, current computational models of CBF regulation are primarily validated against animal data. The computational model presented in Chapter 5 will therefore serve to investigate the dependency on the baseline parameters that CA relies on, particularly focusing on the immediate effect of changes in CBF given by dynamic fluctuations in ABP.

2.2.2 Capillary reactivity

The role of the capillary network has recently gained importance, following the popularisation of the notion that pericyte cells play an important role in linking the metabolic demand of the tissue to the vessel supply. [36], [37] These isolated contractile cells are primarily found on capillary vessels and are thought to play a role in the stabilisation of newly formed capillaries, the maintenance of the blood-brain-barrier and the regulation of CBF. [38]
Their role is linked to their position within the capillary bed: pericytes that are in close proximity to the arterioles are responsible for vessel contraction, whilst pericytes located in proximity of the venules are associated with the maintenance of the blood brain barrier (BBB) and the regulation of immune cell entry into the parenchyma. [38] As a consequence of these structural differences, it has been established that pericytes with different physiological roles respond to different therapeutic targets based on protein expression. [39]
Experimental results by Hall et al. (2014) [40] on CBF regulation in rats have shown that capillary dilation occurs faster than arteriolar dilation, with pericytes actively inducing vasodilation. This was concluded from the neuronal activity releasing

messengers before arteriole dilation has occurred, with pericytes showing a baseline relaxed tone. The difference in signal between arteriolar and capillary response is however not yet clear, both in time and in nature. [40]

The assumption of the purely passive response of capillaries has therefore largely now been abandoned, as numerous experimental results [40], [41] have underlined their importance in CBF regulation, attributing to pericytes a significant component of the response to neural activation. Furthermore, the disruption of the active regulatory mechanisms that occur in the capillary bed have been associated with permanent tissue damage, leading up to the formation of β-amyloid plaques that characterise brain degenerative diseases such as Alzheimer's and dementia. [41], [42]

2.2.3 Blood flow reduction

An adequate supply of blood as well as the structural and functional integrity of blood vessels are all essential for healthy brain functioning. Indeed, low CBF and blood brain barrier (BBB) dysfunction are both indications of neurodegenerative disorders in both humans and animals. In a human experimental study by Ruitenberg et al. (2005) [43], it was found that individuals with greater CBF velocity, as shown by transcranial Doppler measurements in the middle cerebral artery, were less likely to develop dementia or hippocampal and amygdalar atrophy.

Similarly, individuals with mild cognitive impairment (MCI) or early Alzheimer's disease (AD) were found to develop early CBF reductions in the posterior cingulate gyrus and precuneus, as shown by arterial spin labelling. [43] It should however be noted that progression from MCI to AD is associated with more global and severe (up to 40%) CBF reductions, which includes other central nervous system (CNS) regions besides the posterior cingulate gyrus and precuneus, such as bilateral parietotemporal, frontal and occipital cortex, parahippocampal gyrus, hippocampus, and entorhinal cortex. [44]

Figure 2.7 illustrates the commonalities of vascular dysfunction across neurodegenerative diseases, highlighting the specific regions where CBF shortfalls and BBB dysfunctions are evident during the early stages of each disease. Disruptions

of the BBB were found to be related to an increased vascular permeability and dysfunction in transporters. [44]

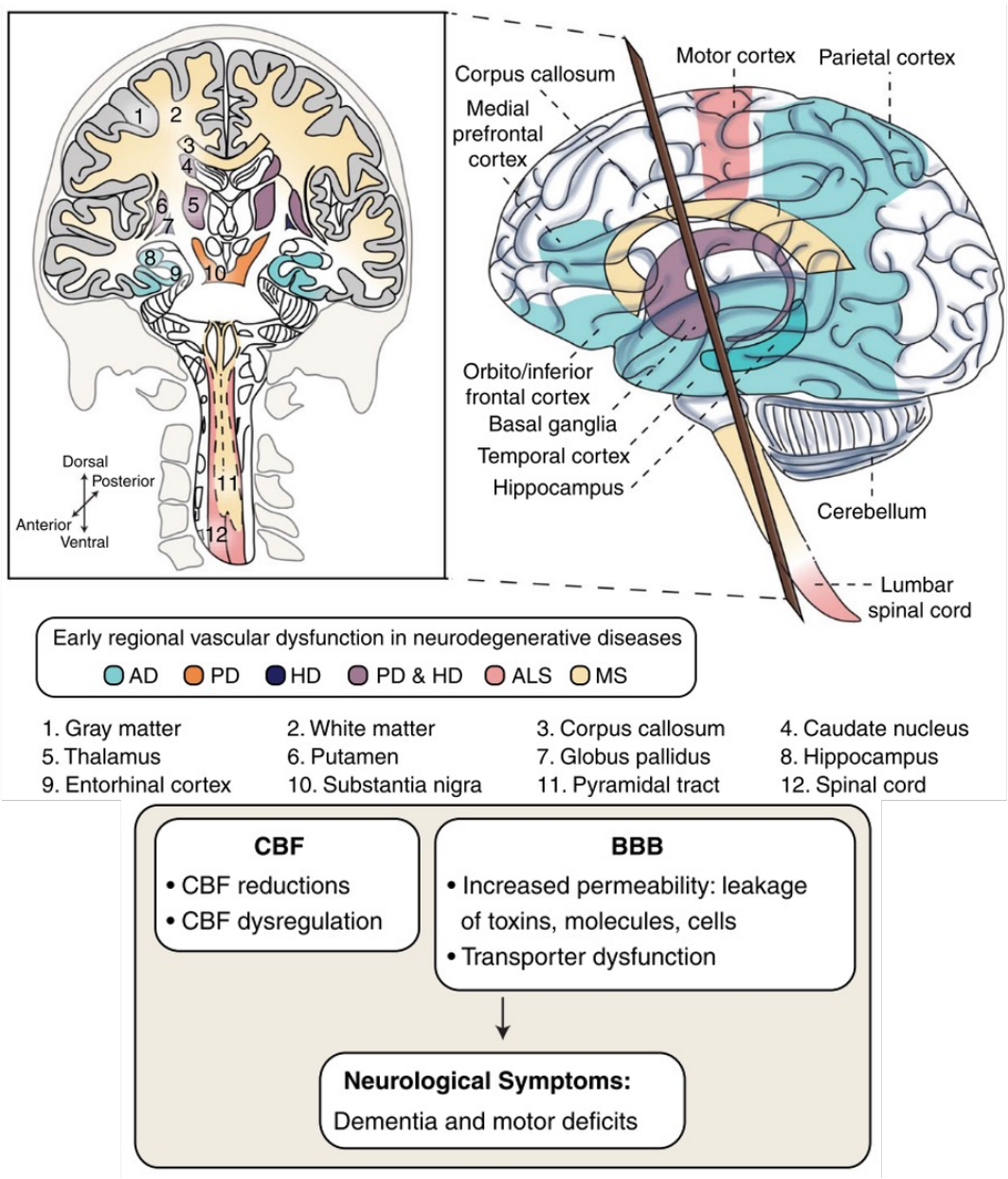

Figure 2.7: Region-specific brain vascular dysfunction including deficiencies in CBF maintenance and BBB breakdown are commonly found in the early stages of multiple neurodegenerative disorders. Sweeney et al. (2018) [44] highlighted the brain regions where these dysfunctions occur and the brain degenerative diseases associated to these disruptions in perfusion. The quoted diseases are Alzheimer's disease (AD), Parkinson's disease (PD), Huntington's disease (HD), amyotrophic lateral sclerosis (ALS) and multiple sclerosis (MS). Figure modified and reproduced from [44].

2.2.4 Cellular metabolism

A constant nutrient supply is essential for the functioning of neurons and other cells in the brain. Cellular metabolism relies highly on glucose supply, as about 75% of it goes to the generation of adenosine triphosphate (ATP) which is the cell's primary source of energy. [2] The metabolic processes taking place inside the cell can be distinguished as two types: aerobic and anaerobic. Aerobic metabolism relies on oxygen for the formation of ATP through adenosine diphosphate (ADP) by a chemical reaction that is described as follows:

$$6O_2 + C_6H_{12}O_6 + 36ADP + 36P_i \rightarrow 6CO_2 + 6H_2O + 36ATP \tag{2.1}$$

This oxidative phosphorylation of glucose produces 36 ATP moles as a primary product and CO_2 and water as by-products. A reversed reaction would generate energy, through the breakdown of ATP into ADP. A less energy efficient way of ATP production that occurs in the absence of oxygen (i.e. anaerobic metabolism) is represented by the anaerobic process as follows:

$$C_6H_{12}O_6 + 2ATP + 2NAD^+ + 4ADP + 2P_i \rightarrow 2C_3H_4O_3 + 4ATP + 2NADH + 2H^+ \tag{2.2}$$

Anaerobic metabolism is thus energy consuming before it is energy generating, as it requires 2 ATP moles for the reaction itself and only generates 4 ATP moles as primary product. [2] If sufficient O_2 is present and CO_2 is produced as a by-product, pyruvic acid ($2C_3H_4O_3$) is passed to the mitochondria where it enters the Krebs cycle, resulting in a further energy extraction process. In the cases of O_2 deficit or dysfunctional mitochondria, pyruvic acid is converted into lactic acid, generating additional ATP. Figure 2.8 summarises the link between neural and metabolic activity in the brain tissue.

Both the Krebs cycle and oxidative phosphorylation take place in the mitochondria, thus except for O_2 and CO_2 that diffuse freely, all other molecules need to be transported inside. Pyruvic acid, ADP and phosphate are produced outside and

therefore must be moved inside, whilst ATP and NADH must be carried outside. ATP is then used for the powering of ionic pumps (potassium, sodium and chloride ions). ADP can be converted into a mixture of ATP and adenosine monophosphate (AMP), with AMP having the ability to degrade into adenosine which can influence vasoconstriction. Moreover, glycogen can be stored by astrocytes (characteristic glial cells of the brain and spinal chord), which can be used as an energy reserve providing protection against hypoglycaemia for several minutes. Functional tasks activate metabolic activity and therefore the circular process of ATP consumption and generation is representative of the neural and metabolic activity codependency. [2]

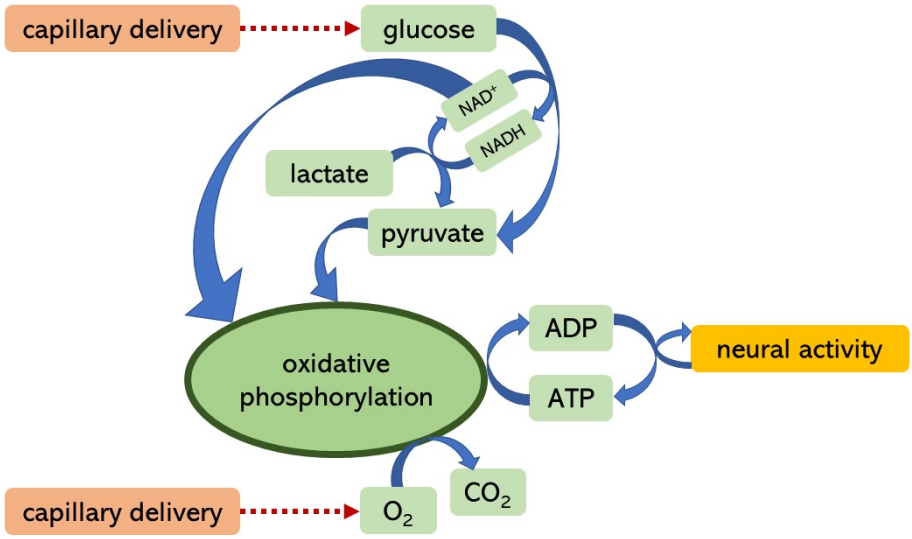

Figure 2.8: Oxygen and glucose are delivered (dotted red arrow) through the blood by capillary vessels. Subsequently, glucose transforms into pyruvate through glycolisis and enters the mitochondria. Here, together with oxygen molecules, it starts the oxidative phosphorylation process generating energy in form of ATP.

2.3 Cerebral diseases

Numerous experimental studies [40], [37], [36] have highlighted the role of pericytes in the diameter variation of small vessels. The pathways through which this is achieved have also been elucidated in great part. [45] Pericyte cell dysfunction is associated with numerous neural diseases, illustrated in Figure 2.9. Indeed, changes

in pericyte morphology at the electron microscope level, suggestive of decreased function and degeneration, have been reported in brain tissue from epilepsy and multiple sclerosis patients, while pericyte coverage of capillaries from aged rats has been shown to be less than in younger controls. [46]

2.3.1 Alzheimer's disease

In both, genetic and sporadic Alzheimer's disease patients, β-amyloid agglomerates are observed. To pericytes, the exposure and internalisation of β-amyloids is toxic. While the agglomeration of β-amyloids occurs within the microvasculature, the perivascular space has the role of clearance pathway for β-amyloids that surround the brain cells (see Figure 2.9a). Pericytes might be involved in this clearance process across the BBB as they express proteins that act as β-amyloid receptors. [42] It is as yet unclear whether Alzheimer's disease is the consequence of an overproduction of β-amyloid or an impaired clearance of them. Their accumulation causes plaques that induce endothelial cell damage, impair CBF and decrease neuronal reactivity. [46]

2.3.2 Ischaemic stroke

Arteriolar occlusions cause ischaemia in the capillary level, resulting in a disrupted CBF. Even after the removal of the occlusion, the microvasculature can often fail to fully to reperfuse the tissue. Activated leukocytes impair the re-perfusion of capillaries through platelets aggregation and fibrin deposition. This phenomenon occurs as a consequence to the BBB disruption (see Figure 2.9b). Pericytes have also been shown to constrict as a result of oxygen deficiency within the tissue, further aggravating the neural damage caused by leukocyte vessel occlusion. [46]

2.3.3 Diabetic retinopathy

Diabetic retinopathy causes the loss of the vast number of pericytes found in the retina. This loss results in haemorrhages and blocked capillaries, leading to blindness in some patients. [46] Elevated levels of glucose cause metabolic dysfunction and reduced cellular fragmentation in both mitochondria and pericytes (Figure 2.9c).

These detrimental effects could have a significant influence on the accelerated apoptosis associated with the retinal pericytes in diabetic retinopathy. [47]

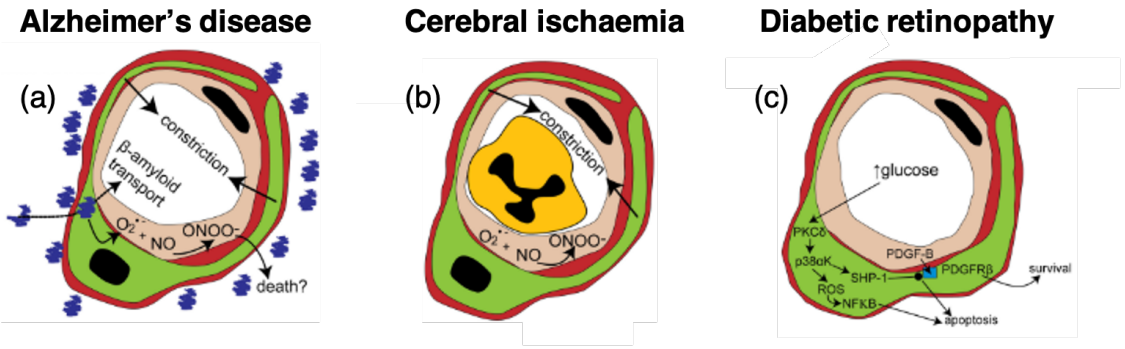

Figure 2.9: Capillary constriction linked diseases: (a) Alzheimer's Disease; (b) cerebral ischaemia; (c) diabetic retinopathy. The outermost layer is the basal lamina (red); the pericyte (green) is wrapped around the endothelial cell (beige); β-amyloid plaques (blue) and polymorphonuclear leukocyte (yellow). Modified picture taken from Hamilton et al. (2010) [46]

2.4 Modelling techniques

The cerebral vascular network is highly complex and active, therefore mathematical models can be used as a valuable means of understanding its behaviour. Depending on the nature of the physiological mechanism to be understood, different modelling techniques can be applied. Hence, there is no overall right or wrong approach to answering physiological questions mathematically. Indeed, widely accredited models range from compartmental models that are often used to replicate the whole brain, to network models that meticulously describe the microvasculature and biochemical feedback models that simulate nutrient metabolism in tissue voxels.

Each model therefore has its characteristic advantages, yet a common trait is the ability of breaking them down or coupling them depending on the purpose of the study. For example, the modelling method presented in Chapter 5 is a combination of lumped parameter and network modelling, enabling an in-depth study of the correlation between flow, metabolism and neural activity.

2.4.1 Whole brain models

The validity of the Monro-Kellie doctrine [48] is a common assumption in whole brain models. This approach relies on the notion that the rigidity of the skull translates into a constant total volume of the brain. This translates in a nil change in brain tissue, CBV and CSF, as changes in one are compensated by the other two. As blood and water are considered incompressible, brain tissue presents the most significant variability, translating in a varying ICP.
The first substantive attempt to mathematically define an active CBF regulation model was made by Ursino (1988a) [49]. This model successfully replicates experimental data and is based on compartmental and electrical equivalent modelling notions.

Compartmental models

A bi-compartmental model, with the arterial and venous being the only compartments is an elementary approach to studying CBF as a function of ABP and vessel resistance. Using Poiseuille's equation the drop in pressure between the arterial and the venous compartment can be defined as:

$$P_a - P_v = q(R_a + R_v) \tag{2.3}$$

with the arterial compartment being driven by arterial blood pressure P_a and the flow q passing from arterial to venous and exciting at venous pressure P_v. If vessels were rigid, their resistance would be constant and flow would therefore be linearly related to pressure. In reality however, the initial passive response is overcome by an active one. The baseline of the passive response r can be determined through the relationship between arterial resistance, blood volume and vessel compliance. Indeed, arterial resistance is proportional to blood volume in the inverse second power:

$$R_a = \overline{R_a} \left(\frac{\overline{V_a}}{V_a} \right)^2 \tag{2.4}$$

where arterial blood volume is:

$$V_a = C_a P_a \tag{2.5}$$

as ICP is negligible and vessel compliance is invariant. Ultimately, assuming a negligible P_v:

$$\frac{q}{\overline{q}} = \frac{P_a}{\overline{P_a}} \frac{1}{\left(1 - r + r\left(\frac{\overline{P_a}}{P_a}\right)^2\right)} \tag{2.6}$$

where the baseline arterial resistance fraction is:

$$r = \frac{\overline{R_a}}{\overline{R_a} + R_v} \tag{2.7}$$

For autoregulation to be achieved, this passive response needs to be overcome. This baseline condition has a sensitivity of $1 + 2r\%/\%$, being significantly higher than the rigid one where for every % increase in pressure there is a % increase in flow (i.e. 1%/% sensitivity). As arteries are physiologically equipped (i.e. thick wall) to significantly vary the vessel diameter, the active response of vessels is almost exclusively attributed to arterial compliance (e.g. in form of capacitors in an electrical equivalent model). [24]

Electrical equivalent models

In the cerebral vasculature, lumped parameter models often rely on equivalent electrical circuits for the representation of blood flow behaviour. Current is replaced by flow, voltage becomes blood pressure and resistance represents vessel resistance. The earliest models of this kind represented the brain vasculature as a three-compartment Windkessel model. [50] Subsequently, Carlson et al. (2008) [51] proposed a seven-compartment model representing: the upstream artery, large arteriole, small arteriole, capillary, small venule, large venule and downstream vein; with arteries being the active component of the model.

More recently, a compartmental model including 40 individual large arterial vessels and the circle of Willis was proposed by Ursino and Giannessi (2010) [52]. This model relies on an equivalent electrical circuit using resistance and compliance to

model the behaviour of vessels and a feedback mechanism to model autoregulation. The widely used Ursino and Di Giammarco (1991) [53] model, adds passive, active and viscous components to the vessel tone and control is achieved though the adjustment of the active tone by setting an activation factor M. The two distinct mechanisms through which control occurs are dependent on the vessel compartment. The response of the first compartment is influenced by changes in pressure:

$$\frac{dM_1}{dt} = \frac{1}{\tau_1}\left(-M_1 + \frac{2}{\pi}\tan^{-1}\left(\frac{P_a - P_v - P_{an} + P_{vn}}{P_{ref}}\right)\right) \tag{2.8}$$

where τ_1 is a constant, P_a and P_v are arterial and venous pressure with P_{an} and P_{vn} being their corresponding baseline values and P_{ref} is a constant parameter representing the change in perfusion pressure at which the regulatory mechanism exerts half of its maximum action. Similarly, the second compartment responds to changes in flow as follows:

$$\frac{dM_2}{dt} = \frac{1}{\tau_2}\left(-M_2 + \frac{2}{\pi}\tan^{-1}\left(\frac{(q - q_n)}{q_n}\frac{1}{q_{ref}}\right)\right) \tag{2.9}$$

where τ_2 is a constant, q is blood flow with q_n being its respective baseline value and q_{ref} being the percentage change in CBF at which the regulatory mechanism exerts half its maximum action. The two responses are then combined with the effects of autoregulation and CO_2 reactivity before being finally combined in a sigmoidal function expressing the activation factor M.

Using this as a basis, the model proposed by Payne (2006) [54] includes a third feedback component that models neural activation. The sigmoidal function is then presented in the formulation of arterial compliance dependent on the three stimuli:

$$\frac{dx_q}{dt} = \frac{1}{\tau_q}\left(-x_q + G_q\left(\frac{q - \overline{q}}{\overline{q}}\right)\right) \tag{2.10}$$

$$\frac{dx_{CO_2}}{dt} = \frac{1}{\tau_{CO_2}}\left(-x_{CO_2} + \frac{P_{aCO_2}}{\overline{P_{aCO_2}}}\left(0.3 + 3\tanh\left(\frac{P_{aCO_2}}{\overline{P_{aCO_2}}} - 1.1\right)\right)\right) \tag{2.11}$$

$$\tau_1^2\frac{d^2x_M}{dt} + \tau_2\frac{dx_M}{dt} + x_M = u \tag{2.12}$$

where the three state variables: x_q, x_{CO_2} and x_M represent the flow, arterial CO_2 concentration and neural feedback of the model. On the other hand, τ_q, τ_{CO_2}, τ_1, τ_2 are time constants; G_q is a scaling factor and u is neural activation which is considered to be of unit magnitude. Their combination gives the total feedback x that feeds into the asymmetrical sigmoidal curve as follows:

$$x = x_M + x_{CO_2} - x_q \tag{2.13}$$

$$C_a = \overline{C_a} + \frac{1}{2}\left(\Delta C_a^{\pm} \tanh\left(\frac{2x}{\Delta C_a^{\pm}}\right)\right) \tag{2.14}$$

where ΔC_a^+ represents the positive change in amplitude when $x > 0$ and ΔC_a^- represents the negative change in amplitude when $x < 0$.

2.4.2 Network models

With the aim of gaining insight into spatial heterogeneity, network models can be developed. These represent models that enable the investigation of local changes in tissue perfusion. Working outward from the capillary level, Boas (2008) [55] presented a network of bifurcating vessels, with a 20% increase in diameter for every new generation of arterioles and an equivalent increase in dimension for venules (see Figure 2.10). Overall, the venules are larger than the arterioles, the length of capillary vessels is $250\mu m$ and the length of all other vessels is $100\mu m$. The governing equations of the model correspond to the ones used in the new model presented in Chapter 5.

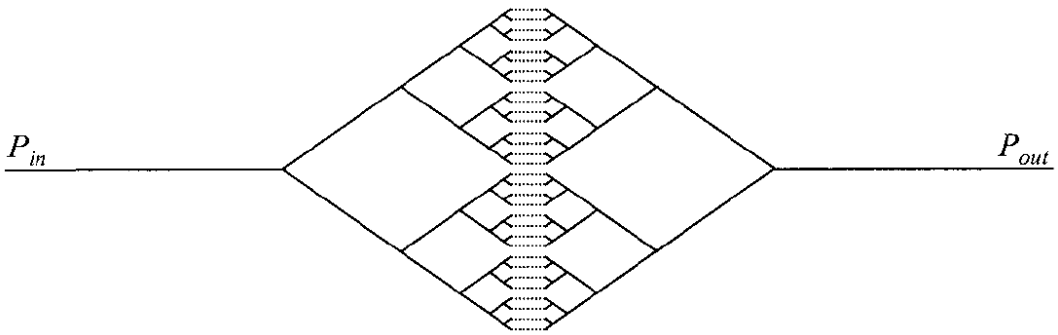

Figure 2.10: Schematic representation of the model proposed by Boas (2008) where the dashed lines represent the microvascular vessel group. [55]

Boas defines the baseline value of the oxygen partial tissue pressure as 15 mmHg, following the data distribution presented by Vovenko (1999) [56]. The average O_2 saturation levels presented are lower, and the velocity is higher than in-vitro results. The model illustrates the effect of diameter reduction and oxygen consumption on the network, yet it does not describe diameter autoregulation or any collateral circulation.

A new microvasculature model was thus proposed by Payne and Lucas [57], investigating the time response of the network to tissue oxygenation alterations. The model follows the geometry proposed by Boas, presenting a network of 13 vessel generations (6 arteriole, 1 capillary, 6 venous). It is assumed that each vessel supplies a separate tissue compartment and O_2 diffusion between them is neglected. Unlike in the study by Boas (2008) [55], the haematocrit is kept at a constant value, following the assumption that in a bifurcating network with a constant cross-sectional area within each generation the haematocrit reaches a constant value.

The overall response time of the network was found to be approximately $6s$, suggesting that the flow response to increases in metabolic activity can not be driven solely by alterations in tissue oxygenation levels as the reaction time is too slow. The total volume of the proposed network is approximately 0.006 mm^3, however, as the proposed network is scale invariant it can be scaled to a larger tissue volume with the same properties.

2.4.3 Biochemical feedback models

To best understand the drivers of physiological phenomena, it is necessary to delineate the relationships between the numerous players (e.g. receptors, transmitters and nutrients) that govern biochemical reactions. However, biochemical feedback models rely on a large number of equations to faithfully replicate all these interactions, at the expense of scalability. In particular, voxel-based morphometry studies are a popular approach to studying brain tissue in health and disease.

The study of Banaji et al. (2005) [58] is a good example of how combining

biochemical feedback modelling techniques (typical of studies focused on brain tissue) with compartmental modelling, can provide insightful conclusions on the whole brain. This model studies intracellular pH, CO_2 levels, intracellular Ca^{2+}, nitric oxide and the effect of vascular tone in 5 compartments (the vascular system, arterial smooth muscle cells (SMCs), extracellular space, intracellular space and the mitochondria). While being physiologically representative, experimentally validating the conclusions of such models is not trivial, as extracting specific parameter values from patient data is very difficult.

The Banaji et al. (2005) model represents the first step towards an *in silico* brain model of blood flow circulation. Indeed, the model is based on the Ursino and Lodi (1988) model, while including a series of biochemical and vascular smooth muscle processes. To do that, three communicating sites are defined:

1. The vascular system: where vessels in each compartment (proximal, distal and capillary) are arranged in parallel and flow is unidirectional and laminar;

2. The brain tissue: which is organised in the extra-cellular, the extra-mitochondrial and the mitochondrial compartment;

3. The vascular smooth muscles: whose behaviour is regional (proximal arterial and distal arterial).

Comprising a total of over 80 equations, the Banaji et al. (2005) model can be decomposed in its three compartments, as the model's variables and processes either describe processes within the compartment or the communication mechanisms between compartments. Numerous [59], [60] models focused on describing the complexity of the metabolic interactions within brain tissue have been proposed since, but the model by Banaji et al. (2005) remains a widely popular one and is therefore quoted here as an example.

It is worth noting, that while modelling in system biology involves a high volume of parameters to be defined, the quantitative determination of these has

been largely debated. In their study, Gutenkunst et al. (2007) [61] argue that experimental parameter determination results in a model with few "stiff" parameter combinations, as in vivo measurements of biochemical parameters are difficult to obtain. Hence, Gutenkunst et al. (2007) [61] point towards the introduction of "sloppy" patterns in the model's parameter definitions, with the aim of delivering good fits with loose parameter definitions. Ultimately, the authors suggest that focusing on the exact determination of parameter values is an inefficient approach to creating biologically representative models.

2.4.4 Capillary bed models

Given importance of the microvasculature in delivering nutrients to brain tissue, multiple modelling techniques were designed to study capillary vessel behaviour and therefore compensate for the inability of extracting data from imaging techniques. With the aim of validating the model's results with experimental data, non-human models of the capillary bed are also commonly found across the literature. Typically, computational models either aim to analyse vessel behaviour in detail within a tissue voxel (cast models) or large statistical data sets of vessel characteristics extrapolated from experimental data. Table 2.1 provides an overview of the capillary modelling techniques of the past 35 years.

With about 10,000 capillaries in a tissue voxel of about $1mm^3$ in size, the difficulty of realistically representing the geometry of the capillary bed is evident. Moreover, the statistical models that rely on experimental data also need to account for the fact that the stiffness of brain tissue and vessels significantly increases in a matter of minutes (i.e. by about 30% in 3 minutes). [62] This makes the accurate representation of an active vasculature bed increasingly difficult.

An advantage of the cast models is the possibility of coupling them with biochemical feedback models in order to gain detailed insights into interactions upon which the neurovascular coupling is based. On the other hand, the primary limitation of these models is the difficulty in scaling them, to gain insights on how the brain behaves as a whole. Statistical models, on the contrary, have the advantage of

allowing the study of a large number of networks, analysing the brain's heterogeneity within a single or even multiple specimens. However, statistical models are very costly as they rely on experimental data that is often very difficult to obtain (particularly for large animals).

Model	Type	Vessel number	Voxel size	Species
Zagzoule et al. [63]	lumped parameter	∼400,000	whole brain	human
Secomb et al. [64]	cast	50	∼33mm^3	rat
Boas et al. [55]	network	254	n/a	rat
Lorthois et al. [65]	cast	∼10,000	1.6mm^3	human
Su et al. [59]	statistical	∼1000	∼0.125 mm^3	human

Table 2.1: List of selected capillary models characterised by type (cast or statistical), vessel number, supplied tissue volume and species.

2.5 Summary

To ensure an adequate tissue perfusion, the brain relies on a tightly regulated system of vessels. Both large and small, each vessel category has a specific and indispensable function. Arteries operate at the highest blood pressure, regulating flow through a SMC driven compliance. Capillaries penetrate the white matter and supply the tissue with nutrients through a network of predominantly bifurcating vessels. Ultimately, nutrient-poor blood flows back to the heart through a series of veins and sinuses.

Being highly sensitive to perfusion changes, the brain relies on an autoregulation mechanism, driven by an active response of the arteries and arterioles. The regulatory drivers differ in nature, being either global (i.e. set by the systemic circulation) or local. Nutrient supply takes place in the microvasculature of the brain, targeting in particular the capillary network. Pericytes, smooth contractile cells found on capillary vessels, have been recently proved to actively regulate capillary vessel diameter. A dysfunction in this further regulating mechanism is linked to several pathological conditions such as dementia , Alzheimer's and diabetic

retinopathy. It is clear that all these factors are interlinked and changes in one therefore result in an alteration in behaviour of the other.

Describing the relationship between blood pressure, flow and nutrient consumption is therefore of key importance when aiming to uncover the progression of brain degenerative diseases. To compensate for what imagining techniques cannot provide, numerous mathematical modelling techniques have been deployed. Depending on the nature of the question being investigated, compartmental-, whole brain-, network-, capillary bed- or even biochemical feedback-models can be applied.

A process cannot be understood by stopping it.
Understanding must move with the flow of the process,
must join it and flow with it.

— Dune (1965), Frank Herbert

3
Neurovascular coupling

Contents

3.1 Blood 34
3.2 Poiseuille's Law 35
3.3 Viscosity 36
3.4 Metabolic sensitivity in the neurovascular unit 37
3.4.1 Oxygen sensitivity 38
3.4.2 Glucose consumption 38
3.4.3 Pericyte activity 39
3.4.4 Neurons 41
3.4.5 Metabolite interactions 41
3.5 Modelling glucose consumption 43
3.5.1 Relating metabolism and blood flow 47
3.6 Summary 51

Before introducing the new physiologically representative model of CBF, it is necessary to first define the properties of blood and the methods that were used to define its flow through the vessels. Here, blood viscosity in relation to vessel diameter and vascular resistance and compliance are introduced. Changes in vessel diameter are driven by the neurovascular coupling mechanism, whose complex relationship between variables is a primary obstacle for computational modelling of the brain.

3.1 Blood

Blood is composed of red blood cells (RBCs) named erythrocytes, white blood cells (WBCs) known as leukocytes, platelets and plasma. Healthy RBCs are biconcave discs, about 8μm in diameter and red in colour as they are a nearly fully saturated solution of haemoglobin. Indeed their composition can be divided into 65% water, 32% haemoglobin and 3% membrane components. The membrane is a highly flexible double phospholipid layer about 7.5 nm thick, enabling the cell to deform when passing through capillaries. A further attribute of the membrane is its high permeability to chloride, bicarbonate and water, but not to sodium, potassium and macromolecules. The cell's shape and the haemoglobin's ability to reversibly combine with oxygen, enable an efficient oxygen transport of about 20 ml/100 ml of blood. The haematocrit is the fraction of blood occupied by RBCs and in healthy humans it ranges between 40-45%.

Unlike erythrocytes, leukocytes have a more complex internal structure enabling an aerobic (i.e. oxygen dependent) as well as anaerobic (i.e. oxygen independent) metabolisation. Their primary role is scavenging micro-organisms and generating antibodies in the immune system. Depending on their specific task, they are classified as granulocytes, lymphocytes and monocytes. Their shape is spherical, with a diameter ranging between 7-22 μm. Platelets are spherical or oval shaped structures, with a diameter of 2-4μm and a membrane about 8 nm thick. They play a role in the prevention of bleeding, alongside vasoconstriction, by aggregating upon contact with ADP. [2]

All these organelles are suspended in blood plasma, a straw-yellow aqueous solution containing proteins, minerals and electrolytes. Plasma makes up about 55% of the total blood volume and its function is the circulation of nutrients such as glucose, amino acids and fatty acids, and the removal of waste products such as carbon dioxide, urine and lactic acid. [19]

3.2 Poiseuille's Law

Vessel resistance is a factor of major importance in blood flow regulation. Models of brain vasculature often define flow through Poiseuille's equation:

$$Q = \frac{\Delta P}{R} \tag{3.1}$$

where Q is CBF, ΔP is the change in pressure and R is the resistance to flow defined as:

$$R = \frac{8\mu L}{\pi r^4} \tag{3.2}$$

where μ refers to dynamic viscosity, and L and r are vessel length and radius respectively. It is important to note that this calculation of flow is valid only for the assumption of a Newtonian fluid with steady laminar flow in an axisymmetric vessel. [24]

Despite its inhomogeneous composition, blood is most often considered a Newtonian fluid. This simplification is acceptable down to a length scale of $10 - 100\mu m$ in vessel diameter, where the cross-section corresponds to the size of an erythrocyte. Newtonian fluids follow the law:

$$\tau = \mu\dot{\gamma} \tag{3.3}$$

with τ being the shear stress, μ the dynamic viscosity and $\dot{\gamma}$ the strain rate. In reality however, the relationship between the shear stress and the strain rate is a curve with its origin point indicating the minimum shear stress for a significant strain rate. With an elevated flow velocity however, the relationship becomes more linear as the shear stress increases rapidly with strain rate. This renders the assumption of Newtonian fluid behaviour in large vessels acceptable. [2]

A common non-Newtonian representation of blood behaviour was proposed by Casson, with τ_y as yield stress.

$$\sqrt{\tau} = \sqrt{\tau_y} + \sqrt{\mu\dot{\gamma}} \tag{3.4}$$

where τ_y=0.004 Pa, as proposed by Cebral et al. (2002) [66] and $\mu = 0.004$ Pa.s as proposed by Nakamura et al. (1988) [67]. Ultimately, the absence of a standard

model for blood renders the comparison between various modelling methods difficult, in addition to the already existing obstacle of data scarcity. [2]

3.3 Viscosity

Blood viscosity is different in large and small vessels. In blood vessels whose diameter is smaller than $0.1mm$, RBCs flow aligned along the centreline with a velocity higher than the one of the surrounding plasma. This phenomenon indicated the dependence of viscosity on haematocrit and is known as the Fåhræus–Lindqvist effect. [68]

Many relationships between blood viscosity and haematocrit have been proposed over the years. One of the main conclusions that have been drawn is that there is a significant difference between viscosity measured in vitro or in vivo. The relationship proposed by Secomb and Pries (2013) [69], based on in vitro data, represents the empirical relationship between the two parameters as follows:

$$\mu_{rel} = 1 + (\mu_{0.45} - 1)\frac{(1 - H_D)^C - 1}{(1 - 0.45)^C - 1} \tag{3.5}$$

where

$$\mu_{0.45} = 220e^{-1.3D} + 3.2 - 2.44e^{-0.66D^{0.645}} \tag{3.6}$$

$$C = (0.8 + e^{-0.075D})(-1 + \frac{1}{1 + 10^{-11}D^{12}}) + \frac{1}{1 + 10^{-11}D^{12}} \tag{3.7}$$

This relationship is shown in Figure 3.1a, indicating that viscosity decreases gradually until the vessel diameter reaches 7μm in size. Between 7μm and 3μm it shows almost no alterations, then exponentially increases for diameters below 3μm because RBCs are too large to pass through the vessel. The same authors present a second relationship between viscosity and haematocrit, for in vivo empirical data:

$$\mu_{rel} = (1 + (\mu^*_{45} - 1)\frac{(1 - H_D)^C - 1}{(1 - 0.45)^C - 1}(\frac{D}{D - 1.1})^2)(\frac{D}{D - 1.1})^2 \tag{3.8}$$

where

$$\mu^*_{0.45} = 6e^{-0.085D} + 3.2 - 2.44e^{-0.06D^{0.645}} \tag{3.9}$$

Ultimately, the two models present the same qualitative conclusion: viscosity decreases up to a critical minimum diameter and promptly increases subsequently. However, the in vivo model shows that values for viscosity are much higher, as shown in Figure 3.1b. Reitsma et al. (2007) [70] attribute this evident distinction between in vitro and in vivo data, to the presence of glycocalyx in the latter. The glycocalyix is the outer layer of endothelium, a network of membrane-bound proteoglycans and glycoproteins. [71] Despite the differences between the two models, the most widely used one remains the one given by Equation 3.5.

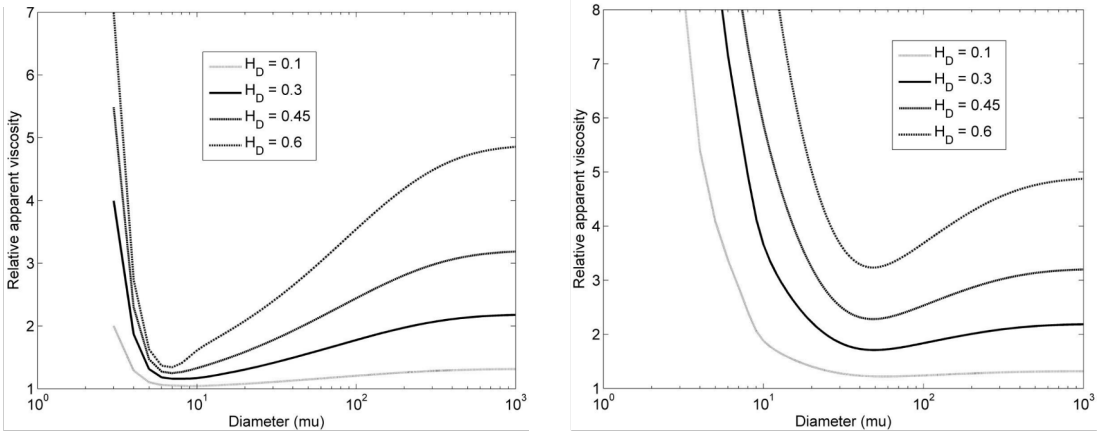

(a) In vitro viscosity model. **(b)** In vivo viscosity model.

Figure 3.1: (a) Empirically derived dependence of blood viscosity on haematocrit in an in vitro model; (b) Empirically derived dependence of blood viscosity on haematocrit in an in vivo model. Figures reproduced without changes from [2].

3.4 Metabolic sensitivity in the neurovascular unit

Nutrient sensitivity is governed by a series of biochemical reactions that are interdependent from each other, making it difficult to investigate each variable individually. However, an in-depth understanding of these interactions and feedback mechanisms can provide useful insights on the magnitude of the vasculature's sensitivity to fluctuations in individual nutrients.

3.4.1 Oxygen sensitivity

Neurons and neuronal functions are generally viewed as highly sensitive to hypoxia with disruptions of oxygen supply to the brain causing detrimental damage within minutes. Although there is not a clearly defined critical oxygen tension ($P_{t_{O_2}}$) at which hypoxic damage will occur in neurons, in the rat cortex a $P_{t_{O_2}}$ value in the range 6.8 - 8.8 mmHg has been estimated to be an indication for oxidative metabolic disruption. [72] Under physiological conditions, $P_{t_{O_2}}$ measurements in rats range from 6 mmHg to 40 mmHg within the cortex and from 1 mmHg to 60 mmHg across all brain regions with proximal structures displaying large variations in oxygen tension. [73]

During embryonic development, oxygen tension is low in the fetal brain (0.076 - 7.6 mmHg) and hypoxia is essential for proper embryo morphological development. Within the developing brain, oxygen tension acts as a regulator of neurogenesis with low oxygen promoting progenitor expansion in cortical neurogenic regions and decreasing dopaminergic neurogenesis in the midbrain. [74] Additionally, in the adult brain, hypoxic injury caused by ischaemic stroke triggers increased neuronal stem cell proliferation and neurogenesis. [75],[40] This evidence supports a role for hypoxia as a regulatory mechanism in neuronal function and indicates that physiological hypoxia occurring in the adult brain may play a functional role. [72]

3.4.2 Glucose consumption

Neural activity is linked to an increase in glucose consumption in the brain tissue. This nutrient consumption is not homogeneous within the brain, indeed regions with a high activity and a large cerebral metabolic rate of glucose (CMR_{glc}) are the ones with the highest capacity for glucose delivery. The transporters and enzymes facilitating this process have the ability to match delivery to consumption rates and are therefore adjustable to consumption rates. [76]

There is a distinction in response between short-term (i.e. seconds) and long-term (i.e. hours) glucose level fluctuations. Momentary changes in glucose supply are moderated by CBF, whereas a prolonged insufficiency spanning over days or

weeks is modulated by transporter genes and protein expression. [76] This suggests that a strong correlation exists between CBF, capillary density, distribution of glucose transporters and CMR_{glc}.

3.4.3 Pericyte activity

First discovered in 1837 by Charles Rouget, pericytes are elongated cells located intermittently on the endothelial layer of pre-capillary arterioles, capillaries and post-capillary venules (see Figure 3.2). The degree of coverage depends on the tissue type, however the approximate ratio of pericytes to endothelial cells in the human brain is 1 : 3. For mice, the ratio is almost identical, making them suitable for experimental studies of pericyte-induced capillary vasomotion. [36]

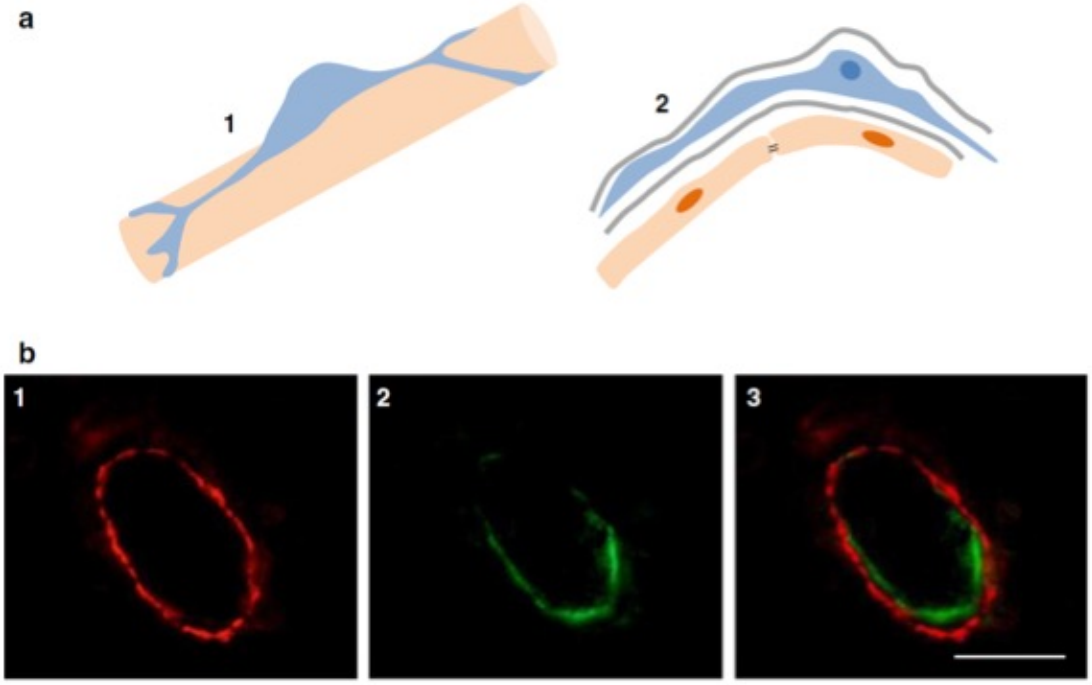

Figure 3.2: (a) Graphical representation of pericytes wrapping around the endothelial layer longitudinally (1) and transverse section (2); (b) fluorescent markers can be used to identify pericytes where the pericyte is in red (1) and endothelial layer is in green (2). The scale bar in the section b(3) measures $20\mu m$. Modified picture taken from [36].

In vitro experiments have shown that pericytes have the ability to regulate capillary diameter. A study by Hamilton et al. (2010) [46] suggests that the two key factors that render capillaries more likely to be driving agents of CBF regulation,

compared to arterioles are: their proximity to neurons, and their number. In fact, in the hippocampus, the average distance between a neuron and a capillary is $8 - 23\mu m$, depending on the cell layer, while the average distance between a neuron and an arteriole is $70 - 160\mu m$.

This suggests that capillaries have a more advantageous position compared to arterioles, for sensing neuronal activity and responding to it by regulating CBF. From the relative spacing of capillaries and arterioles, each capillary perfuses a tissue volume with a diameter of $15 - 50\mu m$, while arterioles perfuse a volume of diameter $140 - 320\mu m$. The greater density of capillaries also means that capillary level regulation of blood flow could potentially allow more spatially-restricted changes in blood flow on occurrence of a localised increase in neuronal activity. [46]

The classical concept is that energy demand and energy production in the brain are linked mainly by metabolic processes such as glucose oxidation and ADP hydrolysis to ATP. However, the complexity of the relationship between brain perfusion and metabolic activity cannot be reduced to a simplistic cascade of glycolysis products inhibited by enzymes. Indeed, over the last decade emerging concepts of metabolic regulatory mechanisms have started considering the role of so called "second messenger" ions, such as calcium (Ca^{2+}). [77]

Since brain activation causes an increase in both sodium Na^+ and potassium K^+ and neurons are excitable cells, membrane depolarization occurs. As a consequence of the opening of the voltage-gated K^+ channels and the increase of K^+ in the extracellular space, an influx of Ca^{2+} occurs. This important extracellular messenger has a significant effect on neurons (i.e. inciting transmitter release) and astrocytes (i.e. glycolysis stimulation). [77] Moreover, Ca^{2+} has proven to be an active stimulant of pericyte cell activity. Increased levels of Ca^{2+} lead to cell relaxation, resulting in a capillary diameter increase. A larger diameter ensures for more CBF delivered to the tissue, sustaining the increased metabolic demand during brain activation. The correlation between the Na^+/K^+ gate activity and Ca^{2+} flux can be defined as [78]:

$$Ca^{2+} = \frac{Ca^{2+} \cdot (Na^+)^2}{\overline{(Na^+)^2}} \tag{3.10}$$

Along with the relationship quoted in Equation 3.10, Chapman et al. (1979) [78] introduce Equation 3.11 where the influence of K^+ is also considered:

$$Ca^{2+} = \frac{\overline{Ca^{2+}}}{\overline{Na^+}} \cdot (Na^+)^n \cdot \frac{\overline{K^{n-2}}}{K^{n-2}} \tag{3.11}$$

where $\overline{(Na^+)^2}$ and $\overline{K^{n-2}}$ represent the baseline values of sodium and potassium respectively. However, Equation 3.11 is only used for a number of ions $n > 2$. We assume that the number of ions of Na^+ and K^+ is the same and equal to 2 and we therefore rely on Equation 3.10 for our model acknowledging the limitations implied with its simplicity.

3.4.4 Neurons

Neurogenic control is spatially variable across the vasculature, meaning that different vessels are governed by nerve fibres originating from different parts of the nervous system. Surface vessels are controlled by extrinsic nerves (i.e. the peripheral nerve ganglia) whilst internal vessels are controlled by intrinsic nerves (i.e. intrinsic brain neurons). Indeed, the sympathetic nervous system plays an active role in setting vascular tone as well as the upper autoregulation limit. In contrast, the parasympathetic system does not present a significant contribution to the flow maintenance process. [25]

The functional distinction between nerve fibres allows a high degree of control, making it possible to study the different responses to stimuli. These differences in time response and nature of neurogenic control serve to underline the complexity of the neurovascular coupling mechanism, on both the global and local scale. All these factors, heterogeneous in response, cooperate in order to ensure a constant supply of blood and nutrients to brain tissue.

3.4.5 Metabolite interactions

Figure 3.3 shows a simplified schematic of the relationship between the CBF regulating variables and the time hierarchy at which they occur. As neuronal computations are energetically demanding, the most effective way of providing large

amounts of energy is oxidative phosphorylation (see Chapter 2), therefore making the process dependent on O_2 consumption. In parallel, brain activity causes an increase in Ca^{2+} levels in the tissue, activating pericyte cells as a result. The activity of pericytes induces a capillary dilation which reduces the overall microvasculature network resistance. Ultimately, the collective effect of resistance and compliance change is manifested in the form of CBF variations that match supply and demand.

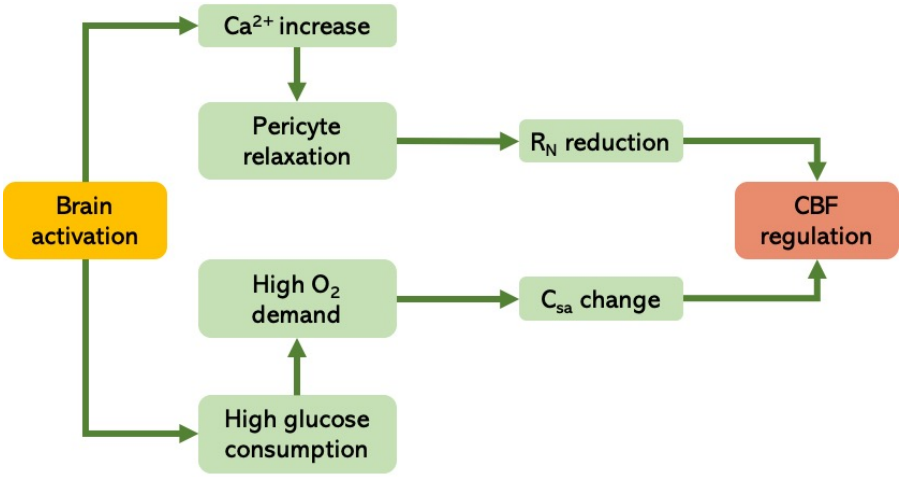

Figure 3.3: Schematic of the physiological cascade of events relating neural activity to CBF regulation. Brain activation induces an increase in Ca^{2+} in the tissue, activating pericytes, which by relaxing dilate capillaries ultimately reduce the resistance of the capillary bed (R_N). Simultaneously, neural activity increases nutrient consumption, with oxygen sensitivity of the tissue driving the compliance of small arteries (C_{sa}). The combined effect of these two cascades of events regulates CBF, aiming to supply the nutrient consumption increase given by brain activation.

A simplified illustration of the physiological and chemical activity describing the interaction between neural activity and metabolites is shown in Figure 3.4. The aim is to provide a visual aid to the understanding of the interdependency of the differential equations described in Section 3.5. Furthermore, Figure 3.4 highlights a key difference in the oxygen and glucose exchange between capillaries and tissue. Indeed, oxygen diffuses freely while glucose can only penetrate the tissue through a transporter.

There are three main glucose transporters (GLUT1, GLUT3, GLUT5) that enable this, each transporting glucose to a specific organelle (neurons, astrocytes and mitochondria respectively). For simplicity, the differences between the three

transporters were neglected here and their presence was accounted for by including a time-delay parameter of glucose transport in the mathematical model in Section 3.5.

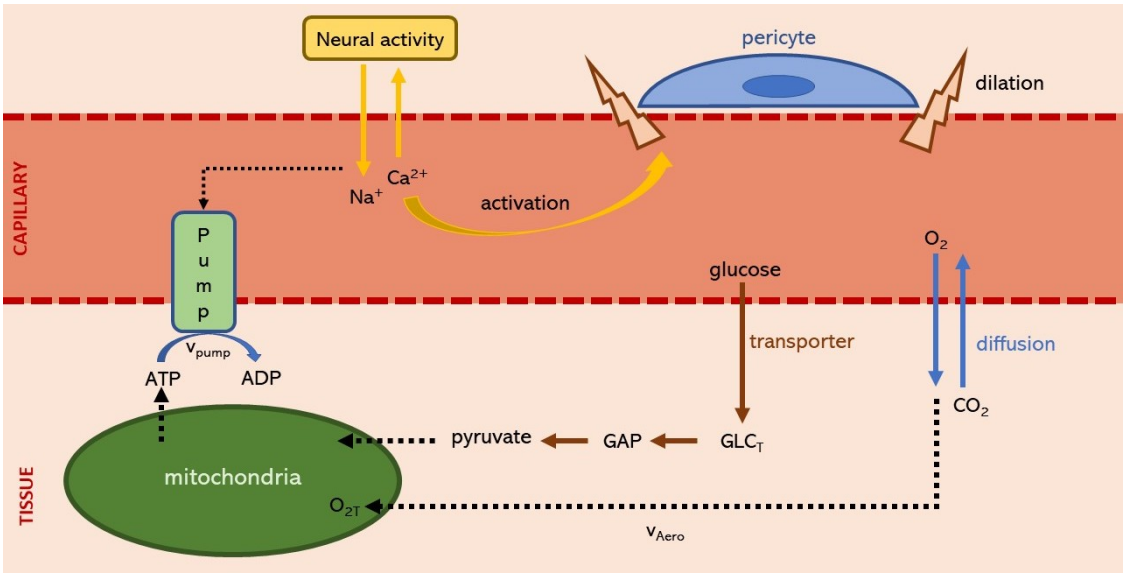

Figure 3.4: A simplified representation of pericyte activity and nutrient exchange between capillary and tissue. A key difference between oxygen and glucose supply is that while oxygen diffuses freely, glucose relies on transport proteins. This is taken into account by including a time delay variable in the glucose model.

3.5 Modelling glucose consumption

The mathematical models of glucose and oxygen consumption presented here are based on the work on Aubert et al. (2001) and (2002) [79], [80] and describe the metabolic processes taking place in a tissue voxel of approximately 1mm^3. Three key assumptions were made to ensure computational feasibility while maintaining physiological accuracy:

1. Intracellular and intra-capillary concentrations are the same as the very thin capillary wall renders its presence negligible when considering nutrient exchange.

2. To describe the coupling between the sodium pump and ATP it is assumed that the link between electrical and metabolic cerebral activity is achieved through the consumption of ATP by Na/K ATPase.

3. A time hierarchy of reactions was assumed, meaning that the sequential reactions relating one process (i.e. differential equation) to another, are what allows us to describe what happens from glucose to pyruvate.

In the model, fluctuations in intracellular glucose concentration GLC_T are represented as the difference between the velocity of glucose transport through the blood-brain-barrier v_{GLC_m} and the velocity of the hexokinase-phosphofructokinase system v_{HK-PFK}.

$$\frac{d(GLC_T)}{dt} = v_{GLC_m} - v_{HK-PFK} \tag{3.12}$$

Intracellular concentration of glyceraldehyde-3-phosphate GAP changes according to:

$$\frac{d(GAP)}{dt} = 2v_{HK-PFK} - v_{PGK} \tag{3.13}$$

where v_{PGK} is the velocity of phosphoglycerate kinase. Finally, the rate of adenosine triphosphate ATP production is given by:

$$\frac{d(ATP)}{dt} = [-2v_{HK-PFK}+v_{PGK}+v_{PK}-v_{ATPases}-v_{pump}+v_{trans}+v_{CK}][1-\frac{d(AMP)}{d(ATP)}]^{-1} \tag{3.14}$$

where v_{PK} is the velocity of pyruvate kinase, $v_{ATPases}$ is the velocity of ATPases, v_{pump} is the one of the sodium potassium pump, v_{trans} is the velocity of the ATP-ADP translocase and v_{CK} is that of creatine kinase. It is assumed that the total concentration of adenosine nucleotides is equal to a constant A:

$$ATP + ADP + AMP = A \tag{3.15}$$

where ADP and the equilibrium constant of adenylate kinase q_{ak} are:

$$ADP = \frac{ATP}{2}[-q_{ak} + \sqrt{q_{AK}^2 + 4q_{AK}(\frac{A}{ATP} - 1)}] \tag{3.16}$$

$$q_{ak} = \frac{ADP^2}{ATP.AMP} \tag{3.17}$$

It can thus be deduced that the ratio of the rate of change of AMP and ATP can be defined as:

$$\frac{d(AMP)}{d(ATP)} = -1 + \frac{q_{AK}}{2} - \frac{1}{2}\sqrt{q_{AK}^2 + 4q_{AK}(\frac{A}{ATP} - 1)} + \frac{q_{AK}A}{ATP\sqrt{q_{AK}^2 + 4q_{AK}(\frac{A}{ATP} - 1)}} \tag{3.18}$$

Furthermore, it was necessary to relate the glycolitic pyruvate generation to oxygenation levels within the tissue and the vasculature. Fluctuations of intracellular oxygen concentration O_{2T} were represented as the difference between the velocity of oxygen transport through the BBB v_{O2m} and the velocity of the mitochondrial oxygen consumption v_{Aero}.

$$\frac{d(O_{2T})}{dt} = v_{O2m} - v_{Aero} \tag{3.19}$$

Similarly, the rate of change of the capillary oxygen concentration O_{2C}, was defined as the difference of the velocity of the oxygen transport through the capillary v_{O2c} and v_{O2m}.

$$\frac{d(O_{2C})}{dt} = v_{O2c} - \frac{1}{r_c}v_{O2m} \tag{3.20}$$

The capillary glucose concentration GLC_c can be calculated as the average of the arterial GLC_A and venous GLC_V concentration. Its rate of change is defined as the difference between the velocity of glucose transport through the BBB and that of glucose transport in the capillaries:

$$GLC_c = \frac{GLC_A + GLC_V}{2} \tag{3.21}$$

$$\frac{dGLC_c}{dt} = v_{GLC_c} - \frac{1}{r_c}v_{GLC_m} \tag{3.22}$$

$$v_{GLC_c} = 2\frac{CBF}{V}\frac{1}{r_c}(GLC_A - GLC_C) \tag{3.23}$$

Mitochondrial respiration v_{mito} was related to the ATP/ADP ratio according to the now well-established hypothesis by Gjedde (1997) [81]. Further variables

included in the model of metabolic activity were the intracellular oxygen O_{2T} (defined in Equation 3.19) and pyruvate PYR:

$$v_{mito} = V_{max,mito} \frac{PYR}{K_{m,mito} + PYR} \frac{1}{1 + (\frac{ATP}{ADP.K_{I,mito}})^{na}} \frac{O_{2T}}{K_{O2T+O_{2T}}} \tag{3.24}$$

where $V_{max,mito}$ is the maximal rate of mitochondrial activity, $K_{m,mito}$ is the Michaelis constant of pyruvate uptake by the mitochondria, $K_{I,mito}$ is the inhibition constant, n_a is the Hill coefficient related to ATP/ADP and K_{O2T} is the Michaelis constant for oxygen. Table 3.1 presents a complete list of baseline values, extrapolated from Aubert et al. (2002) [82], which the model relies on.

Parameter	**Value**	**Units**	**Definition**
A	2.212	mM	total concentration of adenosine nucleotide
ADP	0.012	mM	adenosine diphosphate concentration
AMP	0.000071	mM	adenosine monophosphate concentration
ATP	2.2	mM	adenosine triphosphate concentration
CBF/V	0.021	1/s	fraction of CBF and blood volume
GAP	0.0057	mM	glycerdehyde-3-phosphate concentration
GLC_A	4.8	mM	arterial glucose concentration
GLC_C	4.56	mM	capillary glucose concentration
GLC_T	1.2	mM	intracellular glucose concentration
O_2T	0.0046	mM	intracellular oxygen concentration
O_2C	7.01	mM	capillary oxygen concentration
r_c	0.01	-	ratio between capillary and intracellular volume
$v_{ATPases}$	0.149	mM/s	flow velocity of ATPases
v_{PGK}	0.028	mM/s	velocity of phosphoglycerate kinase
v_{PK}	0.026	mM/s	velocity of pyruvate kinase
v_{pump}	0.16	mM/s	velocity of the sodium potassium pump
v_{trans}	0.05	mM/s	velocity of ATP-ADP translocase pump
$K_{I,mito}$	183.3	-	mitochondrial respiration rate vs. ATP/ADP
$K_{m,mito}$	0.3	mM	Michaelis constant
na	0.0.8	-	Hill coefficient
PYR	0.16	mM	pyruvate concentration

Table 3.1: Baseline values of the glucose modelling, extracted from Aubert et al. (2002) [82]

3.5.1 Relating metabolism and blood flow

Brain activation defined by neural activity, is related to an increase in metabolism. Experimental data on brain activation in healthy humans presented by Frahm et al. (1996) [83] and Krueger et al. (1999) [84], suggest that upon visual stimulation CBF increases in a range of 20-50%. Hence, the dynamic response of metabolic changes in the tissue was evaluated by increasing CBF by 40% and maintaining it over the entire duration of the stimulation.

Figure 3.5 shows that a 40% increase in CBF results in a 2000% increase in ATP from baseline in about 5 minutes, followed by a 13% decrease in ADP within the same time. On the other hand, Figure 3.6 shows how the increase in CBF translates to a 1.8% increase in glucose in the capillaries and a 60% decrease in the tissue.

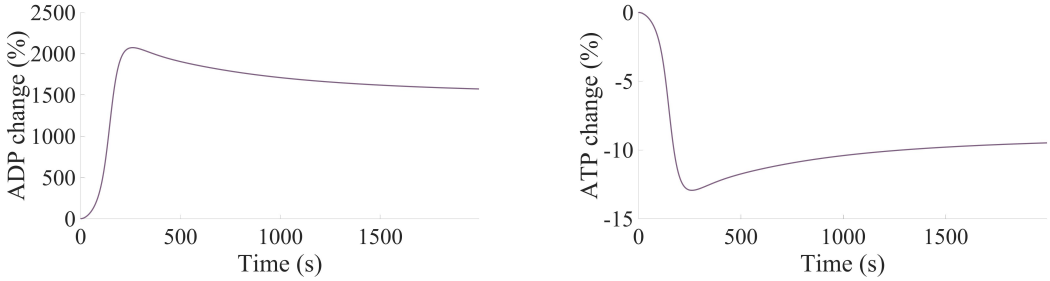

(a) ADP variation. **(b)** ATP variation.

Figure 3.5: ADP (a) and ATP (b) percentage variation upon a 40% increase in CBF at $t = 0$.

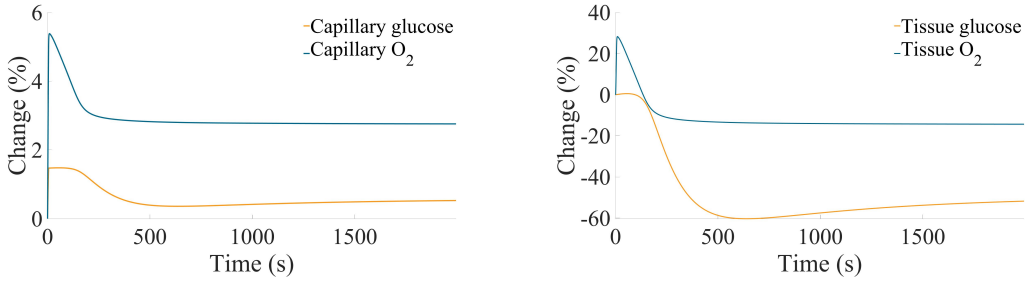

(a) Capillary oxygen and glucose variation. **(b)** Tissue oxygen and glucose variation.

Figure 3.6: Capillary (a) and tissue (b) oxygen and glucose levels percentage variation upon a 40% increase in CBF at $t = 0$.

Figure 3.5 serves to indicate both the immediate and long-term changes in metabolism. Given that neurovascular coupling happens in a time frame of seconds to minutes, only the changes happening in the initial part (i.e. approx. first 200s) of the simulation are relevant when aiming to define the relationship between neural demand and glucose supply. Further implications of the slow ADP and ATP concentration change are discussed in Chapter 7.

The cerebral metabolic rate of oxygen ($CMRO_2$) increase depends on the ATP/ADP ratio and intracellular oxygen and pyruvate concentrations. Hence, it can be calculated as the ratio of the instantaneous mitochondrial respiration and its baseline value $\overline{v_{mito}}$:

$$CMRO_2 = \frac{v_{mito}}{\overline{v_{mito}}} \tag{3.25}$$

A common assumption is that the cerebral metabolic rate of glucose CMR_{glc} and CBF are linked in a way that suggest that linear changes in CMR_{glc} result in a linear change of $CMRO_2$. However, experimental findings by Sokoloff (1991) [85] show that the respiratory quotient (RQ) (i.e. the ratio of CO_2 production and $CMRO_2$) is 0.97. If all energy metabolism were the oxidation of glucose to H_2O and CO_2, the respiratory quotient would be 1.

Hence, a value of 0.97 indicates that almost all of the O_2 generates CO_2 but it does not support the notion that all glucose is oxidised to H_2O and CO_2. [86] Indeed, in healthy individuals the ratio $CMRO_2/CMR_{glc}$ is about 4.9, as can be derived from the values presented in Table 3.2, with an upper limit for the ratio being 5.5 as reported by Sokoloff (1991). [85]

Fox et al. (1988) [87] found that upon stimulation, the brain increased CMR_{gluc} by 50% while $CMRO_2$ only increased by (a statistically insignificant) 5%. This suggests that (locally) upon activation there is an uncoupling between CMR_{glc} and $CMRO_2$. This raises two interesting questions:

1. How much of the phosphorylated glucose is actually oxidised?

2. What is the relationship between the three parameters: $CMRO_2$, the rate of glucose oxidation and the rate of glucose phosphorylation?

Parameter	Value	Units
$CMRO_2$	151	μM/100 g/ min
CMR_{glc}	31	μM/100 g/ min
CBF	58	ml/100 g/min
CO_2 production	156	μM/100 g/ min
O_2/glucose ratio$_{max}$	5.5	μmol/μmol
RQ	0.97	-

Table 3.2: Median values from experimental data from healthy humans presented by Sokoloff (1991) [85].

If the entirety of glucose in the brain tissue were to be oxidised, the ratio $CMRO_2$: CMR_{glc} would be 6:1, as $1\mu M$ of glucose would generate $6\mu M$ of oxygen.

$$C_6H_{12}O_6 \rightarrow 6H_2O + 6CO_2 \tag{3.26}$$

However, Table 3.2 shows that the ratio of CMR_{glc} and $CMRO_2$ is below 6. This can be explained by the fact that the brain also produces lactate corresponding to 13% of pyruvate production. This fraction of the lactate pool is removed from the brain and is thus not oxidized to H_2O and CO_2. It is thus to study the relationship between $CMRO_2$ and CMR_{glc}, we must take into account the variability of lactate LAC. [88] To address this, Lin et al. (2010) [89] proposed the following formulation:

$$CMR_{glc} = \frac{1}{2}(LAC + \frac{1}{3}CMRO_2) \tag{3.27}$$

Intracellular lactate LAC_i is given by the difference between the velocity of lactate dehydrogenase v_{LDH} and the BBB transport of lactate v_{LACm}. [80]

$$\frac{dLAC_i}{dt} = v_{LDH} - v_{LACm} \tag{3.28}$$

$$v_{LDH} = {k_{LDH}}^{+} \cdot PYR \cdot NADH - {k_{LDH}}^{-} \cdot LAC \cdot NAD^{+} \tag{3.29}$$

$$v_{LACm} = T_{max,LAC}\left(\frac{LAC_i}{LAC_i + K_{t,LAC}} - \frac{LAC_c}{LAC_c + K_{t,LAC}}\right) \tag{3.30}$$

where ${k_{LDH}}^{+}$, ${k_{LDH}}^{-}$, PYR and $T_{max,LAC}$ are all constants and the reduced form of nicotinamide adenosine nucleotice $NADH$ is derived from:

$$\frac{dNADH}{dt} = v_{PGK} - v_{LDH} - v_{mito} \tag{3.31}$$

Following the outlined modelling approach, Figure 3.7a shows how a 40% increase in CBF induces a 220% increase in lactate and a respective 110% increase in CMR_{glc}. Figure 3.7b shows how the percentage change in CMR_{glc} is about 10 times the change in $CMRO_2$, settling to a new value in about 30 minutes and 1 minute respectively.

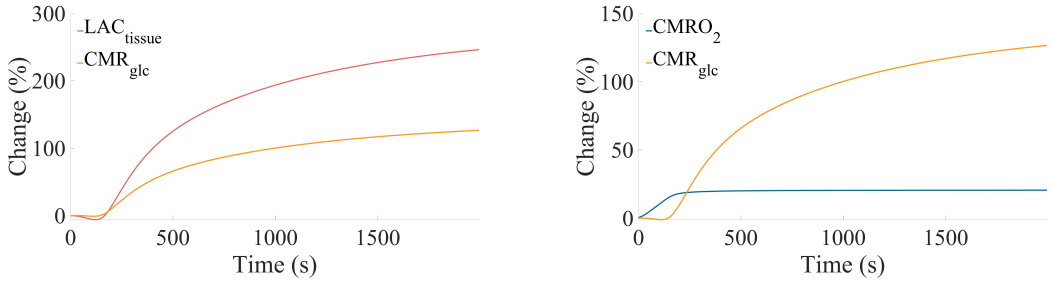

(a) LAC and GLC_t variation. **(b)** $CMRO_2$ and CMR_{glc} variation.

Figure 3.7: LAC , GLC_t (a) and $CMRO_2$ and CMR_{glc} percentage variation in the tissue upon a 40% increase in CBF at $t = 0$.

To more clearly delineate the relationship between CBF and nutrient metabolism, six additional scenarios were investigated: 1% CBF increase, 2.5% CBF increase, 5% CBF increase, 10%CBF increase, 20% CBF increase and 30% CBF increase. Table 3.3 summarises the results of the changes in metabolism, as well as tissue and capillary concentration of both glucose and oxygen for different CBF increases.

CBF increase	1%	2.5%	5%	10%	20%	30%	40%
$CMRO_2(\%)$	0.58	1.24	2.55	5.26	10.51	16.19	20.57
$CMR_{glc}(\%)$	0.0049	0.0054	0.012	0.029	0.059	35.04	126.60
$O_{2tiss,min}(\%)$	-0.0073	-0.15	-1.06	-3.17	-7.3	-12.85	-15.87
$GLC_{tiss}(\%)$	0	0	-0.68	-3.47	-15.03	-36.94	-60.32
$O_{2,cap}(\%)$	0.35	0.58	1.00	1.79	3.18	4.36	5.38
$GLC_{cap}(\%)$	0.10	0.16	0.27	0.49	0.87	1.19	1.48

Table 3.3: Comprehensive overview of the metabolic response to a step-wise increase in CBF. The changes in concentrations of the O_2 and glucose in the capillaries and tissue are presented along with the metabolic increase of each nutrient.

The presented values highlight two key conclusions. The first is that glucose reserves in the tissue can sustain a CBF increase up to about 5%, indeed GLC_{tiss} is negative beyond this threshold. Moreover the glucose content supplied by the vessels (GLC_{cap}) is lower than the demand in the tissue, meaning that there is a decoupling between supply and demand.

The second conclusion involves the change in oxygen consumption, which is is negative even for a 1% increase in CBF. This highlights the higher sensitivity of the brain in fluctuations of oxygen concentration. On the contrary to the glucose supply, the oxygen supplied by the capillaries matches the demand of the tissue ($O_2, cap > O_2, tiss$), which justifies why in Figure 3.7b the $CMRO_2$ reaches a new steady value more rapidly compared to CMR_{glc}.

3.6 Summary

As nutrient supply occurs in the microvasculature of the brain, the haemodynamic characteristics of blood flow were defined mathematically. Next, an overview of the metabolic sensitivity in the neurovascular unit was presented, particularly focusing on oxygen and glucose consumption in the tissue. The cascade of events from the onset of brain activation and leading up to CBF regulation is discussed and summarised in Figure 3.3, with the aim of serving as a roadmap for the model's description of neurovascular coupling.

While prolonged changes in glucose metabolism are governed by hormones, short-term changes are moderated by CBF. Hence, only rapid changes (occurring in a time frame ranging from seconds to few minutes) are relevant when investigating neurovascular coupling. The tight coupling between CBF, capillary density and CMR_{glc} is the reason behind our investigation of the time scale of these interactions. Following the approach described by Aubert et al. (2001) and (2002) glucose concentration was modelled within the supplying capillaries (GLC_C) and the tissue (GLC_T) where it is consumed. Furthermore, to link neural activity to metabolic activity and later Ca^{2+}-induced pericyte activity, the Na/K pump reactivity was studied as a function of ATP variations.

The speed of metabolic change in the tissue in relation to changes in CBF was studied, showing that a 40% increase in CBF results in an increase of CMR_{glc} of about 126% and an increase in $CMRO_2$ of about 20%. The speed of change was also evaluated and it was ultimately concluded that CMR_{glc} change is too slow to be a key regulator in the fast process that characterises the CA, being about 10 times slower than the $CMRO_2$ change.

The disparity between supply and demand was highlighted in Table 3.3 for both O_2 and glucose, ultimately supporting the notion that the brain relies on a tight coupling between tissue and vasculature. Indeed, even small changes in CBF, as was highlighted by the computational analysis, result in a metabolic increase that can not be met by the nutrient reserves present in the tissue for more than a few minutes. These conclusions underline the need for rapid regulatory mechanisms that can link the metabolic demand of the tissue to a vascular response.

No amount of experimentation can prove me right;
a single experiment can prove me wrong.

— Albert Einstein (1879 - 1955)

4 Experimental data analysis

Contents

4.1 Experimental setup 54
4.2 Capillary diameter variation 55
4.2.1 Processing 56
4.2.2 Selection 57
4.2.3 Vessel trace 58
4.2.4 Imaging depth 60
4.3 Frequency analysis 63
4.3.1 Imaging depth dependence 65
4.4 Data fitting 66
4.4.1 Time constants 69
4.5 Statistical significance 70
4.6 Calcium concentration 73
4.7 Local metabolic and haemodynamic changes 74
4.7.1 Blood flow and volume 75
4.7.2 Oxygen metabolism 80
4.8 Summary 84

Numerous studies [40], [90] support the notion that the active presence of pericytes within the capillary bed plays an important role in cerebral tissue perfusion. Pericytes can regulate capillary diameter in both the retina and cortex, and the ones located in the somatosensory cortex dilate vessels as a result of sensory stimulation. Indeed, pericytes are excitable cells, whose resting membrane potential $(-32 - 70mV)$ can be varied through different ion channels such as Ca^{2+}. [45]

Moreover, active capillary dilation would deliver O_2 with much greater spatial precision than arterioles. [40] With the aim of quantifying the capillary diameter increase, the pericyte response to a visual stimulus is presented here. Ultimately, as the visual stimulus causes neural activation which in turn results in an increase of Ca^{2+} in the tissue (see Figure 3.3), the local Ca^{2+} change was also experimentally quantified and analysed here. The experimental results and conclusions on capillary dilation as a result of pericyte activity are reported in Milanovic et al. (2021) [91], while the metabolic consumption changes in the tissue surrounding the vessel are presented in Shaw et al. (2021) [92].

4.1 Experimental setup

The raw data presented in this section were collected by Dr. Kira Shaw and Prof. Catherine Hall at the University of Sussex and subsequently analysed here. Figure 4.1 shows a schematic representation of the experimental setup, along with the type of visual stimulation (i.e. VR maze and drifting gratings) used to induce movement and neural activity in the C57BL/6J background mice. Pericyte responses to local increases in neuronal activity were experimentally determined using two-photon imaging of the visual cortex in awake mice expressing a genetically encoded Ca^{2+} indicator in excitatory neurons and with the vascular lumen labelled with injected Texas Red dextran.

Two distinct sets of data were used for the experimental part of the study, as changes in diameter and $CMRO_2$ cannot be assessed simultaneously. Indeed, to measure the net cerebral blood flow and haemoglobin oxygenation a parallel set of experiments was performed using a probe (VMS Oxy, Moor Instruments) that combines laser doppler flowmetry and haemoglobin spectrometry. This instrument is placed over the entire cranial window and records regional net haemodynamics from across the tissue and not from selected vessels. The effect of the placement of the probe on each animal and the differences between imaging sessions are negligible, as discussed in detail by Shaw (2021) [92] (see supplementary Figure 10a). Moreover, the LDF probe that was used has an excitation-detection fibre separation of $500\mu m$ and an

excitation wavelength of $780nm$ therefore, unlike other fibre designs, it has a deep sampling depth, with a median depth sampled of $0.9mm$. This suggests that vessels found in the depth range $0 - 2mm$ can contribute to the recorded signal.

On the other hand, to measure pericyte-induced vessel dilation, capillaries were imaged using a two-photon microscopy objective. A custom MATLAB script was used to extract the diameter of vessels from two-photon imaging along the full width at half maximum (see Shaw (2021) [92]). In brief, a skeleton was produced in the center of the vessel and an intensity profile measured along a perpendicular line to this vessel skeleton (as the vessel was fluorescent and the background was dark). The diameter was calculated from the full width at half maximum of the intensity profile, and averaged across a overlapping, progressing window of five skeleton pixels for spatial smoothing. These measurements were then averaged per frame along the entire vessel length, leaving an averaged continuous diameter trace over time. For the overall average diameter of the vessel these continuous traces were again averaged over time to give one value. Ultimately, the experimental approach is reported in Milanovic et al. (2021) [91] and Shaw et al. (2021) [92] and its limitations are discussed in Chapter 7.

4.2 Capillary diameter variation

With the aim of investigating the capillary response to neural activation, a total of 26 capillary vessels from 6 mice were studied. The diameter of the studied vessels ranges between $2 - 13\mu m$ (see Figure 4.2), with vessels being located at imaging depths between $0\mu m - 350\mu m$. To induce neural activation, mice were visually stimulated for $5s$ at $10s$ intervals and the capillary vessel response was observed (see Figure 4.3a). As visual stimulation results in an increase in vessel diameter and a Ca^{2+} increase in the tissue surrounding the vessel, the Ca^{2+} trace (see Figure 4.3b) and the diameter change (see Figure 4.3c) of each vessel were tracked.

From the total number of vessels used for the experiment, 8 were selected for the validation of the blood flow model presented in Chapter 5. The first exclusion factor for the data was vessel diameter. An acceptable range of $6 - 10\mu m$ was decided

upon, as the capillary diameter defined within the microvasculature network of the mathematical model presented is $8\mu m$.
This modelling choice is based on the results presented by Cassot et al. (2006) [15], according to which vessels above the established $8\mu m$ threshold can be categorised as arterioles while those below are capillaries. A further selection criteria is the vessel's ability to present a clear response to the Ca^{2+} stimuli. A more detailed description of the data classification process is shown in Section 4.2.2.

Moreover, it is important to underline the fact that 4 of the 8 selected vessels stem from Mouse 3 (see Figure 4.2 and Table 4.3). As this is 50% of the total data the experimental part of this study is based upon, the derived limitations are discussed in depth in Chapter 7.

4.2.1 Processing

For the purpose of this study, the most relevant measurement is the vessel diameter variation that occurs during the visual stimulus. Hence, only the data processing of the diameter variation is given here. To obtain an average value of the maximum capillary dilation after the visually-induced Ca^{2+} increase, the following five steps were taken:

1. The vessel trace data for each vessel were normalised to the vessel's baseline diameter.

2. For each vessel, the experiment was conducted multiple times (3-8), hence an average of all the experiments was taken.

3. The average vessel trace from point (2) was segmented in 10 sections, one for each visual stimulus interval.

4. The 10 segments of capillary diameter variation from point (3) were superimposed and averaged, obtaining therefore the average response to a $5s$-long visual stimulus for each vessel.

5. Point (4) therefore provides the average response of each vessel that can be averaged among each other delivering a single response pattern that is indicative of all 26 vessels.

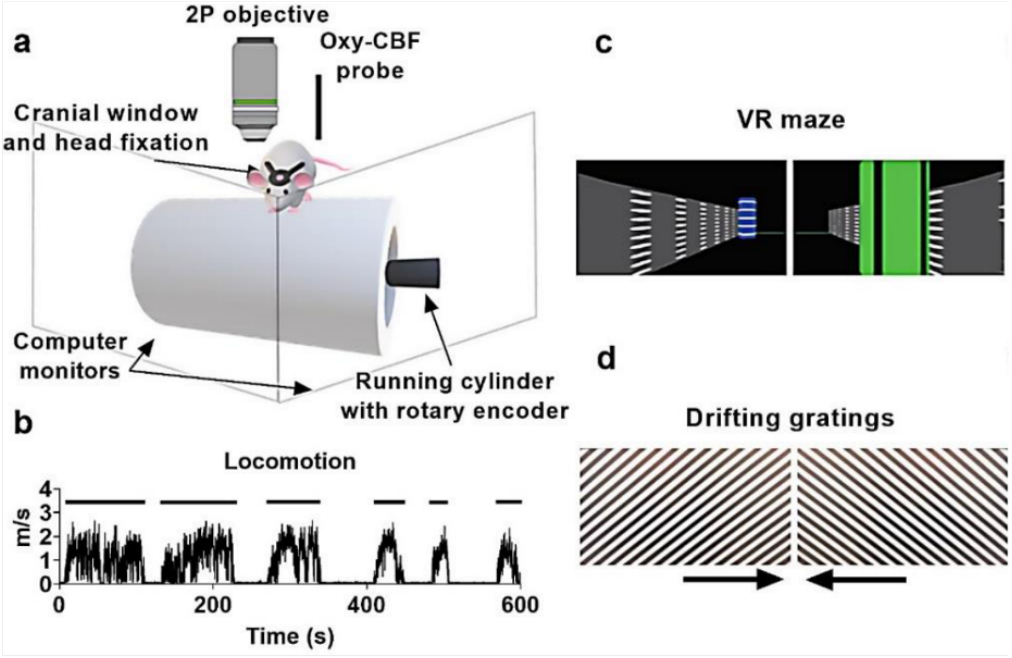

Figure 4.1: Illustration of the imaging setup, used with permission of Shaw and Hall. (a) Awake mouse walking on a rotating cylinder with a fixed probe on the head; (b) locomotion recording of moving and still mouse; (c) virtual reality maze and (d) drifting gratings used as visual stimulation.

4.2.2 Selection

Various considerations were made in order to select the appropriate vessels for the analysis. The two criteria that were implemented for the selection of the vessels to be examined are the vessel's diameter and the presence of a response. In particular, the capillary diameter range that is relevant for this study is $6 - 10\mu m$. Therefore, capillaries outside of this range were not considered for the blood flow modelling described in Chapter 5. However, with the aim of investigating the difference in dilating ability of large and small capillaries, the model fit was also conducted for vessel in the $2 - 6\mu m$ diameter range.

Moreover, a statistical approach based on the coefficient of variance (CV) was

implemented in order to distinguish between a present and an absent response. The analysis was conducted in the $10s$ prior to the stimulus ($t = 12.5s$). Given the mean value μ and the standard deviation σ of the vessel trace, the CV was evaluated as follows:

$$CV[\%] = \frac{\sigma}{\mu} \cdot 100 \tag{4.1}$$

The threshold of acceptance was $CV \leq 1\%$. Therefore, capillaries whose pre-stimulus vessel trace data exceeded this threshold were neglected.

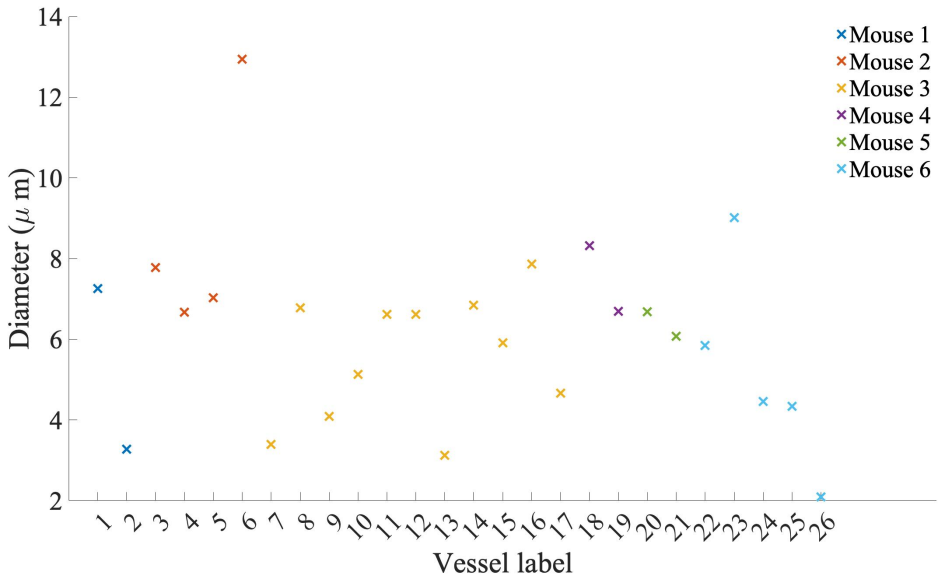

Figure 4.2: Baseline diameters of capillary vessels. The 26 vessels considered were taken from 6 different mice, each represented by one colour.

4.2.3 Vessel trace

The capillary diameter variation was evaluated for all responsive vessels and the differences in response between large and small vessels were highlighted in terms of peak dilation and response time.

Vessel diameter 6-10 μm

The number of vessels considered for the model fit whose function simulates active capillary dilation in the network model presented in Chapter 5 is 8. Figure 4.4

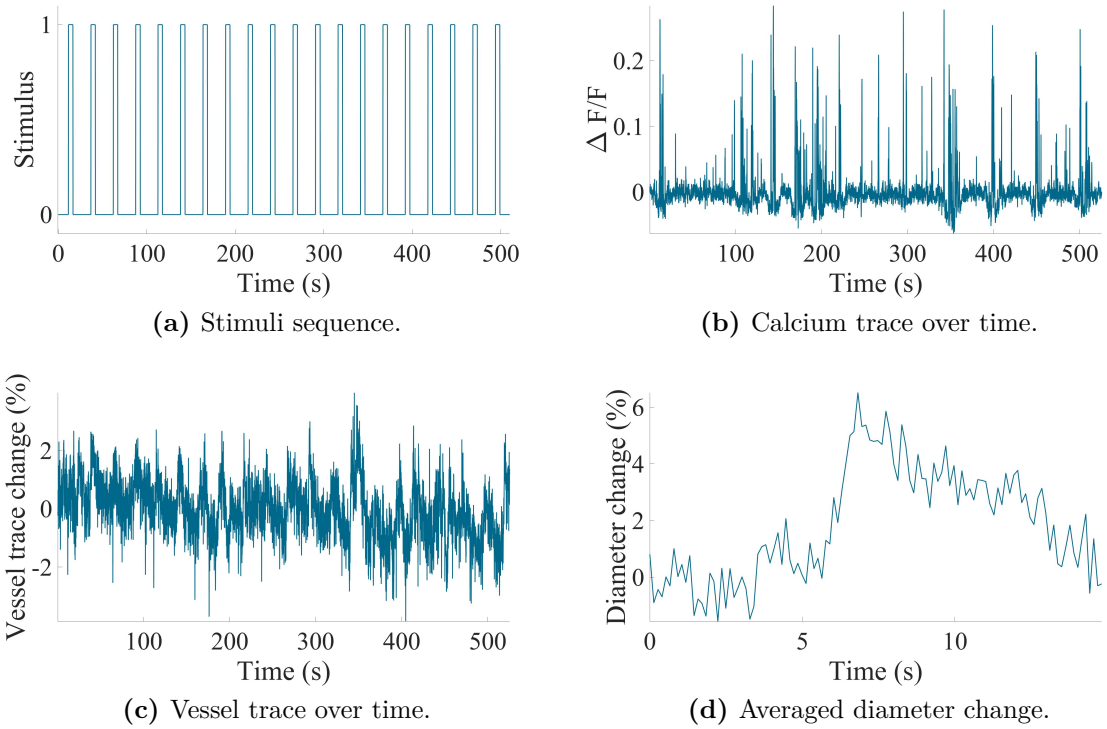

(a) Stimuli sequence.

(b) Calcium trace over time.

(c) Vessel trace over time.

(d) Averaged diameter change.

Figure 4.3: Example of data processing for Vessel 1 (a) visual stimulus intervals; (b) Ca^{2+} trace over time; (c) normalized vessel trace over time; (d) ensemble average of diameter change.

illustrates the difference in magnitude of the peak response between two scenarios: when all 26 vessels are considered versus when the relevant 8 capillaries selected following the criteria outlined in Section 4.2.2 were considered. For all 26 vessels, the peak dilation was identified to be a 1.25% increase from the baseline value, as shown in Figure 4.4a. In comparison, analysing only the 8 selected vessels resulted in an average maximum dilation of 2.62%, as shown in Figure 4.4b.

Vessel diameter 2-6μm

The response of the 12 vessels in the diameter range $2-6\mu m$ was analysed, following the same steps outlined in Section 4.2.2. Figure 4.5a shows that the average peak increase in capillary diameters for all small capillaries is about 1.23% from the baseline. Following the same exclusion principles, 6 vessels were excluded from the analysis. The four vessels included in the analysis are: V13, V2, V7 and V24. The

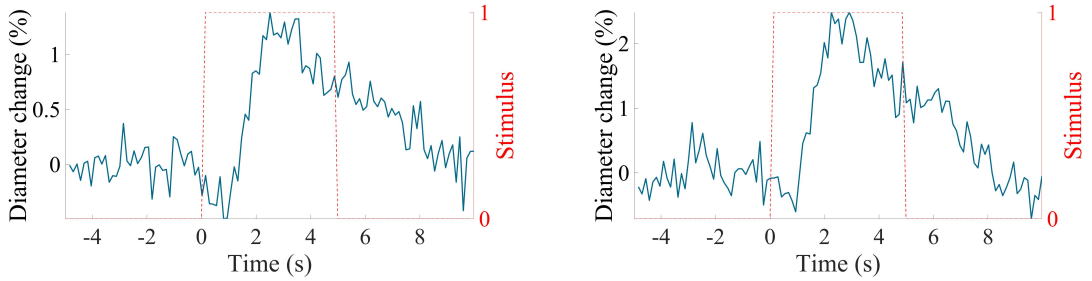

(a) Averaged vessel trace for 26 vessels. **(b)** Averaged vessel trace for 8 vessels.

Figure 4.4: Averaged capillary diameter change to a 5s visual stimulus for all 26 (a) and 8 responsive (b) vessels.

ensemble average across the four responsive vessels showed that the peak dilation is about 2.52% from baseline, as shown in Figure 4.5b.

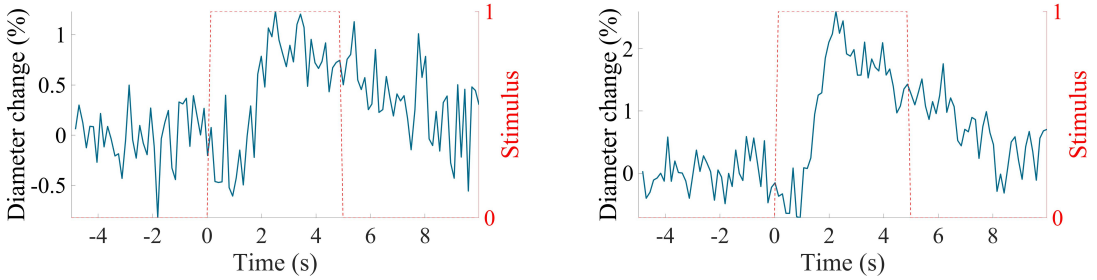

(a) Averaged vessel trace for 12 vessels. **(b)** Averaged vessel trace for 4 vessels.

Figure 4.5: Averaged capillary diameter change to a 5s visual stimulus for all 12 (a) and 4 responsive (b) vessels.

4.2.4 Imaging depth

The collected vessel trace data are taken from a wide range of imaging depths $0-350\mu m$. Here, the total range was divided into 4 categories: $0-50\mu m$, $50-150\mu m$, $150-250\mu m$ and $250-350\mu m$ with the aim of studying the possible depth-dependent differences in capillary dilation abilities. Figure 4.6 shows the pericyte-induced dilation of a capillary vessel found at a depth of $0-50\mu m$. To facilitate visualization, the red line outlines the vessel wall at rest and the red triangles direct attention towards the areas of dilation. Similarly, Figure 4.7, Figure 4.8 and Figure 4.9 present examples of capillaries imaged at $50-150\mu m$, $150-250\mu m$ and $250-350\mu m$

depths respectively.

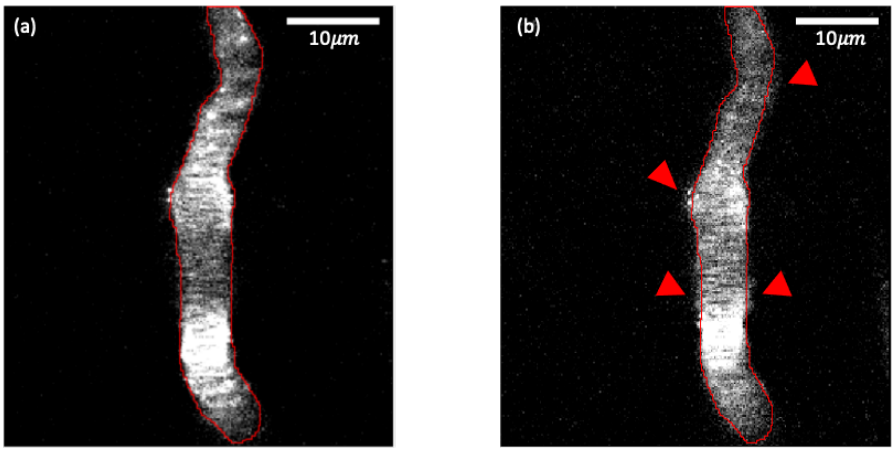

Figure 4.6: Capillary vessel imaged at $0 - 50\mu m$ depth, where (a)shows the vessel at rest and (b)shows the vessel dilation.

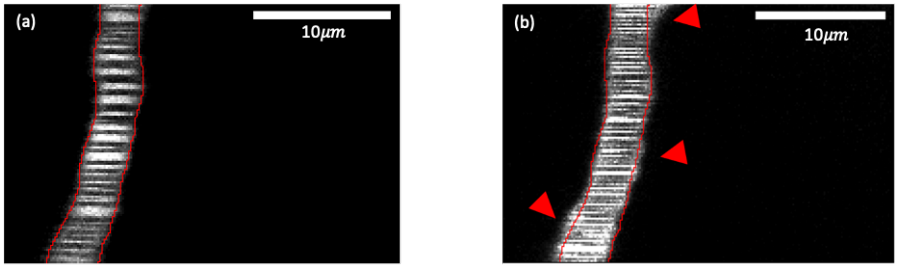

Figure 4.7: Capillary vessel imaged at $50 - 150\mu m$ depth, where (a)shows the vessel at rest and (b)shows the vessel dilation.

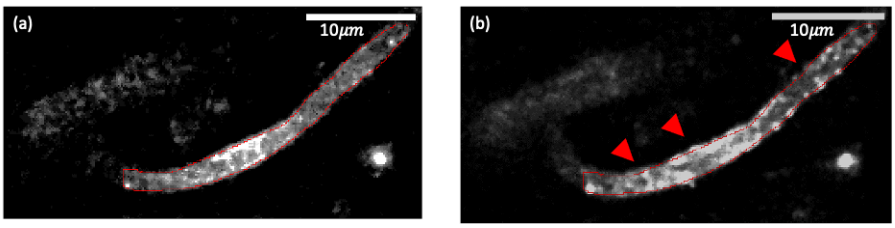

Figure 4.8: Capillary vessel imaged at $150 - 250\mu m$ depth, where (a)shows the vessel at rest and (b)shows the vessel dilation.

Figure 4.10 highlights the differences in peak dilation across the 4 ranges of imaging depths. The sole exclusion principle for this analysis was the lack of response ($CV \geq 1\%$) to the Ca^{2+} increase in the surrounding tissue. However, it also needs to be considered that there are significant variations between the vessel

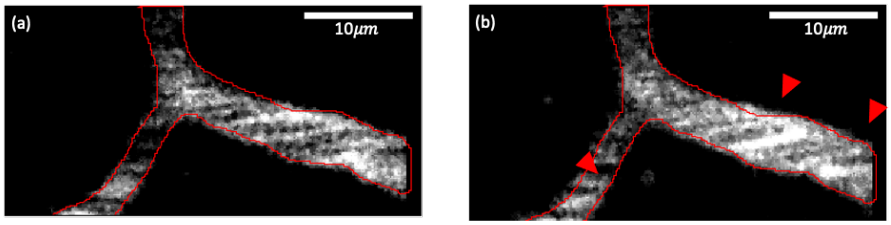

Figure 4.9: Capillary vessel imaged at $250 - 350\mu m$ depth, where (a)shows the vessel at rest and (b)shows the vessel dilation.

groups compared at the different depths. For instance, the number of vessels imaged differs for each category, as does the vessel diameter. Further implications on the heterogeneity of vessel groups considered across the 4 imaging depth ranges are discussed in Chapter 7.

Table 4.1 summarises the vessel classification described. It was found that the average peak dilation for the $0 - 50\mu m$ depth range was 2.11%, for the $50 - 150\mu m$ range it was 2.60%, for the $150 - 250\mu m$ it was 2.37% and for the $250 - 350\mu m$ range it was 3.2%.

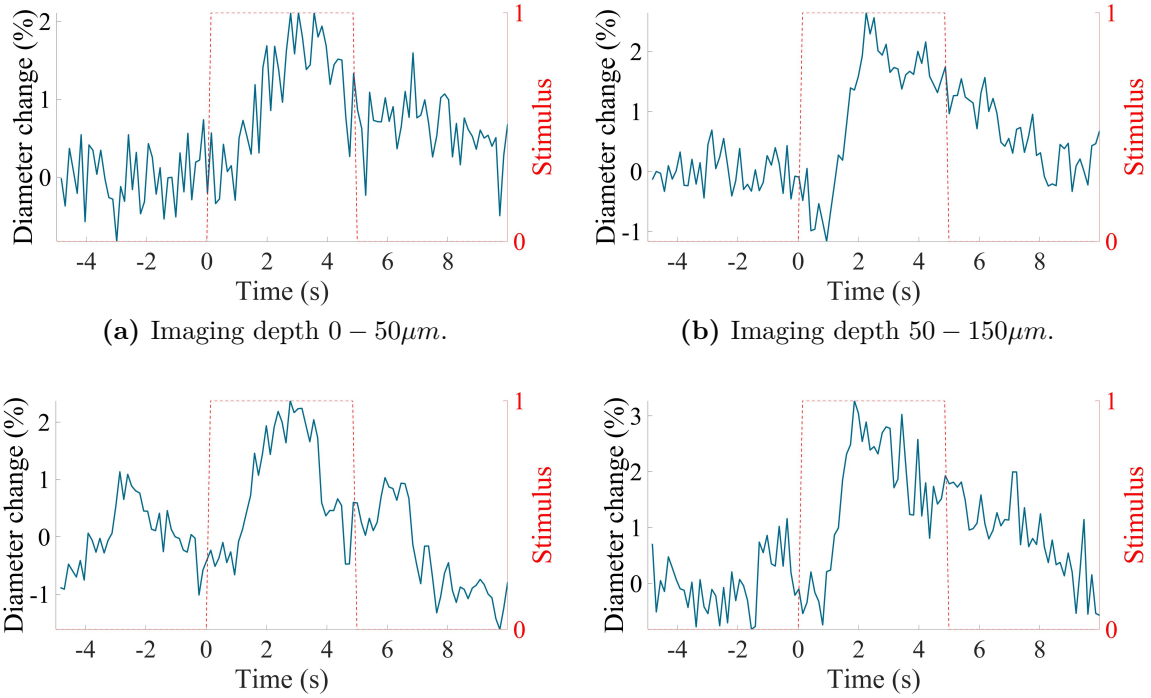

(a) Imaging depth $0 - 50\mu m$.

(b) Imaging depth $50 - 150\mu m$.

(c) Imaging depth $150 - 250\mu m$.

(d) Imaging depth $250 - 350\mu m$.

Figure 4.10: Averaged capillary diameter variation upon visual stimulation across 4 imaging depth ranges.

Diameter $6-10\mu m$				
Imaging depth	$0-50\mu m$	$50-150\mu m$	$150-250\mu m$	$250-350\mu m$
Vessel	-	V4, V15, V22	V11, V16, V23	V1, V18
Peak dilation (%)	-	2.42	2.37	3.2
Diameter $2-6\mu m$				
Imaging depth	$0-50\mu m$	$50-150\mu m$	$150-250\mu m$	$250-350\mu m$
Vessel	V13	V2, V7, V24	-	-
Peak dilation (%)	2.11	2.79	-	-

Table 4.1: Imaging depth dependent vessel dilation across 4 imaging depth categories. The average peak dilation is reported for large and small capillaries.

4.3 Frequency analysis

In order to better illustrate the oscillating signals in the vessel trace, a frequency analysis was performed. It is important to note that the power spectrum can only reach half the speed at which the diameter trace data was collected, setting the frequency measurement limit to 3 Hz. The locomotion frequency is 0.1 Hz and thus, significant power peaks are present in this frequency range.

Welch's method was used in order to estimate the spectral density, which is carried out by dividing the time signal into consecutive blocks of equal length, forming a periodogram for each block and ultimately averaging. The code was developed in MATLAB and the results of the analysis are thus presented here. To investigate the difference in power spectra between capillary diameter sizes, and be consistent with the analysis in Section 4.2, the vessels were divided in small vessels ($2-6\mu m$) and large vessels ($6-10\mu m$). As in previous sections, the small vessels were studied for completion but the results were not considered when developing the mathematical model presented in Chapter 5, which only accounts for the behaviour of large capillaries.

Figure 4.11 shows the frequency analysis for large vessels. Next to the unnormalised spectra trace, a normalized power spectra trace is presented in order to facilitate the visualization of the locomotion frequency peak at 0.1 Hz (highlighted by a vertical dotted line). Similarly, Figure 4.12 presents the frequency analysis results for small

vessels. Finally, Figure 4.13 presents the average unnormalized and normalized spectra trace of all capillary vessel diameters.

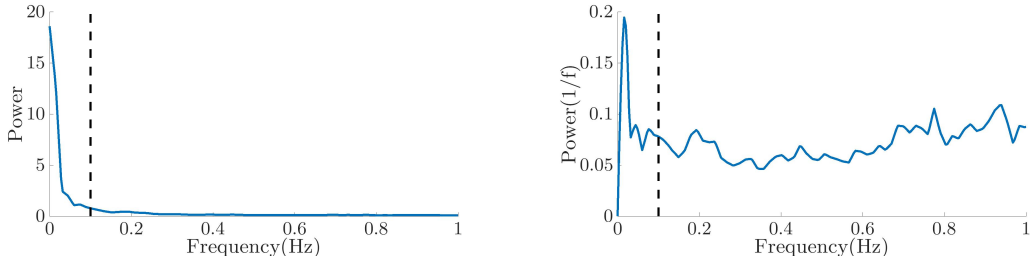

(a) Unnormalised power spectra trace. **(b)** Normalized power spectra trace.

Figure 4.11: Large vessels $(6-10\mu m)$; Unnormalised power spectra trace (a) Normalized power spectra trace for 1/f noise (b). The locomotion frequency is illustrated by a vertical dotted line at 0.1 Hz.

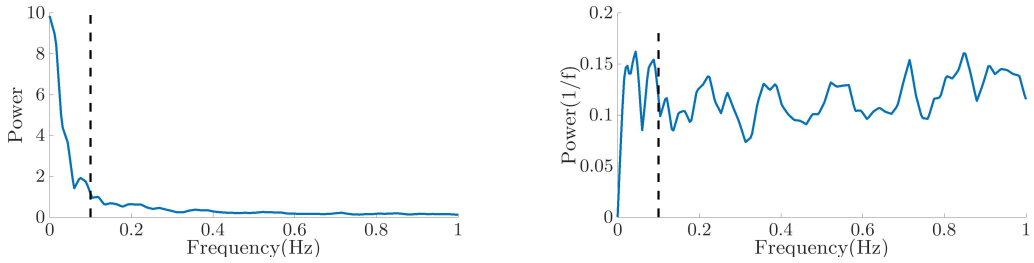

(a) Unnormalised power spectra trace. **(b)** Normalized power spectra trace.

Figure 4.12: Small vessels $(2-6\mu m)$; Unnormalised power spectra trace (a) Normalized power spectra trace for 1/f noise (b). The locomotion frequency is illustrated by a vertical dotted line at 0.1 Hz.

In both, Figure 4.11 and Figure 4.12, the unnormalised power spectra trace presents a clear power peak at 0.1 Hz, indicating the vasodilation induced by the visual stimulus. The normalized trace however, indicates multiple peaks for the small vessels (see Figure 4.12b). This could be attributed to the fact that the average vessel diameter for small vessels is $3.56\mu m$, making the 2.52% diameter variation a significantly small locomotion that is thus subject to noise.

Physiological phenomena such as heart beat and breathing were not detected in the frequency analysis as their frequency range is 5-15 Hz [93] (being closer to the upper limit when the mouse is moving), which is outside the experimental detection limit of 3 Hz. Moreover, making further conclusions on the power spectra trace from the

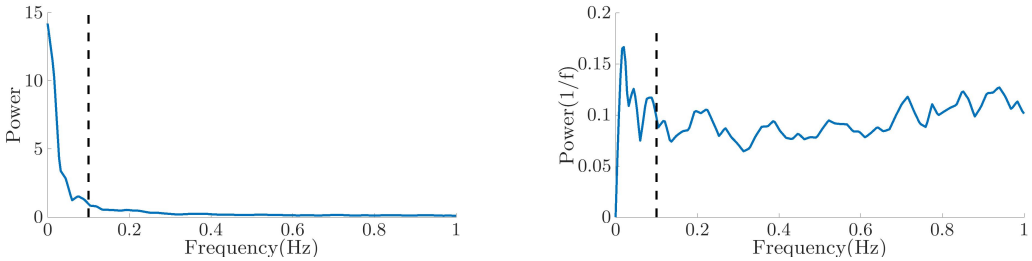

(a) Unnormalised power spectra trace. **(b)** Normalized power spectra trace.

Figure 4.13: All vessels $(2-10\mu m)$; Unnormalised power spectra trace (a) Normalized power spectra trace for 1/f noise (b). The locomotion frequency is illustrated by a vertical dotted line at 0.1 Hz.

above defined analysis is beyond the capabilities of the experimental equipment used and the scope of the research. Ultimately, the frequency analysis results for each individual vessel are reported in the Appendix.

4.3.1 Imaging depth dependence

To investigate a potential correlation between imaging depth and power spectra, the frequency analysis was conducted by grouping vessels per imaging depth category. Figure 4.14 presents the unnormalized and normalized spectra trace for vessels (V13) found in the $(0-50\mu m)$ depth range. As in this depth category only one vessel is present, no conclusions on the average behaviour of vessels in this part of the tissue can be drawn.

Figure 4.15 presents the unnormalized and normalized spectra trace for 6 vessels (V2, V4, V7, V25, V22, V24) found in the $(0-50\mu m)$ depth range. Here, half of the vessels have a small diameter while the remaining half has a large diameter, presenting therefore a highly heterogeneous tissue segment. On the other hand, Figure 4.16 shows the average unnormalized and normalized power spectra for 3 vessels (V11, V16, V23), all being in the large diameter range. Similarly, Figure 4.17 illustrates the unnormalized and normalized power spectra for 2 vessels (V1, V18) with large diameters.

Given the uneven distribution of vessel diameters across imaging depths and the low number of vessels, it is not possible to outline conclusions on depth-

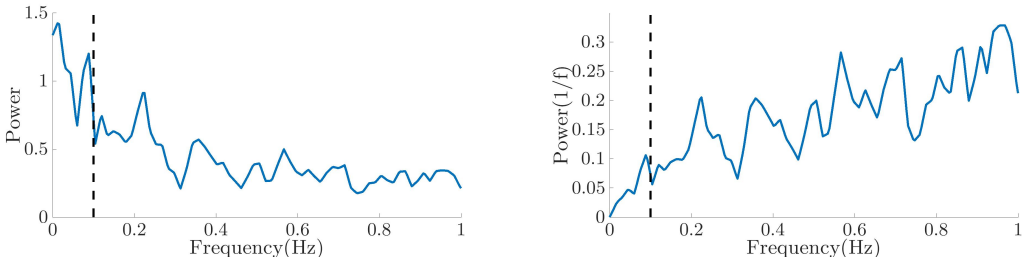

(a) Unnormalised power spectra trace. **(b)** Normalized power spectra trace.

Figure 4.14: Imaging depth $(0 - 50\mu m)$; Unnormalised power spectra trace (a) Normalized power spectra trace for 1/f noise (b). The locomotion frequency is illustrated by a vertical dotted line at 0.1 Hz.

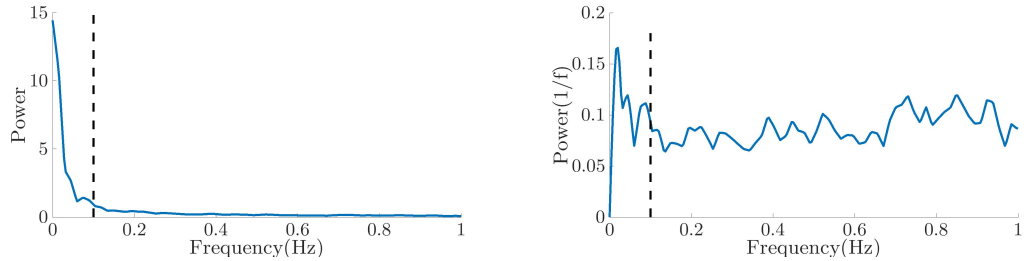

(a) Unnormalised power spectra trace. **(b)** Normalized power spectra trace.

Figure 4.15: Imaging depth $(50 - 150\mu m)$; Unnormalised power spectra trace (a) Normalized power spectra trace for 1/f noise (b). The locomotion frequency is illustrated by a vertical dotted line at 0.1 Hz.

dependent power spectra. While all power spectra indicate peaks in the locomotion frequency range, vessels in the $0 - 150\mu m$ imaging depth present a higher oscillatory behaviour (see Figure 4.14 and Figure 4.15) than vessels in the $150 - 350\mu m$ imaging depth (see Figure 4.16 and Figure 4.17). A hypothesis for this distinction in response is outlined in Chapter 7.

4.4 Data fitting

With the aim of providing a model that could be used for various signals, the function was solved in the s-domain using the Laplace transform and subsequently converted back to the time domain, to compare it with the data. First, it is necessary to define the visual stimulus on which the function will be based. The stimulus was thus modelled as a rectangular pulse function $x(t)$ as shown in Figure 4.18 and defined by:

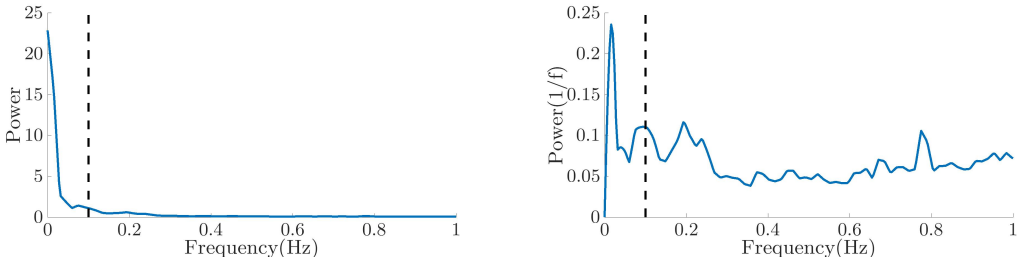

(a) Unnormalised power spectra trace. **(b)** Normalized power spectra trace.

Figure 4.16: Imaging depth $(150 - 250\mu m)$; Unnormalised power spectra trace (a) Normalized power spectra trace for 1/f noise (b). The locomotion frequency is illustrated by a vertical dotted line at 0.1 Hz.

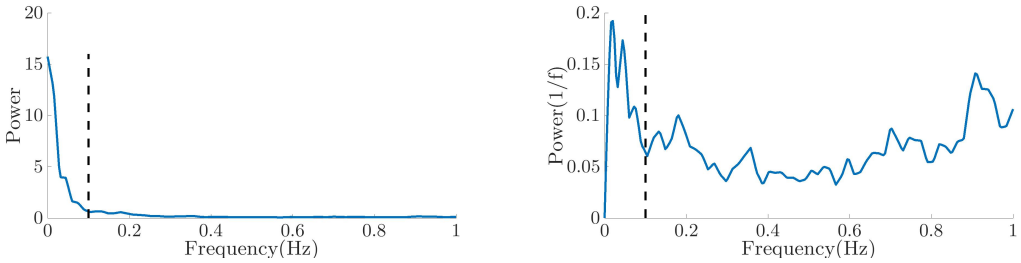

(a) Unnormalised power spectra trace. **(b)** Normalized power spectra trace.

Figure 4.17: Imaging depth $(250 - 350\mu m)$; Unnormalised power spectra trace (a) Normalized power spectra trace for 1/f noise (b). The locomotion frequency is illustrated by a vertical dotted line at 0.1 Hz.

$$x(t) = u(t) - u(t - T) \tag{4.2}$$

where $u(t)$ is a Heaviside function and the width is $T = 5s$, which corresponds to the duration of the Ca^{2+} increase as shown in Figure 4.18.

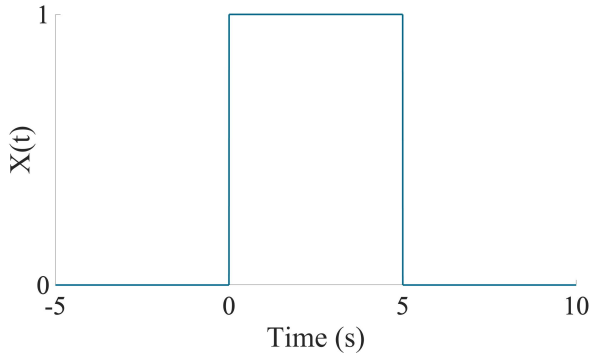

Figure 4.18: Rectangular function representing the single stimulus over time.

Being an overshoot function, the model fit was then evaluated from a standard second order model as follows:

$$F(s) = \frac{K(s+\alpha)}{s(s+\beta)(s+\gamma)} \tag{4.3}$$

where α, β, γ and K are time constants. The inverse Laplace transform of $F(s)$ is $f(t)$ and combined with the stimulus equation $x(t)$ then gives:

$$y(t) = u(t)f(t) - u(t-T)f(t-T) \tag{4.4}$$

With the aim of quantifying the accuracy of the model fit, the statistical significance of each time constant on Equation (4.3) was evaluated in Section 4.5. In particular, Table 4.4 and Table 4.5 summarize the mean values, standard deviations, p-values, R-squared and root mean square error for the model fits dependent on capillary diameter and imaging depth (See Figure 4.19 and Figure 4.20).

Vessel diameter 6-10 μm

Figure 4.19a shows the model fit to the visual stimulus-induced percentage variation of the capillary diameter with respect to its baseline value. With $T_\alpha = 1/\alpha$, $T_\beta = 1/\beta$ and $T_\gamma = 1/\gamma$, the time constants of the transfer function are: $T_\alpha = 33.33s$, $T_\beta = 2.38s$, $T_\gamma = 0.90s$ and $K = 4.8$. It can be calculated that the maximum diameter variation is 2.44% from the baseline value and that the reaction time, defined as the time between the onset of the stimulus and the peak diameter change, is about 1 s.

Vessel diameter 2-6 μm

Figure 4.19b shows the result of the model fit for small capillaries. The parameters defining the laplacian are: $T_\alpha = 20s$, $T_\beta = 5s$, $T_\gamma = 0.90s$ and $K = 4$. The peak dilation of the model fit is 2.34% and the reaction time is about 2 s.

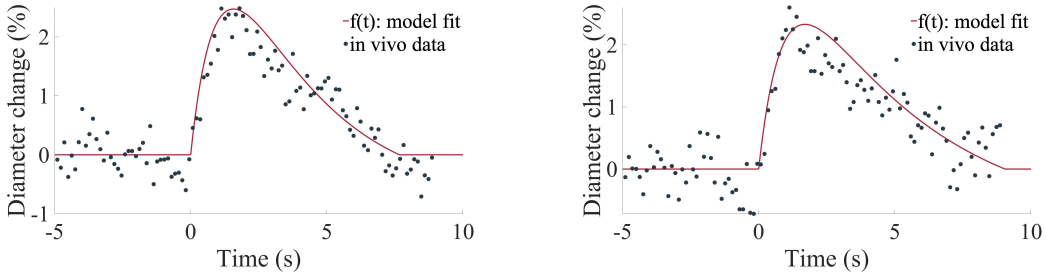

(a) Capillary diameter $6-10\mu m$. **(b)** Capillary diameter $2-6\mu m$.

Figure 4.19: Model fit with respect to capillary diameter $(6-10\mu m)$ (a) and $(2-6\mu m)$ (b) percentage change data points.

Imaging depth dependent dilation

To investigate the influence of imaging depth on the extracted model fit, each of the 4 categories of imaging depths was fitted individually. For this analysis, all the responsive vessels were considered and their response are shown in Figure 4.20. Table 4.2 illustrates the different peak values of the model fit curve for each category of imaging depth.

Imaging depth	$0-50\mu m$	$50-150\mu m$	$150-250\mu m$	$250-350\mu m$
Peak dilation (%)	2.11	2.38	2.38	2.85
T_α (s)	20	16.48	12.26	10
T_β (s)	5.0	4.44	4.38	2.5
T_γ (s)	0.90	1.37	1.01	0.45
K (s)	3.0	3.51	4.16	1.5

Table 4.2: Model fit peak dilations for each imaging depth category.

4.4.1 Time constants

As illustrated in Table 4.3, the time constants vary with the imaging depth. Figure 4.21 illustrates how the time constants vary over distance. Table 4.4 summarises the respective imaging depth time constant parameters, the mean values, standard deviations and error bars.

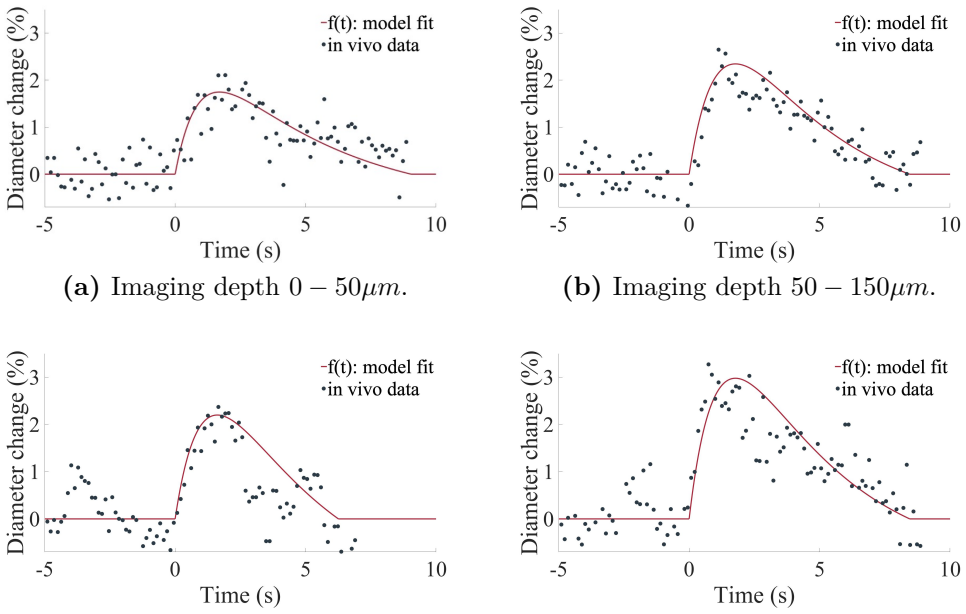

(a) Imaging depth $0 - 50\mu m$. **(b)** Imaging depth $50 - 150\mu m$.

(c) Imaging depth $150 - 250\mu m$. **(d)** Imaging depth $250 - 350\mu m$.

Figure 4.20: Model fit across 4 imaging depths for all responsive vessels.

4.5 Statistical significance

A statistical analysis was performed to investigate the differences in response to visual stimuli, between large $(6 - 10\mu m)$ and small $(2 - 6\mu m)$ capillary vessels and imaging depths. Table 4.5 summarises the results of the correlation analysis.

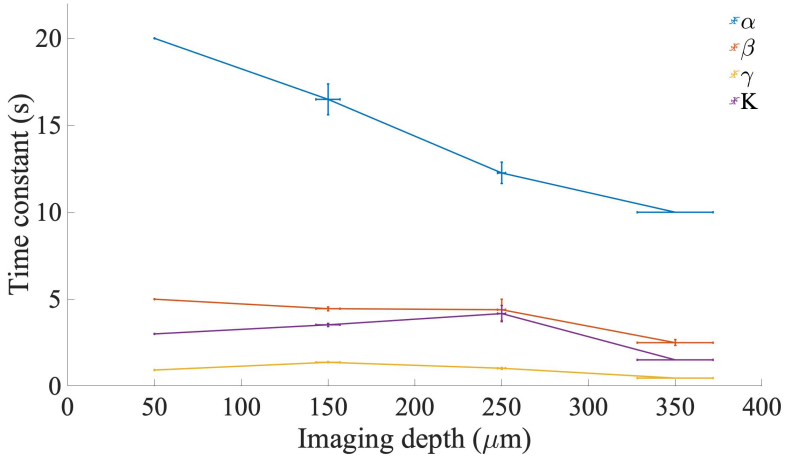

Figure 4.21: Time constants variation with imaging depth (per depth category) and respective error bars.

Vessel	D (μm)	D_{ch} (%)	d (μm)	CV (%)	$1/\alpha$ (s)	$1/\beta$ (s)	$1/\gamma$ (s)	K
V1	7.26	3.6	257.7	0.86	10.0	4.0	1.43	4.5
V2	3.28	3.0	138.5	0.42	20.0	5.0	1.42	3.7
V3	7.77	-	-	-	-	-	-	-
V4	6.67	3.4	137.8	0.61	16.66	3.33	1.66	4.0
V5	7.02	-	-	-	-	-	-	-
V6	12.94	-	-	-	-	-	-	-
V7	3.39	2.6	142.6	0.77	20.0	5.0	1.25	3.7
V8	6.78	-	-	-	-	-	-	-
V9	4.08	-	-	-	-	-	-	-
V10	5.13	-	-	-	-	-	-	-
V11	6.61	2.1	158.4	0.37	12.5	4.0	1.11	3.0
V12	6.62	-	-	-	-	-	-	-
V13	3.12	2.5	0	0.37	20.0	5.0	0.90	3.0
V14	6.84	-	-	-	-	-	-	-
V15	6.10	3.4	92.9	1.15	20.0	5.0	1.11	3.7
V16	7.86	3.2	142.2	0.98	10.0	2.5	1.11	6.0
V17	4.66	-	-	-	-	-	-	-
V18	8.14	3.5	345.4	1.08	10.0	3.33	1.43	4.7
V19	6.69	-	-	-	-	-	-	-
V20	6.68	-	-	-	-	-	-	-
V21	6.07	-	-	-	-	-	-	-
V22	6.84	1.4	149.5	0.32	11.11	5.0	1.11	2.0
V23	9.01	2.2	153.4	1.22	14.28	6.66	0.83	3.5
V24	4.45	3.0	65.2	0.68	11.11	3.33	1.66	4.0
V25	4.34	-	-	-	-	-	-	-
V26	2.08	-	-	-	-	-	-	-

Table 4.3: Comprehensive table of all capillary vessel diameters and dilation, depth and time constants for relevant vessels, where D is the diameter, D_{ch} is the diameter change, d is the depth and CV is the coefficient of variance.

Diameter significance

A statistical analysis (i.e. a two sample t-test) showed that there is a statistically significant difference ($p = 0.034$) between the peak dilation of the large and small capillary vessels.

Imaging depth significance

It was found that the response of vessels also differs for various imaging depths. To compare 4 groups of imaging depths ($0 - 50\mu m, 50 - 150\mu m, 150 - 250\mu m$ and

Depth	$0-50\mu m$	$50-150\mu m$	$150-250\mu m$	$250-350\mu m$
μ_{T_α}	20.0	20.0	10.0	20.0
μ_{T_β}	5.0	4.0	4.0	4.0
μ_{T_γ}	0.90	1.11	1.11	1.11
σ_{T_α}	0	4.35	2.15	0
σ_{T_β}	0	0.86	2.11	0.47
σ_{T_γ}	0	0.25	0.16	0
err_{T_α}	0	1.77	1.24	0
err_{T_β}	0	0.22	1.21	0.33
err_{T_γ}	0	0.06	0.09	0

Table 4.4: Mean values μ, standard deviations σ and error-bars err for each time constant per imaging depth category.

$250-350\mu m$), the ANOVA test was applied. A statistically significant difference was proven ($p < 0.001$). A post-hoc analysis also showed that all groups are statistically different from each other.

Time constants variation

The t-test was performed in order to investigate the statistical significance of the difference of the time constant parameters in the small and large capillary vessels. The comparison of the T_α time parameters revealed no statistical significance ($p = 0.53$), the decay rate T_β yielded a positive statistical significance ($p = 0.025$), whereas T_γ resulted in no statistical significance ($p = 0.35$) (see Table 4.5).
This suggests that the smaller vessels have an overall slower response time, compared to the larger ones. It is worth noting that given the low number of examined vessels, it would be insightful to repeat the experiment with a higher number of vessels before concluding that larger capillaries have a faster response to visual stimuli. A further discussion on the depth-dependent time constant variation is presented in Chapter 7. For ease, a comprehensive list of the data on vessel diameters, dilations and imaging depths in shown in Table 4.3.

Variable	p-value	R^2	R^2 -adjusted	RMSE
T_α	0.062	0.30	0.24	3.85
T_β	0.44	0.06	-0.034	1.16
T_γ	0.40	0.07	-0.02	0.27
K	0.24	0.14	0.05	0.98.

Table 4.5: Individual time constant data analysis reporting the p-value, R-squared, R-squared adjusted and root mean square error (RMSE).

4.6 Calcium concentration

The calcium signal was processed for 12 responsive vessels (out of a total of 26 vessels), irrespective of diameter, following the steps outlined in Section 4.2.1. Figure 4.22 shows the total and the average Ca^{2+} concentration change in the tissue surrounding small and large capillary vessels, as a result of visual stimulation. A statistical difference ($p < 0.001$) was found when comparing the fitted function of the 4 small vessels and the 8 large vessels selected for the model (Figure 4.23). Table 4.6 illustrates all the characteristic values of the fitted function of the Ca^{2+} as a result of the visual stimulus.

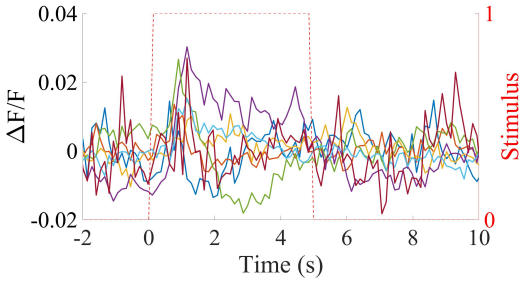

(a) Ca^{2+} trace for all small vessels.

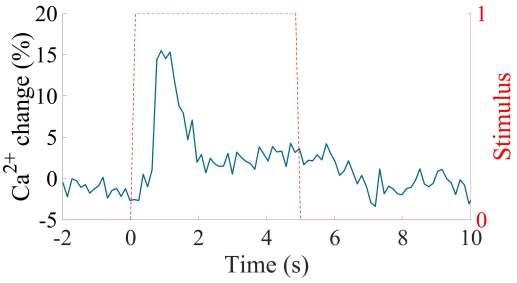

(b) Average Ca^{2+} change for small vessels.

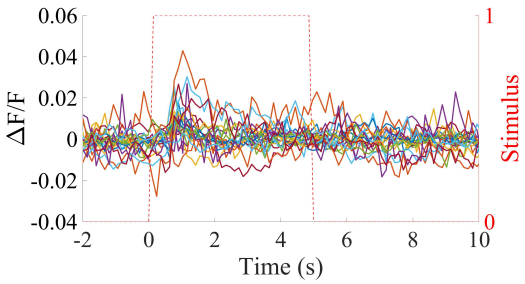

(c) Ca^{2+} trace for all large vessels.

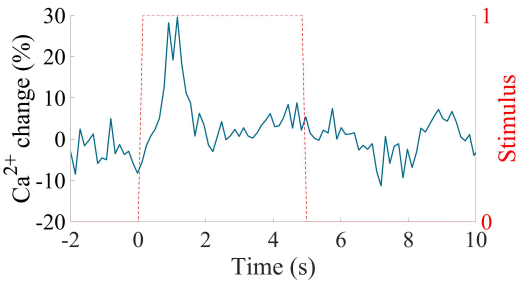

(d) Average Ca^{2+} change for large vessels.

Figure 4.22: Ca^{2+} concentration change during the neural activation.

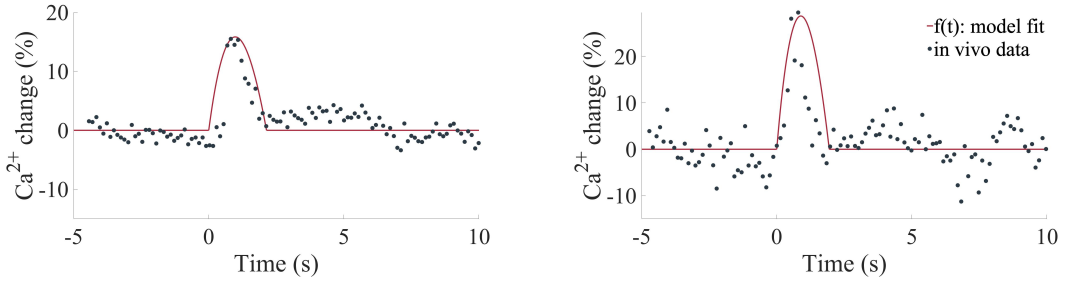

(a) Ca^{2+} fitted function for 4 small vessels. **(b)** Ca^{2+} fitted function for 8 large vessels.

Figure 4.23: In response to the visual stimulus, the peak Ca^{2+} increase is (a) 15.84% for vessels with $2-6\mu m$ diameter; and (b) 28.77% for vessels with $6-10\mu m$

Diameter	$2-6\mu m$	$6-10\mu m$
Vessel number	4	8
Ca^{2+} peak (%)	15.84	28.77
T_α (s)	8.8	8.1
T_β (s)	0.021	0.021
T_γ (s)	0.5	0.45
K (s)	0.07	0.035

Table 4.6: Time constant values for the Ca^{2+} fitting function.

It was experimentally determined that the increase in Ca^{2+} concentration in the tissue surrounding large capillaries is nearly double the Ca^{2+} increase measured in the area surrounding small vessels (i.e. 28.77% compared to 15.84%). This can be attributed to the fact that larger capillaries are the first generation of vessels that follows the arterioles, and the pericytes located there are therefore more eligible for capillary dilation, as suggested by numerous authors [94], [45].

The higher Ca^{2+} concentration in the tissue surrounding large capillaries could also explain why large capillaries have a greater ability to dilate and a faster response compared to small capillaries. Further implications of the difference in Ca^{2+} increase across the capillary bed are discussed at length in Chapter 7.

4.7 Local metabolic and haemodynamic changes

Neuronal activity is manifested as an increase in local Ca^{2+} levels, causing the pericytes to dilate vessels, subsequently causing an increase in CBF and CBV. The

neural activity in the tissue region surrounding the capillary requires energy (i.e. nutrients), resulting in an increase in localised metabolic activity.
To quantify the relationship between diameter increase and metabolic demand, the local tissue $CMRO_2$ was extrapolated from the experimentally determined changes in CBF. However, as diameter increase and CBF change can not be determined simultaneously (see Section 4.1), a separate set of 46 measurements was used for investigating local changes in blood flow and metabolism in the tissue. Following the experimental analysis, measurements were selected for the study following the same criteria outlined in Section 4.2.2.

4.7.1 Blood flow and volume

Following the experimental procedure described in Section 4.1, mice were stimulated visually and their vascular response was observed. The stimuli were $5s$ in duration, over a time frame of $500s$ in total. Of the 46 measurements that were conducted, 23 were included in the analysis, following the exclusion criterion outlined in Section 4.2.2.
A laser doppler flowmetry spectroscopy probe enabled the monitoring of the blood flow change, deoxygenated haemoglobin and the total haemoglobin (which is assumed to be the equivalent of CBV). Figure 4.24 shows the change in CBF across all 23 selected measurements. The peak of 5.53% increase from baseline is reached in about $3s$ after the start of the stimulation. The average value of CBF increase derived here, is in agreement with the results presented by Shaw et al. (2021) in Nature Communications [92]. Similarly, Figure 4.25 shows the average change in total haemoglobin across all 23 measurements is 3.25%, which is also in agreement with the average value derived by Shaw et al. (2021) [92].

As the data was derived from 5 mice, each animal contributing a different number of viable measurements, the average increase in CBF and CBV of each mouse was determined. It is important to note that each measurement was conducted under the same experimental conditions and thus, no variability between sessions was detected (as shown in Supplementary Figure 10 by Shaw et al. (2021) [92]).

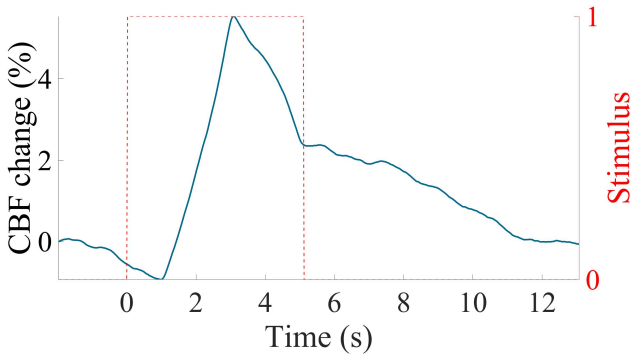

Figure 4.24: In response to a visual stimulus at $t = 0s$, CBF increases by an average of 5.53% across 23 measurements.

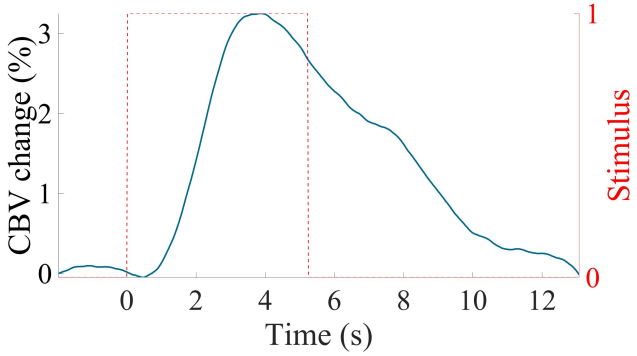

Figure 4.25: In response to a visual stimulus at $t = 0s$, CBV increases by an average of 3.25% across 23 measurements.

The experimental setup does not provide spacial information, and it is thus only possible to obtain a net measure of the CBF, Hbt and $CMRO_2$ changes in the imaging window. Thus, no conclusions can be drawn from this data on the reason for variability of the number of viable measurements per animal and the magnitude of the average response. However, a hypothesis could be that these differences in response can be attributed to factors such as: a more perfusion-favourable capillary network geometry and larger vessel diameter. Both these factors have shown to play a role in capillary response, in the data presented in Section 4.4 in Chapter 4 and the literature presented in Chapter 2. A further discussion and implications on these experimental limitations are presented in Chapter 7.

CBF

Figure 4.26 shows the response of Mouse 1, presenting the average peak increase

in CBF is 5.53% over the 4 viable measurements. Figure 4.27 illustrates that in Mouse 2, the visual stimulus causes a 5.15% increase in CBF over 9 viable measurements. Only a single measurement was viable for Mouse 3, presenting a 1.41% increase in CBF, as shown in Figure 4.33. Mouse 4, whose response is presented in Figure 4.34, presented 3 viable measurements, with an average CBF increase of 9.04%. Ultimately, 4 viable measurements in Mouse 5, yielded an average CBF increase of 5.39% as a result of visual stimulation, as shown in Figure 4.35.

CBV

Figure 4.31 illustrates the behaviour of Mouse 1, as a response to visual stimulation, showing that the average peak increase in CBV (which is here assumed to be the equivalent of Hbt) is 4.02% over the 4 viable measurements. Similarly, Figure 4.32 illustrates that in Mouse 2, the visual stimulus causes a 3.05% increase in CBV over 9 viable measurements. On the other hand, only a single measurement was viable for Mouse 3, presenting a 0.54% increase in CBV, as shown in Figure 4.33. Mouse 4, whose response is presented in Figure 4.34, presented 3 viable measurements, with an average CBV increase of 6.71%. Finally, the 4 viable measurements in Mouse 5, yielded an average CBV increase of 3.35% as a result of visual stimulation, as shown in Figure 4.35. It is important to note that the Hbt trace was recorded and is here assumed to be the equivalent of CBV, as highlighted in each figure caption. The differences in CBV change for each of the 5 mice are quantified here and discussed in Chapter 7.

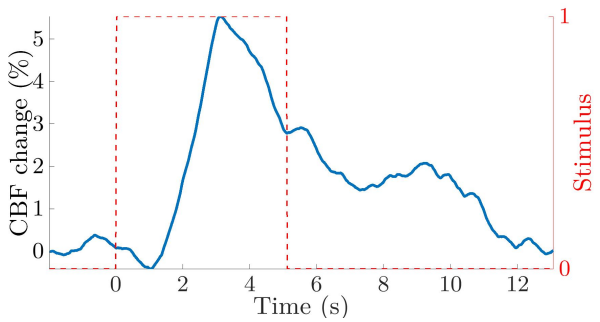

Figure 4.26: Mouse 1; in response to a visual stimulus at $t = 0s$, the average peak CBF (i.e. the equivalent of the Hbt measurement) increase over 4 measurements is 5.53%.

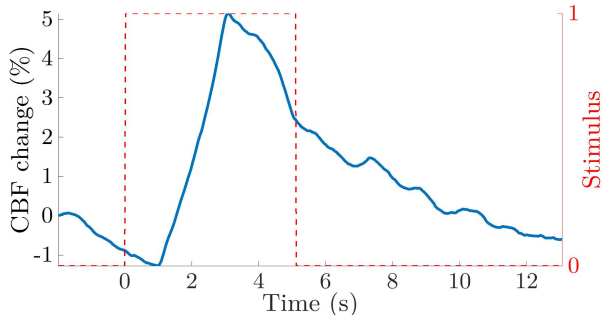

Figure 4.27: Mouse 2; in response to a visual stimulus at $t = 0s$, the average peak CBF (i.e. the equivalent of the Hbt measurement) increase over 9 measurements is 5.15%.

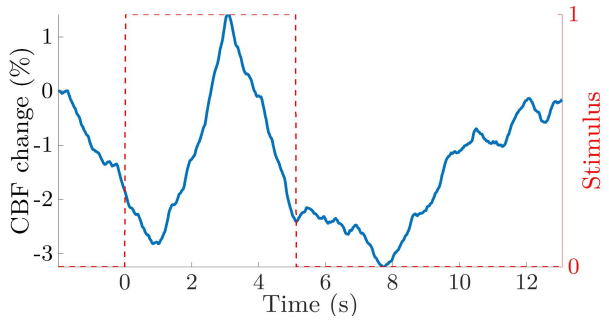

Figure 4.28: Mouse 3; in response to a visual stimulus at $t = 0s$, the average peak CBF (i.e. the equivalent of the Hbt measurement) increase over 1 measurement is 1.41%.

Grubb's exponent

In an attempt to relate the experimentally determined changes in CBF to changes in CBV, Grubb's exponent was fitted to the data, following the equation defined by Grubb et al. (1974) [95]:

$$CBV = 0.8 \cdot CBF^{\alpha} \tag{4.5}$$

where α is known as the Grubb exponent and its original value is 0.38. Given that this value was derived from rhesus monkeys, a number of studies have attempted to find a better fit for relating the two parameters in humans. At present, there is still a lack of consensus and the proposed values range from 0.29 to 0.73, as suggested by Ito et al. (2003) [96] and Rostup et al. (2005) [97] respectively. Figure 4.36 shows that across the range of values suggested by the literature, $\alpha = 0.73$ appears to be Grubb's exponent value that fits the experimental data most closely.

Figure 4.36 shows that with the original α exponent of 0.38 the relationship

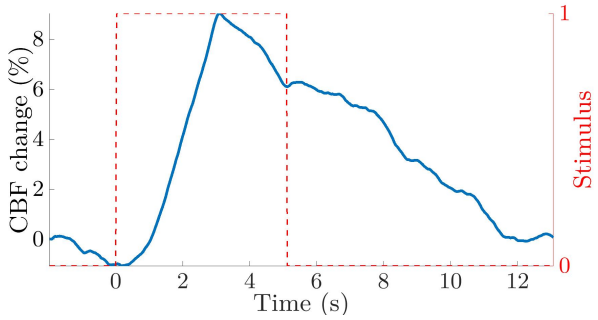

Figure 4.29: Mouse 4; in response to a visual stimulus at $t = 0s$, the average peak CBF (i.e. the equivalent of the Hbt measurement) increase over 3 measurements is 9.04%.

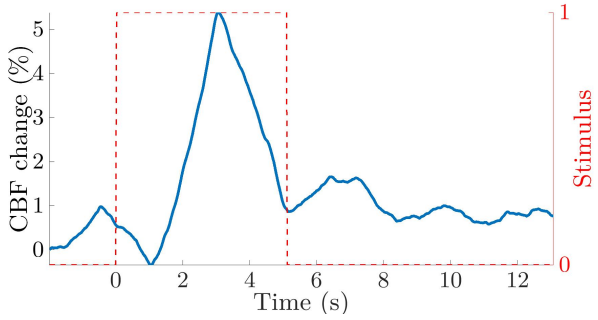

Figure 4.30: Mouse 5; in response to a visual stimulus at $t = 0s$, the average peak CBF (i.e. the equivalent of the Hbt measurement) increase over 4 measurements is 5.39%.

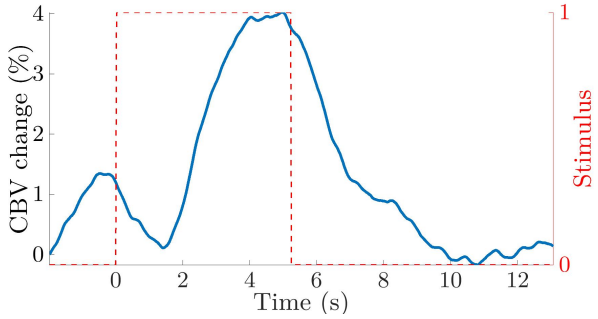

Figure 4.31: Mouse 1; in response to a visual stimulus at $t = 0s$, the average peak CBV (i.e. the equivalent of the Hbt measurement) increase over 4 measurements is 4.02%.

between CBV and CBF is strongly non-linear, whereas for higher values (such as 0.73 [96]) approaching the value 1, the relationship appears to become more linear, given the Equation 4.5.

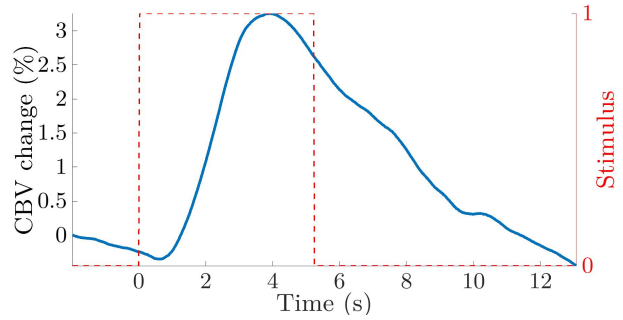

Figure 4.32: Mouse 2; in response to a visual stimulus at $t = 0s$, the average peak CBV (i.e. the equivalent of the Hbt measurement) increase over 9 measurements is 3.05%.

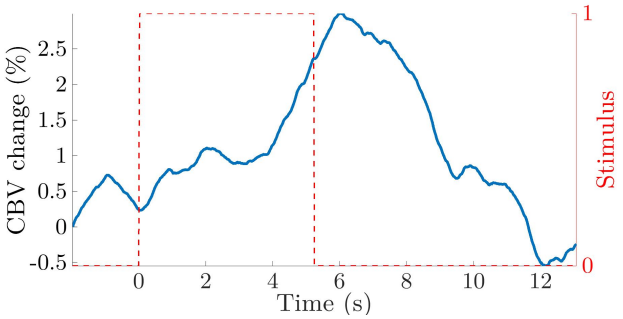

Figure 4.33: Mouse 3; in response to a visual stimulus at $t = 0s$, the average peak CBV (i.e. the equivalent of the Hbt measurement) increase over 1 measurement is 0.54%.

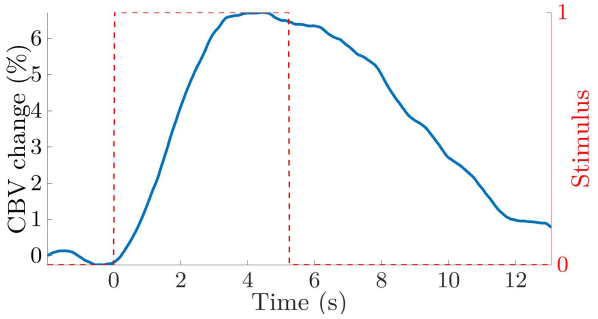

Figure 4.34: Mouse 4; in response to a visual stimulus at $t = 0s$, the average peak CBV (i.e. the equivalent of the Hbt measurement) increase over 3 measurements is 6.71%.

4.7.2 Oxygen metabolism

With the aim of relating pericyte cell activation to an increase in nutrient metabolism within the tissue, the visual stimuli were related to the $CMRO_2$. As no direct measurement of $CMRO_2$ is possible, its value was determined through the following relationship, as done by Royl et al. (2008) [98] and Shaw et al.(2021) [92]:

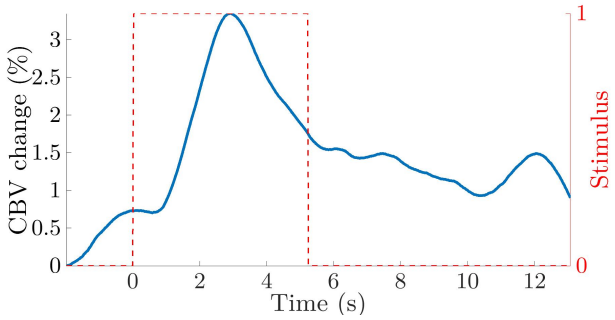

Figure 4.35: Mouse 5; in response to a visual stimulus at $t = 0s$, the average peak CBV (i.e. the equivalent of the Hbt measurement) increase over 4 measurements is 3.35%.

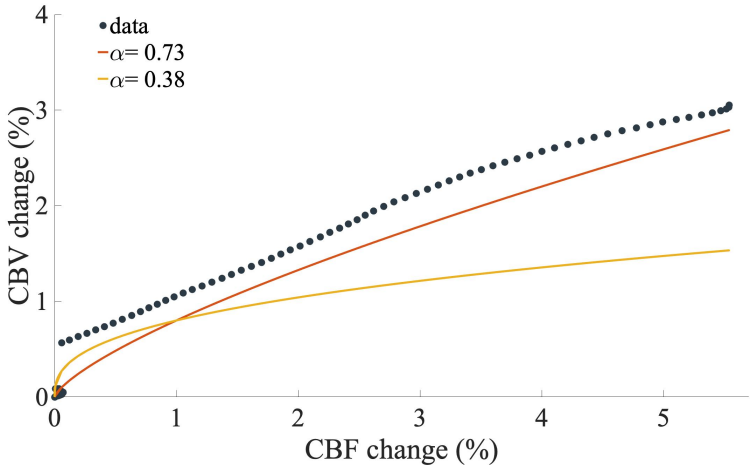

Figure 4.36: The relationship between CBF and CBV is best represented with a Grubb exponent of 0.73.

$$CMRO_2 = CBF \cdot \frac{Hbr}{Hb} \tag{4.6}$$

where Hbr and Hb are deoxygenated haemoglobin and total haemoglobin respectively. Here, the relative change of $CMRO_2$ is derived from CBF and the relative changes of Hbr and Hb. It is however worth noting that the measurements of $CMRO_2$ are not fully quantitative, as they rely on the use of arbitrary units of deoxy- and total-haemoglobin and CBF, so do not inform about the actual number of oxygen molecules consumed. Further implications of this method are described in the Supplementary Data section of Shaw et al. (2021) [92].

The $CMRO_2$ change was computed for all 23 measurements and an average trace was identified. Figure 4.37 illustrates the change in $CMRO_2$ as a result of the visual

stimulation. Ultimately, oxygen metabolism was found to increase by 6.09% from its baseline value within $2s$ of the stimulation. As for CBV and CBF, the measurements were grouped for each mouse and the average $CMRO_2$ increase is shown.

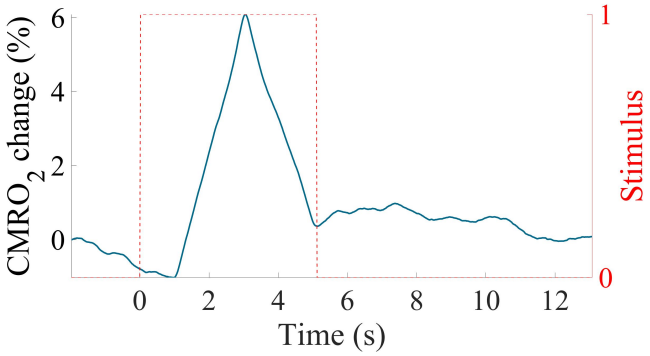

Figure 4.37: In response to a visual stimulus at $t = 0s$, $CMRO_2$ increases by an average of 6.09% across 23 measurements.

Figure 4.38 illustrates the behaviour of Mouse 1, as a response to visual stimulation, showing that the average peak increase in $CMRO_2$ is 4.39% over the 4 viable measurements. Similarly, Figure 4.39 illustrates that in Mouse 2, the visual stimulus causes a 6.57% increase in $CMRO_2$ over 9 measurements. For Mouse 3, only a single measurement was viable, presenting a 5.58% increase in $CMRO_2$, as shown in Figure 4.40. Mouse 4, whose response is presented in Figure 4.41, presented 3 viable measurements, with an average $CMRO_2$ increase of 7.50%. Ultimately, the 4 viable measurements in Mouse 5, yielded an average $CMRO_2$ increase of 5.39% as a result of visual stimulation, as shown in Figure 4.42.

Figure 4.43 illustrates the localised changes in CBF, CBV and $CMRO_2$ in the tissue. The OEF change was calculated with a two-step approach. The relationship between OEF and $CMRO_2$ is as follows:

$$OEF = \frac{CMRO_2}{CBF} \tag{4.7}$$

hence, for small changes, the change in OEF can be derived from:

$$OEF_{ch}\% = CMRO_{2,ch}\% - CBF_{ch}\% \tag{4.8}$$

Furthermore, given the importance of the time response, the mean transit time (MTT) was calculated. Indicating the length of time a certain blood volume spends in the capillary circulation, the MTT was derived from:

$$MTT = \frac{CBV}{CBF} \tag{4.9}$$

while the change in MTT can be expressed as the difference of cerebral blood volume and blood flow:

$$MTT_{ch}\% = CBV\% - CBF\% \tag{4.10}$$

Figure 4.44 highlights how in response to a visual stimulus, which causes a local Ca^{2+} concentration increase in the tissue, OEF initially increases by about 0.70% and subsequently drops to a peak minimum value of -2.02%. The MTT shows a delayed response with respect to the OEF, increasing by about 1.07% and decreasing to a minimum point at -2.50% change, before returning back to baseline conditions about 5 s time after the end of the visual stimulation.

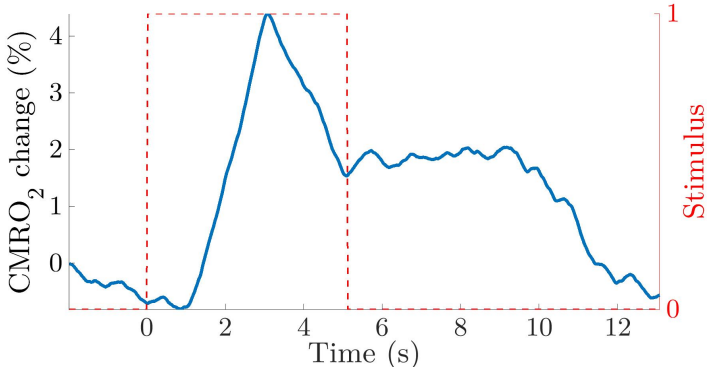

Figure 4.38: Mouse 1; in response to a visual stimulus at $t = 0s$, the average peak $CMRO_2$ increase over 4 measurements is 4.39%.

The implications of the results derived from the experimental study of visual stimulus-induced metabolic changes are discussed in Chapter 7, where the limitations of the study are analysed and potential future steps for improvement are outlined.

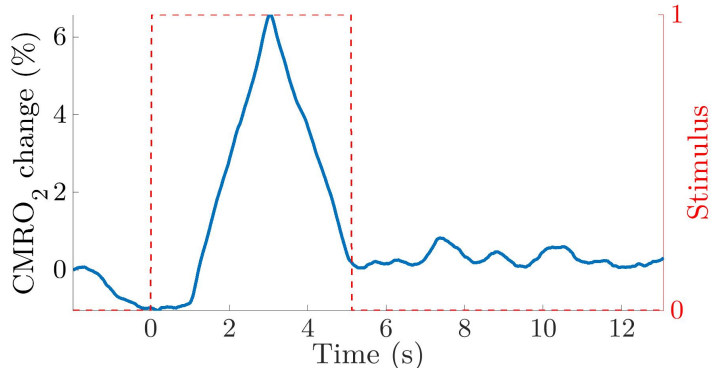

Figure 4.39: Mouse 2; in response to a visual stimulus at $t = 0s$, the average peak $CMRO_2$ increase over 9 measurements is 6.57%.

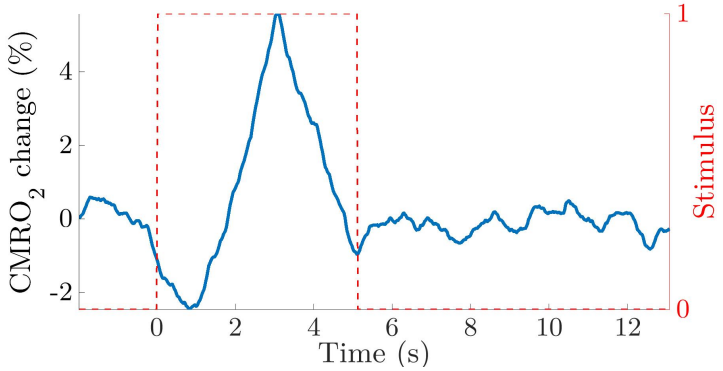

Figure 4.40: Mouse 3; in response to a visual stimulus at $t = 0s$, the average peak $CMRO_2$ increase over 1 measurement is 5.58%.

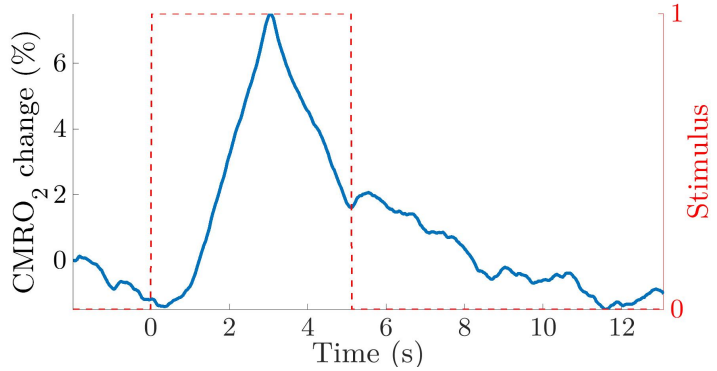

Figure 4.41: Mouse 4; in response to a visual stimulus at $t = 0s$, the average peak $CMRO_2$ increase over 3 measurements is 7.50%.

4.8 Summary

Raw in vivo data on pericyte-induced capillary dilation were obtained from mice who were visually stimulated. The change in vessel diameter, the increase in Ca^{2+}

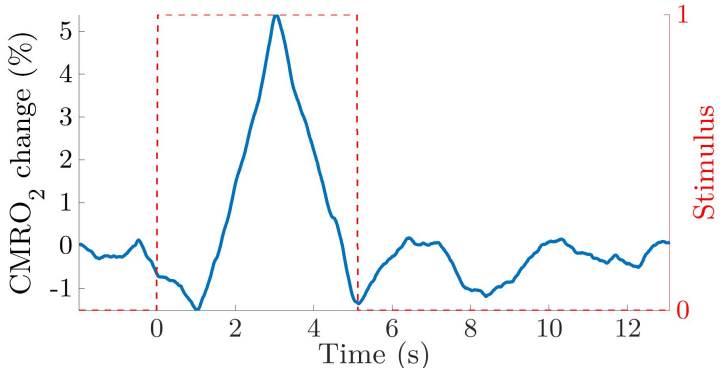

Figure 4.42: Mouse 5; in response to a visual stimulus at $t = 0s$, the average peak $CMRO_2$ increase over 4 measurements is 5.39%.

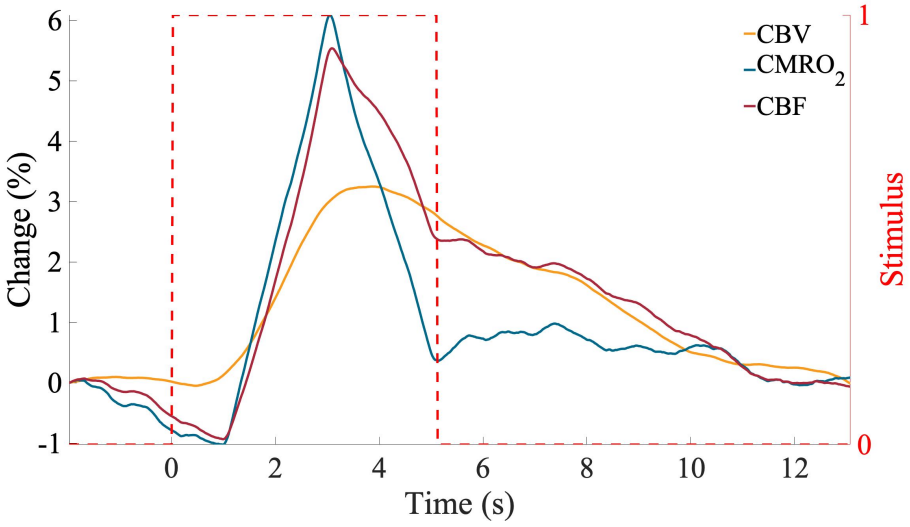

Figure 4.43: The local increase in calcium results in a CBV increase by 3.25% (yellow); CMRO2 increase by 6.09% (blue) and a CBF increase by 5.53% (red).

in the tissue surrounding the vessel, and the changes in CBF, CBV and $CMRO_2$ were quantified. Two distinct sets of experimental data were used as changes in capillary diameter and CBF can not be assessed simultaneously.

To quantify the increase in vessel diameter following the visual stimulation, 26 vessels were studied in 6 mice. Not all 26 vessels were considered for the analysis. The two discriminating factors were vessel diameter ($6 - 10\mu m$ acceptable range) and a clear response to the stimulus (see Section 4.2.2).

The number of vessels with a clear post-stimulus diameter change is 12, 8 of which had a large diameter ($6 - 10\mu m$) and 4 of which had a small diameter ($2 - 6\mu m$).

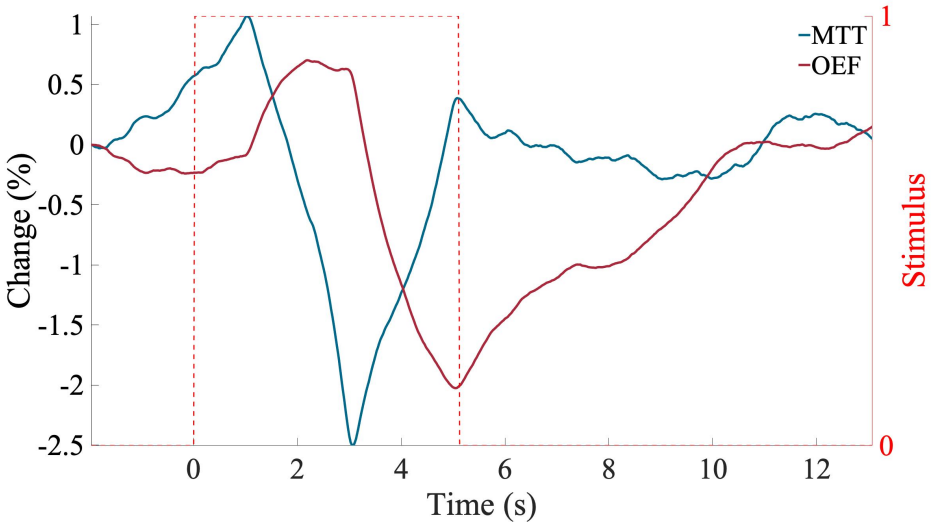

Figure 4.44: In response to a stimulus at $t = 0s$, OEF increases by 0.70% and subsequently drops by a maximum of -2.02% while MTT increases by a maximum of 1.07% and drops by -2.50%.

The peak dilation for capillaries with a large diameter was found to be about 2.62% achieved in about 1 s. In comparison, smaller capillaries responded with a peak dilation of 2.52% in about 2 s. The comparison of the response of both vessel groups proved to be statistically significant. With the aim of extrapolating a function that describes the active capillary dilation which was included in the cerebrovascular model presented in Chapter 5, a Laplace transform was used.

The studied vessels were imaged at different depths and a depth-dependent diameter change analysis was therefore conducted across 4 different imaging depths. It was found that the average peak dilation for the $0 - 50\mu m$ depth range was 2.11%, for the $50 - 150\mu m$ range it was 2.60%, for the $150 - 250\mu m$ it was 2.37% and for the $250 - 350\mu m$ range it was 3.2%. To study the change in CBF, a new set of measurements from 5 mice was used. As the experimental setup (also used in Shaw et al.(2021) [92]) cannot provide spacial information, only a net measure of CBF, CBV and derived $CMRO_2$ could be extrapolated from the imaging window. It was found that pericyte-induced vessel dilation results in a CBF increase of about 5.53% and a 3.25% increase in CBV (assumed to be the equivalent of the Hbt measurement). As a function of the changes in CBF and CBV, $CMRO_2$ in

the tissue surrounding the dilating vessels was evaluated. Ultimately, the visual stimulation of the mice was found to result in a $CMRO_2$ increase of 6.09%.

Our main business is not to see what lies dimly at a distance,
but to do what lies clearly at hand.

— Thomas Carlyle (1795 - 1881)

5 Cerebrovascular model

Contents

5.1 Electrical circuit 89
5.1.1 Lumped parameter model 90
5.2 Network model 93
5.2.1 Flow 95
5.2.2 Oxygen supply 96
5.3 Model feedback 99
5.3.1 Flow 99
5.3.2 Oxygen 100
5.3.3 Oxygen and pericytes 101
5.3.4 Neural activation 101
5.4 BOLD signal 102
5.5 Summary 103

This chapter illustrates the modelling methodology applied to study the role of the microvasculature bed and pericytes in regulating CBF, ultimately reported in Milanovic et al. (2021) [91] Aiming for an extended model of cerebral autoregulation that provides local as well as global insights on the regulating abilities of metabolism and pericyte cells activity, a new model combining lumped parameter and network modelling techniques was designed here. An advantage of such coupled models is their ability to relate local changes in tissue metabolism to blood flow. This was achieved through the implementation of a microvasculature network that comprises

vessels with diameters ranging from few μm to hundreds of μm.
Local nutrient metabolism in the tissue was set to influence the compliance of small vessels, which together with the active role of pericyte activity and neural activation regulate CBF on a global scale. Four distinct feedback mechanisms are proposed here for the regulation of vessel compliance, thus enabling the quantification of the individual and collective effect of the 4 regulatory variables.
Under steady state conditions, the models aimed to replicate the CA curve, while the dynamic simulations highlighted the the ability of each model to rapidly modulate CBF increases resulting from ABP increase. While acknowledging the difficulty of computationally representing the complex physiology that characterizes blood flow regulation in the brain, by selecting the dominant regulatory variables for the vessel compliance mechanism, it was possible to emulate human dynamic CBF regulation with a good level of agreement with available experimental data.
The model presented here comprises 34 equations, 21 variables and 11 parameters (defined in Table 5.1) and can be computed in MATLAB. Using the ode45 solver for the differential equations provided sufficient accuracy for the solutions with a short run time of approximately 16.3 s. It is possible to use the aforementioned characteristics of the model as a comparison with existing models (see Table 2.1 in Chapter 2), yet each model aims to investigate a particular aspect of the CBF regulation mechanism and the confrontation is thus not consistent. These characteristics, combined with the chosen modelling approach (i.e. electric equivalent for large vessels and network model for small vessels), should thus serve as self-standing indicators of the complexity of the model itself.

5.1 Electrical circuit

The proposed model is a multi-scale representation of the total brain vasculature. As shown in Figure 5.1, large vessels are represented by lumped parameters while the microvasculature is studied through a network model. The variable compliance and resistance of the network are denoted with an arrow. Only small arteries and the microvasculature network are assumed to have a variable resistance and they

are therefore the vessels with active regulatory abilities. On the other hand, large arteries, large veins and small veins were assumed to have a constant resistance.

The series of small vessels is repeated in parallel $N = 3.38 \times 10^6$ times (see Equation 5.1), generating a complete brain model. In Figure 5.1, the elements of the circuit are: P_a arterial pressure; R_{la} resistance of large arteries; R_{sa} resistance of small arteries; R_N resistance of microvasculature bed; R_{sv} resistance of small veins; R_{lv} resistance of large veins; P_v venous pressure; q_{in} and q_{out} are the in- and out-flow of the microvasculature; P_{sa} and P_{sv} are nodal pressures. A complete description of the baseline values of the parameters and constants is provided in Table 5.1

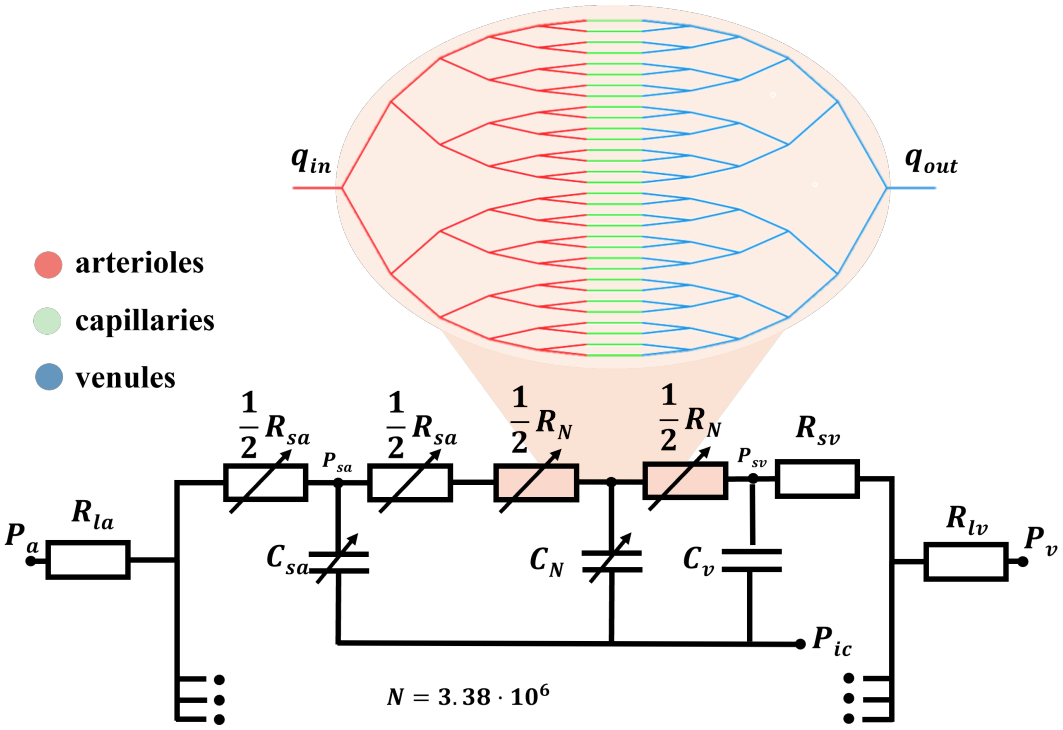

Figure 5.1: Schematic representation of the haemodynamic model. A network model representing the behaviour of 6 arteriole generations (red), 1 capillary bed (green) and 6 venule generations (blue) is incorporated in a lumped parameter model whose elements reflect the active or passive role of arteries and veins.

5.1.1 Lumped parameter model

As commonly found in the literature [49], [54], a system of equivalents between hydrodynamic and electrical circuits is used to describe the behaviour of large brain vessels. Since flow regulation is manifested through changes in radius, which is

directly linked to vessel resistance, the analogue circuit consists of a series of resistors and capacitors representing vessel resistance and compliance respectively. The arterial compartment comprises regulating small arteries (R_{sa}) and non regulating large arteries (R_{la}). Hence, the large vessels are assumed to have a constant resistance and volume whilst those of the small vessels are variable. This is justified by the common assumption that it is primarily small arteries and arterioles that govern active regulation. [99], [41]

The vessels of the microvasculature are assumed to have a variable diameter (i.e. pericyte-regulated capillary diameter) and therefore the total resistance (R_N) is variable. The venous compartment is composed of small veins (R_{sv}) and large veins (R_{lv}), both are constant yet the venous volume changes through its compliance (C_v). ICP is assumed to be constant (10 mmHg) here. For a model with variable ICP, the compliance of the tissue should be considered [49], which is not done here. Moreover, the mechanisms of ICP regulation are yet to be defined, as it is unclear whether ICP is passively modulated by the vasculature or by metabolic signalling. [100]

In order to provide a model of the entire cerebral vasculature, the series of resistors and capacitors was duplicated N times. This scaling factor N was obtained by calculating the ratio between the baseline values of CBF and flow within the microvasculature network:

$$N = \frac{\overline{q}}{\overline{q_N}} = \frac{12.5ml/s}{3.7 \times 10^{-6}ml/s} = 3.38 \times 10^6 \tag{5.1}$$

where $\overline{q_N}$ is calculated as the flow within the network obtained as the ratio between the pressure drop within the vessel ΔP and the resistance of the vessel R:

$$\overline{q_N} = \frac{\Delta P}{R} \tag{5.2}$$

Governing equations

The relationship between oxygen, pericytes and neural activity defined in Figure 3.3 is here defined in a series of governing equations. Blood vessel resistance varies

with the fourth power of its radius, while vessel volume varies with the square of the radius. Therefore, an equation relating volume to radius is given as:

$$\frac{V_{sa}}{\overline{V_{sa}}} = \sqrt{\frac{\overline{R_{sa}}}{R_{sa}}} \tag{5.3}$$

The rate of change of arterial volume can be related to the compliance and transmural pressure:

$$\frac{dV_{sa}}{dt} = \frac{d(C_{sa}(P_{sa} - P_{ic}))}{dt} \tag{5.4}$$

The rate of change of venous volume is given by:

$$\frac{dV_v}{dt} = C_v \frac{d(P_{sv} - P_{ic})}{dt} \tag{5.5}$$

where venous compliance is inversely proportional to transmural pressure:

$$C_v = \frac{1}{k_{ven}(P_{sv} - P_{ic} - P_{v1})} \tag{5.6}$$

and k_{ven} and P_{v1} are the venous elastance coefficient and the venous compliance pressure offset respectively. Venous volume is therefore given by:

$$V_V = \frac{1}{k_{ven}} ln(P_{sv} - P_{ic} - P_{v1}) + V_{vn} \tag{5.7}$$

where V_{vn} is a constant. The conservation of volume at the nodes enables to calculate the pressure in the haemodynamic model:

$$\frac{dP_{sa}}{dt} = \frac{1}{C_{sa}} \left(\frac{P_a - P_{sa}}{R_{la} + 0.5R_{sa}} - q - \frac{dC_{sa}}{dt}(P_{sa} - P_{ic}) \right) \tag{5.8}$$

$$\frac{dP_{sv}}{dt} = \frac{1}{C_v} \left(q - \frac{P_{sv} - P_v}{R_{lv}} \right) \tag{5.9}$$

The total blood volume (CBV) can then be calculated as a sum of all compartmental volumes.

$$CBV = V_A + V_V + V_{net} \tag{5.10}$$

where arterial volume V_A and network volume V_{net} are calculated from:

$$V_A = V_{la} + V_{sa} \tag{5.11}$$

$$V_{net} = \sum_{i=1}^{13} V_{b,i} \cdot N. \tag{5.12}$$

Variable	Magnitude	Definition
N	3.38×10^{6}	number of parallel vessels
k	2.96×10^{-7}	scaling factor (1/N)
$\overline{q}$	12.5×k (ml)	baseline CBF [54]
$\overline{C_{sa}}$	0.125×k (ml/mmHg)	baseline compliance of SA [54]
ΔC_{sa}^{+}	2.87×k	C_{sa} positive change [54]
ΔC_{sa}^{-}	0.164×k	C_{sa} negative change [54]
R_{la}	0.4×N (mmHg s/ml)	resistance of LA [54]
R_{lv}	0.56×N (mmHg s/ml)	resistance of LV [54]
$\overline{R_{sa}}$	5.03×N (mmHg s/ml)	baseline resistance of SA [54]
R_{sv}	1.18×N (mmHg s/ml)	resistance of SV [54]
R_N	2.98×10^{-5}×N (mmHg s/ml)	microvasculature resistance
$\overline{P_v}$	6 (mmHg)	baseline venous pressure [54]
P_{ic}	10 (mmHg)	intracranial pressure [54]
P_{v1}	-2.25 (mmHg)	venous compliance pressure offset [54]
P_{net}	25 (mmHg)	network outlet pressure [57]
$\overline{p_t}$	38.1 (mmHg)	baseline O_2 partial tissue pressure
V_{la}	1×k (ml)	volume LA [54]
$\overline{V_{sa}}$	12×k (ml)	baseline volume SA [54]
V_{vn}	28×k (ml)	venous volume offset [54]
$V_{tot,net}$	8.56×10^{-6} (ml)	total network volume
$V_{a,net}$	2.17×10^{-6} (ml)	network arterial volume
$V_{v,net}$	5.63×10^{-6} (ml)	network venous volume
$V_{c,net}$	7.84×10^{-7} (ml)	network capillary volume
k_{ven}	0.186/k (1/ml)	venous elastance coefficient [54]
c_{hb}	0.2 mlO_2 (1/ml)	O_2 carrying capacity/ unit volume [57]
α_t	2.6×10^{-5} (mlO_2/ml.mmHg)	O_2 solubility in brain tissue [57]
M	$30\times10^{-9}/4.46\times10^{-5}$ (mlO_2/ml)	O_2 metabolism in brain tissue [57]
K	5×10^{-11} (ml/mm.s.mmHg)	O_2 permeability of vascular wall [57]
H	0.42	haematocrit [54]
ρ	1040 (kg/m^3)	blood density [54]
E	1600×10^{3} (Pa)	Young modulus [101]
ν	$3\times7.5\times10^{-6}$ (mmHg.s)	kinematic viscosity [101]

Table 5.1: Baseline values and constant parameters used in the model.

5.2 Network model

The network model proposed by Payne and Lucas (2018) [57] is a bifurcating vessel model consisting of 13 vessel generations (6 arteriolar, 1 capillary and 6 venous) and was used here to replicate the microvasculature bed. The aim of the network

is to represent all the generations of blood vessels responsible for oxygen delivery. Vessel lengths were calculated by matching the data from Zweifach (1974) [102] and their thickness by matching the data from Harper and Bohlen (1984) [103].
In the model all capillaries have a diameter of $8\mu m$. Vessels with a diameter greater than $8\mu m$ are considered to be part of the arteriolar bed while those with a diameter below $8\mu m$ were not considered as RBCs have a diameter of about $8\mu m$, meaning that for smaller capillaries it would have been necessary to take account of the change of blood viscosity caused by the deformation of RBCs. Moreover, flow in the capillaries whose diameter is smaller than those of RBCs is no longer Newtonian, as defined in Chapter 3.
Conservation of flow from one generation to the next gives the flow velocity:

$$D_i^2 v = 2D_{i+1}^2 v_{i+1} \tag{5.13}$$

where D is the vessel diameter, v is flow velocity and i and $i+1$ represent consecutive vessels. It can be noted that the flow in each vessel is halved in every subsequent generation. The haematocrit was kept constant at a value of 0.42 over the entire study. This is based on the study by Gould and Linninger (2015) [104] that shows that in a network of equally bifurcating vessels, the haematocrit can be reduced to a constant. Values of all characteristic vessel parameters can be found in Table 5.2.

Vessel generation	n -	D (μm)	L (μm)	h (μm)	v (mm/s)	μ (mPa·s)
A1	1	23.97	1267.6	4.84	8.2	1.59
A2	2	19.17	930.3	4.25	6.41	1.5
A3	4	15.28	543.6	3.81	5.05	1.42
A4	8	12.08	302.3	3.49	4.03	1.34
A5	16	9.46	161.2	3.27	3.29	1.28
A6	32	7.32	154.7	3.14	2.75	1.23
C	32	8	243.9	0.309	2.3	1.24
V6	32	11.51	473.9	1.15	1.11	1.33
V5	16	14.53	272.3	1.45	1.4	1.4
V4	8	17.79	426.6	1.78	1.86	1.48
V3	4	21.45	632.5	2.15	2.56	1.55
V2	2	25.7	844.2	2.57	3.57	1.62
V1	1	30.77	936.3	3.08	4.97	1.7

Table 5.2: Vessel parameters for the bifurcating network of 13 generations (6 arterial, 1 capillary and 6 venous): number of vessels n per generation, vessel diameter D, vessel length L, wall thickness h, velocity v and dynamic viscosity μ.

5.2.1 Flow

Moving away from Poiseuille's simplified calculation of flow, a new formulation proposed by Payne and El-Bouri (2018) [105] was implemented. This formulation of flow calculation was chosen for the current model because it was designed particularly for dynamic changes in flow in vessels whose diameter is smaller than 1mm. Inlet and outlet flow were therefore calculated for each generation through the following equations:

$$\begin{pmatrix} q_{in} \\ q_{out} \end{pmatrix} = \alpha_0 \begin{pmatrix} p_{in} \\ p_{out} \end{pmatrix} - \frac{r^2}{\nu} \alpha_2 \frac{d}{dt} \begin{pmatrix} p_{in} \\ p_{out} \end{pmatrix} \tag{5.14}$$

$$\alpha_0 = \frac{1}{R} \begin{pmatrix} 1 & -1 \\ 1 & -1 \end{pmatrix} \tag{5.15}$$

$$\alpha_2 = \frac{1}{6R} \begin{pmatrix} 1 & -1 \\ 1 & -1 \end{pmatrix} + \frac{4}{3} \frac{\beta}{R} \begin{pmatrix} -2 & -1 \\ 1 & 2 \end{pmatrix} \tag{5.16}$$

$$\beta = \frac{\nu RC}{8r^2} \tag{5.17}$$

where ν is kinematic viscosity, resistance is given by Equation 3.2 and compliance is given by:

$$C = \frac{3\pi r^3 L}{2Eh} \tag{5.18}$$

This yields the formulation of blood volume under dynamic conditions:

$$V_b = \frac{C}{2}(p_{in} + p_{out}) \tag{5.19}$$

The difference of inlet and outlet flow can then be expressed through the conservation of blood volume as:

$$\frac{dV_b}{dt} = q_{in} - q_{out}. \tag{5.20}$$

The total resistance of the network R_N is represented as the sum of all the resistances of each generation. Therefore R_N was calculated through Equation 3.2.

$$R_N = \sum_{i=1}^{13} R_i = 2.98 \times 10^{-5} mmHg \cdot s/ml \tag{5.21}$$

5.2.2 Oxygen supply

The rate of movement of O_2 molecules across the vessel wall is termed oxygen flux j and usually presented in the units mol/m^2/s. Flux is directly related to the diffusion coefficient D_t, wall permeability K and concentration gradient ΔC across the wall which is the driving force of diffusion. The diffusion coefficient depends on the substance, mass and temperature whilst the overall permeability depends on wall thickness h. Flux can therefore be defined by Fick's law of diffusion as [106]:

$$j = -K\frac{\Delta C}{h} \tag{5.22}$$

The notion of mass conservation can be applied to O_2 transport in blood vessels so that the difference between the quantity entering a vessel ($q \times c_{in}$) and the one exiting the vessel ($q \times c_{out}$) equals the flux:

$$j = \frac{q}{\pi D L}(c_{in} - c_{out}) \tag{5.23}$$

where D and L are vessel diameter and length respectively and c_{in}, c_{out} are inlet and outlet concentration. The metabolic demand ensures that the necessary amount of oxygen is provided to the tissue. Within the vessels, O_2 is transported via convection and diffusion whereas in tissue it occurs solely via diffusion. It is assumed that each vessel supplies a separate tissue voxel, with diffusion between these volumes being neglected. The governing equations for oxygen delivery follow:

$$V_b\frac{1}{2}\left(\frac{dS_{in}}{dt} + \frac{dS_{out}}{dt}\right) + \frac{1}{2}(q_{in} + q_{out})(S_{out} - S_{in}) = -\frac{2\pi K r L}{h c_{Hb} H}\left(\frac{1}{2}(p_{in} + p_{out}) - p_t\right) \tag{5.24}$$

$$\frac{dp_t}{dt} = \frac{1}{\alpha_t V_t}\left(\frac{2\pi K r L}{h}\left(\frac{1}{2}(p_{in} + p_{out}) - p_t\right) - M_{O_2} V_t\right) \tag{5.25}$$

where V_b is the blood volume, V_t is the supplied tissue volume, S_{in} and S_{out} are inlet and outlet saturation, V_b is blood volume, q_{in} and q_{out} are inlet and outlet flow, r is the vessel radius, L is the vessel length, K is oxygen permeability of vascular wall, p_{in} and p_{out} are inlet and outlet vessel pressure, p_t is tissue partial pressure, α_t is the solubility of oxygen in brain tissue, M_{O_2} is oxygen metabolism of brain tissue, H is haematocrit and h is vessel wall thickness. The blood volume of vessels is defined as:

$$V_b = \pi r^2 L. \tag{5.26}$$

Balancing the oxygen transfer from each vessel with the metabolic demand of the supplied tissue volume and assuming that each vessel supplies an independent tissue voxel, the supplied volume V_t is given as:

$$V_t = \frac{c_{Hb} H q \overline{\Delta S}}{M_{O_2}} \tag{5.27}$$

where c_{Hb} is the oxygen carrying capacity per unit volume of red blood cells. The equations were solved for each of the 13 vessel generations. It was found that the baseline pressure drop across the network is 34.19 mmHg and that oxygen saturation drops from 94% to 57%. Figure 5.2a highlights the gradually decreasing nodal pressures along the vessel generations, being highest for arterioles and lowest in venules. The most significant drop in oxygen saturation was found in the last 3 generations of arterioles and capillaries (see Figure 5.2b), suggesting that they are the vessels that govern tissue oxygen perfusion.

Using baseline values of nodal blood pressure and oxygen saturation the volumes of the tissue voxels supplied by each generation were quantified, highlighting that the last generation of arterioles and the capillary bed supply the largest volumes, as shown in Figure 5.2c. Furthermore, oxygen partial tissue pressure was calculated for every voxel, showing that the lowest values occur in the last generations of arterioles and capillary bed (see Figure 5.2d).

With the aim of validating the data of partial pressure in the blood, the results were fitted against the Severinghaus equation (1979) [107] which relates pressure and oxygen saturation in the vessels (see Figure 5.3a).

$$S_{O_2} = \frac{1}{(1 + (\frac{23400}{p_b^3 + 150 p_b}))} \tag{5.28}$$

The total volume of tissue supplied equals $1.74 \times 10^{-4} mL$ and was obtained by the total sum of the multiplication of the volume of the supplied voxel by the number of vessels within the generation. The volume averaged partial tissue pressure at baseline conditions was found to be 13.54 mmHg and was obtained as follows:

$$\langle \overline{p_t} \rangle = \sum_{i=1}^{13} \frac{p_{t,i} V_{t,i}}{\sum_{i=1}^{13} V_{t,i}} \tag{5.29}$$

where i represents the generation number. This value is in good agreement with the one suggested by Vovenko (1999) [56], which amounts to approximately 15 mmHg. To observe the behaviour of the microvasculature network during changes in blood pressure, the change of $\langle \overline{p_t} \rangle$ over a wide range of blood pressure p_{in} at the inlet of the first generation was analysed (see Figure 5.3b).

The pressure entering the first generation of arterioles (A1) with a baseline value of 57.8 mmHg, was varied over a range of 40-100 mmHg. This was done to validate the assumption that changes in arterial pressure in the lumped parameter model will consequently alter the pressure within the generations of the microvascular bed and therefore also the volume averaged partial tissue pressure of oxygen. The characteristic concave nature of the plot should be noted, with the baseline value of the volume averaged partial tissue pressure lying at its vertex. Table 5.3 presents an overview of all the characteristic generation values presented in Figure 5.2.

Vessel generation	Δp_b (mmHg)	S_{O_2} (%)	V_t ($\cdot 10^{-5}$ml)	p_t (mmHg)
A1	6.93	94	0.4	34.1
A2	5.87	93	0.5	32.52
A3	4.02	92	0.6	30.55
A4	2.7	89	2.3	22.54
A5	1.82	84	2.4	16.03
A6	2.35	76.5	4.7	11.07
C	2.62	66.5	4.7	15.57
V6	1.27	61	0.2	15.11
V5	0.61	59.75	0.7	14.52

V4	0.89	58.75	0.1	14.51
V3	1.31	58.25	0.1	14.52
V2	1.78	57.75	0.1	14.44
V1	2.01	57.25	0.1	13.48

Table 5.3: Vessel parameters for the bifurcating network of 13 generations (6 arterial, 1 capillary and 6 venous): pressure drop Δp_b, oxygen saturation S_{O_2}, supplied tissue volume V_t and oxygen partial tissue pressure p_t.

5.3 Model feedback

The compliance of small arteries is assumed to be the governing factor of cerebral blood flow here. Hence, its feedback will determine the model's response. With the aim of identifying the most physiologically representative modelling technique, four distinct feedback mechanisms were investigated here: a flow feedback (F_0), an oxygen-feedback (F_1), an oxygen and pericytes feedback ($F_1 + F_2$), and an oxygen, pericytes and neural feedback ($F_1 + F_2 + F_3$).

5.3.1 Flow

The flow dependent feedback x_q, is given by the formulation presented by Payne (2006) [54]:

$$\tau_q \frac{dx_q}{dt} = -x_q + G_q \left(\frac{q - \overline{q}}{\overline{q}} \right) \tag{5.30}$$

where τ_q is a time constant and G_q is a scaling factor. The role of the time constant is to introduce a delay in the response, since changes in flow q are a byproduct of chemical stimuli. The compliance of small arteries C_{sa} is therefore a sigmoidal curve whose behaviour is governed by changes of flow. The positive or negative value of x_q determines whether the amplitude of compliance change is positive (ΔC_{sa}^{+}) or negative (ΔC_{sa}^{-}) respectively.

$$C_{sa} = \overline{C_{sa}} + \frac{1}{2} \Delta C_{sa}^{\pm} \tanh \left(\frac{2x_q}{\Delta C_{sa}^{\pm}} \right) \tag{5.31}$$

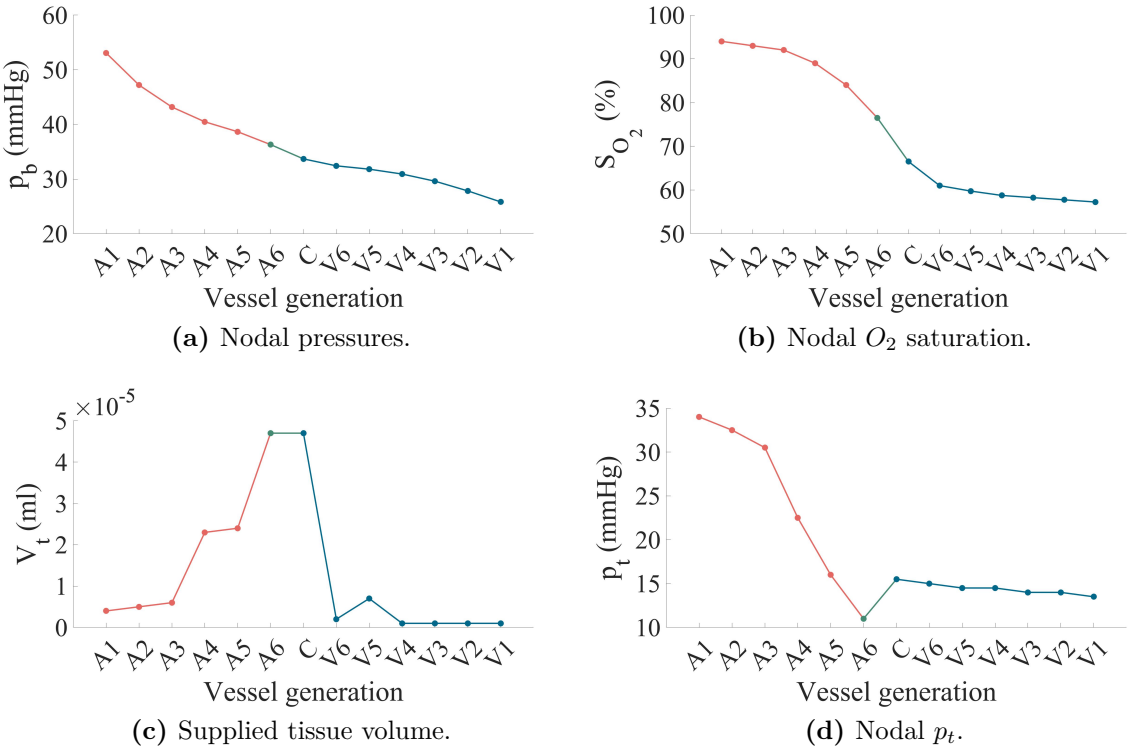

(a) Nodal pressures. **(b)** Nodal O_2 saturation. **(c)** Supplied tissue volume. **(d)** Nodal p_t.

Figure 5.2: Baseline conditions for the microvasculature network. Across the 13 generations of arterioles (red), capillaries (green) and venules (blue), the (a) pressure drop; (b) oxygen saturation drop are shown (c) tissue volume supplied and (d) oxygen partial tissue pressure.

5.3.2 Oxygen

A novel equation for arterial compliance has been developed, in order to relate its changes to variations in oxygen partial tissue pressure. Unlike the compliance in Equation 5.31, the oxygen-sensitive arterial compliance has an immediate response. No time constant is present, as we assume a rapid response for simplicity.

$$C_{sa} = \overline{C_{sa}} + \frac{1}{2}\Delta C_{sa}^{\pm} \tanh\left(\frac{\langle \overline{p_t} \rangle - \overline{p_t}}{p_s}\right) \tag{5.32}$$

where the amplitude of the compliance changes depending on the difference between the volume averaged partial tissue pressure $\langle \overline{p_t} \rangle$ and the baseline value of partial tissue pressure $\overline{p_t}$. If $(\langle \overline{p_t} \rangle - \overline{p_t}) > 0$ then the amplitude is ΔC_{sa}^{+}, otherwise it is ΔC_{sa}^{-}. The magnitude of the scaling factor p_s was initially assumed to be 10% of $\overline{p_t}$.

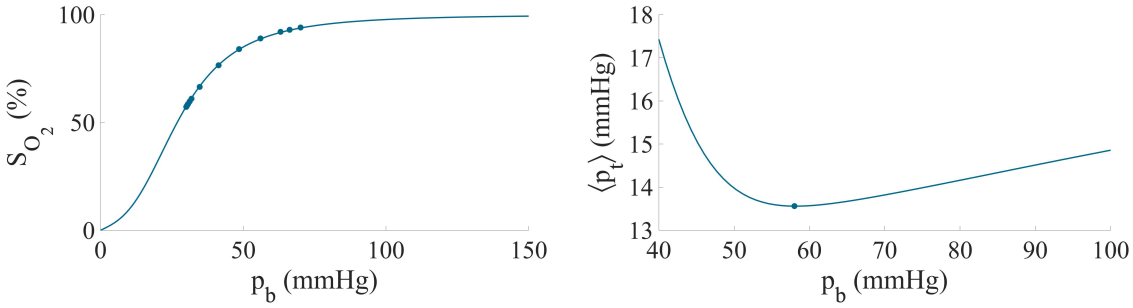

(a) Severinghaus fit.

(b) $\langle \overline{p_t} \rangle$ over a range of inlet pressure.

Figure 5.3: (a) Nodal blood pressure (p_b) and oxygen saturation (S_{O_2}) for each generation are denoted with a circle, showing the fitted Severinghaus function; (b) volume averaged oxygen partial tissue pressure $\langle \overline{p_t} \rangle$ sensitivity to changes in inlet pressure P_{in} in the first generation of the microvasculature with the baseline value marked.

5.3.3 Oxygen and pericytes

To include pericyte-induced vasodilation in the capillaries the model fit presented in Section 4.4 was imposed as a diameter variation of the capillary vessel generation in the network model. Pericyte activity results in a 2.5% increase in diameter for 75% of the capillary vessels (a recurrent percentage in the literature [40]). As the partial tissue pressure $\overline{p_t}$ is a function of the vessel diameter, the compliance of the network C_N can therefore be expressed following the same principles defined in Equation 5.32:

$$C_N = \overline{C_N} + \frac{1}{2}\Delta C_N^{\pm} \tanh\left(\frac{\langle \overline{p_t} \rangle - \overline{p_t}}{p_s}\right) \tag{5.33}$$

where $\overline{C_N}$ is the baseline value of the network's compliance and the amplitude ΔC_N is positive if $(\langle \overline{p_t} \rangle - \overline{p_t}) > 0$ and negative otherwise.

5.3.4 Neural activation

In order to close the loop between increased metabolic demand, CBF and ABP change and pericyte activity, a model of neural activation was introduced. This further regulatory mechanism is linked to the $CMRO_2$ variation recorded through pericyte activity, Figure 4.37. The time delay in the response is about $1s$, which in the neural activation function translates to a $\tau = 1s$ delay. Using a second order dynamic model, we represent neural activation as:

$$\frac{d^2x_n}{dt} = \frac{1}{\tau}(n - \tau^2\frac{dx_n}{dt} - x_n) \tag{5.34}$$

where $n = 0.4$ is the experimentally fitted parameter signalling neuronal activity. In this feedback model, neural activation acts in addition to the oxygen sensitivity and the pericyte activity and the compliance of the network can therefore be defined as:

$$C_N = \overline{C_N} + \frac{1}{2}\Delta C_N^{\pm} \tanh\left(\frac{\langle\overline{p_t}\rangle - \overline{p_t}}{p_s} + x_n\right) \tag{5.35}$$

where $\overline{C_N}$ is the baseline value of the network's compliance and the amplitude ΔC_N is positive if the argument of the sigmoidal function is positive and negative otherwise.

5.4 BOLD signal

The BOLD signal is a useful tool for detecting changes in neural activity in the human brain. While the BOLD signal is related to neural activity, the relationship between them is complex, involving a combination of changes in $CMRO_2$, CBF and CBV. The relationship between these variables was first defined by Davis et al. (1988) [108]

$$\frac{\Delta BOLD}{BOLD} = M_{BOLD}\left(1 - \left(\frac{CMRO_2}{CMRO_2|_0}\right)^{\beta}\left(\frac{CBF}{CBF_0}\right)^{\alpha-\beta}\right) \tag{5.36}$$

where M_{BOLD} represents the maximum possible BOLD signal change and corresponds to the BOLD signal one would measure is all the deoxyhaemoglobin present at baseline were removed from the voxel.

The M_{BOLD} value used here is 8.71, as experimentally determined by Ferná ndez-Seara et al. (2016) [109] in the human grey matter. Five healthy subjects were studied during a gas breathing challenge in order to establish the potential of a dual acquisition sequence for M-mapping and the quantification of $CMRO_2$ changes. Within Equation 5.36, α represents the Grubb's exponent (0.18) while β is assumed to be 1.5 at 3T [109]. $CMRO_2|_0$ and CBF_0 are the baseline values of the cerebral metabolic rate of oxygen and blood flow respectively.

5.5 Summary

A new mathematical model of cerebral autoregulation was presented here. In order to investigate the CBF regulatory ability of metabolic signalling and pericyte activity, a network model comprising arterioles, a capillary bed and venules was integrated within a lumped parameter model. Thus, a model representing the complete vasculature of the brain was designed.

The network model is a bifurcating vessel model consisting of 13 vessel generations (6 arteriolar, 1 capillary and 6 venous) and was used used here to replicate the microvasculature bed. The network was used to closely study the oxygen supply of each vessel generation. Using baseline values of nodal blood pressure and oxygen saturation the volumes of the tissue voxels supplied by each generation were quantified, highlighting that the last three generations of arterioles and the capillary bed supply the largest volumes, as shown in Figure 5.2.

These results served to highlight the important role of the capillary bed in supplying the brain tissue with nutrients. Hence, it was assumed that the metabolic signalling aimed to modulate changes in CBF is linked to an active role of the capillary bed. It is thus that small vessel compliance was assumed to be the CBF modulating agent, as small arteries and the microvasculature bed are the only vessels with actively varying resistance (see Figure 5.1).

The feedback mechanism driving vessel compliance determined the model's response. With the aim of identifying the most physiologically representative modelling technique, and quantifying the regulatory ability of each variable, four distinct feedback mechanisms were investigated: a flow feedback (F_0), an oxygen-feedback (F_1), an oxygen and pericytes feedback ($F_1 + F_2$), and an oxygen, pericytes and neural feedback ($F_1 + F_2 + F_3$). Finally, with the aim of linking neural activation which is considered in the fourth feedback model to $CMRO_2$ changes in the tissue, the BOLD signal was mathematically defined.

However beautiful the strategy,
one should occasionally look at the results.

— Winston Churchill (1864 - 1965)

6 Simulation results

Contents

6.1 Steady state 105
6.1.1 Small vessel compliance 105
6.1.2 Blood flow 107
6.1.3 Blood volume 110
6.2 Dynamic response 112
6.2.1 Oxygen partial tissue pressure 112
6.2.2 Vessel compliance 113
6.2.3 Blood flow 114
6.2.4 Cerebrovascular resistance 116
6.2.5 Blood volume 119
6.2.6 $CMRO_2$ and BOLD 120
6.3 Summary 121

With the aim of investigating the model's ability to replicate a physiologically accurate CBF regulation, a steady state analysis and a dynamic analysis were conducted. Under steady state conditions, the CA mechanism that allows CBF to be maintained constant over a wide range of ABP was studied. Hence, this analysis allows us to draw conclusions about the magnitude of the vessel's ability to regulate flow. In addition, the dynamic analysis serves to obtain insights on the time scale of the regulatory mechanism. The model's reaction speed was investigated with four distinct feedback mechanisms: a flow feedback (F_0), an oxygen-feedback

(F_1), an oxygen and pericytes feedback ($F_1 + F_2$), and an oxygen, pericytes and neural feedback ($F_1 + F_2 + F_3$). Finally, both the static and the dynamic model predictions were validated with experimental data. The results of the study are summarized in Milanovic et al. (2021) [91].

6.1 Steady state

To understand how the four models behave over a wide range of arterial blood pressure, the change in arterial compliance and cerebral blood flow were investigated. The compliance of small vessels was studied as it is the mechanism through which all four feedback models moderate CBF. Indeed, as shown in Figure 5.1, small arteries and the microvasculature network are the only vessels whose resistance is variable and they are therefore the vessels responsible for an active CBF regulation.

Small vessel compliance thus depends on metabolic and neural signals, explored through 4 different modelling approaches (i.e. 4 feedback mechanisms). Ultimately, the ABP range over which CBF is maintained constant was studied for each of the four compliance regulation methods, in order to compare the efficacy of each feedback mechanism in simulating cerebral autoregulation.

6.1.1 Small vessel compliance

In the first model that aims to emulate CBF regulation in the brain through an electrical equivalent model, Ursino(1988a) [49] defines arterial compliance as the sum of all arterial vessel compliances and presents its variability depending on ICP. Following an analogous approach, we explored the variability of the vessel compliance depending on ABP. All the four feedback models tested here are a function of the compliance of small arteries. Figure 6.1 shows the C_{sa} and C_N variance over a range (40 -180 mmHg) of ABP and Table 6.1 illustrates the peak values of arterial compliance induced by each feedback mechanism.

Validating arterial compliance is only possible indirectly, by validating changes in CBF and CBV and thus estimating changes in vessel diameter as a consequence. Hence, to our knowledge, no experimental data (whether in animals nor humans)

exists to validate the model's predictions of compliance change as a function of ABP shown in Figure 6.1. All four feedbacks mechanisms highlight that the compliance of vessels changes with great magnitude for values of ABP below the baseline, while for ABP above the baseline, vessels do not alter their compliance greatly (see Table 6.1). This suggests that arteries have a greater ability in modulating CBF change under low pressure conditions, compared to their ability to regulate CBF under high blood pressure.

The change in small arterial vessel volume shown in Figure 6.2 follows the trend of the compliance of small arteries, highlighting greater volume changes for low blood pressure across all four feedback mechanisms (see Table 6.1). This relationship between volume and compliance can be justified by the fact that under steady state conditions, vessel compliance can be defined as the ratio between the change in blood volume and the change in blood pressure.

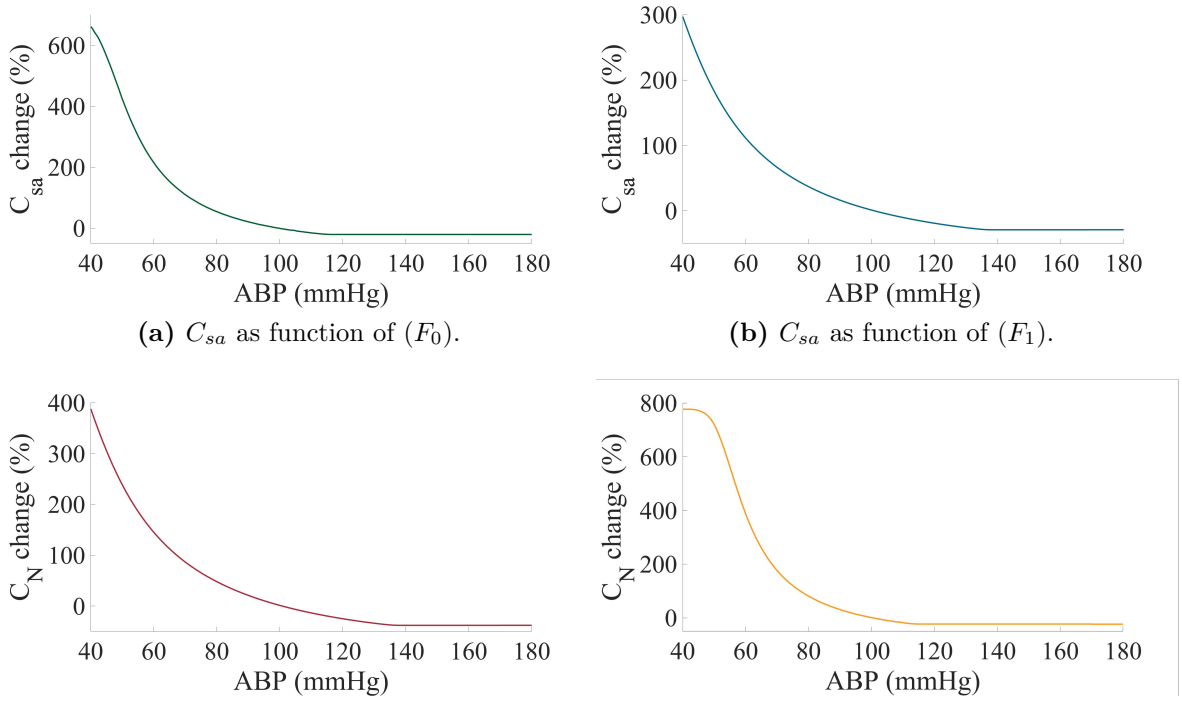

(a) C_{sa} as function of (F_0).

(b) C_{sa} as function of (F_1).

(c) C_N as function of $(F_1 + F_2)$.

(d) C_N as function of $(F_1 + F_2 + F_3)$.

Figure 6.1: Vessel compliance across four feedbacks: (a) the flow (F_0) based; the oxygen (F_1) based; (c) the oxygen and pericytes $(F_1 + F_2)$; (d) the oxygen, pericytes and neural feedback $(F_1 + F_2 + F_3)$.

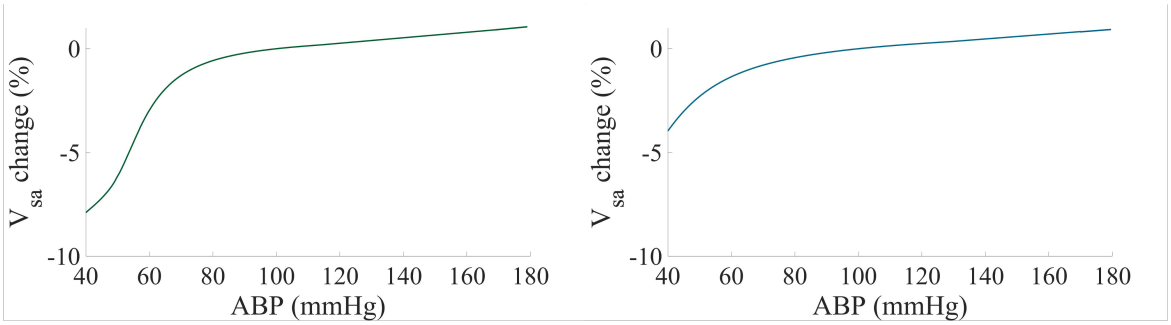

(a) V_{sa} as function of (F_0).

(b) V_{sa} as function of (F_1).

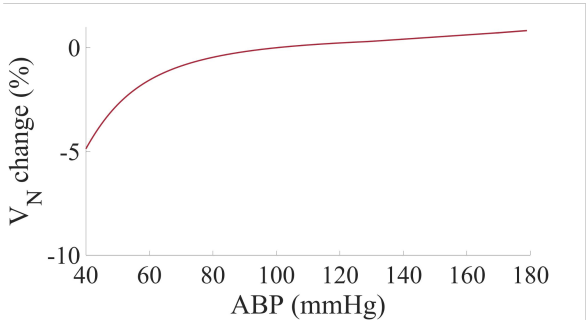

(c) V_N as function of ($F_1 + F_2$).

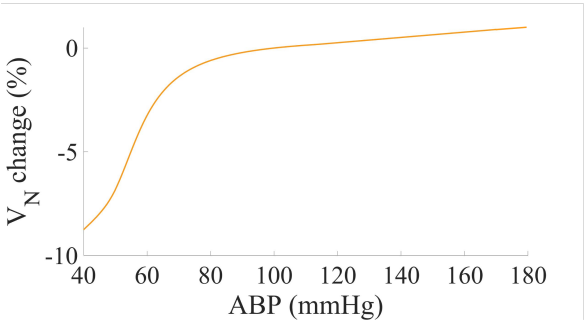

(d) V_N as function of ($F_1 + F_2 + F_3$).

Figure 6.2: Vessel volume change across four feedbacks: (a) the flow (F_0) based; the oxygen (F_1) based; (c) the oxygen and pericytes ($F_1 + F_2$); (d) the oxygen, pericytes and neural feedback ($F_1 + F_2 + F_3$).

6.1.2 Blood flow

Solving the governing equations defined in Chapter 5 under steady state conditions, the change of CBF was observed over a wide range of ABP (40-180 mmHg). All four feedback mechanisms proved to be in good agreement with the literature as CBF was maintained constant between 60 mmHg and 120 mmHg (see Figure 6.3).

Given that this study is focused on analysing the dynamic CBF change induced by small increases in ABP from the baseline (See Section 6.2), the CA plateau is the primary region of interest of the SS CA show in Figure 6.3. Hence, attention should be drawn to the data fit in the 60-120mmHg range, rather than the CBF response beyond the LLA and ULA.

Moreover, it is important to highlight that the data points shown in Figure 6.3 are frequently cited data of cats and mice [110]. Here, each data point is an average of several (10-30) measurements conducted and was ultimately super-imposed on the

model's results for each feedback mechanism. This type of model-fit representation is an established approach adopted by several authors such as Ursino (1998) [110] and Payne (2006) [54] and ultimately corresponds to the results published by Milanovic et al. (2021) [91]. However, for completion, a statistical analysis of the goodness-of-fit was performed for each feedback mechanism and the results are shown in Table 6.2.

Aiming to compare each of the feedback models to an experimentally determined CA curve, the model's results were plotted against the same set of data points presented by Ursino (1998) [110]. Therefore, in this study we define *validation* as the act of developing a model independently of the experimental data and ultimately plotting the model's output along with the data points in order to compare them. The models show a significant difference in the range of the upper and lower autoregulation limit (see Table 6.1), which strongly depend on the parameters of the compliance equation. The nature of the difference in vessel compliance for a wide range of ABP is discussed in Section 7.4.1.

To effectively compare the ability of each feedback mechanism in maintaining a CA plateau, the LLA and the ULA were identified for each of the four feedback models (Table 6.1). As discussed in Chapter 2, it should be noted that there currently is not a precise and strict value for LLA and ULA in humans in the literature [111],[112],[113], as the CA range is influenced by multiple variables (e.g. gender and age). In this study, a healthy CA was assumed to be in the ABP range of 60-120 mmHg. Further considerations on the implications of this choice are outlined in Section 7.4.1.

For the flow feedback model (F_0), the LLA is 81.3 mmHg and the ULA is 119.4 mmHg; in the oxygen feedback model (F_1), the LLA is 71.8 mmHg and the ULA is 128.4 mmHg; in the pericyte and oxygen feedback model ($F_1 + F_2$), the LLA is 78.3 mmHg and the ULA is 120.1 mmHg; and in the neural, pericyte and oxygen feedback model ($F_1+F_2+F_3$), the LLA is 82.2 mmHg and the ULA is 121.3 mmHg. The nature of the difference in compliance saturation is discussed in detail in Section 7.4.1.

Table 6.1 and Figure 6.3 illustrate the CA limits highlighting an evident difference in CA plateau range for each of the four feedback models. The flow-based models

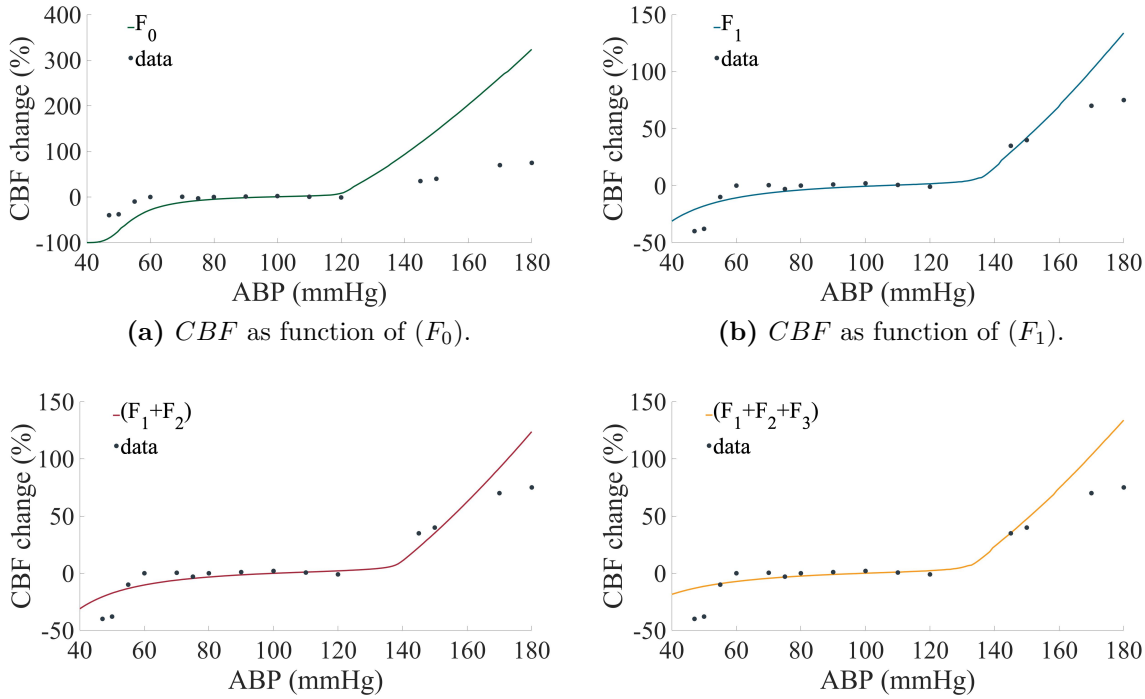

(a) CBF as function of (F_0). **(b)** CBF as function of (F_1).

(c) CBF as function of $(F_1 + F_2)$. **(d)** CBF as function of $(F_1 + F_2 + F_3)$.

Figure 6.3: Cerebral autoregulation across a wide range of ABP for all four feedbacks: (a) the flow (F_0) based; the oxygen (F_1) based; (c) the oxygen and pericytes $(F_1 + F_2)$; (d) the oxygen, pericytes and neural feedback $(F_1 + F_2 + F_3)$. The models have been validated with data points from cats and mice cited in the literature [110].

appears to be the one with the shortest plateau, meaning that in this case arterial compliance is lower. On the other hand, the remaining 3 feedback models where arterial compliance depends on the metabolic demand of the tissue, present very similar CA extremes. Further implications of the model's ability to regulate CBF under steady state conditions are presented in Section 7.4.1.

Finally, it is worth noting that the CBF is pushed beyond the CA plateau range only under extreme blood pressure conditions, meaning that the most interesting ABP range to be analysed in the dynamic study is the one within the CA plateau. Indeed, it is within the CA range that CBF can be modulated rapidly. Also, human experimental data that can be used for the validation of the computational model presented here are only available for CBF changes within the CA range.

With the aim of defining the goodness-of-fit of the model to the data, Table 6.2 reports the p-value, R-squared, R-squared adjusted and root mean square error

Feedback	F_0	F_1	$F_1 + F_2$	$F_1 + F_2 + F_3$
LLA (mmHg)	81.3	71.8	78.3	82.2
ULA (mmHg)	119.4	128.4	120.1	121.3
CA plateau (mmHg)	38.1	56.6	41.8	39.1
CBF_{min} change (%)	-99.95	-31.18	-31.04	-18.11
CBF_{max} change (%)	323.83	133.87	123.76	133.87
$C_{sa,N,max}$ change (%)	691.04	296.95	387.86	776.84
$V_{sa,N,max}$ change (%)	-7.89	-3.96	-4.87	-8.75

Table 6.1: Overview of the characteristic responses of all 4 feedback models. The table shows the differences in lower limit of autoregulation (LLA), upper limit of autoregulation (ULA); peak CBF change; minimum CBF change; the peak small vessel compliance change $C_{sa,N,max}$ and the maximum $V_{sa,N,max}$ small vessel volume change.

(RMSE) specific to each feedback mechanism. The p-values of each feedback mechanism indicate a statistically significant difference (<0.05) and the error evaluations vary greatly. It can be hypothesized that this divergence in error estimates and the p-values, are primarily driven by the values outside the CA plateau range (i.e. beyond the LLA and ULA limits), given by the different saturation of the arterial compliance which drives CBF change (as discussed in Section 6.1.1).

A significant limitation in the validation of SS CA models is the low availability of consistent data. In addition to the difficulty in translating animal experimental data to human models, the lack of consistency between non-invasive human experimental setups and the physiological variability in the population inhibit a robust validation methodology for SS CA. [29], [30], [31]. Chapter 7 further elaborates on these limitations, however it is important to highlight that the purpose of this study is to investigate the rapid CBF regulation happening on a microvascular level, and therefore the focus on the results lies in the dynamic response study (See Section 6.2) rather than the steady state analysis.

6.1.3 Blood volume

The neural feedback model ($F_1 + F_2 + F_3$), was validated against experimental data in rats by Lee et al. (2001) [114], as it is the model that most closely replicates physiological reality. Indeed, as discussed in Chapter 2, metabolic signalling is

Feedback	F_0	F_1	$F_1 + F_2$	$F_1 + F_2 + F_3$
p-value	0.012	0.023	0.024	0.031
R^2	0.94	0.862	0.858	0.862
R^2 - adjusted	0.94	0.861	0.857	0.861
RMSE	7.99	12.33	12.50	12.31

Table 6.2: Evaluation of the goodness-of-fit of the SS model to the data. For each feedback mechanism, the p-value, R-squared, R-squared adjusted and root mean square error (RMSE) are reported.

entangled with neural signalling, and it is thus physiologically accurate to consider both variables as CBF regulators.

Figure 6.4 shows a well fitted flow and volume relationship for venous volume (V_v), arterial volume (V_a) and total cerebral blood volume (CBV). The venous and arterial blood volume increases correspond to the experimental data shown in Figure 6.4, where a 26% increase in CBF corresponds to an approximate 6% change in V_v and a 12% increase in V_a. The changes in blood volumes were determined by Lee et al. [114], by inducing hypercapnia in rats and measuring the relative changes in venous and total blood volume using diffusion weighted ^{19}F NMR. Their data are in good agreement with previously published data on the CBF and CBV relationship in monkeys described by Grubb et al. (1974) [95].

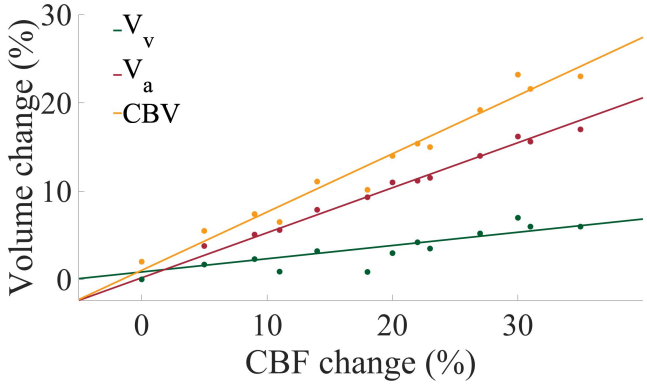

Figure 6.4: Blood flow and volume relationship for venous volume (V_v), arterial volume (V_a) and total cerebral blood volume (CBV) for the neural feedback model. Experimental data on rats were extracted from Lee et al. [114].

6.2 Dynamic response

To further investigate on the physiological accuracy of the oxygen-feedback model, its dynamic response was evaluated. The magnitude of this response can serve as an indicator for the overall influence of oxygen sensitivity during an active blood flow regulation response.

6.2.1 Oxygen partial tissue pressure

To investigate the time response to changes in oxygen partial tissue pressure, the governing equations of the model were solved under dynamic conditions and a 10% increase in ABP was imposed at time $t = 0s$, after running the solver for an initial simulation time of 5 s to ensure stable baseline conditions. As a result, oxygen partial tissue pressure increased by 18.93% and after about 8 s settled to a 2.62% higher baseline compared to the value prior to the stimulus (see Figure 6.5). The implications of the magnitude and time response of this oxygen content increase in the tissue and how it relates to $CMRO_2$ and vessel compliance are discussed in Chapter 7.

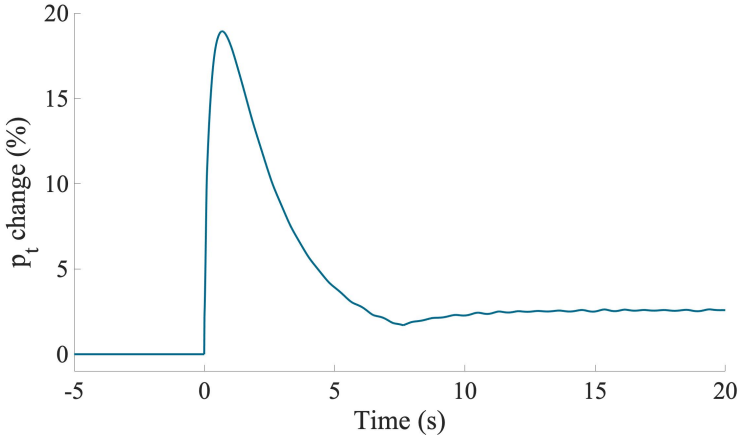

Figure 6.5: Partial tissue pressure increases by 18.93% upon a 10% increase in ABP at $t = 0$ and settles to a 2.62% higher baseline in about 6 s.

6.2.2 Vessel compliance

Small vessel compliance drives CBF modulation in the computational model presented here. Figure 6.6 shows the dynamic variability of arterial compliance across all four feedback mechanisms for a 10% increase in ABP at $t = 0$. In the flow based model (F_0), a 10% increase in ABP results in a 20.27% decrease in C_{sa}, settling to a new baseline level in about 2 s. On the other hand, in the oxygen feedback model (F_1), C_{sa} drops by 6.86% and settles to a new value in about 8 s. Including pericyte activity and therefore extending the ability to actively vary the vessel diameter also to capillaries, the small vessel compliance C_N drops by 19.48% in about 5s for the ($F_1 + F_2$) model. On the other hand, including neural activation sensitivity as a vessel compliance regulator, changes C_N by 19.49% in about 3 s (see Table 6.4).

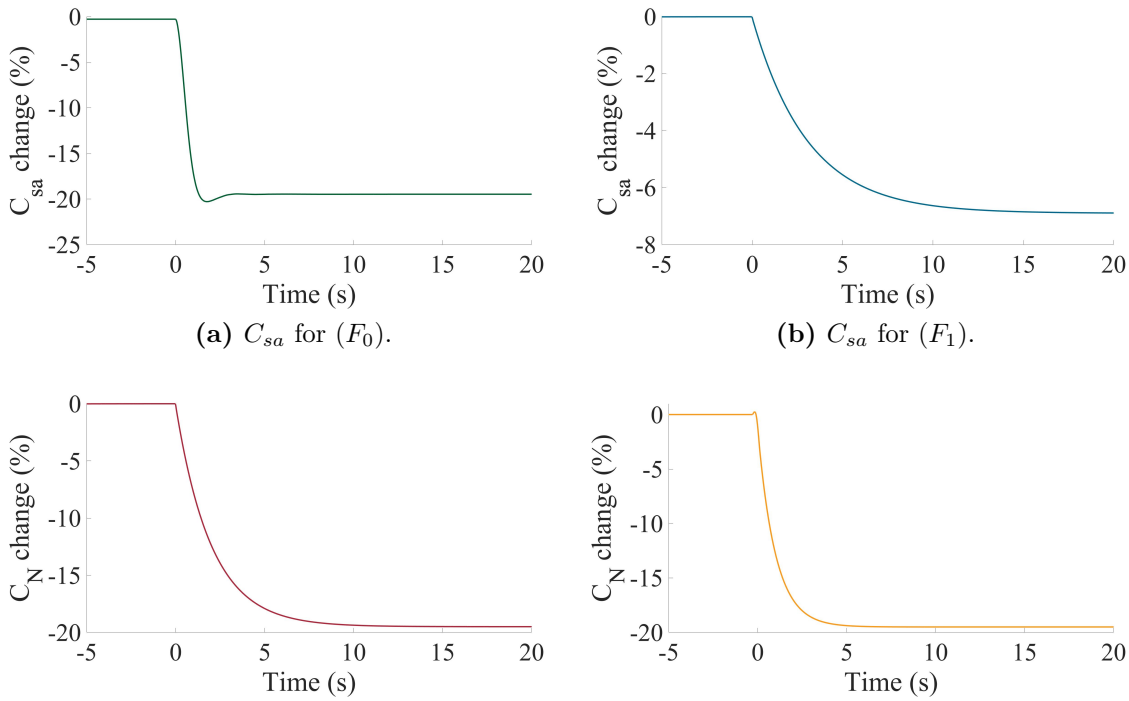

(a) C_{sa} for (F_0). **(b)** C_{sa} for (F_1).

(c) C_N for ($F_1 + F_2$). **(d)** C_N for ($F_1 + F_2 + F_3$).

Figure 6.6: Vasculature compliance during dynamic CBF regulation in the for all four feedbacks: (a) the flow (F_0) based; (b) the oxygen (F_1) based; (c) the oxygen and pericytes ($F_1 + F_2$); (d) the oxygen, pericytes and neural feedback ($F_1 + F_2 + F_3$).

6.2.3 Blood flow

Dynamic changes in flow were investigated with the same approach. Following the impulse, CBF increased by about 23% in the flow based model, by 30% in the oxygen based model, by 34% in the model including pericytes and by 26% in the model including neural activation (see Figure 6.7).

Next to the ability of moderating the high pressure-induced CBF increase, an insightful measure for comparing the four feedback mechanisms is the response time. The latter is defined as the elapsed time between the CBF increase onset and the first return to the baseline value. Figure 6.7 shows that the time responses of CBF are about 2 s for the flow based, about 11 s for the oxygen based, 6 s for the oxygen and pericyte driven model and about 4 s when neural activity is included as a further regulator. Table 6.4 summarises all CBF change and response time values.

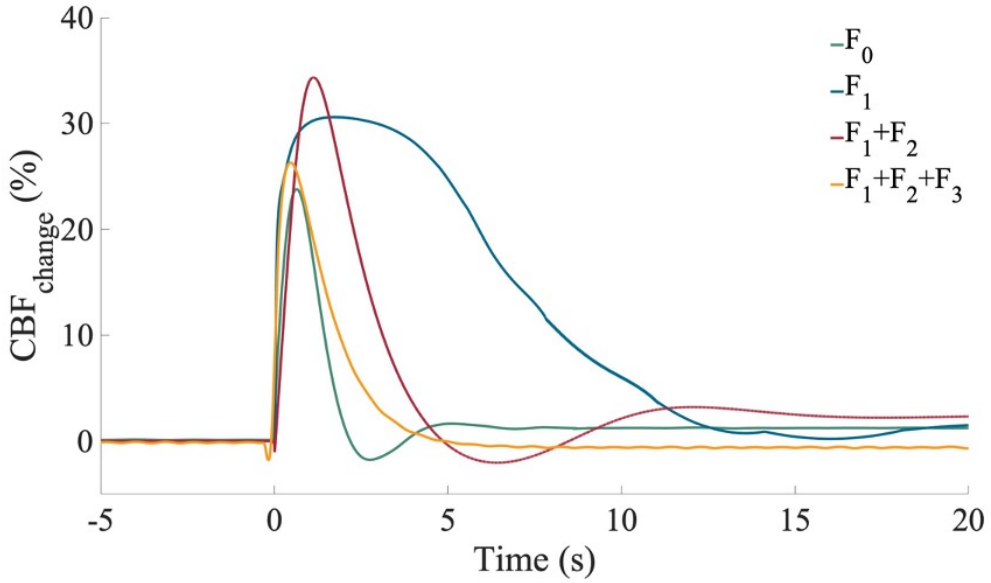

Figure 6.7: Cerebral blood flow variation upon a 10% increase in ABP at $t = 0$ for all four feedbacks: (green) the flow (F_0) based; (blue) the oxygen (F_1) based; (red) the oxygen and pericytes ($F_1 + F_2$); (orange) the oxygen, pericytes and neural feedback ($F_1 + F_2 + F_3$).

The feedback model including neural activation fits experimental data on cerebrovascular reactivity presented by Parthasarathy et al. (2018) [115] on dynamic CBF regulation in 11 healthy people. Using the thigh cuff method and non-invasive

monitoring, changes in CBF relative to ABP fluctuations are quantified. The study concludes that a 10% change in blood pressure corresponds to a maximum change in CBF in the range 11.2% - 27.8%. This is in agreement with the fourth feedback model including neural activation ($F_1 + F_2 + F_3$), which is regarded as the most physiologically accurate among the four, where CBF peaks to 26% in response to a 10% ABP increase.

Parthasarathy et al. (2018) [115] also provide a validation for the response time. Indeed, their experimental data, retrieved with Transcranial Doppler (TCD) measurements, show that the time it takes for the flow to reach baseline after an increase induced by ABP changes, ranges between 3-5 s. This value is very close to the neural feedback model whose response time is about 4 s (see Table 6.4).

CA shows us that the brain is capable of regulating changes in flow for a wide range of ABP values, but the dynamic response has so far only been explored for a 10% increase in ABP starting from baseline conditions (i.e. $\overline{ABP}$=100 mmHg). Figure 6.8 presents the results of the $(F_1 + F_2 + F_3)$ feedback model for the dynamic CBF change induced by a 10% increase in ABP starting from six baseline conditions.

Two new conditions below the original baseline ABP were tested: for $\overline{ABP}$= 60 mmHg, the peak CBF increase is 12.23% and then settles to a new baseline condition which is 6.12% higher, in about 7 s; while for $\overline{ABP}$= 80 mmHg CBF peaks at 20.92%, settling to a new baseline which is 4.7% higher compared to the original one with a response time of about 6 s.

Similarly, two new conditions above the original ABP were tested: for $\overline{ABP}$= 120 mmHg, the peak CBF increase is 31.66% and then settles to a new baseline condition which is 2.68% lower in about 6 s; while for $\overline{ABP}$= 140 mmHg CBF peaks at 35.71%, settling to a new baseline which is 6.41% lower compared to the original one with a response time of about 6 s. Table 6.3 summarises all the characteristic values of the responses shown in Figure 6.8.

Figure 6.9 is a representation of the the dynamic CBF responses for six different conditions of baseline ABP. The difference in shape and peak CBF change is

$\overline{ABP}$ (mmHg)	60	80	100	120	140
CBF_{max} (%)	12.23	20.92	26.32	31.66	35.71
$\Delta\overline{CBF}$(%)	+6.12	+4.7	0	-2.68	-6.41
Response time (s)	7.2	6.5	4.1	6.1	6.3

Table 6.3: Overview of the dynamic responses for six different $\overline{ABP}$ conditions. The peak CBF percentage change (CBF_{max}) is quantified, along with the percentage difference in baseline value ($\Delta\overline{CBF}$) and total response time.

represented along with the steady state cerebral autoregulation curve of the feedback mechanism including neural activation ($F_1 + F_2 + F_3$).

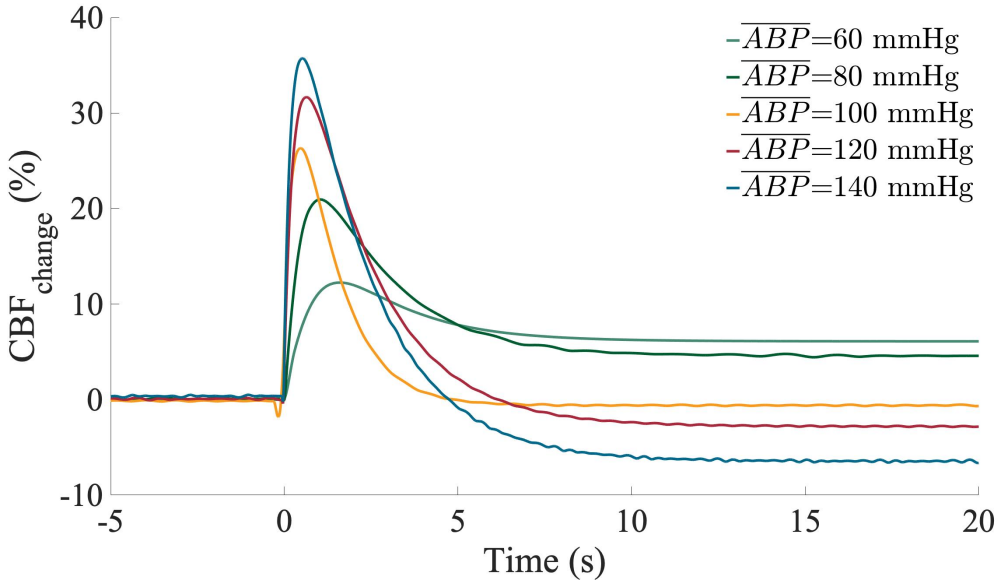

Figure 6.8: Cerebral blood flow variation upon a 10% increase in ABP at $t = 0$ for six baseline conditions of $\overline{ABP}$: 60mmHg (light green), 80 mmHg (dark green), 100mmHg (orange), 120mmHg (red) and 140mmHg (blue).

6.2.4 Cerebrovascular resistance

The change of cerebrovascular resistance (CVR) can be used as a further measure of comparison between the feedback models and experimental data. CVR is defined as the ratio of ABP and CBF and therefore the change of CVR variation over time provides a measure of dynamic autoregulation. Figure 6.10 shows the CVR over time for all four feedback mechanisms. Following the impulse, CVR increased by 2.16% in the flow based model, by 2.78% in the oxygen based model, by 3.12% in the

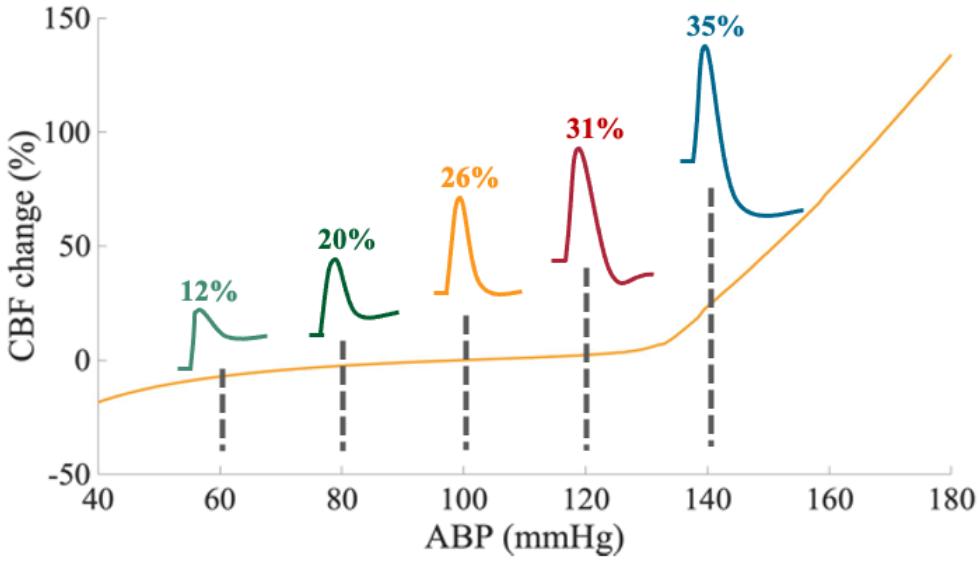

Figure 6.9: Graphic representation of the dynamic CBF change upon a 10% increase in ABP for six baseline conditions of $\overline{ABP}$ over the steady state CA curve.

model including pericytes and by 3.38% in the model including neural activation. In relation to the experimental results presented by Parthasarathy et al. (2018) [115], where the peak CVR value ranges between 2-10%, the model's results for all four feedback methods are in good agreement.

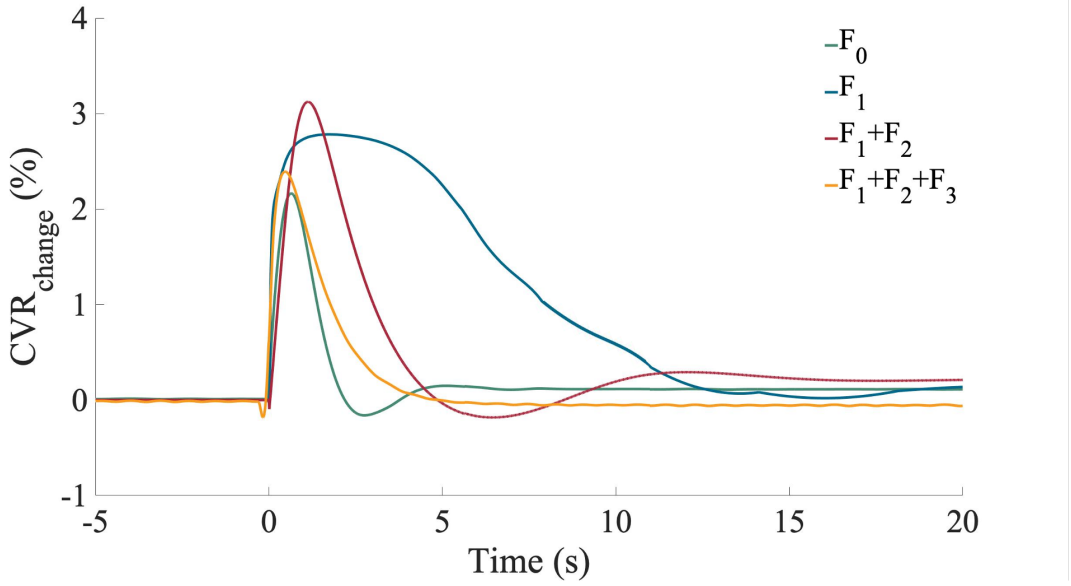

Figure 6.10: Cerebrovascular resistance variation upon a 10% increase in ABP at $t = 0$ for all four feedbacks: (green) the flow (F_0) based; (blue) the oxygen (F_1) based; (red) the oxygen and pericytes ($F_1 + F_2$); (orange) the oxygen, pericytes and neural feedback ($F_1 + F_2 + F_3$).

Figure 6.11 shows the different rates of relative CVR change ($drCVR/dt$) during dynamic autoregulation for each of the four feedback mechanisms. The segment of rCVR change that is most interesting for a comparison is that from the peak value of CBF change to when CBF change is closest to 0% and is therefore the one represented by the lines in Figure 6.11.

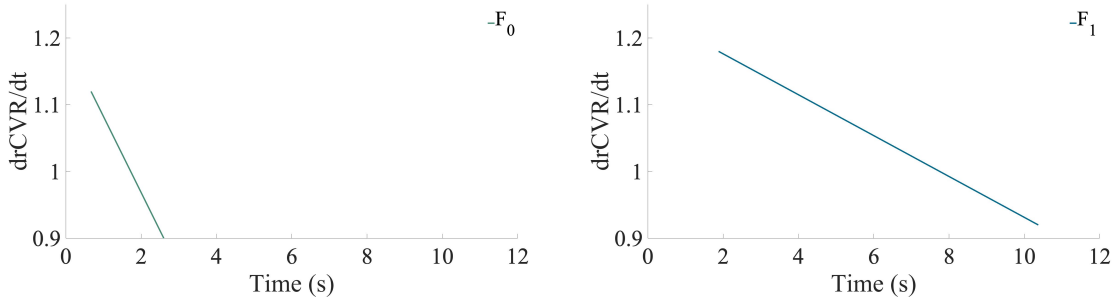

(a) rCVR change for (F_0).

(b) rCVR change for (F_1).

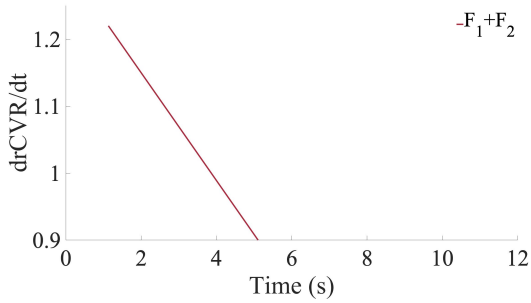

(c) rCVR change for ($F_1 + F_2$).

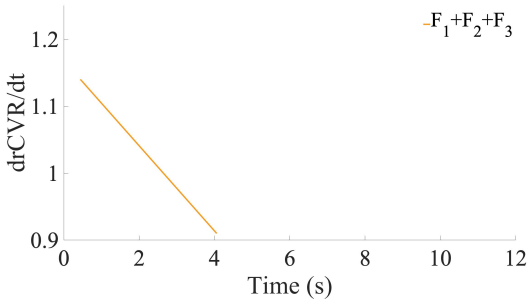

(d) rCVR change for ($F_1 + F_2 + F_3$).

Figure 6.11: Cerebrovascular resistance change ($drCVR/dt$) during dynamic CBF regulation in the for all four feedbacks: (a) the flow (F_0) based; the oxygen (F_1) based; (c) the oxygen and pericytes ($F_1 + F_2$); (d) the oxygen, pericytes and neural feedback ($F_1 + F_2 + F_3$).

Ultimately, to quantify the rate at which the vasculature's resistance must change to compensate a unit percentage change in ABP, the rate of regulation (ROR) was evaluated for each feedback model. The ROR can be defined as [115]:

$$ROR = \left(\frac{drCVR}{dt}\right)\frac{\overline{ABP}}{ABP_{max}} \tag{6.1}$$

where $drCVR/dt$ is the slope of the relative CVR change, $\overline{ABP}$ is the baseline ABP (i.e. 100 mmHg) and ABP_{max} is the maximum ABP value (i.e. 110 mmHg). The ROR for the flow model (F_0) is 0.10 s^{-1}, meaning that the resistance of

cerebral microvasculature changes at a rate of 10% per second to compensate for a 1% increase in ABP. For the oxygen model (F_1) the ROR is 0.027 s^{-1}, including pericytes in the ($F_1 + F_2$) model increases the ROR to 0.073 s^{-1}, while adding neural activation in the ($F_1 + F_2 + F_3$) results in a ROR of 0.055 s^{-1}. Table 6.4 presents an overview of all the values.

Feedback	F_0	F_1	$F_1 + F_2$	$F_1 + F_2 + F_3$
$C_{sa,max}$ (%)	20.27	6.86	19.48	19.49
CBF_{max} (%)	23.79	30.58	34.33	26.32
Response time (s)	2.3	10.8	5.8	4.1
CBV_{max} (%)	13.04	16.71	17.57	14.88
$V_{A,max}$ (%)	10.56	13.53	14.23	12.11
$V_{V,max}$ (%)	2.47	3.17	3.33	2.76
CVR_{max} (%)	2.16	2.78	3.12	3.38
ROR (%/s)	10	2.7	7.3	5.5

Table 6.4: Overview of the dynamic responses of all 4 feedback models. The table shows the maximum changes in arterial compliance $C_{sa,max}$, flow CBF_{max}, total blood volume CBV_{max}, arterial blood volume $V_{A,max}$, venous blood volume $V_{V,max}$, cerebrovascular resistance CVR_{max}, response time and rate of regulation ROR.

6.2.5 Blood volume

The dynamic response of the blood volume compartments was studied for the model closest to physiological reality: the model including neural activity ($F_1 + F_2 + F_3$). Figure 6.12 shows how a 26.32% dynamic increase in CBF corresponds to a 14.88% increase in CBV in the model. Experimental data on CBV variation in 9 healthy subjects presented by Ito et al. (2003) [96] were used to validate the results of the final feedback model ($F_1 + F_2 + F_3$). Their study shows that for a CBF increase 30.5 ± 14.6 %, CBV varies by 9.6 ± 5.7%, which is in very good agreement with the model's results.

Given the active response of the arteries and the passive response of the veins, the changes in blood volume were investigated for each of the vessel types individually. The model including neural activation ($F_1 + F_2 + F_3$) showed that the baseline value of V_A rises by 11.98% after the impulse and that of V_V rises by about 2.76% before settling to baseline condition. These results suggest that arteries are the vessels

that dominate CBV change. No difference in the response time was observed, as the passive nature of the veins can only reflect the changes in the arterial vessels. The sum of both volume compartments yields the total CBV whose impulse response shows an increase of about 15%, as shown in Figure 6.12.

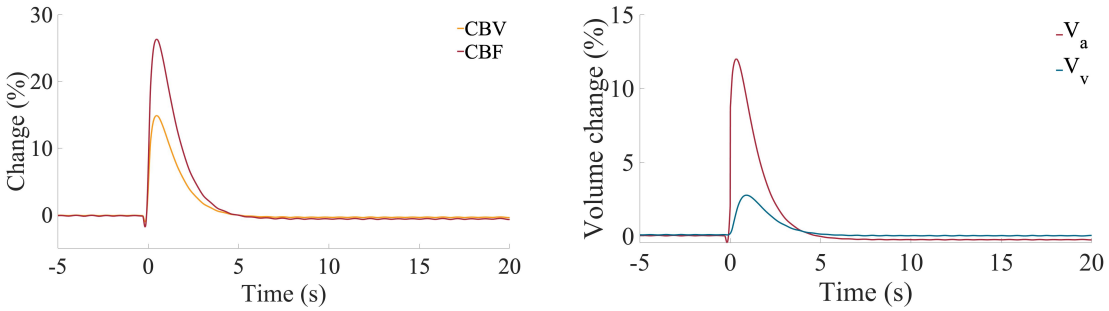

(a) CBV and CBF change. **(b)** V_a and V_v change.

Figure 6.12: In the feedback ($F_1 + F_2 + F_3$) model: (a) CBV increases by 14.88% and flow by 26.32 upon a 10% increase in ABP at $t = 0$; and (b) arterial volume (V_a) increases by 11.98% and venous volume increases by 2.76%.

6.2.6 $CMRO_2$ and BOLD

In Chapter 4 we found that upon neural activation (i.e. visual stimulation), oxygen metabolism in the tissue surrounding the vessel increases by about 6% (see Figure 4.37). To investigate the differences between local and global metabolic changes upon stimulation, the $CMRO_2$ was studied also in the computational model with neural feedback ($F_1 + F_2 + F_3$). Figure 6.13(a) shows a 9.10% increase in response to a 10% increase in ABP.

The model's result for the relationship between the BOLD signal and the $CMRO_2$ change is in good agreement with the experimental data presented by Fernández-Seara et al. (2016) [109]. The study reports on five healthy males who were exposed to a gas breathing challenge and a motor paradigm, showing an average 12% and 13% increase in $CMRO_2$ in the left and right motor cortex respectively. Moreover, Fernández-Seara et al. (2016) report a measured BOLD signal change of 0.82% and and 0.90% in the left and right motor cortex respectively.

The BOLD signal was modelled and the resulting BOLD change from a 10% increase in ABP is shown in Figure 6.13(b). Fernández-Seara et al. (2016) [109] report that the average BOLD increase for five healthy humans following a stimulus is about 0.86%. This is in good agreement with our model's results where BOLD increases by 0.76% following a 26% CBF change in the neural feedback ($F_1 + F_2 + F_3$) model.

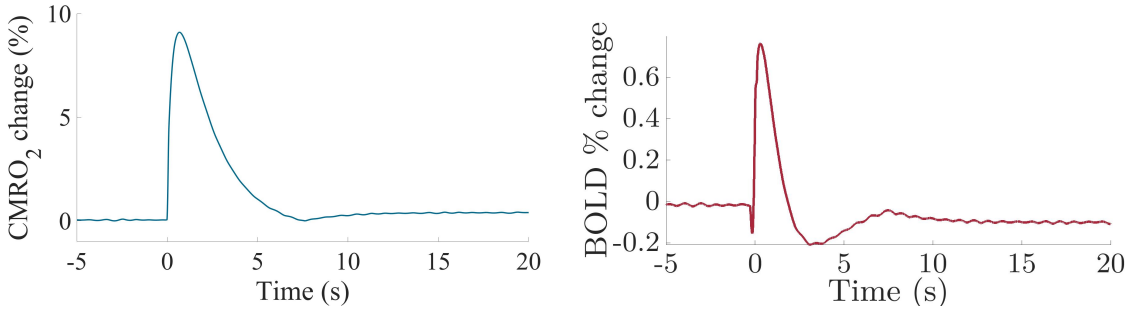

(a) Oxygen metabolism. **(b)** BOLD signal.

Figure 6.13: $CMRO_2$ increases by 9.10% (a) and BOLD increases by 0.74% (b) upon a 10% increase in ABP at $t = 0$.

As the exact values defining the equation for the BOLD signal (Equation 5.36) are still being defined, the relationship of the $BOLD$ signal and the M_{BOLD} parameter defined in Equation 5.36 as the maximum BOLD change, a range of M_{BOLD} values was tested. Figure 6.14 shows the peak BOLD response varying for values of M_{BOLD} ranging from 1 to 10, as experimentally determined for different brain areas. [116] Within the model, a value of 8.71 was used for M_{BOLD}, as it represents the mean value across all brain areas reported by Fernández-Seara et al. (2016) [109]. This is a good assumption for the vasculature model presented here, as the aim is to study the whole brain CBF regulation. Chapter 7 outlines further implications of the chosen BOLD modelling technique.

6.3 Summary

The results of the steady state and dynamic analysis of the computational model are presented here. Under steady state conditions, the model's ability to simulate CA

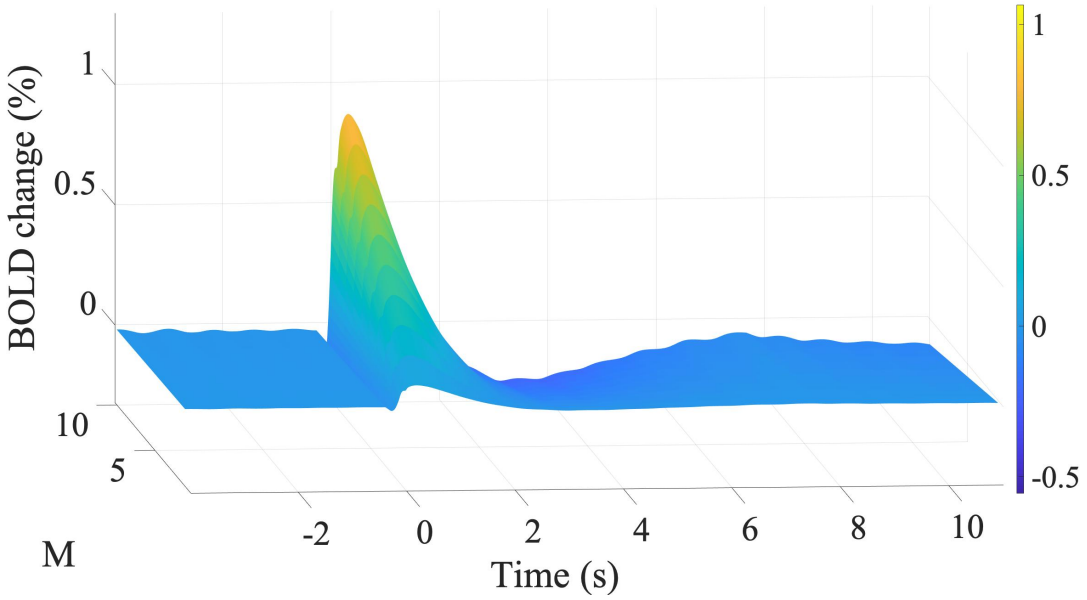

Figure 6.14: Simulation results of the variation in BOLD response across a range of M_{BOLD} values (1-10) experimentally determined by Bulte et al. (2007) [116] for different brain areas. The scale bar indicates the range of peak BOLD signal change.

over a wide range of ABP was studied for all four feedback mechanisms and a good agreement with experimental data was established across all feedback mechanisms (see Figure 6.3). Indeed, all four feedback mechanisms exhibit a CA plateau, it being the widest for the oxygen feedback model (see Table 6.1).

As changes in CBF are driven by a variation in small vessel compliance, the compliance was also studied across a wide range of ABP. It was found that compliance changes with a much greater magnitude when ABP decreased below the baseline value, compared to when ABP increases above the baseline value (see Figure 6.1). The respective change in blood volume was also highlighted for each feedback mechanism (see Figure 6.2).

The dynamic analysis enabled the comparison of ABP-driven changes in CBF both in terms of response speed and peak change. From the results shown in Figure 6.7 which represent the CBF increase in response to a 10% increase in ABP, it was concluded that the feedback model including neural activation ($F_1 + F_2 + F_3$) is the one closest to physiological reality. Indeed, the response speed was found to be about 4s and the CBF increase resulted in about 26% from the baseline value

(see Table 6.4).Finally, the increase in $CMRO_2$ and BOLD in response to changes in CBF were studied and found to successfully replicate the metabolic increases mentioned across human experimental studies.

Keep Thou my feet; I do not ask to see
The distant scene; one step enough for me.

— *Lead, Kindly Light* (1833), John Henry Newman

7 Discussion

Contents

7.1 Cerebral perfusion 125
7.2 Nutrient consumption 126
7.2.1 Glucose 127
7.2.2 Oxygen 128
7.3 Methods 131
7.3.1 Experimental procedure 131
7.3.2 Modelling approach 132
7.4 Computational results 133
7.4.1 Feedback mechanisms 133
7.4.2 Vessel compliance 134
7.4.3 Blood flow 136
7.4.4 Blood volume 140
7.4.5 $CMRO_2$ and BOLD 141
7.5 Pericyte activity 143
7.5.1 Large and small capillaries 144
7.5.2 Blood flow and volume 146
7.5.3 Calcium signalling 148
7.6 Study limitations 149
7.6.1 Experimental 149
7.6.2 Computational 150
7.7 Summary 153

This chapter aims to link the the experimental results presented in Chapter 4 to the modelling results outlined in Chapter 6. In Chapter 5 we defined a computational approach suited to study this heterogenous vessel response to changes

in flow, metabolism and neural activity. We found that the cerebrovasculature is heterogeneous in its nature in terms of geometry and vessel response mechanisms. Vessel diameter, vessel tone and the proximity with neurons are all factors that contribute to the heterogeneity of vasculature response.

7.1 Cerebral perfusion

In a healthy brain, CBF is maintained by the autoregulatory mechanism of vasoconstriction and vasodilation when CPP is increased or decreased respectively. Hence, during autoregulation while CBF is maintained constant, the drop in CBV is compensated by the cerebrovascular reserve. When CPP surpasses the ULA, CBF increases as a result. Alternatively, when CPP decreases below the LLA, CBF decreases. Furthermore, when CBF drops and $CMRO_2$ remains unchanged, OEF increases, which is considered pathological and is indicative of tissue hypoxia. Figure 7.1 outlines the relationship between the haemodynamic response and the CPP, with $CMRO_2$ being the most controversial.

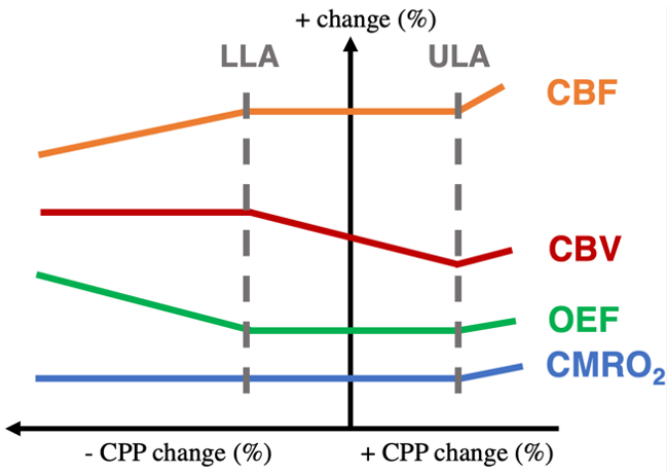

Figure 7.1: Haemodynamic response to a decrease in CPP.

As outlined in Chapter 2, it is not a single variable that regulates CBF on a microvasculature level. Instead, evidence [89], [117], [118] supports the notion that CBF is governed by regional metabolism and that these fluctuations in metabolic demand are linked to local neural activity. While a strong correlation between $CMRO_2$, CMR_{glc} and CBF was found, no single parameter can be said to regulate

CBF under all conditions and in all length scales of the vasculature.
Ultimately, CBF can increase in two ways: by increasing the blood perfusing the tissue per second (i.e. through vasodilation), or by increasing the velocity of the blood flow but leaving the blood volume constant. The first mechanism is the most interesting one, as already in 1937 Dunning and Wolff [119] defined a correlation between the high number of capillaries in a brain region and the number of synapses. This suggests an important role of the microvasculature in regulating flow, through a blood volume change mechanism. Moreover, the fact that dynamic changes in blood flow are faster than changes in blood volume (see Figure 6.12) implies that capillaries are more likely to change their diameter frequently and intermittently, to ensure an even perfusion of the tissue. [120]
Computational models such as the one proposed by Ursino et al. (1998) [110] relating CO_2 and CBF make it an appealing feedback modelling approach, however it is not a direct way of relating metabolic activity and CBF modulation as extracellular CO_2 is the *byproduct* of metabolism. Indeed, changes in CBF are linearly related to changes in arterial and pre-capillary CO_2 partial pressure, but the relationship does not preserve its linear form for large changes in CO_2. [121]
For the aforementioned reasons, CO_2 was not included among the feedback formulations used to define the computational model in Chapter 5. Previous models of CA also rarely include the effects of arterial CO_2 as the relationship is intricate, involving multiple regulatory players.

7.2 Nutrient consumption

With neuronal activity driving every action of the brain and consuming 75% of its energy supply, a constant flow of nutrients is imperative for a healthy brain function. In particular, the brain relies on two essential nutrients: glucose and oxygen. As glucose metabolism relies heavily on the presence of oxygen (as outlined in Section 2.2.4), fluctuations of oxygen content are inevitably tightly coupled with glucose consumption in the tissue.

7.2.1 Glucose

While prolonged changes in glucose metabolism are governed by hormones, short-term changes are moderated by CBF. The tight coupling between CBF, capillary density and CMR_{glc} makes the investigation of the time scale of these interactions an interesting study. Following the approach described by Aubert et al. (2001) [79] glucose concentration was modelled within the supplying capillaries (GLC_C) and the tissue (GLC_T) where it is consumed.

Furthermore, to link neural activity to metabolic activity and later visual stimulation-induced pericyte activity, the Na/K pump reactivity was studied as a function of ATP variations. As neurovascular coupling is a rapid mechanism, only short-term changes in glucose are of relevance for the model presented here. Indeed, these interactions occur in a time frame not longer than a few minutes. Figure 3.5a shows how a 40% increase in CBF results in a 2000% ADP increase from baseline in about 5 minutes, followed by a 13% decrease in ATP within the same time (Figure 3.5b). The increase in ADP can directly be related to the increase in CBF, as more blood flow means more nutrient supply.

ADP is the "unprocessed" form of energy that can be stored in the mitochondria before being transformed into ATP, which explains why its increase is not moderated by a messenger. Furthermore, after prolonged periods of time, excess ADP is expelled by the mitochondria into the extracellular space where it is removed as waste. On the other hand, the relatively small deviation from baseline of ATP suggests that ATP regeneration is replaced by glycolysis, caused by an accumulation of lactate over time (see Figure 3.7a).

The change of the ATP/ADP ratio as a result of increased CBF, translated to a 1.8% increase in glucose in the capillaries and a 60% decrease in the tissue, as shown in Figure 3.6. The variations of both oxygen and glucose show good agreement with the experimental data of the human visual cortex presented by Frahm et al. (1996) [83] and Krueger et al. (1999) [84]. The decreases in tissue and capillary glucose concentrations are justified by the fact that due to the higher neuronal activity (related to the increase in CBF), more glucose is consumed. Indeed,

Figure 3.7 shows how glycolysis induces a 220% increase in lactate and a respective 98% increase in CMR_{glc}.

Ultimately, Figure 7.2 highlights that even a small increase in CBF results in a decoupling between the metabolic rate ($CMRO_2$ and CMR_{glc}) and the supply ($O_{2,cap}$ and GLC_C). Indeed, a 5% increase in CBF appears to be the threshold where vascular supply can meet tissue demand in the absence of an active vaso-regulatory mechanism. Therefore, this analysis served as the foundation for suggesting the need for a fast and active regulatory mechanism, such as pericyte cell activity. Table 3.3 presents a summary of all the flow-dependent percentage increases of nutrient demand in the tissue and nutrient supply in the capillaries.

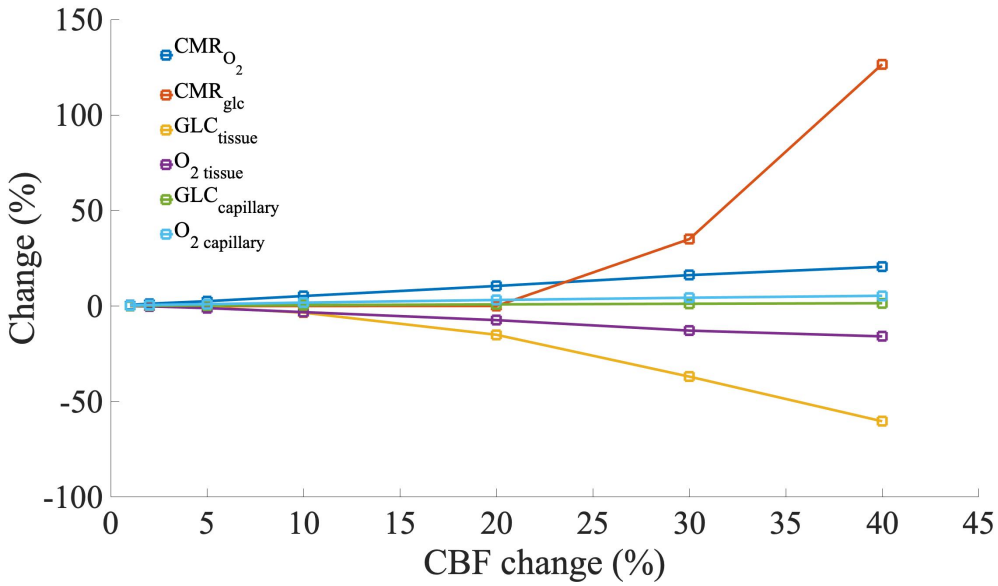

Figure 7.2: Metabolic parameters variability resulting from CBF increase.

7.2.2 Oxygen

Strong evidence [122], [123], [124] supports the notion that hypoxia plays a key role as a CBF regulatory mechanism. During neural activation however, $CMRO_2$ increases by a relatively small fraction compared to glucose metabolism. Experimental studies in humans by Frahm et al. (1996) [83] have shown that for every 50% increase in glucose metabolism, oxygen consumption increases by about 5%. Similarly, in a study on $CMRO_2$ variability in the human visual cortex upon neural activation,

Fox et al. (1988) [87] shows that a 48% increase in glucose consumption relates to a 8% increase in $CMRO_2$.

These values are in good agreement with our computational model's result shown in Figure 3.6, where for every 50% increase in CMR_{glc}, $CMRO_2$ increases by about 6%. Furthermore, the simulation's results correspond to the experimental data on pericyte activity that show an average 6% increase in $CMRO_2$ as a result of neural activation and capillary dilation (see Figure 4.37).

The difference in the magnitudes of the metabolic increases for glucose and oxygen, as well as the difference in the time of the response, indicates that there is a likely decoupling between the two. Table 3.3 highlights the non-linear relationship between the increase in $CMRO_2$ and CMR_{gluc} and Figure 3.7b illustrates how without an active regulatory mechanism, neither oxygen nor glucose can regulate CBF. Figure 3.7b also shows that $CMRO_2$ reaches a peak saturation much faster than CMR_{glc} (i.e. about 1 minute compared to 30 minutes). This suggests that oxygen is a more suitable parameter to be considered in the modelling of cerebral autoregulation. Nevertheless, it should be noted that CA is intrinsically a short-term regulation mechanism and that glucose likely plays a role in regulating long-term (i.e. more than 5 minutes) changes in CBF.

Within the bifurcating network shown in Section 5.2 the highest drop in oxygen partial pressure was found to occur in the last three generations of the arterioles and the capillary generation. These generations are also the ones supplying the largest volume of tissue, as shown in Figure 5.2. This further strengthens the hypothesis that compared to large vessels, the microvasculature plays a dominant role in the effective nutrient supply to the tissue, as both hypoxia and ischaemia are associated with an insufficient oxygen supply. [124]

Adding pericyte activity as a further variable in the quest for defining a physiologically representative CBF regulation model, once again highlights the essential role of the capillary bed as a regulatory mechanism. Indeed, literature data [37] suggest that the majority of contractile pericytes are positioned along the first generation of capillary vessels. The experimental analysis presented here showed

how pericyte-induced capillary dilation and relaxation resulted in a 6% $CMRO_2$ increase in about 5s (see Figure 4.37). Comparing this to an absence of pericytes, where the increase in oxygen metabolism is not driven back to the baseline value, highlights the case for their effectiveness and role in nutrient supply regulation.

Within the mathematical model of the whole brain vasculature introduced in Chapter 5, changes in oxygen content within the tissue (see Figure 6.5) have been shown to be slow relative to the changes in blood flow (see Figure 6.7). This result differs when considering an individual vessel of the microvasculature (see Figure 4.37 and Figure 4.24) and possibly even the microvasculature network in its entirety. Here, the changes in $CMRO_2$ occur at a much faster rate ($2s$ compared to the $8s$ in a whole brain model) and the ratio of CBF to $CMRO_2$ change is 1:1. This could be justified by the activity of pericyte cells, whose proximity to the neurons enables a fast change in vessel diameter. Moreover, a faster response of small vessels compared to large vessels, supports the now widespread notion [41], [125] that an early stage of blood flow regulation in response to metabolic and myogenic stimuli occurs within the microvasculature.

An interesting result was also found from the OEF calculation. As defined by Equation 4.8, when the change in CBF is larger than the change in $CMRO_2$, OEF decreases. Figure 4.44 shows how OEF decreases for 5 s during the stimulus and takes an additional 6 s to recover the baseline value after the end of the stimulus. This observation allows us to derive two key conclusions. The first is that in the absence of an active regulatory mechanism, $CMRO_2$ can can only increase by up to 5% where CBF is able to match it. This is the hypothesis that was drawn from Figure 7.2 and that supports the experimental results of pericyte activity that yielded the insights on $CMRO_2$ and CBF increase upon neural activation.

The second conclusion that we can draw from the OEF study is that the total response time for variations in oxygen partial tissue pressure is 10.8 s, which is too slow for an effective CA. This corresponds to the value yielded by the dynamic analysis of the oxygen feedback-based (F_1) model (Figure 6.7) and to the study

by Payne (2018) [57] where the oxygen delivery from the vasculature to the tissue was found to be dependent on a time constant of about 6 s.

7.3 Methods

This study aims to elucidate the relationship between metabolic demand and CBF regulation by defining a mathematical model that replicates physiology reliably. To create such a model, both experimental and computational tools were needed. As a large part of the the CBF regulatory mechanism is attributed to pericyte cells whose evidence of capillary dilation only made a relatively recent appearance in the literature, an experimental model was used to define their behaviour. Subsequently, their activity was translated into mathematical formulations that were incorporated in the computational model of the human brain vasculature.

7.3.1 Experimental procedure

While in most instances mice data drastically differ from human data, in the case of pericyte-induced capillary dilation, the translatability of the two data sets is an acceptable first approximation. Indeed, the ratio of pericyte to endothelial cell in mice corresponds to the ratio found in humans (i.e. 1:3) and is therefore, as suggested by numerous authors [126], [127] a good proxy. Since we are only focusing on the local diameter change of single capillaries, the difference in the network distribution of vessels in mice and humans is not directly relevant.

The goal was to determine the relationship between the change in capillary diameter and oxygen metabolism (through CBF) in the surrounding tissue. Due to experimental limitations, it is however not possible to assess vessel trace and CBF changes simultaneously. Hence, two sets of data were used and the measurements of the diameter change were done separately from those of CBF change but following the same procedure outlined in Chapter 4.

From the full range of capillary diameters ($2 - 12\mu m$), only vessels in the range of $6 - 10\mu m$ were considered. While acknowledging that vessels outside of the established acceptable range are also classified as capillaries, the network model

presented in Chapter 5 is based on vessel dimensions extrapolated by Zweifach et al. (1974) [102], Bohlen (1984) [103] and Intaglietta et al. (1971) [128], where vessels in the capillary bed have a diameter of $8\mu m$. Hence, to be able to most accurately translate the experimental results into the model, the capillary diameters had to be similar in magnitude. As the mathematical model includes neural activation on which pericytes rely, the experimental setup consisted of visually stimulating the mice. This caused neural activity spikes which resulted in Ca^{2+} peaks which could be detected with probes.

7.3.2 Modelling approach

The cerebrovascular model presented here is a whole brain model where large arteries and veins are modelled as an electrical circuit model and the microvasculature is a bed of 13 generations of bifurcating vessels (see Figure 5.1). As discussed in Chapter 2, while lumped parameter models are very commonly used throughout the literature, there are more sophisticated methods to study the macrovasculature in the regulation of CBF (e.g. 3D models considering the vessel geometry). These alternative techniques allow us to gain insights on the behaviour of the vessel wall (i.e. deformability) and the role of spatial distribution (i.e. the relationship between vessel depth and CBF regulating abilities). However, this was not the scope of the model defined in Chapter 5, where an electrical equivalent model was used as a bridge between ABP changes and nutrient supply in the microvasculature.

The literature [129], [57], [41] strongly supports the notion that the microvasculature plays a crucial sensory role for changes in the metabolic demand of the tissue, which in this study, is considered to be the primary regulator of CBF. Hence, a model that would allow for a more precise investigation of metabolic demand in the tissue and small vessel supply, was designed. The bifurcating network model representing the microvascular bed was extensively validated with data found in the literature (i.e. vessel diameter, length and thickness), as outlined in Chapter 4. Moreover, choosing to reproduce only bifurcations, therefore neglecting other types of vessel branching (e.g. trifurcations), was based on data by Cassot et al. (2006) [15] which

show that over 94% of vessel branching are bifurcations. The model was particularly useful for comparing the magnitude of CBF regulatory ability between vessel types (i.e. oxygen sensitivity in the arterioles and pericyte activity in the capillaries) but also to highlight the need for an actively regulating microvasculature bed for a fast CBF regulation in the whole cerebrovascular model.

7.4 Computational results

In an attempt to define a physiologically representative model, four possible feedback mechanisms with increasing physiological accuracy were studied. The following sections will discuss the differences of the four feedback models in changing small vessel compliance, blood flow and volume.

7.4.1 Feedback mechanisms

The four feedback mechanisms proposed in Chapter 5 produced insights on the effectiveness of a flow, a metabolic and a neural activation driver for CA. In particular, the differences in the nature of the feedback mechanisms were highlighted in their ability to change vessel compliance and regulate CBF. Under steady state conditions, the models showed how different feedback mechanisms result in a significant difference in compliance saturation and a CA plateau width. Indeed, Table 6.1 shows that the flow feedback (F_0) model has the narrowest CA plateau (38.1 mmHg) and the oxygen model (F_1) has the widest CA plateau (56.6 mmHg). Including pericytes to the model ($F_1 + F_2$) results in a CA width of 41.8 mmHg whereas adding neural activity reduces it further to 31.9 mmHg.

Alternatively, in the dynamic simulation where ABP was increased by 10% from the baseline value, the models' responses differed in terms of CBF peak increase and time. Following the impulse, CBF increased by 23.79% in the flow based model, by 30.58% in the oxygen based model, by 34.33% in the model including pericytes and by 26.32% in the model including neural activation (Figure 6.7). The time responses of CBF are 2 s for the flow based, about 11 s for the oxygen based, 6 s for the oxygen and pericyte driven model and about 4s when neural activity is included

as a further regulator. Potential reasons behind these differences in regulation speed and CBF peak increase are discussed in detail in the following section.

7.4.2 Vessel compliance

For the flow feedback model (F_0) and the oxygen feedback model (F_1), the vessels with an active ability to regulate flow are assumed to be only the small arteries. Hence, the compliance of the vessels is referred to as C_{sa} and is related to changes in flow (Equation 5.31) or oxygen partial tissue pressure (Equation 5.32) through a hyperbolic tangent function. On the other hand, the feedback models including pericyte activity ($F_1 + F_2$) and neural activation ($F_1 + F_2 + F_3$), also include the compliance of capillary vessels. As outlined in Section 5.3, the function describing the compliance of capillary vessels was extrapolated from the experimental data on pericyte-induced capillary diameter variation shown in Chapter 4.

Steady state

Figure 6.1 highlights the difference in vessel compliance sensitivity, showing how the flow (F_0) and the neural and metabolic ($F_1 + F_2 + F_3$) models have the highest compliance sensitivity. This means that they present the highest peak of the compliance variation in the narrowest plateau range (Table 6.1). On the other hand, the C_{sa} for the oxygen feedback (F_1) and the pericyte feedback ($F_1 + F_2$) model are very similar in both the range of ABP before peak compliance saturation is reached. Being a function of the change of blood volume and pressure, experimentally quantifying vessel compliance is very difficult. Hence, the change of blood volume of regulating vessels over a wide range of ABP was studied. Figure 6.2 highlights how volume decreases for ABP below baseline and increases when ABP is above the baseline value. The negative change in vessel volume is greater than the positive change across all four feedback mechanisms, further strengthening the hypothesis that vessels are better at constricting than at dilating, under extreme ABP conditions.

Dynamic state

In the flow based model (F_0), a 10% increase in ABP results in a 20.27% decrease in C_{sa}, settling to a new baseline level in about 2 s. Compliance of small arteries in the oxygen feedback model (F_1), C_{sa} drops by 6.86% and settles to a new value in about 8 s. Figure 6.6 highlights the differences in vessel compliance change in terms of magnitude and speed of change. As C_{sa} is linked to the oxygen partial tissue pressure, the dynamic change of p_t was also investigated.

Figure 6.5 shows how p_t increases by 18.93% and settles to a new 2.62% higher baseline in about 6 s. The time of the response reflects the experimentally determined local change in $CMRO_2$ (see Figure 4.37) and therefore provides a further link between the modelling results and the experimental measurements of pericyte-regulated CBF and oxygen concentration in the tissue. Furthermore, the fact that p_t settles to a higher baseline value compared to the one prior to stimulation corresponds to experimental data showing an increased $CMRO_2$ baseline after stimulation (see Figure 4.37).

Including pericyte activity and therefore extending the ability to actively vary the vessel diameter also to capillaries, the small vessel compliance C_N drops by 19.48% in about 6 s for the $(F_1 + F_2)$ model. Finally, including neural activation sensitivity as a vessel compliance regulator, changes C_N by 19.49% in about 4 s (see Figure 6.6). These results suggests that oxygen might play a prevailing role in regulating the saturation of vessel compliance, while pericytes play a more important role in regulating the speed of the response, as outlined by the dynamic regulation of CBF in Figure 6.7.

Buxton (2010) [130] supports the hypothesis that metabolic regulators, such as $CMRO_2$, act as slow modulators of CBF peaks caused by neural activity. On the other hand, pericytes are characterised by a fast active response [40] whose effect is magnified by their elevated number in the microvasculature bed. Furthermore, previous studies [131], [132] suggest that in addition to their active role, pericytes also have a passive CBF regulation ability as their activity causes a reduction in

the vessel wall stiffness, allowing for an easier passive dilation. Further implications of pericyte activity are discussed in detail in Section 7.5.

7.4.3 Blood flow

Changes in CBF were studied in Chapter 6 under static and dynamic conditions. The steady state CA plateau can be replicated by all four feedback mechanisms such that it fits experimental data well. However, the more interesting condition is the dynamic analysis, as it enables the comparison of the speed of the response along with the magnitude of the CBF modulation ability of each feedback mechanism.

Steady state

Under steady state conditions all the feedback models present a clear CA curve and fit the experimental data [110], as shown in Figure 6.3. Table 6.1 highlights the differences in the plateau of CA in each of the four feedback scenarios, showing the widest ABP range for the oxygen (F_1) and the pericytes ($F_1 + F_2$) model. Furthermore, beyond the limits of lower and upper regulation points, these two feedback models present CBF curves that saturate less steeply compared to the other feedback models. Indeed, it is the models that rely on the feedback of flow (F_0) and neural activity ($F_1 + F_2 + F_3$) that present the highest CBF change values for 180 mmHg of ABP (342% and 146% of CBF increase respectively).

The width and slope of the CA plateau are still a controversial topic, given their dependency on numerous parameters (e.g. age, gender) [133] and difficult reproducibility because of the variety of different measurement methods [134]. Hence, choosing a suitable data set for the validation of the model presented here is not a trivial task. Moreover, the model presents in Chapter 5 also relies on animal data (i.e. pericyte activity in mice), making the validation of the steady state CA not the most insightful way of evaluating the model's ability of representing human physiology.

However, as steady state CA is only a short-term regulating mechanism, the more interesting regulation happens under dynamic conditions, which will therefore be

discussed more in detail. Experimental data of CA in humans [135], [30], [136] suggests that the width of the CA plateau is indeed more narrow compared to the CA plateau found in animals, with vessel compliance saturating more promptly above the ULA, compared to the saturation of vessel compliance below the LLA. This would suggest that vessels are more efficient at constricting than at dilating, in critical conditions of ABP.

This hypothesis can physiologically be justified by the fact that elevated (i.e. beyond the ULA) blood pressure in small vessels, such as capillaries, can damage the endothelial layer. In the latter, blood pressure induced wall damage is even more critical as the vessel wall is very thin and is effectively the only layer that separates the blood flow duct from the tissue and other organelles that line the capillary walls. It is therefore no surprise that numerous studies have shown that a tight CBF regulation is essential for maintaining an intact microvasculature and that lesions in the capillary bed quickly lead to irreversible damage to the brain tissue (e.g. stroke) and vasculature (e.g. aneurysms). [137]

Dynamic state

Under dynamic conditions, comparing the four feedback mechanisms enabled the quantification of each of the models' reaction speed and its ability to mitigate a high increase in CBF. In particular, the response time was defined as the elapsed time between the CBF increase onset and the first return to the baseline value. Figure 6.7 shows that going from the fastest to the slowest model, the reaction times are as follows: flow (F_0) feedback with a 2.3 s response time, neural and metabolic ($F_1 + F_2 + F_3$) feedback with a 4.1 s response time, pericyte feedback ($F_1 + F_2$) with a 5.8 s response time and the oxygen feedback (F_1) being the slowest with a response time of 10.8 s.

Table 6.4 summarises all the characteristic values of (i.e. CBF peak and response time) of each feedback mechanism, showing that in order of decreasing magnitude, a 10% increase in ABP results in a CBF peak that is 34.33% for the oxygen and pericytes model ($F_1 + F_2$), 30.58% for the oxygen (F_1) feedback, 26.32% for the one

involving neural activity ($F_1 + F_2 + F_3$) and is lowest for the flow model (F_0) which presents a 23.79% peak increase in CBF.

Comparing these values with experimental data on CBF modulation in 11 healthy humans [115], it was concluded that 2 out of 4 of the feedback models are in agreement with the experimentally established range of CBF peak increase as a result of brain activation (11.2%-27.8%). The flow (F_0) and the neural activity ($F_1 + F_2 + F_3$) model both fit human data on pressure-driven CBF modulation well, however as the flow model is not the physiologically representative one, further analysis (i.e. on CBV, $CMRO_2$ and BOLD) was only conducted for the model including neural feedback.

Nevertheless, it should be noted that the experimentally determined wide range of CBF modulation, indicates once more how under the same conditions, a range of healthy physiological responses is found across the population. The same study by Parthasarathy et al. [115] also provides data on the response time, concluding that a healthy response time is in the 3-5 s range, which fits the feedback model ($F_1 + F_2 + F_3$) that includes neural activity very well.

As the baseline of a healthy ABP can slightly vary across the population, the sensitivity of the model to changes in the baseline operating value of ABP was tested. Figure 6.8 shows that when ABP is below the original baseline value (<100mmHg), the dynamic peak CBF increase resulting from a 10% increase in ABP is lower compared to the scenario when $\overline{ABP}$ is 100mmHg. Furthermore, in the case of a new baseline ABP below the original one, CBF settles to a new value that is higher compared to the initial state. This indicated that CBF is not effectively modulated, as the active regulation of vessels is not able to return CBF to the initial state.

Similarly, for baseline ABP values higher than the original (>100mmHg), the dynamic CBF response to a 10% increase in ABP does not result in an effective CBF modulation, as CBF settles to a new value that is higher than the value prior to the stimulus. Moreover, Table 6.3 highlights that the response time of the

$(F_1 + F_2 + F_3)$ model increases when $\overline{ABP} \neq$100mmHg.

In Chapter 6 the cerebrovascular resistance was defined as a further tool of comparison between the feedback models. Figure 6.10 shows that the 10% increase in ABP corresponds to a CVR in the 2-3% range across all four feedback models which is in good agreement with human experimental data [115] where the range is 2-10%. Figure 6.11 shows the relative CVR rates of change ($drCVR/dt$) of each model, where the slope of each line served as a further variable of comparing the performance of each feedback.

By establishing the rate of change of the vascular reactivity, it was possible to define the ROR of each model (see Equation 6.1), which represents the percentile rate of change of the vasculature resistance per second. Ultimately, it was found that in order of increasing magnitude: the ROR across the models is lowest for the oxygen model (F_1) with a 2.7%/s value, increases to 5.5%/s in the neural activity model ($F_1 + F_2 + F_3$), reaches 7.3%/s for the oxygen and pericytes model ($F_1 + F_2$) and is highest in the flow model (F_0) with a 10%/s ROR.

While the ROR analysis presents the flow feedback (F_0) based model as the one with the most rapidly changing resistance, it can be disregarded because of its lack of physiological representability. Hence, the most interesting comparison of ROR values is the one between the feedback model that includes pericytes ($F_1 + F_2$) and the model that includes neural activation ($F_1 + F_2 + F_3$). While the analysis showed that for a ($F_1 + F_2$) feedback the resistance of the microvasculature changes by 7.3%/s to compensate for a 1% change in ABP, compared to a lower (5.5%/s) change in the neural model, the higher rate can be attributed to a higher CBF peak (see Figure 6.7).

Indeed, the CBF increase for the feedback model that includes pericytes is 8.1% higher than the CBF peak that includes neural activation and the difference in response time is about 2 s. Hence, the large delta in CBF peak and the small delta in response, explains the higher ROR for the oxygen and pericytes model.

With the exception of the flow feedback mechanism (F_0) whose nature is not physiologically representative, all other 3 feedbacks replicate a cascade of physiological sequences that result in a variation of the vessel compliance. It is important to note that of the last 3 feedback models, one does not exclude the other. Instead, they complement each other up to the final feedback definition ($F_1 + F_2 + F_3$) where the neural activity is used to induce pericyte activity in the capillaries and subsequently oxygen sensitivity in the tissue.

Ultimately, the comparison of the feedback methods highlighted the importance of each regulatory variable but even more so, underlined that physiological CBF regulation is likely to depend on the collective contribution of each feedback variable. Indeed, the oxygen sensitivity of the tissue is a key driver of the saturation of the arterial compliance and pericytes act to increase the speed of the total response by giving the capillary bed an active role in the CBF regulation mechanism. Neural signalling increases the speed of the response even further, ultimately obtaining a physiologically representative response (see Figure 6.7).

These conclusions are in agreement with the literature [24] which suggests that metabolic messengers play a key role in linking the demands of the tissue to the supply by the vessels but that alone, they are too slow to be relied on in an organ where the coupling between demand and supply is as time-sensitive as in the brain. Indeed, one of the crucial roles of neural signalling is the speedy transport of information. A further aid to this intricate exchange of information is the geometry of the microvasculature bed, that ensures that neurons are in close proximity of the astrocytes and pericytes that subsequently signal changes in vessel diameter to the surrounding capillaries.

7.4.4 Blood volume

The change in arterial, venous and total blood volume over a wide range of CBF is shown in Figure 6.4 for the neural feedback ($F_1 + F_2 + F_3$) model. Animal experimental data [114] show a good fit with the model's predictions, where a 25% increase in CBF corresponds roughly to a 15% increase in CBV. Only the neural

feedback model was validated with experimental data as it is the one that most closely represent physiological reality, as discussed above.

The peak CBV increase following the 10% change in ABP was identified for each feedback mechanism (see Table 6.4). In decreasing order of magnitude, the CBV peak change in the oxygen and pericytes model ($F_1 + F_2$) is 17.57%, 16.71% for the oxygen model (F_1), 14.88% for the neural model ($F_1+F_2+F_3$) and is lowest (13.04%) in the flow model (F_0). These values correspond to the respective changes in CBF with an almost linear relationship, contrasting Grubb's non-linear expression that relates CBF to CBV (see Figure 6.4). Moreover, the changes in arterial and venous volumes were investigated separately, with the aim of quantifying the contribution of each vessel type to the total change in CBV. It was found that the largest change in volume occurs in the arteries, and that the increase is in good agreement with the experimental data presented by Lee et al. (2001) [114]. The large change in arterial volume can be attributed to the high variability in vessel compliance, which actively contributes to regulate CBF, compared to the passive response of the veins.

7.4.5 $CMRO_2$ and BOLD

The computational model presented in Chapter 5, relies on metabolic signalling for CBF modulation. In particular, the final model comprising neural activation ($F_1 + F_2 + F_3$) bridges the gap between $CMRO_2$ and capillary response, by introducing a neural activity variable. Hence, as the most complete and physiologically accurate model of the four, it was validated against experimental data on $CMRO_2$ and CBF change.

Figure 6.13a shows how a 10% ABP change and the respective 26% CBF change correspond to a 9.10% increase in $CMRO_2$.

This result is in good agreement with experimental data by Fernández-Seara et al. (2016) [109], that shows that in a cohort of five healthy male subjects, stimulation resulted in an average 12.5% $CMRO_2$ increase.

Moreover, in Chapter 4 it was found that pericyte activation resulting in capillary dilation leads to an approximately 6% increase in $CMRO_2$ in the surrounding

tissue (see Figure 4.37). It should be noted that the 3% delta between the experimentally determined $CMRO_2$ increase in brain tissue and the computationally determined $CMRO_2$ change can be attributed to the difference between local and global metabolic changes. Ultimately, the data on metabolic increases induced by stimulation of the motor cortex reported by Fernández-Seara et al. (2016) [109], are global quantities, which show good correspondence with our computational results based on the neural feedback model.

The BOLD signal time course can serve to give insights on the ability of metabolites to regulate CBF and their influence on the overall response time of the system. However, it should be noted that changes in the BOLD signal are an indirect measure of the underlying metabolic interactions. Here, the BOLD signal was studied as a function of CBF, CBV and $CMRO_2$ (see Equation 5.36) and the effect of the variability of a wide range of values for the maximum BOLD increase (M_{BOLD}) was investigated.

With the feedback model including neural activation ($F_1 + F_2 + F_3$), a 0.76% BOLD increase resulting from a 26% increase in CBF (see Figure 6.13b) was found, which is in good agreement with human experimental data [109], [116]. Figure 6.14 shows the BOLD change over a wide range (1-10) of M_{BOLD} values, as the exact parameters that govern the BOLD signal (see Equation 5.36) are yet to be defined.

Moreover, an interesting result drawn from Figure 6.14 is the increasing undershoot during CBF modulation. Indeed, as M_{BOLD} increases, so does the undershoot peak value and the time it takes to settle back to baseline. This result is in agreement with experimental data on human brain activation measured by Frahm et al. (1996) [83]. A possible explanation for this relationship between the M_{BOLD} value and the undershoot magnitude, could be that an elevated $CMRO_2$ persists even after CBF returned to baseline. In Chapter 4 it was experimentally shown that $CMRO_2$ modulation is slower than CBF modulation on a local level (see Figure 4.37 and Figure 4.24), which further supports the hypothesis of a delayed oxygen consumption change. Therefore, a slow $CMRO_2$ adaptability would suggest that the undershoot in the BOLD signal is of metabolic origin.

Alternatively, the BOLD undershoot could also be explained by the undershoot of CBF (see Figure 6.7). It is however worth noting that in the computational model presented here, CBF changes are also driven by $CMRO_2$, which therefore might be an indirect influence to the BOLD signal undershoot. Ultimately, disentangling CBF and $CMRO_2$ changes from a single output like the BOLD signal is not a trivial task, calling for the use of multi-modal measurement techniques.

7.5 Pericyte activity

The experimental part of the study had the scope of quantifying the ability of pericytes, which are Ca^{2+} excitable cells, to vary the diameter of capillaries. Two distinct sets of data were used, the first set of 26 vessels was used to investigate changes in diameter and the second set of 46 measurements was used to study $CMRO_2$ variations in the imaged tissue. From a total of 26 vessels whose diameter change was analysed, 8 fitted the selection criteria highlighted in Section 4.2.2 and were subsequently used for the development of the mathematical model. Similarly, out of the 46 measurements used to study CBF variability induced by pericytes, 23 were selected for the analysis.

The two selection criteria were vessel diameter and vessel responsiveness to visual stimuli. The diameter was chosen in order to fit the capillary bed vessel diameter within the model, while responsiveness was defined through a coefficient of variance threshold ($CV \leq 1\%$) (see Table 4.3). One of the reason 14 of the 26 vessels were not responsive could be that the pericytes sitting on the capillary walls did not have dilation capabilities.

Indeed, it was shown [138] that sometimes different types of pericytes can respond to the same fluorescent dye, making it impossible to distinguish them in imaging. Figure **??** shows the vessel trace of a capillary whose diameter does not change in response of a visual stimulus. Experimental studies [139], [45] suggest that non-contractile pericytes express Ca^{2+} concentration sensitive channels in order to generate depolarising currents that act as pace-setters for vasomotion in the upstream arterioles.

7.5.1 Large and small capillaries

As outlined in Section 7.3, capillaries in the diameter range $6-10\mu m$ were considered for the modelling study. These capillaries were defined in Chapter 4 as large vessels, whereas the capillaries in the $2-6\mu m$ diameter range can be defined as small vessels. A model fit was defined for both vessel categories and statistically different responses were identified, in terms of peak vessel dilation and imaging depth.

Diameter change

Upon stimulation, large capillaries reach an average peak dilation of 2.62% from baseline (see Figure 4.19a) and small capillaries reach a higher peak dilation value of 2.52% from baseline (see Figure 4.19b). This statistically significant difference in diameter suggests that larger capillaries have a larger potential to vary diameter. Several authors [140],[40] support the notion of first order capillaries (i.e. the generation of vessels below arterioles) having a stronger ability to vary vessel diameter, compared to both arterioles and smaller capillaries.
The reason for this could be that pericytes in the middle capillary bed (where the diameter is smaller) don't possess the morphological ability to contract capillaries. [45] Second order capillaries are likely to contribute to CBF regulation through an entirely different mechanism, such as the decrease of the vessel's stiffness during neural activity, therefore allowing for an easier passive dilation. [132],[141] Moreover, experimental data by Anzabi et al. (2021) [94] confirm that the haemodynamic response originates in the capillary bed and that first order capillaries (i.e. those with a larger diameter) present the most significant and rapid changes in diameter.

Interestingly, Figure 4.5a shows that following Ca^{2+} stimulation, the capillary diameter initially constricts by about 0.7%, which may be explained by the fact that at rest, pericytes are in a contracted state. [140] This means that before dilating the capillary, pericytes need to actively overcome the depolarising effect of Ca^{2+} ions. The fitted functions of the vessel trace in Figure 4.19a and Figure 4.19b highlight that the dilation occurs significantly faster than the constriction. Indeed, the dilation happens in about 1 s while returning to baseline diameter from the point

of peak dilation takes about 6 s for large and small capillaries. This dissonance in response time is in accordance with the literature [142],[92] and is explained by the fact that pericyte dilation is a stimulus-induced state, making it a faster reaction than the passive relaxation of pericytes.

A frequency analysis using Welch's method was performed, with the aim of investigating the regular oscillating signals in the vessel trace. Next to the unnormalized vessel trace where a peak for the vasodilation frequency at 0.1 Hz is to be found, a normalized vessel trace was also computed in order to more clearly present the distinction between peaks. Large vessels ($6 - 10\mu m$) present a distinguishable peak at 0.1 Hz, indicating that the predominant signal can be attributed to vasodilation (see Figure 4.11).

Instead, small capillaries ($2-6\mu m$) present more frequent peaks of similar magnitude within the 0-1 Hz frequency range (see Figure 4.12). This can be attributed to the fact they exhibit about half the diameter change of large vessels (es defined in Section 4.2.2), which in addition to the fact that they have a much smaller baseline diameter, makes them more susceptible to external vasomotion stimuli. Furthermore, the average vasodilation presented by small capillary vessels is about $0.2\mu m$, thus approaching the resolution limit of the experimental apparatus.

A depth-dependent frequency analysis is also presented in Chapter 4, it is however not possible to derive a conclusion on the characteristic behaviour of vessels at different depths for two reasons: firstly, the number of vessels in each depth category is different (sometimes a single vessel is present, as in the $0-50\mu m$ depth range) and secondly, the vessel diameter is not evenly distributed across the depth ranges (only large vessels in the $150 - 250\mu m$ and $250 - 350\mu m$ depths). Hence, as extensively discussed in Section 7.6, the low number of analysed vessels is a significant limitation. Ultimately, the frequency analysis for each vessel is presented in the Appendix.

Imaging depth

The 12 vessels (8 large and 4 small) analysed in Chapter 4 were found to lie in different imaging depths. All the depths were categorised in four groups: $0 - 50\mu m$,

$50-150\mu m$, $150-250\mu m$ and $250-350\mu m$. Figure 4.20 shows the fitted curves for each imaging depth category. A clear difference between peak dilation values was found and is presented in Table 4.2. The highest capillary dilating ability was identified in the imaging depth range $250-350\mu m$ (see Table 4.1). Based on these data, it is difficult at this stage to conclude whether this distinguishing dilating capacity should be attributed to the depth at which the vessels were situated or their diameter. Indeed, all the vessels in the $250-350\mu m$ range were large capillaries $(6-10\mu m)$ which we found to have a greater vasodilatory ability compared to small ones (see Section 4.4).

Figure 4.21 shows the time constant variation per imaging depth and Table 4.5 is a comprehensive list of all the values. T_α shows a decreasing trend with increasing imaging depths while the other time constant parameters (T_β and T_γ) do not present a clear trend. However, definite conclusions on the nature of the relationship between the time constants and the imaging depth can not be drawn as the number of vessels is not the same per imaging category and is too low for statistical analysis. Indeed, Table 4.1 shows that there is 1 vessel in the $0-50\mu m$ depth, 6 vessels in the $50-150\mu m$ depth, 3 vessels in the $150-250\mu m$ depth and 2 vessels in the $250-350\mu m$ depth.

Moreover, as we concluded that the magnitude of the baseline diameter of the vessel plays a role in defining its peak dilation, we can not formulate a conclusive statement on the role of the imaging depth as only small vessels are found in the $0-50\mu m$ depth, only large vessels are found in the $150-250\mu m$ and $250-350\mu m$ depths and a combination of both is found in the $50-150\mu m$ depth.

7.5.2 Blood flow and volume

As outlined in Chapter 4, two sets of experiments were conducted with the aim of determining first the diameter change and secondly the change in CBF induced by the visual stimulus. As the experimental setup used to quantify local metabolic changes induced by a visual stimulus does not allow for spacial information to be gathered, the net change in CBF and Hbt (assumed to represent CBV) were

recorded.

The measurements were conducted in 5 mice, each animal contributing a different number of viable measurements. All experiments were conducted under the same conditions and no variability between sessions was detected (as reported in Supplementary Figure 10 of Shaw et al. (2021) [92]). Thus, the different number of viable measurements between animals cannot be attributed to a difference in experimental procedure. It can be hypothesized that in instances where no metabolic change was measured, the capillary vessels populating the tissue in the selected imaging window were too small (diameter below $2\mu m$) and thus could only induce a CBF change too small to be detected by the probe. As shown in Chapter 4, the vessel's baseline diameter greatly influences its response ability (i.e. dilation) to visual stimuli.

It was found that upon activation, pericytes induce a 5.53% increase in CBF through a capillary dilation of about 2.5% from baseline. Similarly, Figure 4.25 shows a 3.25% increase in CBV upon stimulation. Using the relationship described by Grubb et al. (1974) [95], the α exponent was identified as 0.73 as being the value that fits the data best (see Figure 4.36). It is worth noting however that the Grubb's exponent value strongly depends upon the conditions under which CBF and CBV are measured. [143]

The literature presents contrasting opinions on the magnitude of the α coefficient, with values ranging from 0.13 [143] to 0.73 [50] and thus, the experimentally determined value by Zheng et al. (2005) [50] which was most closely in accordance with the pericyte activity data presented in Chapter 4 was chosen. The relationship between CBF and CBV is a strongly non-linear one and the results shown in Figure 4.36 should therefore be carefully considered, as the relationship approaches a linear one due to the high exponential value of α. It should also be highlighted that the values of CBF and CBV are experimental values representing changes in local tissue metabolism on a small scale, and thus do not represent the global CBV and CBF values for which Grubb's original definition was intended for.

7.5.3 Calcium signalling

Next to $CMRO_2$ increase in the tissue, the increase of Ca^{2+} concentration is an alternative measure for the net neuronal activity. An advantage of the experimental setup that the pericyte activity data were derived from is the fact that the data correspond to a non-invasive neural stimulus. Here, the Ca^{2+} increase is a result of a visual stimulus and was measured in vivo. The reason for this is that the scope of this experimental approach was to closely replicate and study the physiological phenomenon of neurovascular coupling in its natural state.

The Ca^{2+} concentration-induced pericyte cell activation can be considered as a bridge between the tissue's metabolic demand and the microvascular response. The hypothesis that Ca^{2+} plays a crucial role in coupling neural and metabolic activity is supported by numerous authors [144], [145] who also imply that alterations in Ca^{2+} concentration strongly correlate with cognitive deficits. [146], [147]. Given the experimental and clinical evidence of the impact of fluctuations in Ca^{2+} concentration, the increase in Ca^{2+} in response to neural activation (see Figure 4.22d) was studied and the differences in Ca^{2+} increase observed in the tissue surrounding large and small capillaries were highlighted.

The experimental analysis presented in Chapter 4 enabled the quantification of Ca^{2+} fluctuations in the tissue, both in terms of response time and concentration. The calcium increase was quantified across all 12 responsive vessels. Figure 4.22 illustrates the Ca^{2+} concentration peaking within 1 s of neural activation at $t = 0$ and settling back to a new baseline value within 1 s. This quick (2 s) response was shown to differ in magnitude for large and small capillaries (see Table 4.6). Indeed, the peak Ca^{2+} increase for large capillaries is 28.77% while it is 15.84% for small capillaries.

This almost 2-fold difference in peak response suggests that large capillaries might be able to dilate more because their pericytes are stimulated with a stronger Ca^{2+} increase. One reason for a larger increase in Ca^{2+} in the tissue surrounding large capillaries could be the proximity of neurons to larger capillaries. Indeed, experimental data [40] suggest that proximity to neurons is a key factor for a fast

vessel response.

Ultimately, it should also be noted that the diameter change of the capillaries has been solely associated with the visual stimulus-induced Ca^{2+} increase and not to vasomotion, as when the vessel trace was shuffled and decoupled from the Ca^{2+} trace, dilations occurred less frequently (i.e. 5.1% of the time). It is for this reason that it is possible to confidently establish the direct relationship between the visual stimulus that leads to a Ca^{2+} concentration-induced capillary dilation and the local increase in metabolic demand (i.e. $CMRO_2$ increase shown in Figure 4.37).

7.6 Study limitations

This thesis is an attempt to mathematically define the intricate process of CBF modulation in order to identify and quantify the role of three dominant regulating mechanisms. To do so, a series of experimental and computational research techniques was defined by weighing the benefits of an approach against its limitations. While the successful outcomes of both the experimental and the computational analysis were described above, the limitations of the used methods are now outlined here.

7.6.1 Experimental

In the experimental model, 3 primary limitations should be addressed. The first and most obvious compromise for the experimental part of the study was using mice data on pericyte cell activity for a human whole brain vasculature model. Previous studies [40], [38] however, advocate for the good translatability of data from mice pericytes to humans because of the same pericyte-to-endothelial cell ratio (3:1) in both species. As the scope of our study was to quantify the vasodilation of single isolated capillaries, the differences in network geometry between mice and humans were felt to be of no significant importance. A review on the clinical translatability of pericyte data by Cathery et al. (2018) [127] discussed the potential of in vitro studies and the translatability of results between pericytes found in different organs, ultimately highlighting the strong advantage of in vivo animal studies per pericytes located in the brain.

Secondly, the number of viable vessel responses (see Section 4.2.2) is low, potentially weakening the conclusions on the different contractility ability of small versus large capillaries. It would therefore be necessary to repeat the same experimental analysis for a greater number of vessels to check the robustness of the conclusions drawn from the data in Chapter 4.

Moreover, it should also be noted that 50% of the vasodilation data stem from Mouse 3 (see Figure 4.2). A known reason for this is that the vasculature geometry of the mouse was favorable for the imaging during the visual stimulation. Indeed, as mentioned in Chapter4, the probe used to track the change in diameter focused on the vessel that most clearly appeared in the imaging window.

Nevertheless, despite a small total number of responding vessels, *all* the vessel responses indicate the same conclusion, meaning that the final results are supported by consistent evidence.

Thirdly, a significant limitation of the experimental validation is the impossibility of measuring diameter and metabolic rate variations simultaneously. Indeed, the imaging methods used to study the response of the animals to visual stimuli can only image either $CMRO_2/Hb$ or Ca^{2+}/vasomotion. This results in 2 sets of data, obtained in different instances, to be compared with each other. Although the experimental procedure is the same in both scenarios, the inability of monitoring all the variables within the same measurement should be noted.

7.6.2 Computational

Defining a balance between physiological accuracy and mathematical feasibility is a common dilemma in computational studies of biological models. Here, the primary 5 limitations of the vascular geometry and the 3 limitations resulting from the definition of the interaction of metabolic variables are outlined.

Model geometry

The first limitation of the model's geometry is that only small vessels were attributed a varying resistance. This was done as the small arteries and capillaries are most

sensitive to metabolic changes in the tissue (see Figure 5.2) and are therefore the primary drivers of CBF modulation within the microvasculature however. However, the thick SMC lining of large arteries allows them to significantly vary their diameter, contributing to an additional CBF regulation. It is possible that the change of resistance of large arteries, which is considered invariant in our model (see Figure 5.1), further contributes to a fast CBF regulation under dynamic conditions.

The second consideration about the adopted vascular geometry concerns the microvasculature network. Given the experimentally determined importance of capillary dilation in Chapter 4, expanding the capillary bed beyond a single generation would be insightful. Indeed, in Section 7.5 the difference in responsiveness of small and large capillaries was discussed, suggesting that the model could be expanded to include capillaries with a diameter below $8\mu m$. This would also enable the computational evaluation of the experimentally determined differences in imaging depth-dependent vessel responsiveness, as smaller capillaries were found in the deeper tissue.

A third limitation regarding the vasculature distribution is the assumption that each vessel of the microvasculature supplies a single independent tissue voxel. In reality however, certain brain areas (e.g. the visual cortex) are known to have a higher vessel to tissue volume ratio compared to others (e.g. the hippocampus). This suggests that the speed of CBF regulation is heterogeneous across different brain areas, as the vasculature density is location-dependent. Experimental studies [92] have shown that the low number of capillaries in some areas of the brain is related to the higher vulnerability to brain hypoxia in those regions. It would therefore be interesting to computationally investigate this phenomenon and to quantify the impact of vasculature density on tissue perfusion. Moreover, the model presented here does not account for nutrient diffusion across tissue voxels, which would further increase the speed of CBF regulation as the nutrient demand would not have to be entirely met by local vascular supply.

The fourth limitation of the cerebrovascular geometry introduced in Figure 5.1 is that it is a complete vasculature model. In reality however, as outlined in Chapter 2,

only about 60% of the population possesses a complete circle of Willis and with it, a complete vasculature network. The assumption of a complete vasculature network could therefore lead to an overestimation of the ability to regulate CBF effectively for sudden changes in ABP. On the other hand, the high variability of vasculature geometry between individuals makes it very difficult to design a model that has the ability to accurately represent the physiology of each individual.

The fifth and final geometrical assumption of the model is the assumption of a constant ICP. The primary reason for this modelling choice is that the parameters governing ICP are largely different from those governing CBF regulation, as defined by Giulioni et al. (1996) [148]. Indeed, to adequately consider ICP, it would be necessary to model the flow of water in the brain and consider the dynamics of the tissue. As the model outlined in Chapter 5 aims to study solely the regulation of blood flow in the brain in relation to the compliance of the vasculature, all other fluid dynamics were neglected.

Parameter definition

Having recognised that it is very challenging to account for all the metabolic players involved in the brain tissue to vasculature communication, choosing between which variables to include in the study and which ones to neglect was a key part of the model development. More precisely, 3 main assumptions limit the results outlined in Chapter 6.

The first limitation is that glucose metabolism was not considered as a vessel compliance regulator, despite being strongly tied with $CMRO_2$. While in Chapter 3 it was computationally determined and experimentally validated that CMR_{glc} is seemingly too slow to play a role in the dynamic regulation of CBF, glucose reserves in the mitochondria serve to satisfy the immediate demands of the tissue. This glucose storage was disregarded and its inclusion could have provided some insight into the slow response of the oxygen feedback model (see Figure 6.7).

The second assumption is an extension of the first, as oxygen storage was also disregarded in the model. Similarly to the glucose storage, the very small oxygen

reserves in the mitochondria could be a way for the tissue to meet an increased nutrient demand caused by neural activity, lasting until the vasculature responds. While experimental studies [40] support the notion that in the absence of pericytes brain tissue quickly becomes hypoxic, including the notion of an oxygen reserve in the form of a time constant that acts upon arterial compliance might have decreased the total response time of both the oxygen and the oxygen and pericyte feedback mechanisms defined by Equation 5.32 and Equation 5.33 respectively.
Ultimately, the third assumption on metabolic variables is the strong dependence on the defined baseline conditions. While some variables like total CBV and baseline CBF are consistently quoted throughout the literature, the range of a healthy $CMRO_2$ and the experimentally determined metabolic increases due to neural activity are quoted as having very wide ranges. [32] This is also the case for the oxygen partial tissue pressure, whose healthy range is 8-60mmHg (with the lower limit being found in the skin [149], so that varying this value within the model would significantly vary the saturation of the arterial compliance. While being a limitation of the model, it is also another example of the great difficulty in designing a model that fits a population whose experimentally determined baseline conditions vary greatly.

7.7 Summary

This chapter discusses the implications of the computational and the experimental results of the study. Firstly, the ability of metabolites to regulate changes in CBF was analysed, ultimately concluding that signalling driven by glucose metabolism is too slow. Indeed, it was found that when CBF increases by 30% the CMR_{glc} increases by about 150%, a change that takes about 5 minutes (see Figure 3.7b). The change in $CMRO_2$ on the other hand is about 10 times faster, making it a better candidate for the metabolic signalling of the change in arterial compliance.

The comparison of the four feedback mechanisms that govern vessel compliance and CBF as a consequence, ultimately yielded that the feedback model that most closely replicates human experimental data is the $(F_1 + F_2 + F_3)$ one. Here, oxygen

sensitivity in the small arteries is combined with pericyte cell activity in the capillaries and neural activation.

Experimentally, the ability of pericytes to regulate capillary diameter, was determined to also be dependent upon the vessel diameter. Indeed, vessels in the 6-10μm diameter responded in half the time by dilating by about 2.62% in about 1 s, compared to vessels in the 2-6μm diameter range which dilated by 2.52% in 2 s. This can be justified by the assumption that large capillaries are closest to the arterioles, and are the ones that experimentally present the largest number of pericytes with dilating abilities.

Ultimately, the study's computational and experimental limitations were discussed, highlighting the assumptions and conclusions that should be strengthened and expanded upon with future analysis. Computationally, it would be insightful to expand the capillary bed of the network model to include smaller vessel generations. On the other hand, the experimental results on the diameter- and imaging depth-dependent capillary dilation should be replicated with a larger vessel number.

Il faut cultiver notre jardin.

We must cultivate our garden.

— Candide (1759), Voltaire

8 Conclusion

Contents

8.1 Synopsis 156
8.2 Result implications 162
8.2.1 Clinical relevance 163
8.3 Future work 165

The majority of currently existing mathematical models of cerebral blood flow autoregulation are flow feedback based. Despite the fact that such models provide results that can be validated with experimental data, the nature of the feedback is not physiologically accurate and therefore can not be regarded as a modelling method that can be used to gain significant physiological understanding of the mechanisms underlying cerebral autoregulation. In order to be clinically significant, new mathematical models need to be designed. Therefore, a mathematical model aiming to define the relationship between the metabolic demand of the tissue and the active vasculature response has been proposed here.

This chapter will briefly summarise modelling practices commonly found in the literature, defining the gap that our model aims to fill. An outline of the computational and experimental techniques used to designed the computational model will follow. Ultimately, the study's results will be summarised and the potential clinical

implications will be discussed, along with the prospect of future research.

8.1 Synopsis

Chapter 1 introduces the clinical need to more precisely understand the tight coupling of blood flow and metabolism in the brain. Quantifying the ability that each regulatory variable has in changing CBF has the potential of providing a clearer picture of how the brain behaves in health and disease. In a time where brain degenerative diseases are the leading cause of disabilities (affecting about 300 M people) and the second leading cause of death (about 10 M people) worldwide [5], it is an imperative for both scientific and governmental institutions to dedicate this research field the resources it needs.
Computational modelling has proved to be an effective research tool, standing out among other research methods for its ethical advantages and cost effectiveness. Indeed, over 50% of experimental studies have proven to be non reproducible, a number that is even higher in the field of biology, where 80% of scientists reported difficulties in reproducing peer-reviewed experimental work. [150] Moreover, as the translatability for animal data to humans is low across all disciplines, with over 90% of animal research failing to be relevant for humans [151], mathematical models are steadily gaining in popularity.
Ultimately, clinical studies [32] have shown a significant variability in cerebrovascular reactivity between individuals of the same age and gender, highlighting the need for patient specific models. Computational tools are therefore currently the only viable investigative tool for broadening our understanding of the neurovascular coupling mechanisms underlying brain health and disease.

Chapter 2 is a concise overview of the anatomy and physiology of the brain. Particular attention was given to describing the vasculature geometry in detail, highlighting the specific role and characteristic function of the arterial, venous and capillary bed. With this basis, the primary regulatory mechanisms that ensure brain homeostasis were introduced. Myogenic, metabolic and systemic factors are

the primary regulators of CBF and changes in one are related to the other, making it increasingly difficult to define and quantify the resulting magnitude of each regulator. These variables can be either local or global in nature, highlighting the heterogeneity of the brain not only in its anatomy but also in its activity.
Ultimately, an overview of various modelling techniques is presented, underlining the fact that the modelling modality strongly depends on the research scope. Indeed, lumped parameter models are commonly used in studies that aim to investigate the brain as a whole, whereas biochemical feedback- and network-models are used to understand the multitude of physiological interactions taking place on a voxel level.

Chapter 3 outlines the haemodynamic laws the proposed mathematical model relies on. Next, an overview of the of the metabolic sensitivity in the neurovascular unit was presented, particularly focusing on oxygen and glucose consumption in the tissue and pericyte cell activity in the capillary beds. The cascade of events from the onset of brain activation and leading up to CBF regulation is discussed and summarised in Figure 3.3.
Finally, the speed of CMR_{glc} change in relation to changes in CBF was studied, drawing assumptions from the model presented by Aubert et al. (2001) [79]. It was concluded that CMR_{glc} change is too slow to be a key regulator in the fast process that characterises the CA, being about 10 times slower than $CMRO_2$ change, as shown in Figure 3.7b. These changes were found to be in agreement with human experimental data [84], [83], ultimately suggesting that glucose plays a role in moderating long-term CBF changes as CMR_{glc} changes are governed by hormones. Moreover, these results highlighted the need for a rapid CBF regulatory mechanisms, ultimately setting the foundation for the inclusion of a pericyte-driven capillary response.

Chapter 4 presents the experimental part of the study, from which the mathematical formulations of active capillary dilation were derived. Two distinct sets of data were used, to determine the capillary dilation and the metabolic activity

of the tissue following neural activation, given the experimental limitation of conducting both measurements simultaneously. The first set was used to investigate changes in diameter and the second set was used to study $CMRO_2$ variations in the tissue.

Conclusively, the increase in capillary diameter established as the result of a visual stimulus-induced pericyte cell activity (see Figure 4.4b) was found to be about 2.5%. Capillary response was then investigated through two different aspects: diameter and imaging depth. To investigate the influence of the vessel diameter on the response, capillaries were divided into large (6-10 μm) and small (2-6 μm) diameter vessels. The fitted curves for diameter change as a result of pericyte activation showed a peak value of 2.44% for large vessels and 2.34% for small vessels (see Figure 4.19b).

Furthermore, the vessel diameter was also accounted for when the Ca^{2+} increase was quantified for large and small capillaries. Indeed, it was found that the Ca^{2+} increase around large capillary vessels is about twice the magnitude of the Ca^{2+} increase in the tissue surrounding small capillary vessels. This significant difference in Ca^{2+} concentration can therefore also be attributed to the difference in dilation ability of each capillary type. An explanation for this phenomenon could be the fact that larger capillaries are the first generation of vessels closest to the arterioles, which are in close proximity of neurons and astrocytes that induce the change in Ca^{2+} concentration in the first place. This assumption is in agreement with experimental data that suggest that the haemodynamic response originates in the capillary bed, with the highest ability of regulating CBF through diameter changes being attributed to pericytes located on first order capillaries. [94]

A stark differentiation of vessel response depending on the imaging depth was highlighted when vessels across four depth ranges ($0-50\mu m$, $50-150\mu m$, $150-250\mu m$ and $250-350\mu m$) were compared. Table 4.1 reports the peak dilations for each depth category. However, as discussed in Section 7.5, the experimental analysis should be repeated with a larger number of vessels to reinforce these preliminary conclusions on depth-dependent diameter variability.

The analysis of the second data set of pericyte cell activity concluded that pericyte activation resulting in capillary dilation leads to an approximately 6% local increase in $CMRO_2$ in the tissue. Similarly, the capillary-dilation induced CBF and CBV increases were found to be about 5% and 3% respectively. It should be noted that the $CMRO_2$ was not directly measured, but was instead derived from the relationship defined in Equation 4.6 relating the oxygenated and deoxygenated haemoglobin in the blood. The visual stimulus-induced change in CBF and $CMRO_2$ both occurred within 2 s, highlighting the rapid response of the capillary vessels.

Chapter 5 introduces the cerebrovascular model. Large vessels were studied through an electrical equivalent model, while the microvasculature's role in regulating CBF was investigated through a bifurcating network model. Figure 5.1 shows how only small arteries and the network model have a variable resistance, meaning that they are the only vessels who actively respond to stimuli and change CBF as a consequence.

After defining the geometrical characteristics (e.g. quantity, diameter and length) of the network model, the vessel generation's ability to supply the surrounding tissue with oxygen was analysed, attributing the highest contribution to the capillary bed (see Figure 5.2). This conclusion served as an additional reason to attribute to capillaries a key role in the model's neurovascular coupling mechanism.

Four methods for varying the compliance of the small arteries and microvasculature network were then defined. The first method is based on flow feedback (F_0), where arterial compliance depends on variations in flow (see Equation 5.31). While being a commonly found definition across the literature [49], [54], it is not physiologically representative as the active vessel response is modulated by metabolic and myogenic variables (as discussed in Chapter 2).

The second feedback mechanism (F_1) substitutes the flow variable in the previous definition of C_{sa} with a change in O_2 partial tissue pressure (see Equation 5.32). The third feedback mechanism ($F_1 + F_2$), complements the oxygen feedback model by adding the contribution of an active capillary diameter change which was

extrapolated from the experimental data shown in Chapter 4. The fourth and last feedback model ($F_1 + F_2 + F_3$) that was designed is a further extension of the third model, having also mathematically defined the role of neural activation in vessel compliance regulation. Having established the model's geometry and four potential CBF-regulating feedback mechanisms, the computational model was set up to identify the most effective method of emulating the coupling of CBF regulation and metabolic demand.

Chapter 6 ultimately introduces the outputs of the proposed cerebrovascular model. A steady state and a dynamic analysis of the model's results were presented. In particular, three key parameters were examined across all four feedback mechanisms: changes in the small vessel compliance, CBF and CBV. Comparing the models allowed the quantification of each regulatory variable and ultimately highlighted the model that most closely represents the physiological reality of CBF regulation in humans.

Starting with the steady state analysis, the model's ability to simulate CA over a wide range of ABP was studied for all four feedback mechanisms and validated with experimental data. It was found that all four experimental models fit experimental data very well, with a similar width of the CA plateau widths (see Table 6.1). The primary differentiating variable in the CA curve of the four feedback mechanisms is presented by the speed of saturation of the compliance of small vessels, which is highest for the flow feedback model, and is represented by the steep increase in CBF change above the ULA.

The dynamic study is however the more interesting one of the two, as it enabled the comparison of ABP-driven changes in CBF both in terms of response speed and peak change. It is thus that from Figure 6.7, it was possible to conclude that the feedback model that relies on oxygen sensitivity, pericyte activity and neural activation ($F_1 + F_2 + F_3$) is the feedback that most closely replicated physiological reality in terms of response speed (4.1 s). Indeed, human experimental data [115] have proven to be in good agreement with the response speed of the model.

From the dynamic analysis, it was also possible to conclude that CBF modulation both in speed and peak increase, strongly depends on the baseline ABP at which the model operates. Indeed, for $\overline{ABP} \neq$100mmHg, CBF was not effectively modulated as it did not return to the original baseline value it had prior to the stimulation (see Figure 6.9).

The change in CBV was also investigated and was found to be primarily driven by the the change in arterial volume, with arteries contributing to 11.98% blood volume increase out of the total 14.88% given by the imposed 10% increase in ABP. These data were also found to replicate experimental data [114] well. As a result of neural activation and CBF change, the global $CMRO_2$ of the tissue was found to be 9.10%, which is in good agreement with the experimental data on local $CMRO_2$ changes presented in Chapter 4 as well as data across the literature [152].

These conclusions are in agreement with the literature [83], [153] which suggests that metabolic messengers play a key role in linking the demands of the tissue to the supply by the vessels but that alone, they are not rapid enough to drive the coupling between demand and supply in time-sensitive organ such as the brain. It is thus that the role of pericyte cells, activated by neural stimuli, was found to be essential for the rapid regulation of CBF. Ultimately, the model's results can serve as the computational confirmation of the experimentally derived conclusion that pericyte dysfunction can be associated to the onset of brain degenerative diseases. [41], [154]

Chapter 7 discussed of the implications of the experimental and computational results. The primary result of the computational analysis is the conclusion that the feedback model including neural activation most closely simulates physiological reality of rapid CBF regulation. On the other hand, the key result that can be drawn from the experimental analysis is that pericyte activity plays a fundamental role in the rapid regulation of CBF within the microvasculature.

The implications of these results were discussed at length, particularly focusing on creating a link between the experimental results and the computational output. The performance of the key drivers of CBF modulation was confronted with experimental

data in animals and humans across the literature, ultimately highlighting the strengths and weaknesses of the model. The computational and experimental limitations were accounted for and methods for improving upon the accuracy of the model were outlined.

8.2 Result implications

Undoubtedly, CBF regulation is a complex physiological phenomenon whose effectiveness depends on the behaviour of multiple interconnected variables. This study particularly focused on defining the metabolic drivers of blood flow regulation in the brain, as the brain's sensitivity to changes in nutrient concentration can be studied both in the magnitude of the concentration fluctuations and time. This tight coupling can be attributed to the fact that in the brain energy is consumed where it is produced, as energy cannot be transported nor stored for more than a few minutes.

As nutrient exchange occurs at a small length scale in the brain, particular effort was dedicated to designing a microvasculature network model that would be adequate for an investigation of the relationship between nutrient supply by the vasculature and demand of the tissue. Designing such a model that bridges the gap between vasculature response and tissue demand, enabled the study of the role of pericyte cells. Computationally, it was determined that the vessel generations which play the crucial role of nutrient supply are the arterioles and the capillaries, and it is thus that studying their active role in driving CBF modulation was the focal point of this research.

Arterioles are very well equipped for an active variation of the diameter, allowing for changes in blood flow, through the presence of SMC in the vessel wall. Hence, the compliance of arterioles could be studied by relating changes in vessel diameter (and therefore vessel wall resistance), to changes in nutrient demand in the supplied tissue volume. On the other hand, while capillaries have also shown to be a key player in CBF regulation, their thin vessel wall does not allow for active changes in vessel diameter.

This is why pericyte activity was included as one of the model's drivers, as experimental data have shown that by lining the outer walls of post-arteriolar capillaries, pericytes enable an active change of millions of capillaries across the microvasculature bed. The role of pericyte activity was thus quantified experimentally in vivo and a function describing their ability in changing capillary diameters was included in the model. As these contractile cells are activated by Ca^{2+} stimuli, which in turn are a result of neural signalling, neural signalling was also included as one of the model's drivers.

In summary, the computational model defined in Chapter 5 aims to quantify the role of three CBF drivers: oxygen, pericytes and neurons. It was concluded that for changes in ABP, oxygen alone plays a key role in defining the peak CBF increase but is weak in modulating the speed of the response. Pericyte activity contributes to the oxygen-dependent small vessel compliance regulation by ensuring a faster response to the stimulus. Ultimately, neural activity further contributes to regulating the response speed in a way that is in good agreement with experimental data on rapid CBF regulation in humans.

The inclusion of neural activity in the model is in truth a necessary step for tying together nutrient demand by the tissue and pericyte activation. Indeed, pericytes act as mediators between the tissue and the vasculature and disregarding neural activation would therefore have been inaccurate. Given the complexity of the metabolic and chemical interactions occurring between the multitude of variables that ensure brain function, the computational model presented here is inevitably a simplistic one, yet it was able to highlight the critical role of the microvasculature bed in a whole brain blood flow regulation system.

8.2.1 Clinical relevance

While acknowledging the limitations of the model presented here (see Section 7.6), several conclusions that might potentially be extrapolated to clinical practice can be drawn. Altogether, the model highlighted the importance of a healthy vasculature in maintaining a healthy brain perfusion. Indeed, the model's vascular driver is

the compliance of small vessels, which strongly depends on vessel wall elasticity and reaction speed. Clinical studies have repeatedly shown [44] that stiff vessels are associated with the onset of brain degenerative diseases, a prospect which can, in great part, be avoided with the adoption of a consistent healthy lifestyle. Indeed, increased brain oxygenation by means of frequent exercise [155], [156], waste clearance during quality sleep [157] and a balanced diet [158], [159], have been categorised as three highly effective preventive actions people can take against cognitive decline. [160]

In this study in particular, the importance of healthy pericyte activity, and therefore a rapidly responsive microvascular bed, was highlighted. Precisely, it was shown how pericyte inactivity leaves the metabolic sensitivity with the challenging task of regulating CBF sufficiently rapidly. Pericyte effectiveness in regulating capillary diameters was mathematically quantified and the results were supported by experimental evidence [40], [94] suggesting that pericyte deterioration might play a key role in the onset of the cascade of events leading up to irreversible brain damage.

Ultimately, the results presented in Chapter 6 and the aforementioned studies suggest that, next to promoting the preventive actions against cognitive decline, it is now essential to direct the scientific efforts towards an extended understanding of the brain's microvasculature. Given the small length-scale at which the neurovascular coupling occurs and the ineffective translatability between post mortem data to the live human physiological reality, imaging techniques can only inform clinicians of disruptions in healthy brain function once these have become irreversible.

It is thus that today, the concern and scientific engagement on brain degenerative diseases should strongly focus on the technological advances that will allow for more precise monitoring and patient-specific insights in to functioning of the smallest brain vessels. Due to the very large, and continuously increasing, number of people affected by brain degenerative diseases across the globe, a considerable effort should be made in developing new computational tools that will complement current imaging methods.

8.3 Future work

The results of the model presented in Chapter 5 can serve as further evidence of the crucial role of the microvasculature in the rapid regulation of CBF, yet the clinical application of such results is yet to be defined. Given the relatively scarce knowledge about the detailed physiological activities occurring in the brain, compared to other organs, a wide array of research topics remain to be tackled. Within the narrow range of the study presented here however, three possible research topics lie in the visible horizon. The first concerns an expansion of capillary activity knowledge, the second suggests the benefit of a more anatomically accurate large vessel model, and the third and last idea revolves about the possibility of coupling the computational vasculature model presented here with a brain tissue model.

Capillary beds with varying diameters

To gain a more detailed knowledge on the crucial role of capillary vessel activity, it would be insightful to expand the model's network section to include multiple generations of capillaries. These generations could differ in diameter size, which has been experimentally shown (see Chapter 4) to be an influential factor in dictating the magnitude of the vessel's peak dilation. Similarly, the vessel's dependency on spacial information, such as imaging depth, could be included as experimental data from Chapter 4 suggest a difference in response time between depth categories.

Patient-specific models

Substituting the model's electrical equivalent analogy for the behaviour of large arteries and veins with a 3-D model of the brain's large vessels, would allow for an extended understanding of how CBF changes in the microvasculature translate to the large vessels. In this way, large vessel geometry could be extrapolated from imaging, where the smallest detectable vessels have a diameter of about 1 mm. The first generations of the network model presented in Chapter 5 could be expanded and ultimately coupled to the extrapolated imaging geometry, as the first generation of arterioles of the network is about 1 mm in diameter.

An advantage of this multi-scale model is the fact that it could enable the study of patient-specific cerebrovascular models, where large vessels modelled in 3-D could be altered in shape or even removed, so as to mimic the high variability of the Circle of Willis present in the population. Doing so would enable the quantification of the vulnerability of specific vasculature geometrical properties over others.

Tissue diffusion

As the model presented here solely focuses on the vasculature while at the same time highlighting the importance of metabolic signalling from the tissue to the vessels, including considerations on nutrient exchange in the tissue would allow a more precise study of the tissue's vulnerability. A good first approach could consist of considering nutrient diffusion in the tissue, which is disregarded in the model presented in Chapter 5, therefore attributing to the tissue an active role in CBF regulation.

Indeed, studying how neighbouring tissue voxels can mediate nutrient supply and consumption before the vasculature reacts, could lead to interesting clinical conclusions. Moreover, as the brain is heterogeneous in geometry and function, creating a coupled tissue and vasculature model would allow for the comparative study of different brain regions as they would present different metabolic consumption rates or response times.

Ultimately, the complexity of the brain presents a research landscape where the difficulty does not solely lie in answering intricate questions but also in defining the right questions. How does a brain degenerative disease start? Where is the line between temporary and irreversible brain damage? These, and many others are questions whose answers are likely to be found through the use of multiple research tools. It is therefore imperative to invest in two things: the development of novel techniques and the focus on interdisciplinary translatability.

Appendices

Figure 1 is a schematic illustration of the visual-stimulus induced vasodilation data processing. The extensive vessel selection process defined in Section 4.2.2 is concisely summarized here.

The frequency analysis for the capillary diameter change induced by visual stimulation presented in Chapter 4 is presented here for each individual vessel. Figure 2 to Figure 9 present the frequency analysis for the large capillary vessels (i.e. diameter $6-10\mu m$). For each vessel, the unnormalised and the normalised power spectra trace for 1/f noise are presented. The normalised trace is presented in order to facilitate the visualisation of the locomotion frequency (0.1 Hz) being the predominant frequency range, as it presents the highest peak. Furthermore, the locomotion frequency value is marked with a dotted line at 0.1 Hz.

Figure 10 to Figure 13 present the frequency analysis for the small capillary vessels (i.e. diameter $6-10\mu m$). As for large vessels, the unnormalized and the normalized power spectra trace for 1/f noise are presented.

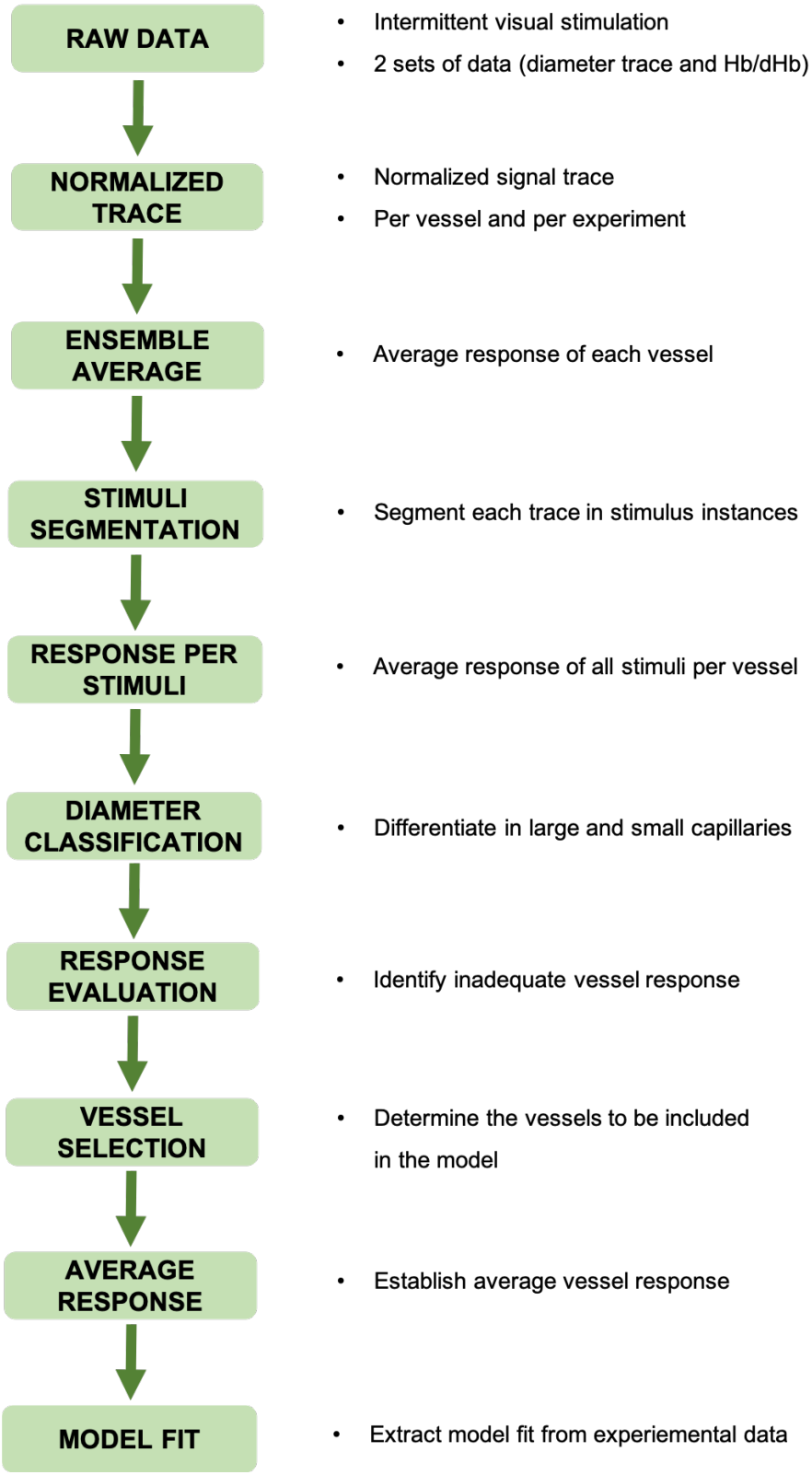

Figure 1: Schematic summary of the process of pericyte activity model definition from raw data.

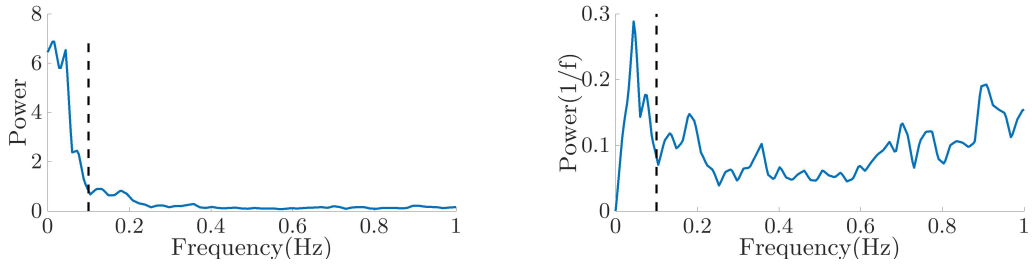

(a) Unnormalised power spectra trace. **(b)** Normalized power spectra trace.

Figure 2: Vessel 1; Unnormalised power spectra trace (a) Normalized power spectra trace for 1/f noise (b).

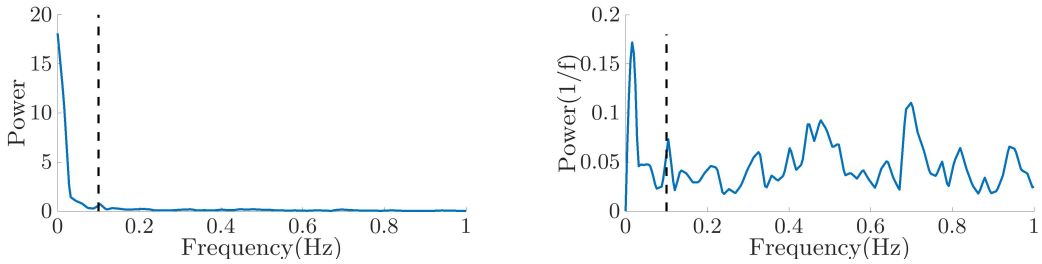

(a) Unnormalised power spectra trace. **(b)** Normalized power spectra trace.

Figure 3: Vessel 4; Unnormalised power spectra trace (a) Normalized power spectra trace for 1/f noise (b).

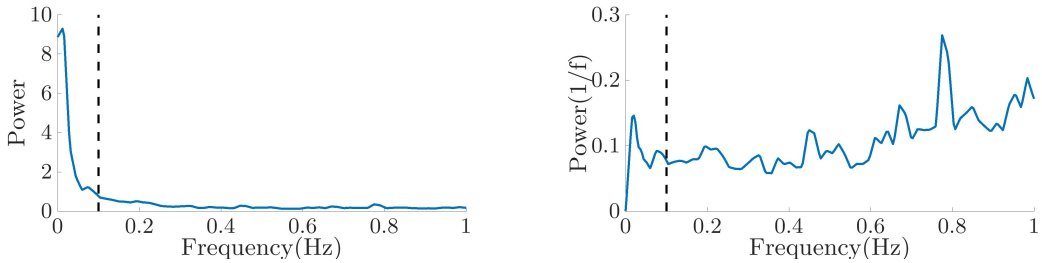

(a) Unnormalised power spectra trace. **(b)** Normalized power spectra trace.

Figure 4: Vessel 11; Unnormalised power spectra trace (a) Normalized power spectra trace for 1/f noise (b).

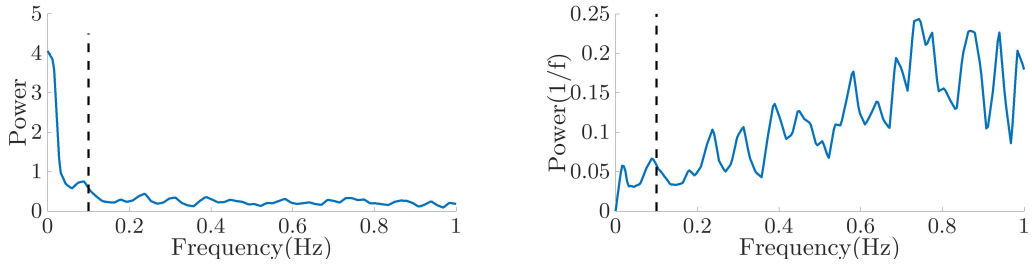

(a) Unnormalised power spectra trace. **(b)** Normalized power spectra trace.

Figure 5: Vessel 15; Unnormalised power spectra trace (a) Normalized power spectra trace for 1/f noise (b).

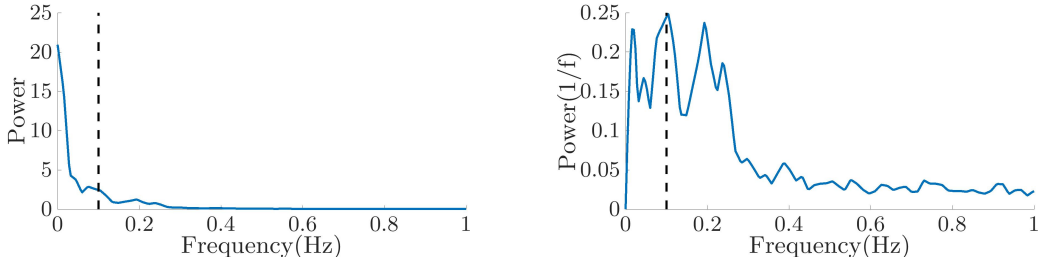

(a) Unnormalised power spectra trace. **(b)** Normalized power spectra trace.

Figure 6: Vessel 16; Unnormalised power spectra trace (a) Normalized power spectra trace for 1/f noise (b).

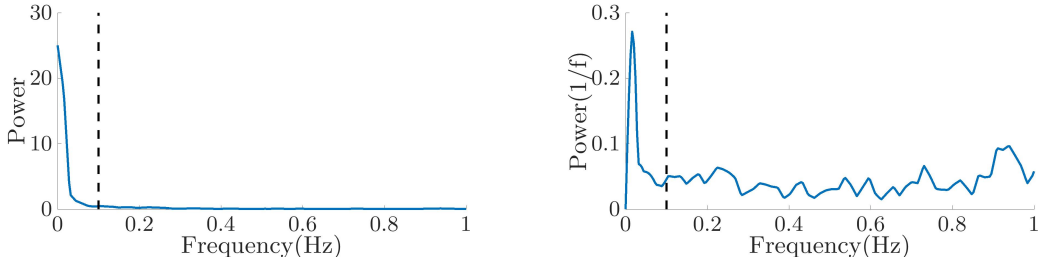

(a) Unnormalised power spectra trace. **(b)** Normalized power spectra trace.

Figure 7: Vessel 18; Unnormalised power spectra trace (a) Normalized power spectra trace for 1/f noise (b).

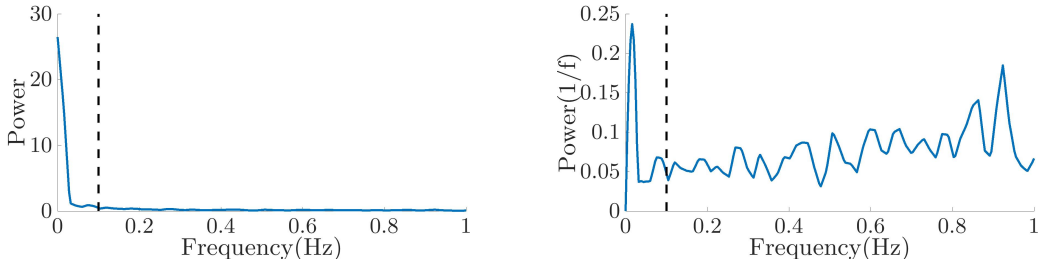

(a) Unnormalised power spectra trace. **(b)** Normalized power spectra trace.

Figure 8: Vessel 22; Unnormalised power spectra trace (a) Normalized power spectra trace for 1/f noise (b).

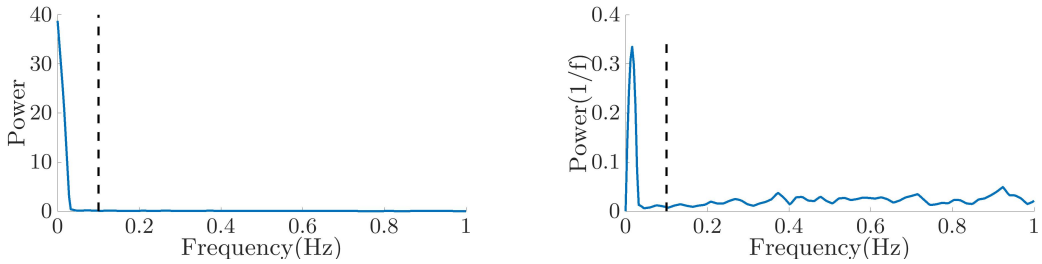

(a) Unnormalised power spectra trace. **(b)** Normalized power spectra trace.

Figure 9: Vessel 23; Unnormalised power spectra trace (a) Normalized power spectra trace for 1/f noise (b).

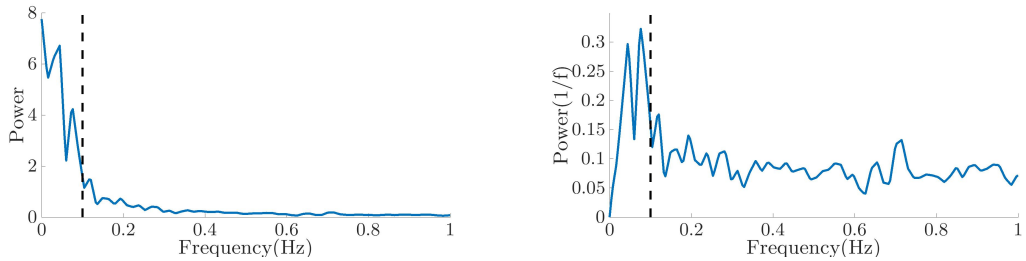

(a) Unnormalised power spectra trace. **(b)** Normalized power spectra trace.

Figure 10: Vessel 2; Unnormalised power spectra trace (a) Normalized power spectra trace for 1/f noise (b).

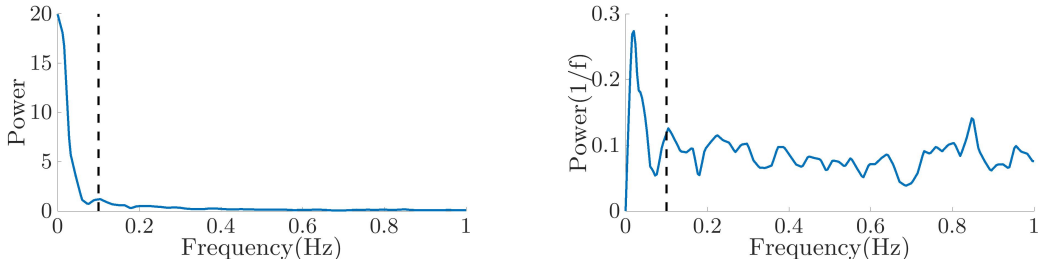

(a) Unnormalised power spectra trace. **(b)** Normalized power spectra trace.

Figure 11: Vessel 7; Unnormalised power spectra trace (a) Normalized power spectra trace for 1/f noise (b).

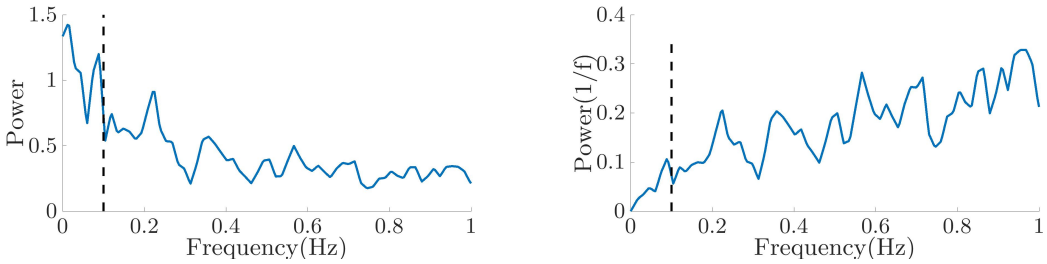

(a) Unnormalised power spectra trace. **(b)** Normalized power spectra trace.

Figure 12: Vessel 13; Unnormalised power spectra trace (a) Normalized power spectra trace for 1/f noise (b).

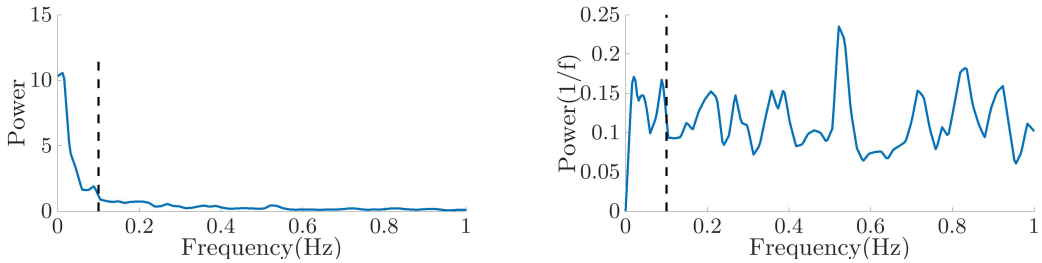

(a) Unnormalised power spectra trace. **(b)** Normalized power spectra trace.

Figure 13: Vessel 24; Unnormalised power spectra trace (a) Normalized power spectra trace for 1/f noise (b).

Education is the kindling of a flame,
not the filling of a vessel.

— Socrates (470 - 399 BC)

References

[1] David J. Begley and Milton W. Brightman. "Structural and functional aspects of the blood-brain barrier". In: *Progress in Drug Research* 61 (2003), pp. 39–78.

[2] Stephen J. Payne. *Cerebral blood flow and metabolism*. World Scientific, 2017.

[3] Stroke association UK. "Stroke statistics". In: *State of the nation* (2018).

[4] Thomas Powell and Carl Baker. "Dementia: policy, services and statistics". In: *House of Commons Library* (2019).

[5] Valery L. Feigin et al. "Global, regional, and national burden of neurological disorders, 1990–2016: a systematic analysis for the Global Burden of Disease Study 2016". In: *The Lancet Neurology* 18.5 (2019), pp. 459–480.

[6] Henri M. Duvernoy, S. Delon, and J. L Vannson. "Cortical blood vessels of the human brain". In: *Brain Research Bulletin* 7.5 (1981), pp. 519–579.

[7] Mohammad Moeini et al. "Compromised microvascular oxygen delivery increases brain tissue vulnerability with age". In: *Scientific Reports* (2018), pp. 1–17.

[8] Committee for Medicinal Products for Human Use. "Guideline on the reporting of physiologically based pharmacokinetic (PBPK) modelling and simulation". In: *European Medicine Agency Report* (2018).

[9] John W. Fenner et al. "The EuroPhysiome, STEP and a roadmap for the virtual physiological human". In: *Philosophical Transactions of the Royal Society: Mathematical, Physical and Engineering Sciences* 366.1878 (2008), pp. 2979–2999.

[10] Christopher K. Willie et al. "Integrative regulation of human brain blood flow". In: *Journal of Physiology* 592.5 (2014), pp. 841–859.

[11] Marilyn J. Cipolla. *The Cerebral Circulation, Second Edition*. Vol. 8. 1. 2016, pp. 1–80.

[12] Alifia Tameem and Krovvidi Hari. "Cerebral physiology". In: *Continuing Education in Anaesthesia Critical Care & Pain* 13.4 (Mar. 2013), pp. 113–118.

[13] Berry Richard G. Alpers Bernard J. and Paddison Richard M. "Anatomical Studies of the Circle of Willis in Normal Brain". In: *Archives of Neurology And Psychiatry* 81.4 (1959), pp. 409–418.

[14] Vassil Papantchev et al. "The role of Willis circle variations during unilateral selective cerebral perfusion: a study of 500 circles". In: *European Journal of Cardio-Thoracic Surgery* 44.4 (2013), pp. 743–753.

[15] Francis Cassot et al. "A novel three-dimensional computer-assisted method for a quantitative study of microvascular networks of the human cerebral cortex". In: *Microcirculation* 13.1 (2006), pp. 1–18.

[16] Xiang Ji et al. " Brain microvasculature has a common topology with local differences in geometry that match metabolic load". In: *Neuron* (2021), pp. 1–20.

[17] Mario Gilberto Báez-Yánez et al. "The impact of vessel size, orientation and intravascular contribution on the neurovascular fingerprint of BOLD bSSFP fMRI". In: *NeuroImage* 163.August (2017), pp. 13–23.

[18] Enedino Hernández-Torres et al. "Anisotropic cerebral vascular architecture causes orientation dependency in cerebral blood flow and volume measured with dynamic susceptibility contrast magnetic resonance imaging". In: *Journal of Cerebral Blood Flow and Metabolism* 37.3 (2017), pp. 1108–1119.

[19] Seed W. A. Caro C.G. Pedley T.J. Schroter R. C. *The mechanics of the circulation*. Cambridge University Press, 2012.

[20] David C. Van Essen, Chad J. Donahue, and Matthew F. Glasser. "Development and evolution of cerebral and cerebellar cortex". In: *Brain, Behavior and Evolution* 91.3 (2018), pp. 158–169.

[21] Roberto Toro et al. "Brain size and folding of the human cerebral cortex". In: *Cerebral Cortex* 18.10 (2008), pp. 2352–2357.

[22] Virginia Fernández, Cristina Llinares-Benadero, and Victor Borrell. "Cerebral cortex expansion and folding: what have we learned?" In: *The EMBO Journal* 35.10 (2016), pp. 1021–1044.

[23] Stephen Smith et al. "Structural Variability in the Human Brain Reflects Fine-Grained Functional Architecture at the Population Level". In: *The Journal of neuroscience: the official journal of the Society for Neuroscience* 39.31 (2019), pp. 6136–6149.

[24] Stephen J. Payne. *Cerebral Autoregulation: Control of Blood Flow in the Brain*. 2016, pp. 1–125.

[25] Edith Hamel. "Perivascular nerves and the regulation of cerebrovascular tone". In: *Journal of applied physiology* (2006), pp. 1059–1064.

[26] James Duffin Philip N. Ainslie. "Integration of cerebrovascular CO2 reactivity and chemoreflex control of breathing: mechanisms of regulation, measurement, and interpretation". In: *American Physiological Society* (2009), pp. 1473–1495.

[27] Niels A. Lassen. "Cerebral blood flow and oxygen consumption in man". In: *The American physiological society* 39.2 (1959), pp. 1183–238.

[28] Svend Strandgaard et al. "Upper limit of cerebral blood flow autoregulation in experimental renovascular hypertension in the baboon." In: *Circulation research* 37.2 (1975), pp. 164–167.

[29] Tianne Numan et al. "Static autoregulation in humans: a review and reanalysis". In: *Medical engineering & physics* 36.11 (2014), pp. 1487–1495.

[30] Caroline A. Rickards. "Cerebral blood-flow regulation during hemorrhage". In: *Comprehensive Physiology* 5.4 (2015), pp. 1585–1621.

[31] Jason W. Hamner and Can O. Tan. "Relative contributions of sympathetic, cholinergic, and myogenic mechanisms to cerebral autoregulation". In: *Stroke* 45.6 (2014), pp. 1771–1777.

[32] Hiroshi Ito, Iwao Kanno, and Hiroshi Fukuda. “Human cerebral circulation: Positron emission tomography studies”. In: *Annals of Nuclear Medicine* 19.2 (2005), pp. 65–74.

[33] Joseph Donnelly and Marek Czosnyka. “Getting hot under the collar: temperature and cerebral autoregulation”. In: *Journal of Emergency and Critical Care Medicine* 2.9 (2018), pp. 89–89.

[34] Julia M. Orshal and Raouf A. Khalil. “Gender, sex hormones, and vascular tone”. In: *American Journal of Physiology - Regulatory Integrative and Comparative Physiology* 286.2 55-2 (2004), pp. 233–249.

[35] Ronney B. Panerai. “Assessment of cerebral pressure autoregulation in humans - a review of measurement methods”. In: *Physiological Measurement* 19.3 (Aug. 1998), pp. 305–338.

[36] Inês Sá-Pereira, Dora Brites, and Maria Alexandra Brito. “Neurovascular unit: A focus on pericytes”. In: *Molecular Neurobiology* 45.2 (2012), pp. 327–347.

[37] Lila Khennouf et al. “Active role of capillary pericytes during stimulation-induced activity and spreading depolarization”. In: *Brain* 141 (2018), pp. 2032–2046.

[38] David Attwell et al. “What is a pericyte?” In: *Journal of Cerebral Blood Flow and Metabolism* (2016), pp. 6–10.

[39] Gabriele Bergers and Steven Song. “The role of pericytes in blood-vessel formation and maintenance”. In: *Neuro-Oncology* 7.4 (2005), pp. 452–464.

[40] Catherine N Hall et al. “Capillary pericytes regulate cerebral blood flow in health and disease.” In: *Nature* 508.7494 (2014), pp. 55–60.

[41] Kassandra Kisler et al. “Pericyte degeneration leads to neurovascular uncoupling and limits oxygen supply to brain”. In: *Nature Neuroscience* 20.3 (2017).

[42] Ross Nortley et al. “Amyloid oligomers constrict human capillaries in Alzheimer’s disease via signalling to pericytes”. In: *Science* 9518 (2018), pp. 1–18.

[43] Annemieke Ruitenberg et al. “Cerebral hypoperfusion and clinical onset of dementia: The Rotterdam Study”. In: *Annals of Neurology* 57.6 (2005), pp. 789–794.

[44] Melanie D Sweeney et al. “The role of brain vasculature in neurodegenerative disorders”. In: *Nature Neuroscience* 21 (2018), pp. 1318–1331.

[45] Theodor Burdyga and Lyudmyla Borysova. “Calcium signalling in pericytes”. In: *Journal of Vascular Research* 51.3 (2014), pp. 190–199.

[46] Nicola B Hamilton, David Attwell, and Catherine N Hall. “Pericyte-mediated regulation of capillary diameter: a component of neurovascular coupling in health and disease”. In: *Neurogenetics* 2 (2010), pp. 1–14.

[47] Kyle Trudeau, Anthony J A Molina, and Sayon Roy. “High glucose induces mitochondrial morphology and metabolic changes in retinal pericytes”. In: *Investigative Ophthalmology and Visual Science* 52.12 (2011), pp. 8657–8664.

[48] Bahram Mokri. “The Monro–Kellie hypothesis: applications in CSF volume depletion”. In: *Neurology* 56.12 (2001), pp. 1746–1748.

[49] Mauro Ursino. “A mathematical study of human intracranial hydrodynamics part 1—The cerebrospinal fluid pulse pressure”. In: *Annals of biomedical engineering* 16.4 (1988), pp. 379–401.

[50] Berwick J Chen D Billings S Mayhew J Zheng Y. Johnston D. “A three compartment model of the hemodynamic response to oxygen delivery to the brain”. In: *Neuroimage* 20.4 (2005), pp. 925–939.

[51] Secomb Timothy Carlson B. Arciero J. “Theoretical model of blood flow autoregulation: roles of myogenic, shear-dependent, and metabolic responses”. In: *American Journal of Physiology* 295.4 (2008).

[52] Mauro Ursino and Massimo Giannessi. “A model of cerebrovascular reactivity including the circle of Willis and cortical anastomoses”. In: *Annals of Biomedical Engineering* 38.3 (2010), pp. 955–974.

[53] Mauro Ursino and Patrizia Di Giammarco. “A mathematical model of the relationship between cerebral blood volume and intracranial pressure changes: the generation of plateau waves.” In: *Annals of biomedical engineering* 19.1 (1991), pp. 15–42.

[54] Stephen J. Payne. “A model of the interaction between autoregulation and neural activation in the brain”. In: *Mathematical Biosciences* 204.2 (2006), pp. 260–281.

[55] Devor A Huppert T Dale A Boas D. Jones S. “A vascular anatomical network model of the spatio-temporal response to brain activation”. In: *Neuroimage* 40.3 (2008), pp. 1116–1129.

[56] Eugene Vovenko. “Distribution of oxygen tension on the surface of arterioles, capillaries and venules of brain cortex and in tissue in normoxia: an experimental study on rats”. In: *Pflügers Archiv* 437.4 (1999), pp. 617–623.

[57] Stephen J. Payne and Lucas Claire. “Oxygen delivery from the cerebral microvasculature to tissue is governed by a single time constant of approximately 6 seconds”. In: *Microcirculation* 25.2 (2018), pp. 1–11.

[58] Murad Banaji et al. “A physiological model of cerebral blood flow control”. In: *Mathematical Biosciences* 194.2 (2005), pp. 125–173.

[59] Shen Wei Su, Mark Catherall, and Stephen J. Payne. “The Influence of Network Structure on the Transport of Blood in the Human Cerebral Microvasculature”. In: *Microcirculation* 19.2 (2012), pp. 175–187.

[60] Bart Spronck et al. “A lumped parameter model of cerebral blood flow control combining cerebral autoregulation and neurovascular coupling”. In: *American Journal of Physiology - Heart and Circulatory Physiology* 303.9 (2012), pp. 143–153.

[61] Ryan N Gutenkunst et al. “Universally sloppy parameter sensitivities in systems biology models”. In: *PLoS computational biology* 3.10 (2007), p. 189.

[62] Johannes Weickenmeier et al. “Brain stiffens post mortem”. In: *Journal of the Mechanical Behavior of Biomedical Materials* 84.January (2018), pp. 88–98.

[63] Mokhtar Zagzoule and Jean Pierre Marc-Vergnes. “A global mathematical model of the cerebral circulation in man”. In: *Journal of Biomechanics* 19.12 (1986), pp. 1015–1022.

[64] Timothy W. Secomb et al. “Theoretical Simulation of Oxygen Transport to Brain by Networks of Microvessels: Effects of Oxygen Supply and Demand on Tissue Hypoxia”. In: *Microcirculation* 7.4 (2000), pp. 237–247.

[65] Sylvie Lorthois, Francis Cassot, and Frederick Lauwers. “Simulation study of brain blood flow regulation by intra-cortical arterioles in an anatomically accurate large human vascular network: Part I: Methodology and baseline flow”. In: *NeuroImage* 54.2 (2011), pp. 1031–1042.

[66] Juan R. Cebral et al. “Blood flow modeling in carotid arteries with computational fluid dynamics and MR imaging”. In: *Academic Radiology* 9.11 (2002), pp. 1286–1299.

[67] Masahide Nakamura and Tadashi Sawada. “Numerical study on the flow of a non-Newtonian fluid through an axisymmetric stenosis”. In: *Bioarchive* 5 (1988), pp. 459–480.

[68] Lindqvist T Fahradeus R. “The viscosity of blood in narrow capillary tubes”. In: *American Journal of Physiology* 96 (1931).

[69] Pries Axel R. Secomb Timothy W. “Blood viscosity in the microvessels: experiment and theory”. In: *Journal of Physiology* 14.6 (2013), pp. 470–478.

[70] Sietze Reitsma et al. “The endothelial glycocalyx: Composition, functions, and visualization”. In: *European Journal of Physiology* 454.3 (2007), pp. 345–359.

[71] H Vink S. Reitsma D. W. Slaaf and Jan van Zandvoort. “The endothelial glycocalyx: composition, functions, and visualization”. In: *European Jounal of Physiology* (2007), pp. 345–359.

[72] Michelle E Watts, Roger Pocock, and Charles Claudianos. “Brain Energy and Oxygen Metabolism: Emerging Role in Normal Function and Disease”. In: 11 (2018), pp. 1–13.

[73] Maria Erecińska and Ian A. Silver. “Tissue oxygen tension and brain sensitivity to hypoxia”. In: *Respiration Physiology* 128.3 (Nov. 2001), pp. 263–276.

[74] Lisa Wagenführ et al. “Oxygen Tension Within the Neurogenic Niche Regulates Dopaminergic Neurogenesis in the Developing Midbrain”. In: *Stem Cells and Development* 25.3 (2015), pp. 227–238.

[75] A Arvidsson et al. “Neuronal replacement from endogenous precursors in the adult”. In: *Nature Medicine* 9.5 (2003), pp. 548–553.

[76] Peter J. Havel. “Peripheral signals conveying metabolic information to the brain: Short-term and long-term regulation of food intake and energy homeostasis”. In: *Experimental Biology and Medicine* 226.11 (2001), pp. 963–977.

[77] Donard Dwyer. *Glucose metabolism in the brain*. Elsevier, 2002.

[78] R. A. Chapman and J. Tunstall. “The interaction of sodium and calcium ions at the cell membrane and the control of contractile strength in frog atrial muscle.” In: *The Journal of Physiology* 305.1 (1980), pp. 109–123.

[79] Agnès Aubert, Robert Costalat, and Romain Valabrègue. “Modelling of the Coupling between Brain Electrical Activity and Metabolism”. In: *Acta Biotheoretica* 49.4 (2001), pp. 301–326.

[80] Agnès Aubert and Robert Costalat. "A model of the coupling between brain electrical activity, metabolism, and hemodynamics: Application to the interpretation of functional neuroimaging". In: *NeuroImage* 17.3 (2002), pp. 1162–1181.

[81] Paul H. Poulsen et al. "In vivo estimation of cerebral blood flow, oxygen consumption and glucose metabolism in the pig by [15O]water injection, [15O]oxygen inhalation and dual injections of [18F]fluorodeoxyglucose". In: *Journal of Neuroscience Methods* 77.2 (1997), pp. 199–209.

[82] Agnes Aubert and Robert Costalat. "A model of the coupling between brain electrical activity, metabolism, and hemodynamics: application to the interpretation of functional neuroimaging". In: *Neuroimage* 17.3 (2002), pp. 1162–1181.

[83] Jens Frahm et al. "Dynamic uncoupling and recoupling of perfusion and oxidative metabolism during focal brain activation in man". In: *Magnetic Resonance in Medicine* 35.2 (1996), pp. 143–148.

[84] Gunnar Krüger et al. "Simultaneous monitoring of dynamic changes in cerebral blood flow and oxygenation during sustained activation of the human visual cortex". In: *NeuroReport* 10.14 (1999), pp. 2939–2943.

[85] Louis Sokoloff. "Measurement of local cerebral glucose utilization and its relation to local functional activity in the brain". In: *Fuel Homeostasis and the Nervous System*. Springer, 1991, pp. 21–42.

[86] Per E Roland, Pere E Roland, and Per E Roland. *Brain activation*. Wiley-Liss New York, 1993.

[87] Peter T Fox, Marcus E Raichle, and Mark A Mintun. "Nonoxidative Glucose Consumption during Focal Physiologic Neural Activity". In: *American Association for the Advancement of Science* 241.4864 (1988), pp. 462–464.

[88] Ai-Ling Lin et al. "Nonlinear coupling between cerebral blood flow, oxygen consumption, and ATP production in human visual cortex". In: *Proceedings of the National Academy of Sciences* 107.18 (2010), pp. 8446–8451.

[89] Ai Ling Lin et al. "Nonlinear coupling between cerebral blood flow, oxygen consumption, and ATP production in human visual cortex". In: *Proceedings of the National Academy of Sciences of the United States of America* 107.18 (2010), pp. 8446–8451.

[90] Hikaru Hashitani et al. "Role of capillary pericytes in the integration of spontaneous Ca2+ transients in the suburothelial microvasculature in situ of the mouse bladder". In: *Journal of Physiology* 596.16 (2018), pp. 3531–3552.

[91] Selena Milanovic et al. "Investigating the role of pericytes in cerebral autoregulation: a modelling study". In: *Physiological Measurement* 42.5 (2021), p. 19.

[92] Kira Shaw et al. "Hippocampus has lower oxygenation and weaker control of brain blood flow than cortex, due to microvascular differences". In: *Nature Communications* (2021), pp. 1–42.

[93] Adriano BL Tort et al. “Parallel detection of theta and respiration-coupled oscillations throughout the mouse brain”. In: *Scientific reports* 8.1 (2018), pp. 1–14.

[94] Maryam Anzabi, Baoqiang Li, and Hui Wang. “Optical coherence tomography of arteriolar diameter and capillary perfusion during spreading depolarizations”. In: *Journal of Cerebral Blood Flow and Metabolism* 0.0 (2021), pp. 1–8.

[95] Robert L. Grubb et al. “The effects of changes in PaCO2 on cerebral blood volume, blood flow, and vascular mean transit time”. In: *Stroke* 5.5 (1974), pp. 630–639.

[96] Hiroshi Ito et al. “Changes in Human Cerebral Blood Flow and Cerebral Blood Volume during Hypercapnia and Hypocapnia Measured by Positron Emission Tomography”. In: *Journal of Cerebral Blood Flow & Metabolism* 23.6 (June 2003), pp. 665–670.

[97] Egill Rostrup et al. “The relationship between cerebral blood flow and volume in humans”. In: *NeuroImage* 24.1 (2005), pp. 1–11.

[98] Georg Royl et al. “Hypothermia effects on neurovascular coupling and cerebral metabolic rate of oxygen”. In: *Neuroimage* 40.4 (2008), pp. 1523–1532.

[99] Marilyn J. Cipolla. “The Cerebral Circulation”. In: *Colloquium Series on Integrated Systems Physiology: From Molecule to Function* 1.1 (Jan. 2009), pp. 1–59.

[100] F. D. McBryde, S. C. Malpas, and J. F.R. Paton. “Intracranial mechanisms for preserving brain blood flow in health and disease”. In: *Acta Physiologica* 219.1 (2017), pp. 274–287.

[101] Stephen J. Payne Wahbi K. El-Bouri. “Multi-scale homogenization of blood flow in 3-dimensional human cerebral microvascular networks”. In: *Journal of theoretical biology* 380 (2015), pp. 40–47.

[102] Benjamin W. Zwifach. “Quantitative Studies of Microcirculatory Structure and Function”. In: *Circulation Research* 34.6 (1974), pp. 858–866.

[103] H Glenn Bohlen. “Microvascular Adaptation in the Cerebral Cortex of Adult Spontaneously Hypertensive Rats”. In: *Hypertension* 6.3 (1984), pp. 408–419.

[104] Ian G. Gould and Andreas A. Linninger. “Hematocrit distribution and tissue oxygenation in large microcirculatory networks”. In: *Microcirculation* 22.1 (2015), pp. 1–18.

[105] W. El-Bouri S. J. Payne. “Modelling dynamic changes in blood flow and volume in the cerebral vasculature”. In: *NeuroImage* 176 (2018), pp. 124–137.

[106] Luciano D. Vander A. Sherman J. *Human physiology: the mechanism of body function*. 2001, pp. 468–469.

[107] R. W. Dick Nickalls. “Inverse solutions of the Severinghaus and Thomas equations which allow PO2 to be derived directly from SO2”. In: *Solutions* (2011), pp. 1–10.

[108] Timothy L. Davis et al. “Calibrated functional MRI: Mapping the dynamics of oxidative metabolism”. In: *Proceedings of the National Academy of Sciences of the United States of America* 95.4 (1998), pp. 1834–1839.

[109] Maria A Fernandez-Seara et al. “Calibrated bold fMRI with an optimized ASL-BOLD dual-acquisition sequence”. In: *Neuroimage* 142 (2016), pp. 474–482.

[110] Mauro Ursino et al. “Interaction among cerebral autoregulation, CO2 reactivity and Intracranial Pressure : a Mathematical Model”. In: *Am J Physiol Heart Circ Physiol* 274.51 (1998), pp. 1715–1728.

[111] Michelle E. Favre and Jorge M. Serrador. “Sex differences in cerebral autoregulation are unaffected by menstrual cycle phase in young, healthy women”. In: *American Journal of Physiology - Heart and Circulatory Physiology* 316.4 (2019), pp. 920–933.

[112] Brian M. Deegan et al. “Elderly women regulate brain blood flow better than men do”. In: *Stroke* 42.7 (2011), pp. 1988–1993.

[113] Caroline A. Rickards et al. “Tolerance to central hypovolemia: the influence of oscillations in arterial pressure and cerebral blood velocity”. In: *Journal of Applied Physiology* 111.4 (2011), pp. 1048–1058.

[114] Sang Pil Lee et al. “Relative changes of cerebral arterial and venous blood volumes during increased cerebral blood flow: Implications for bold fMRI”. In: *Magnetic Resonance in Medicine* 45.5 (2001), pp. 791–800.

[115] Ashwin B. Parthasarathy et al. “Dynamic autoregulation of cerebral blood flow measured non-invasively with fast diffuse correlation spectroscopy”. In: *Journal of Cerebral Blood Flow and Metabolism* 38.2 (2018), pp. 230–240.

[116] Peter A. Chiarelli et al. “A calibration method for quantitative BOLD fMRI based on hyperoxia”. In: *NeuroImage* 37.3 (2007), pp. 808–820.

[117] Joseph C Lamanna et al. “Relationship between brain tissue haemodynamics”. In: *dvances in Experimental Medicine and Biology* 645 (2009), pp. 301–306.

[118] Arnab Ghosh et al. “Hyperoxia results in increased aerobic metabolism following acute brain injury”. In: *Journal of Cerebral Blood Flow and Metabolism* 37.8 (2017), pp. 2910–2920.

[119] Henry S Dunning and Harold G Wolff. “The relative vascularity of various parts of the central and peripheral nervous system of the cat and its relation to function”. In: *Journal of Comparative Neurology* 67.3 (1937), pp. 433–450.

[120] Jorn Overgaard. “Chroma-Memo-Flow Technique for Rapid Sequential Analysis of Regional Cerebral Blood Flow (rCBF) Responses”. In: *Canadian Journal of Neurological Sciences* 5.1 (1978), pp. 1–7.

[121] Jes Olesen. “Cerebral blood flow methods for measurement regulation, effects of drugs and changes in disease”. In: *Brain* 94.5 (1974), pp. 635–646.

[122] Ryan L. Hoiland et al. “Hypoxemia, oxygen content, and the regulation of cerebral blood flow”. In: *American Journal of Physiology - Regulatory Integrative and Comparative Physiology* 310.5 (2016), R398–R413.

[123] Martin M. Brown, J. P.H. Wade, and John Marshall. “Fundamental importance of arterial oxygen content in the regulation of cerebral blood flow in man”. In: *Brain* 108.1 (1985), pp. 81–93.

[124] Philip N. Ainslie and Shigehiko Ogoh. "Regulation of cerebral blood flow in mammals during chronic hypoxia: A matter of balance: Experimental Physiology-Hot Topic Review". In: *Experimental Physiology* 95.2 (2010), pp. 251–262.

[125] Chang Sub Park and Stephen J. Payne. "Modelling the effects of cerebral microvasculature morphology on oxygen transport". In: *Medical Engineering and Physics* 38.1 (2016), pp. 41–47.

[126] Natasha M. O'Brown, Sarah J. Pfau, and Chenghua Gu. "Bridging barriers: A comparative look at the blood-brain barrier across organisms". In: *Genes and Development* 32.7-8 (2018), pp. 466–478.

[127] William Cathery et al. "Concise Review: The Regenerative Journey of Pericytes Toward Clinical Translation". In: *Stem Cells* 36.9 (2018), pp. 1295–1310.

[128] M. Intaglietta and B. W. Zweifach. "Geometrical Model of the Microvasculature of Rabbit Omentum from in Vivo Measurements". In: *Circulation Research* 28.5 (1971), pp. 593–600.

[129] Christoph Leithner and Georg Royl. "The oxygen paradox of neurovascular coupling". In: *Journal of Cerebral Blood Flow and Metabolism* 34.1 (2014), pp. 19–29.

[130] Richard B. Buxton. "Interpreting oxygenation-based neuroimaging signals: the importance and the challenge of understanding brain oxygen metabolism". In: *Frontiers in Neuroenergetics* 2 (2010), pp. 1–16.

[131] Ying Cheng et al. "A three-dimensional single-scan approach for the measurement of changes in cerebral blood volume, blood flow, and blood oxygenation-weighted signals during functional stimulation". In: *NeuroImage* 147 (2017), pp. 976–984.

[132] Ravi L. Rungta et al. "Vascular Compartmentalization of Functional Hyperemia from the Synapse to the Pia". eng. In: *Neuron (Cambridge, Mass.)* 99.2 (2018), pp. 362–375.

[133] Jie Liu et al. "Individual variability of cerebral autoregulation, posterior cerebral circulation and white matter hyperintensity". In: *Journal of Physiology* 594.11 (2016), pp. 3141–3155.

[134] Ronney B. Panerai. "Cerebral Autoregulation: From Models to Clinical Applications". In: *Cardiovascular Engineering* (2008), pp. 42–59.

[135] Li Zhang et al. "Steady-state cerebral autoregulation in older adults with amnestic mild cognitive impairment: Linear mixed model analysis". In: *Journal of Applied Physiology* 129.2 (2020), pp. 377–385.

[136] Svend Strandgaard et al. "Autoregulation of Brain Circulation in Severe Arterial Hypertension". In: *British Medical Journal* 1.5852 (1973), pp. 507–510.

[137] Pablo J. Blanco, Lucas O. Müller, and J. David Spence. "Blood pressure gradients in cerebral arteries: A clue to pathogenesis of cerebral small vessel disease". In: *Stroke and Vascular Neurology* 2.3 (2017), pp. 108–117.

[138] Leon C.D. Smyth et al. "Markers for human brain pericytes and smooth muscle cells". In: *Journal of Chemical Neuroanatomy* 92 (2018), pp. 48–60.

[139] Volker Nehls and Detlev Drenckhahn. "Heterogeneity of microvascular pericytes for smooth muscle type alpha-actin". In: *Journal of Cell Biology* 113.1 (1991), pp. 147–154.

[140] Jinping Cheng et al. "Targeting pericytes for therapeutic approaches to neurological disorders". In: *Acta Neuropathologica* 136.4 (2018), pp. 507–523.

[141] Andrée Anne Berthiaume et al. "Dynamic Remodeling of Pericytes In Vivo Maintains Capillary Coverage in the Adult Mouse Brain". In: *Cell Reports* 22.1 (2018), pp. 8–16.

[142] Claire M. Peppiatt et al. "Bidirectional control of CNS capillary diameter by pericytes". In: *Nature* 443.7112 (2006), pp. 700–704.

[143] Terence S. Leung et al. "Estimating a modified Grubb's exponent in healthy human brains with near infrared spectroscopy and transcranial Doppler". In: *Physiological Measurement* 30.1 (2009), pp. 1–12.

[144] Elisa Mitiko Kawamoto, Carmen Vivar, and Simonetta Camandola. "Physiology and pathology of calcium signaling in the brain". In: *Frontiers in Pharmacology* 3 (2012), pp. 1–17.

[145] Marisa Brini et al. "Neuronal calcium signaling: Function and dysfunction". In: *Cellular and Molecular Life Sciences* 71.15 (2014), pp. 2787–2814.

[146] John M. Power et al. "Age-related enhancement of the slow outward calcium-activated potassium current in hippocampal CA1 pyramidal neurons in vitro". In: *Journal of Neuroscience* 22.16 (2002), pp. 7234–7243.

[147] Ephron S. Rosenzweig and Carol A. Barnes. *Impact of aging on hippocampal function: Plasticity, network dynamics, and cognition.* 3. 2003, pp. 143–179.

[148] Marco Giulioni and Mauro Ursino. "Impact of cerebral perfusion pressure and autoregulation on intracranial dynamics: A modeling study". In: *Neurosurgery* 39.5 (1996), pp. 1005–1015.

[149] Esteban Ortiz-Prado et al. "Partial pressure of oxygen in the human body: a general review". In: *American journal of blood research* 9.1 (2019), p. 1.

[150] Monya Baker and Dan Penny. "Is there a reproducibility crisis?" In: *Nature* 533.7604 (2016), pp. 452–454.

[151] Aysha Akhtar. "The Flaws and Human Harms of Animal Experimentation". In: *Cambridge Quarterly of Healthcare Ethics* 24.4 (2015), pp. 407–419.

[152] Seong Gi Kim et al. "Determination of relative CMRO2 from CBF and BOLD changes: Significant increase of oxygen consumption rate during visual stimulation". In: *Magnetic Resonance in Medicine* 41.6 (1999), pp. 1152–1161.

[153] Otto M. Henriksen et al. "Interindividual and regional relationship between cerebral blood flow and glucose metabolism in the resting brain". In: *Journal of Applied Physiology* 125.4 (Oct. 2018), pp. 1080–1089.

[154] Costantino Iadecola. "The Neurovascular Unit Coming of Age: A Journey through Neurovascular Coupling in Health and Disease". In: *Neuron* 96.1 (Sept. 2017), pp. 17–42.

[155] Laura Mandolesi et al. “Effects of physical exercise on cognitive functioning and wellbeing: Biological and psychological benefits”. In: *Frontiers in Psychology* 9.APR (2018), pp. 1–11.

[156] Guohua Zheng et al. “Aerobic exercise ameliorates cognitive function in older adults with mild cognitive impairment: A systematic review and meta-analysis of randomised controlled trials”. In: *British Journal of Sports Medicine* 50.23 (2016), pp. 1443–1450.

[157] Wei Xu et al. “Sleep problems and risk of all-cause cognitive decline or dementia: An updated systematic review and meta-Analysis”. In: *Journal of Neurology, Neurosurgery and Psychiatry* (2019), pp. 236–244.

[158] Patrick J. Smith and James A. Blumenthal. “Dietary Factors and Cognitive Decline.” In: *Dietary Factors and Cognitive Decline.* 3.1 (2016), pp. 53–64.

[159] Ligia J. Dominguez and Mario Barbagallo. “Nutritional prevention of cognitive decline and dementia”. In: *Acta Biomedica* 89.2 (2018), pp. 276–290.

[160] Chen Zhao et al. “Dietary Patterns, Physical Activity, Sleep, and Risk for Dementia and Cognitive Decline”. In: *Current Nutrition Reports* 7.4 (2018), pp. 335–345.